Lead-free Ceramics for High Temperature Actuator Applications

Thesis by

Amir Khesro

Submitted in partial fulfilment for the degree of

Doctor of Philosophy

Thesis supervisors

Prof. Ian M Reaney
Prof. Derek C Sinclair

Department of Material Science and Engineering

University of Sheffield

October 2016

This thesis is
dedicated to the source of my existence
Mor and Lalda

ځمه، ځمه، ځمه

په فکرونولیوني شوم، په لټون لټون شوم ستړي
خو آخر دغې له راغلم، نه پوهیږم نه پوهیږم
خو زه ځمه ځمه ځمه، تل روان یمه په مخه
یو مقام ته ورروان یم، یو مقام ته به رسیږم
او په لاره چه څه راغله، که تیاره وی که رنړه
زه رنړه کښې یم خوشحاله
خو تیارو نه نه یریږم

غنی خان

On, On and Onwards

I am maddened with cares, and tired of searching
Is that not what I am here for? I don't understand-
But on, on, and onwards I go, ever onwards,
Towards a destiny I will one day reach;
And whatever comes on the way, night or day,

I revel in light
But do not fear the dark.

Ghani Khan

(Translation by *Taimur Khan*)

Outcome of the thesis so far…..

Published articles

- **A. Khesro**, R. Boston, I. Sterianou, D. C. Sinclair, and I. M. Reaney, "Phase transitions , domain structure, and pseudosymmetry in La- and Ti-doped $BiFeO_3$.," *J. Appl. Phys.*, vol. 119, no. 5, p. 054101, 2016.

- **A. Khesro**, D. Wang, F. Hussain, D. C. Sinclair, A. Feteira and I. M. Reaney, "Temperature Stable and Fatigue Resistant Lead-free Ceramics for Actuators," *Appl. Phys. Lett.*, vol. 109, no. 14, p. 142907, 2016.

Patent

- Ian M Reaney and **Amir Khesro**, "Temperature Stable Lead-Free Piezoelectric/Electrostrictive Materials with Enhanced Fatigue Resistance" Patent Application No. GB 1609368.4 (2016)

Conference Presentations

- **Amir Khesro** "PbO-free temperature-stable, fatigue resistant electrostrictive ceramics" Sustainable Functional Materials April 2016, Scarborough, UK

- **Amir Khesro**, "Lead-Free Multi-layered Actuators for High Temperature Actuator Applications", 2016 Joint IEEE International Symposium on the Applications of Ferroelectrics, European Conference on Applications of Polar Dielectrics & Workshop on Piezoresponse Force Microscopy, Darmstadt Germany.

Abstract

In the quest of lead-free ceramics with stable electromechanical strains at higher temperatures, the ternary system 1-*x*-*y*$BiFeO_3$-*x*$REFeO_3$-*y*$RE_{2/3}TiO_3$ (RE = La, Nd) B(RE)FT and pseudo-binary solid solutions (1-*x*)$K_{1/2}Bi_{1/2}TiO_3$-*x*(0.80$BiFeO_3$-0.15$LaFeO_3$-0.05$La_{2/3}TiO_3$), KBT-BLFT, (1-*x*)$K_{1/2}Bi_{1/2}TiO_3$-*x*(0.82$BiFeO_3$-0.15$NdFeO_3$-0.03$Nd_{2/3}TiO_3$, KBT-BNFT and (1-*x*)$K_{0.4}Na_{0.6}NbO_{3-}$ *x*($BiFeO_3$) KNN-BF, were studied. Unlike undoped $BiFeO_3$, B(RE)FT, ceramics in the ternary series can sustain large electric fields up to 8 kV/mm but no ferroelectric/antiferroelectric switching is observed indicating that the coercive fields are very high and therefore these ceramics are not likely to be used for actuator applications.

The pseudo-binary solid solutions KBT-BLFT and KBT-BNFT offer opportunities of fabricating ceramics ranging from conventional ferroelectrics to pure electrostrictors. With increase in BLFT/BNFT concentrations, ferroelectric order is disrupted and relaxor-like behaviour is promoted. Promotion of relaxor-like behaviour is accompanied by an increase in positive strain and decrease in hysteresis of these ceramics. Electromechanical strain up to 0.16 % at 6 kV/mm can be achieved. The optimum strains are predominantly electrostrictive and exhibit fatigue resistant behaviour. More importantly the optimised electromechanical strains are stable up to a temperature of 300 °C making them superior to PZT-based ceramics in terms of temperature stability. The ceramics can be fabricated into a multilayer structure by tape casting technique as demonstrated by a prototype multilayer actuator.

The binary solid solution KNN-BF is very limited and dense ceramics could not be fabricated with $x > 0.01$. Within the limited range studied, ceramics yield a strain of 0.05 % (2kV/mm) but the operating window is strongly hampered by the ferroelectric to ferroelectric phase transition which is close to ~100 °C. With Li doping the strain values could be enhanced to 0.12 % (3 kV/mm), however the room temperature phase is strongly polymorphic in nature and a monotonic decay in properties is observed with increase in temperature making these ceramics unsuitable for high temperature applications.

Acknowledgements

First of all, I would like to acknowledge my supervisor Prof. Ian M Reaney, whose continuous support and academic guidance realised this project. There were times in my PhD, when I was hopeless, you motivated me, encouraged me and appreciated every bit of little efforts that I did. You will always remain an inspiration to me. I am also thankful to my co-supervisor Prof. Derek Sinclair for all the insightful discussions and guidance throughout the project. I am really grateful to Dr. Antonio Feteria for giving me access to his brand new ferroelectric testing system. The experiments were crucial to the project and your kind support and guidance in this regard is highly appreciated. Further I would like to thank Prof. Andrew Bell (University of Leeds) and Prof. Mike Reece (Queen Mary University of London) for giving me access to their respective labs for strain measurements and am thankful to Dr. Aurang Zeb (University of Leeds) and Dr. Ye Tian (Queen Mary University of London) for their help with carrying out these experiments.

I would like to mention, that I benefitted from all the postdocs, who worked in the group, but I want to especially thank Dr. Iasmi Sterianou, Dr. Rebecca Boston and Dr. Dawei Wang, who directly contributed to my work. All the PhD students in electroceramics group were great people to work with and I thank you all for the valuable suggestions and discussions. Thanks to Mr Fayaz Hussain for his help with fabrication of multilayer actuators. Thanks to Andrew Mould for quick repairs and fixes of processing and characterisation equipments. Thanks to Nik Maclaren and Sorby Centre staff for facilitating with X-ray diffraction and electron microscopy.

Special thanks to Abdul Wali Khan University Mardan (AWKUM), for generous funding, without which pursuing a PhD was not possible.

I never travelled abroad before coming to England and living away from home in a different world was not easy. With passage of time, amazing friends like Fayaz, Kashif, Ansar, Andy, Kasim and Sarban came into my life and now Sheffield feels like home. Thank you guys. I am also thankful to chums back home for their countless phone calls and encouragements.

I would like to show deepest appreciations to my parents and siblings, who were always there when I needed a shoulder. Thanks for your unconditional love and support. I will be indebted forever to my wife Naz, who sacrificed her happiness for my career. You were not supposed to live away from me for two long years but you happily accepted it for the sake of my studies. Thanks for standing beside me in through thick and thin. Last but not the least, thanks to my kids (Ayza and Zari), who are a source of unending joy, happiness and smiles.

Amir Khesro

Contents

Chapter 1: Introduction

1.1 Introduction

Piezoelectric materials are indispensable in many areas such as automotive electronics, medical technology, industrial systems and consumer products and are ubiquitous in our lives. A piezoelectric component can work as a sensor, actuator or a transducer and hence encompasses a whole range of applications from devices operating in deep sea to those in aerospace applications [1]. The focus of this project is to seek performant PbO-free actuator materials. Therefore, in addition to conventional ferroelectrics, relaxor ferroelectrics are also of interest because of their ability to produce large electrostrictive strains [2].

A piezoelectric or electrostrictive actuator converts an electrical signal into a precisely controlled mechanical strain. The ability to control physical displacements with high precision is vital for applications such as cameras, phones, microscopes, fuel injectors, micro-pumps, ink cartridges and medical instruments [3]. $Pb(Zr,Ti)O_3$ (PZT)-based piezoelectric and $Pb(Mg_{1/3}Nb_{2/3})O_3$ (PMN)-based electrostrictive ceramics are most widely used in actuator devices due to their large electromechanical coupling coefficients [4]. A major concern is however, that both PZT and PMN contain more than 60 % PbO by weight. The toxic effects of lead are well known. The median lethal dose (MLD50) of Pb is 450 mg/Kg and that of PbO is 4300 mg/Kg. MLD50 refers to the quantity of a substance which is enough to kill half of the tested population. In Europe legislation such as, Restriction of the Use of Certain Hazardous Substances in Electrical and Electronic Equipment (RoHS) and Registration, Evaluation, Authorisation and Restriction of Chemical Substances (REACH) regulates the use, production and import of hazardous substances. At the moment the use of lead in piezoelectric materials is exempt from these regulations due to unavailability of appropriate lead-free materials. But legislation (both in Europe and other countries) against use of lead is getting more strict with time, which has triggered an intense research in lead–free alternatives in piezoelectrics. As a result of more than a decade of active research worldwide three families of lead-free materials have

emerged as potential candidates for replacing lead-based piezoelectrics. Promising lead-free families are those based on $BaTiO_3$ (BT), $Na_{1/2}Bi_{1/2}TiO_3$ (NBT) and $(K,Na)NbO_3$ (KNN). The properties in these materials are good enough to start replacing PZT-based materials for applications operating near room temperature [5]. However, many harsh environments including oil well drilling, aerospace, automobile and power plant engines require actuators to sustain electromechanical strains at elevated temperatures [6]. Which is big challenge for all prominent lead-free materials.

For sake of comparisons it is important to mention that commercially used lead-based materials have their own limitations at higher temperatures. Electromechanical strain in $Pb(Mg_{1/3}Nb_{2/3})O_3$-based ceramics is not stable due to notable temperature dependence of polarisation above the permittivity maximum [7]. For example, $0.90Pb(Mg_{1/3}Nb_{2/3})O_3$-$0.10PbTiO_3$ loses about ~40 % of its room temperature electromechanical strain, when temperature is increased from RT to 80 °C [8,9]. In the case of conventional PZT-based piezoelectrics the operating range is limited by Curie temperature (T_C) which ranges from 300-400 °C and allows operational ranges up to ~175 °C [10]. e.g. PZT4 has a T_C of ~250 °C [11], and can provide temperature stable strains up to ~160 °C, assuming 15 % of variation from the room temperature value as acceptable [12]. Other materials such as $Bi_4Ti_3O_{12}$, $LiNbO_3$ and AlN have very high T_C but the piezoelectric coefficients are too small to be compared with PZT-based ceramics [13]. Hence development of materials for high temperature actuator applications on its own is an active field of research regardless of the toxicity of lead.

However motivation behind this project is to compositionally tailor lead-free materials which are comparable to PZT-based ceramics in both performance and temperature stability. $BiFeO_3$ is a perovskite material well known for its room temperature multiferroic properties. Luckily, it has a very high T_C (~825 °C) and can be a potential candidate for high temperature piezoelectric applications but has not received a lot of attention due to problems in processing and the associated high conductivities which hinders application of high electric fields [14]. Therefore, the premise of the thesis was to address the core issues in $BiFeO_3$ through co-doping initially and then form solid solutions with other lead-

free high T_C perovskites, to achieve appreciable electromechanical strains. The project is completed in three phases.

Phase 1: The first part of the project aims to control processing and conductivity in $BiFeO_3$ by co-doping rare earths (La,Nd)- and Ti- into the perovskite structure. The resulting phase transitions are studied and the viability of these ceramics for actuator applications are explored.

Phase 2: In PZT-based ceramics high performance is achieved through formation of a morphotropic phase boundary between the rhombohedral and tetragonal phases. $BiFeO_3$ has rhombohedral symmetry so it can be used an endmember with other lead-free perovskites of different symmetries to form phase boundaries which can result in enhanced electromechanical properties. Similarly the derivatives of $BiFeO_3$ ceramics with low loss and antiferroelectric order obtained in phase 1, can be also be used as endmembers. Therefore solid solutions between $BiFeO_3$-based endmembers with $K_{1/2}Bi_{1/2}TiO_3$ are fabricated and the electromechanical properties studied as a function of temperature.

Phase 3: Ceramics require very high voltage for achieving usable strain, therefore actuator technologies often rely on multilayer structures to form devices that can operate with manageable voltages. Therefore, the third part of the project is to demonstrate a lead-free prototype multilayer actuator based on optimised composition.

1.2 References

[1] J. Holterman and P. Groen, *An Introduction to Piezoelectric Materials and Applications*. Stiching Applied Piezo, 2013.

[2] K. Uchino, *Ferroelectric Devices*. Marcel Dekker Inc., 2000.

[3] W. Jo, R. Dittmer, M. Acosta, J. Zang, C. Groh, E. Sapper, K. Wang, and J. Rödel, "Giant electric-field-induced strains in lead-free ceramics for actuator applications - Status and perspective," *J. Electroceramics*, vol. 29, no. 1, pp. 71–93, 2012.

[4] D. Damjanovic, N. Klein, J. Li, and V. Porokhonskyy, "What Can Be Expected From Lead-Free Piezoelectric Materials?," *Funct. Mater. Lett.*, vol. 3, no. 1, pp. 5–13, 2010.

[5] J. Rödel, K. G. Webber, R. Dittmer, W. Jo, M. Kimura, and D. Damjanovic, "Transferring lead-free piezoelectric ceramics into application," *J. Eur. Ceram. Soc.*, vol. 35, no. 6, pp. 1659–1681, 2015.

[6] T. Stevenson, D. G. Martin, P. I. Cowin, A. Blumfield, A. J. Bell, T. P. Comyn, and P. M. Weaver, "Piezoelectric materials for high temperature transducers and actuators," *J. Mater. Sci. Mater. Electron.*, vol. 26, no. 12, pp. 9256–9267, 2015.

[7] S.-T. Zhang, A. B. Kounga, W. Jo, C. Jamin, K. Seifert, T. Granzow, J. Rödel, and D. Damjanovic, "High-strain lead-free antiferroelectric electrostrictors," *Adv. Mater.*, vol. 21, no. 46, pp. 4716–4720, 2009.

[8] K. Uchino, *Piezoelectric Actuators and Ultrasonic Motors*. Springer US, 1997.

[9] C. Galassi, M. Dinescu, K. Uchno, and M. Sayer, *Piezoelectric Materials: Advances in Science, Technology and Applications*, vol. 76. Springer Netherlands, 2000.

[10] S. O. Leontsev and R. E. Eitel, "Progress in engineering high strain lead-free piezoelectric ceramics," *Sci. Technol. Adv. Mater.*, vol. 11, no. 4, p. 44302, 2010.

[11] M. W. Hooker, "Properties of PZT-Based Piezoelectric Ceramics Between -150 and 250 °C," *Langely research center*, 1998.

[12] Y. Saito, H. Takao, T. Tani, T. Nonoyama, K. Takatori, T. Homma, T. Nagaya, and M. Nakamura, "Lead-free piezoceramics," *Nature*, vol. 432, pp. 84-87, 2004.

[13] I. Sterianou, "Bismuth-based Perovskites for High Temperature Piezoelectric Applications," University of Sheffield, 2007.

[14] K. Kalantari, I. Sterianou, S. Karimi, M. C. Ferrarelli, S. Miao, D. C. Sinclair, and I. M. Reaney, "Ti-Doping to Reduce Conductivity in $Bi_{0.85}Nd_{0.15}FeO_3$ Ceramics," *Adv. Funct. Mater.*, vol. 21, pp. 3737–3743, 2011.

Chapter 2: Basic Theory and Literature Review

2 Introduction

The first part of the chapter will discuss basic theory of piezoelectric and electrostrictive materials followed by a brief discussion on general strategies to enhance electromechanical coupling. In the second part, lead-free materials studied in this project i.e. $BiFeO_3$, $K_{1/2}Bi_{1/2}TiO_3$ and $(K,Na)NbO_3$ will be reviewed with focus on their possible applications in actuators.

2.1 Basic theory

2.1.1 Piezoelectricity

The name piezoelectricity is derived from ancient Greek '*piezein*' which means to press or to squeeze and '*elecktron'* meaning amber, describing substances that (like amber) can attract other matter when rubbed. Piezoelectricity thus literally means pressure induced electricity.

The phenomenon was discovered in 1880 by the brothers Pierre and Jacques Curies. They observed that certain crystals such as quartz, Rochelle salt, tourmaline and cane sugar were able to generate charge on certain positions of their surfaces when squeezed in a certain direction. Which is now known as the direct piezoelectric effect. In 1881, inverse phenomenon, (strain developed in a material in response to an applied electric field) was predicted by French Physicist Gabriel Lippmann, which was experimentally proved by the Curie brothers in the same year. This phenomenon is now known as the indirect, inverse or converse piezoelectric effect. Thus a piezoelectric material can be defined as, "a material having the ability to convert mechanical energy to electrical energy and vice versa." For a material to show piezoelectric behavior, the material should be dielectric and lack a centre of symmetry [1].

2.1.2 Dielectrics

The word '*dia*' in dielectrics is derived from Greek, which means 'through' or 'across'. Thus dielectrics refer to materials which allow passage of electric field but not particles. Therefore, an ideal dielectric should be a perfect insulator, which does not permit passage of any kind of charged particles including electrons. Thus, application of an external electric field (*E*) can only distort the charge distribution of atoms or molecules in dielectrics by either stretching or rotating. The stretching and/or rotations will result in an array of small dipoles in the direction of electric field. Figure 2.1 illustrates a schematic of the phenomenon. The charges in the yellow box will effectively cancel each other out and leave only opposite charges on each surface resulting in a field opposing the original field. The material is now considered polarised.

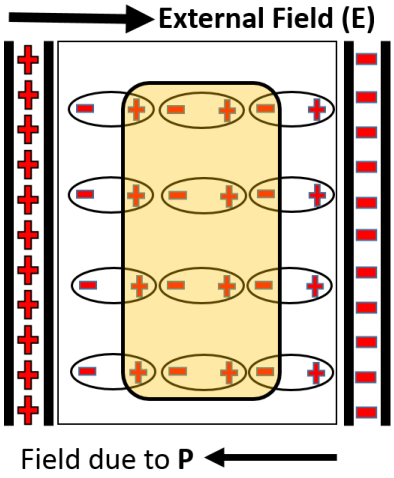

Figure 2.1: Polarisation of a dielectric material under static electric field

The net macroscopic polarisation (*P*) is related to relative permittivity/dielectric constant ($\boldsymbol{\varepsilon_r}$) through equation 2.01.

$$\boldsymbol{P = \varepsilon_0 E\,(\varepsilon_r - 1) = \varepsilon_0 \chi E} \qquad \text{Equation 2.01,}$$

where, $\boldsymbol{\varepsilon_0}$ is permittivity of free space (8.854118×10^{-12} F.m^{-1}) and $\boldsymbol{\chi = \varepsilon_r - 1}$ is dielectric susceptibility. The macroscopic polarisation can also be expressed as a

summation of all polarisations originating at the microscopic level. A dielectric can have one or more of the following five types of microscopic polarisations.

1) Electronic polarisation is displacement of electron cloud with respect to positive nuclei upon application of external field.

2) Atomic/ionic/vibrational polarisation is displacement of ions in a polyatomic molecule with respect to each other upon application of external field.

3) Dipolar or orientational polarisation is only present in dielectrics with permanent dipole moments. Application of an external field re-orients these dipoles in the direction of applied field.

4) Spontaneous or domain wall polarisation is present only in ferroelectrics. Application of an electric field results in movement of boundaries that separate different domains. Ferroelectrics will be discussed in detail in section 2.1.4.

5) Interface or space charge polarisation is present in dielectrics with high concentration of charge carriers. Application of electric field results in a polarisation due to migration of these charge carriers.

Electronic and atomic polarisations originate from the lattice and are thus termed as intrinsic. Dipolar, domain wall and interface polarisations are not directly related to lattice and hence termed as extrinsic. When the external electric field is removed, a polarised dielectric material will tend to go back to its original equilibrium state. Going back to depolarised state is not instantaneous but require a finite time, sometime known as relaxation time. Relaxation time in case of electronic and atomic polarisation is generally very short ($\sim 10^{-12}$ sec) but in case of orientational and interface polarisation, relaxation time can be quite long and varies in a wide range depending on dielectric system. Due to different relaxation times, different microscopic polarisations can be distinguished from each other by looking at response of dielectric material in an oscillating electric field. Resonance of a vibrating system occurs when the driving frequency of oscillating electric field becomes equal to natural frequency of the system. A schematic of frequency dependence of different polarisations is depicted in Figure 2.2.

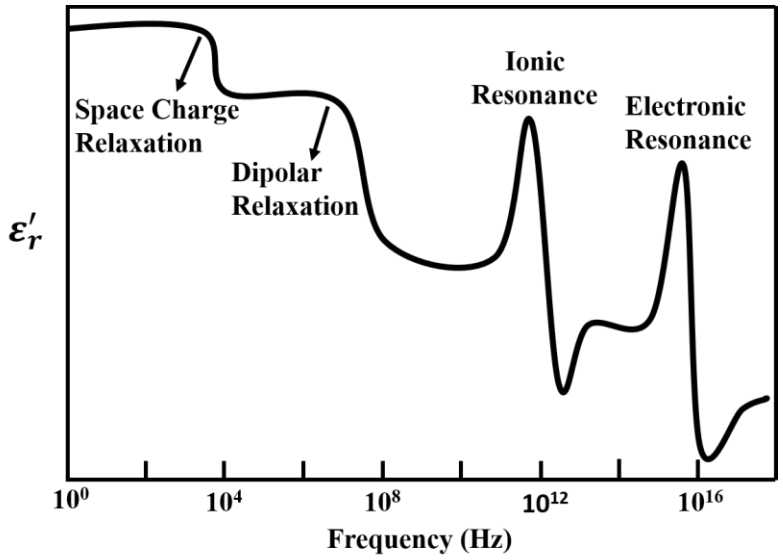

Figure 2.2: Frequency response of dielectric mechanisms (redrawn after [2]).

If the time period of oscillating field is much smaller than the relaxation time of polarisation, then the polarisation will not be able to keep up with oscillating frequency. In other words energy is absorbed by materials dissipated as heat known as dielectric loss due to relaxation. In an ideal dielectric, there are no free charges and phase difference between current and voltage is 90° and relative permittivity will be entirely real. In real dielectrics a finite number of free charges are always present and hence the phase difference between current and voltage is less than 90° *i.e.* (90°-δ), which results in a complex relative permittivity ($\boldsymbol{\varepsilon_r^*}$) depicted in Figure 2.3.

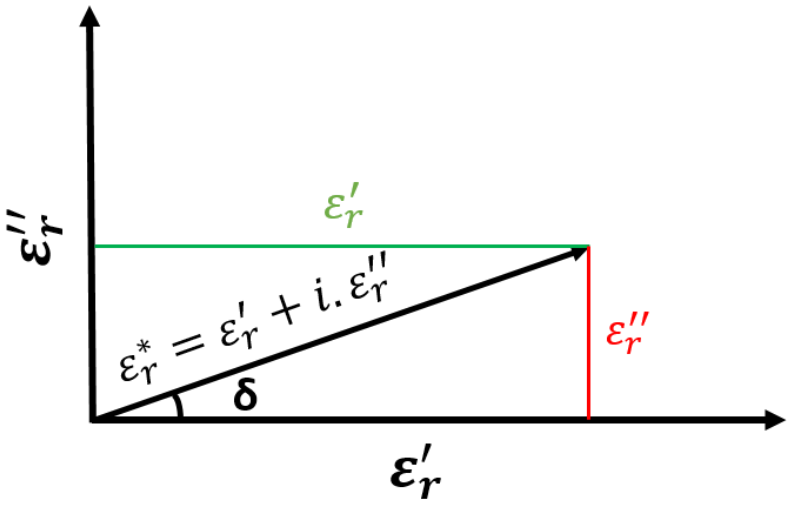

Figure 2.3: Argand diagram of complex permittivity (ε_r^*). Real part is represented by (ε_r') and imaginary part is represented by (ε_r'') (redrawn after [3]).

From Figure 2.3, tan δ can be defined as the ratio of imaginary part ($\boldsymbol{\varepsilon_r''}$) to real part ($\boldsymbol{\varepsilon_r'}$) and is often used to quantify losses in dielectrics. tan δ contains contribution both from relaxation and conduction [3,4].

2.1.3 Classification of dielectrics

All crystalline materials can be represented by 32 crystallographic point groups. 11 out of these point groups are centrosymmetric. All centrosymmetric materials are non-piezoelectric as application of stress does not result in any net polarisation due to symmetric displacement of ions. However, application of electric field can result in a non-linear electromechanical strain. The phenomenon is known as electrostriction and is a property of all dielectrics. Electrostriction will be discussed in section 2.1.6. The remaining 21 point groups are non-centrosymmetric. 20 out of 21 non-centrosymmetric classes show piezoelectricity. The only exception is class 432, which does not show piezoelectricity because the existing symmetry elements combine to cancel out any changes in the dipole moment. Out of these 21 point groups 10 classes are polar and the remaining 11 are non-polar. Non-polar point groups do not have any spontaneous polarisation but can be polarised with application of stress due to their non-

centrosymmetric nature with the exception of class 432. Polar point groups have a spontaneous polarisation and show pyroelectricity. In pyroelectrics the spontaneous polarisation cannot be reversed at known experimental electric fields. However pyroelectrics are not relevant to this work and the focus will be on a sub-class of pyroelectrics known as ferroelectrics, where the spontaneous polarisation can be reversed by an electric field of magnitude less than the dielectric breakdown field. The classification of 32 point groups is illustrated in Figure 2.4 [4].

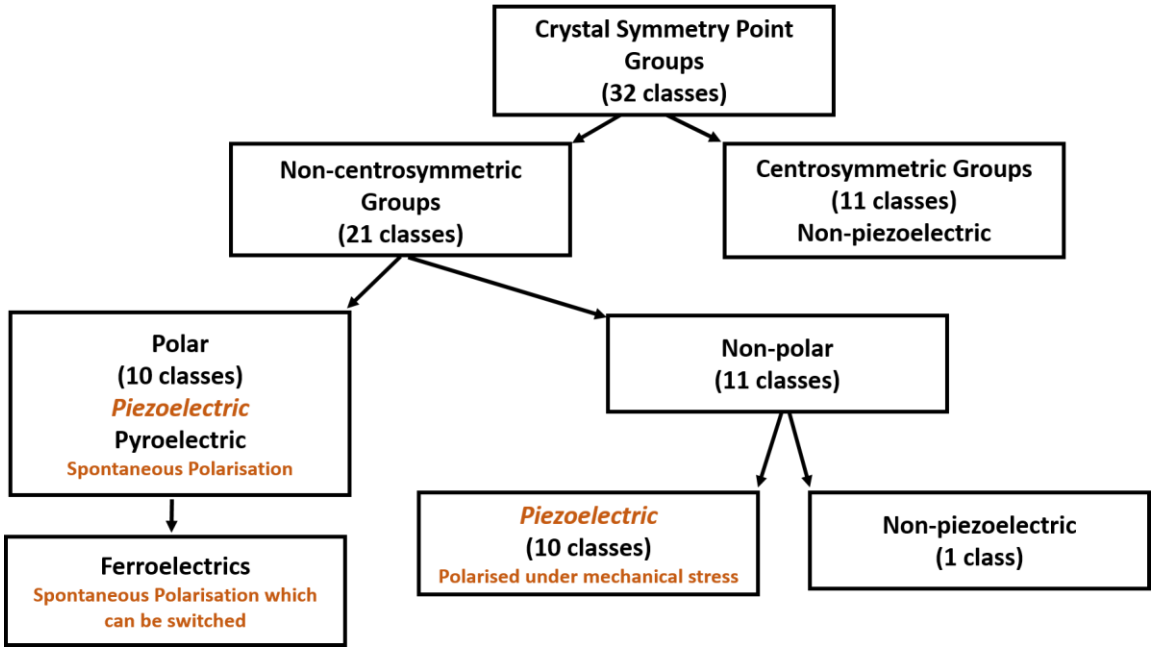

Figure 2.4. Classification of crystals, showing the classes with piezoelectric, pyroelectric and ferroelectric effects (redrawn after [4]).

2.1.4 Ferroelectrics

The prefix ‘ferro’ in ferroelectric is derived from Latin word ferrum, which means iron. Therefore the word ‘ferroelectric’ may be misleading as iron is not essential for ferroelectricity. Ferroelectric is rather an analogy of ferromagnetic due to many similarities of ferroelectrics with ferromagnetics. Ferroelectric materials are defined as materials with spontaneous polarisation that are switchable by an electric field [5]. Most

ferroelectric materials will go through a phase change from polar ferroelectric state to a non-polar paraelectric state at a particular temperature known as Curie temperature (T_C). The symmetry of polar state is always lower than symmetry of paraelectric phase. This transition is accompanied by strong anomalies in dielectric, thermal and elastic properties. In the paraelectric phase, ferroelectrics obey the Curie-Weiss law given in equation 2.02.

$$\varepsilon_r - 1 = \frac{C}{T - T_o} \qquad \text{Equation 2.02,}$$

where C is Curie constant and T_o is Curie-Weiss temperature. In ferroelectrics, $\varepsilon_r \gg 1$, hence $\varepsilon_r - 1 \approx \varepsilon_r$ and the Curie-Weiss law can be approximated to a direct relation between $\frac{1}{\varepsilon_r}$ and temperature (T). A schematic representation of ε_r, $\frac{1}{\varepsilon_r}$ and spontaneous polarisation P_s for first order transition as a function of temperature is shown in Figure 2.5.

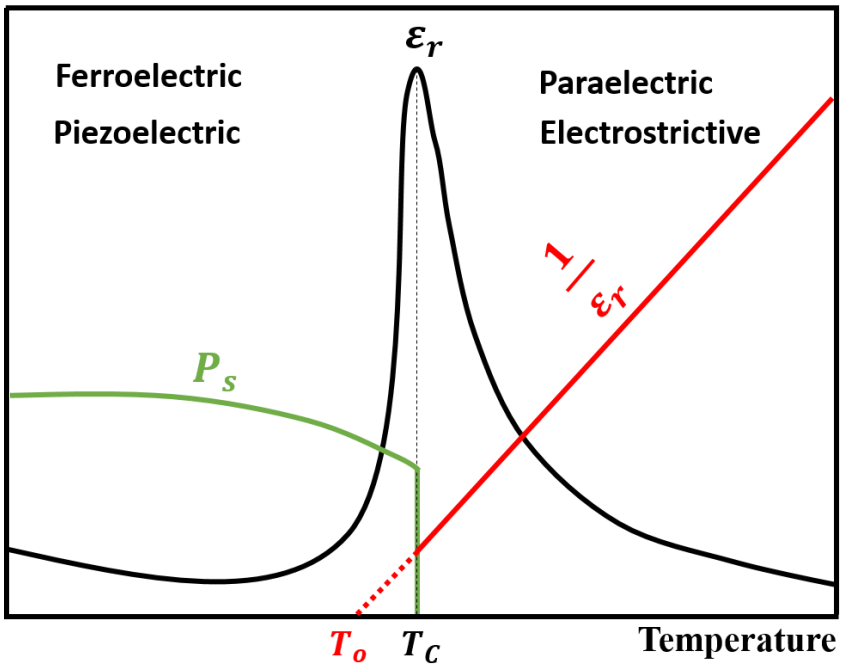

Figure 2.5. Schematic of ε_r, $\frac{1}{\varepsilon_r}$ and P_s vs. T for a first order transition.

T_o can be obtained from x-intercept by extrapolating the trend in plot of $\frac{1}{\varepsilon_r}$ vs. T. Note that $T_o < T_C$ for first order phase transitions, while $T_o = T_C$ for second order phase transition. In a first order phase transition there is a sudden change in order parameter at T_C. In this case order parameter is P_s, which drops discontinuously at T_C and the material loses all ferroelectricity and hence piezoelectricity [6,7].

Ceramic ferroelectrics can be classified into four sub groups on the basis of their unit cell structure, namely: (1) the perovskites (2) the tungsten-bronzes (3) the pyrochlores, and (4) the bismuth layered structures. Of these, perovskites are by far the most important in terms of applications and is focus of this study [8]. Perovskites have an ABO_3 type unit cell where A and B are metallic cations and O the oxygen anion. An ideal perovskite structure is introduced in Figure 2.6.

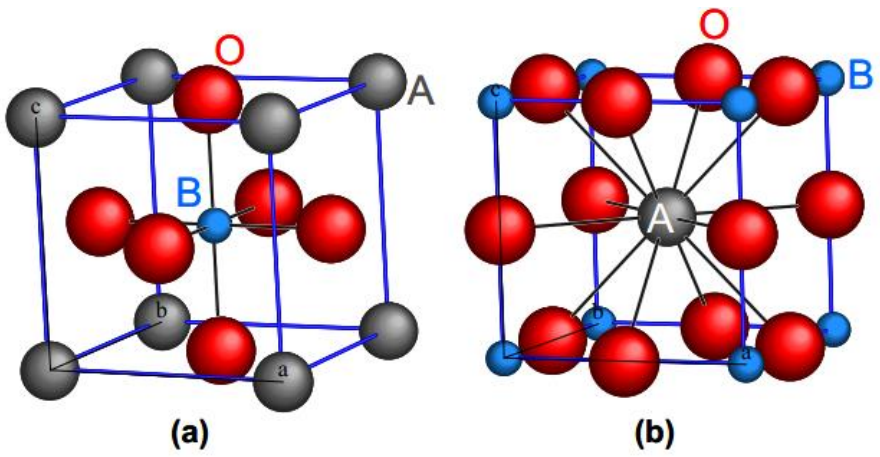

Figure 2.6. Ideal perovskite structure with a) B cation at the center; b) A cation at the center. The A and B site cations are coordinated to 12 and 6 oxygens, respectively, while oxygen is coordinated to 4 A and 2 B cations [9].

In 1926 Goldschmidt introduced an empirical relation given in equation 2.03 to describe ideal perovskite structure based on the packing of ions as rigid spheres.

$$R_A + R_O = \sqrt{2}\,(R_B + R_O) \qquad \text{Equation 2.03,}$$

where, R_A, R_B and R_O are radii of A-site, B-site and O anion, respectively. However, this ideal relationship is rarely satisfied and thus to explain deviation from the ideal relation, Goldschmidt defined the tolerance factor (*t*), equation 2.04 [10].

$$t = \frac{R_A + R_O}{\sqrt{2}\,(R_B + R_O)} \qquad \text{Equation 2.04,}$$

Compounds in the perovskite family are found to exist over the range $0.78 < t < 1.05$ [11]. When $t = 1$, a centrosymmetric cubic structure is favoured and is therefore non-ferroelectric. A typical example is $SrTiO_3$, where $t = 1.002$ at room temperature [12]. For $t > 1$, perovskites generally optimise their coordination environment by off centring the B-site cation resulting in ferroelectric order, as in case of $BaTiO_3$. This happen because the B-site cation is too small to coordinate with neighbouring ions in the cubic phase [13]. Here, it is important to mention that ferroelectric distortion can also arise from lone pair activity of the A-site cation such as occurs in $BiFeO_3$. Both mechanisms can also occur at the same time. For example, in the case of $PbTiO_3$, both Pb and Ti ions contribute to ferroelectric distortion [14]. For $t < 1$, the coordination environment of the A-site cation is optimised by octahedral rotation [13] often called the Glazer Tilt systems. During tilting of the octahedral, corner sharing connectivity is retained and the octahedra are largely undistorted. These rotations do not cause ferroelectricity in cubic perovskites because rotation of octahedra in one direction induces a rotation of the same magnitude in the opposite direction, as shown in Figure 2.7. Hence, centrosymmetry is retained and the material is non-ferroelectric [5].

Figure 6 in reference [5]

Figure 2.7. Tilting of the oxygen octahedra in cubic perovskites (Schematic). Notice that when the central octahedron rotates clockwise, its neighbours in the plane are required to rotate anticlockwise in order to maintain connectivity. As a result final structure is non polar [5].

2.1.4.1 Ferroelectric domains and hysteresis

Ferroelectric domains are the regions of crystals in which spontaneous polarisation is uniformly oriented. The space separating two domains is known as a domain wall. The width of domain walls in ferroelectrics is as small 2-3 unit cells. Hence, change in polarisation from one domain to another is very steep. At the onset of the paraelectric-ferroelectric phase transition, a depolarisation field gives rise to electrostatic energy and mechanical constraints give rise elastic energy and hence energetically a single domain state is not favourable. Domains are formed to minimise these energies. The regions separating different orientations of spontaneous strain tensor and/or polarisation vector are known as ferroelectric (separating only regions of differing polarisation vector) and ferroelastic/ferroelectric (separating different strain tensor and polarisation vector regions) domain walls. The types of domain wall that form in a ferroelectric material depend on symmetry of both ferroelectric and non-ferroelectric phases of the underlying crystal structure. For example in case of tetragonal $PbTiO_3$ the polarisation is along the c-axis of tetragonal unit cell. This gives six possible directions along the c-axis of paraelectric cubic unit cell as shown in Figure 2.8 (a). Electrostatic and elastic energies are minimised by formation of complex domain structure with many 180° and 90° domain walls shown schematically in Figure 2.8 (b). In case of rhombohedral phase of $Pb(Zr,Ti)O_3$ and $BaTiO_3$, the direction of polarisation is along the body diagonal <111> of the paraelectric cubic unit cell. This gives eight possible directions with 180°, 109° and 71° domain walls [7].

Adopted from Figure 6.5 in reference [15]

Figure 2.8. (a) Six possible variants of cubic-to-tetragonal phase transformation. Arrows indicate direction of polarisation and b) schematic of 180° and 90° domain walls [15].

A random distribution of ferroelectric domains result in zero net polarisation, a result of which polycrystalline materials do not exhibit piezoelectricity. However, these domains

can be reoriented in a specific direction by applying a strong electric field (poling, 10-100 kV cm^{-1}) usually at high temperatures. When a poling field is removed, a ferroelectric material retains some of the macroscopic polarisation known as remanent polarisation, as shown in Figure 2.9. The magnitude of remanent polarisation depends on many factors including available domain states, electromechanical boundary conditions at the sample surface and grain boundaries, and the presence of defects in the material.

Figure 7 in reference [7]

Figure 2.9. A polycrystalline ferroelectric with random orientation of grains before and after poling. Note that polarisation is non-zero after poling [7].

The most distinguishing feature of a ferroelectric material is switching of the polarisation state by application of an electric field. Hysteresis is an important consequence of domain wall switching in ferroelectrics. Bipolar hysteresis loops of polarisation vs. electric field (*P*-*E*) and strain vs. electric field (*S*-*E*) are shown in Figure 2.10.

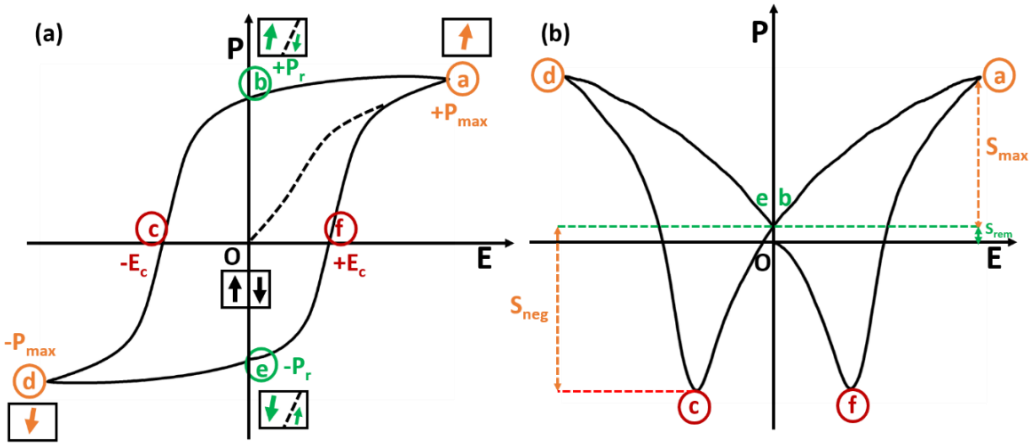

Figure 2.10. (a) *P*-*E* hysteresis loop for a polycrystalline ferroelectric. Rectangles with arrows indicate the polarisation state of material at key points; (b) Corresponding *S*-*E* loop of the same material. The actual loops were measured on (K,Na)NbO_3-based material studied in this project. The symbol used in the figure are explained in text.

In Figure 2.10 point 'O' refers to origin of the plot with zero electric field. At this point net polarisation is zero due to random distribution of domains as indicated by two arrows of the same magnitude but opposite direction. When an electric field is applied, the polarisation increases. The response is linear at low field but becomes strongly non-linear, when the field becomes high enough, so that the domains reorient in direction of the applied field. At point 'a' all possible domain switching has occurred and the polarisation achieved by the material is represented by the maximum polarisation (P_{max}). At this point the material will be expanded as well, giving a maximum strain (S_{max}). An important figure of merit for actuators commonly known as large signal piezoelectric co-efficient d_{33}^* can be defined, and is given by equation 2.05.

$$\boldsymbol{d_{33}^* = \frac{S_{max}}{E_{max}}} \qquad \text{Equation 2.05}^{\$},$$

where, E_{max} is the field at which strain is maximum S_{max}. At point 'b', when the electric field decreases to zero, some of the domains will switch back but an overall non-zero net polarisation is retained known as remanent polarisation (P_r). Similarly residual strain that may be retained at zero field is known as remanent strain (S_{rem}). The field required to achieve the initial state of zero net polarisation is known as coercive field (E_c), indicated by point 'c'. Note that strain is negative (S_{neg}) in this region (b-c), because the field is opposite to the direction of spontaneous polarisation, which results in compression. At the coercive field, the domains switch again and hence applied field becomes parallel to the spontaneous polarisation and the strain becomes positive. A hysteric loop is completed when the field is further increased to maximum on the negative side (point 'd') and then decreased to zero (point 'e'). In the ideal case, *P-E* and *S-E* hysteresis loops are completely symmetric and therefore $+E_c = -E_c$ and $+P_r = -P_r$. However symmetries of the loops can be disturbed by many factors including the presence of charged defects, preparation conditions, mechanical stresses and thermal treatment [7].

$ Some times in the literature d_{33}^* is used for small signal piezoelectric coefficient defined in equation 2.08. However in this text by d_{33}^*, the author mean $\boldsymbol{\frac{S_{max}}{E_{max}}}$ only.

2.1.4.2 Relaxor ferroelectrics

As discussed in the preceding section, ferroelectric phases transform to a paraelectric phase at T_C, above which the Curie-Weiss law is obeyed. However, in some perovskites, unlike the sharp paraelectric-to-ferroelectric transition in normal ferroelectrics, a diffuse phase transition (DPT) is observed. The point where permittivity is maximum is usually represented by T_m and is strongly frequency dependent. These type of perovskites are normally classed as relaxor ferroelectrics or simply relaxors [16]. Early realization of the importance of relaxors came with the observance of large electrostrictive strains in $Pb(Mg_{1/3}Nb_{2/3})O_3$ (PMN) by Smolenskii group [17]. Compositional disorder (mixed cations of different valence distributed randomly amongst equivalent lattice sites) is a common feature of all relaxors. In addition to PMN other typical examples are $Pb_{1-x}La_{2/3x}Zr_{1-y}Ti_yO_3$, $Pb(Sc_{1/3}Ta_{2/3})O_3$ and $(1-x)Pb(Mg_{1/3}Nb_{2/3})O_3$-$xPbTiO_3$. Relaxors usually have high dielectric and electromechanical properties in vicinity of DPT, making them attractive materials for applications in capacitors and actuators. An additional advantage of DPT is the ability to retain properties in a wide range of temperature [18].

Relaxors have a high temperature non-polar paraelectric phase similar to that of normal ferroelectrics, where Curie-Weiss law is obeyed. On cooling from PE state, relaxors transform to ergodic (ER) phase at a temperature called the Burns temperature T_B. The transition from PE to ER does not involve any change in crystal structure at macroscopic or mesoscopic scale and is usually not considered as structural phase transition. However, the ER phase is completely different in terms of physical properties to that observed in the PE phase. This peculiar behavior in the ER state is associated to the development of nano-scale regions (typically 2-10 nm), known as polar nano-regions (PNRs), which are dynamic near T_B. The word ergodic refers to the dynamic nature of these PNRs. As the materials are cooled, the dynamic behavior of PNRs slows down. Upon further cooling down the transition depends on the type of relaxor. Non-canonical relaxor can spontaneously transform to FE phase from ER phase at certain temperature usually called the Curie temperature T_C in analogy to that of normal ferroelectrics. In canonical relaxors, PNRs completed freeze at a temperature (usually hundreds degree below T_B known as the freezing point, T_f). The relaxor is now known to be in the non-ergodic (NER) phase. The

PNRs are randomly oriented and hence the macroscopic state in NER phase is non-polar. However with application of a high electric field, the NER phase can be transformed irreversibly to FE phase [19, 20]. A prototypical dielectric response of canonical relaxor is shown in Figure 2.11.

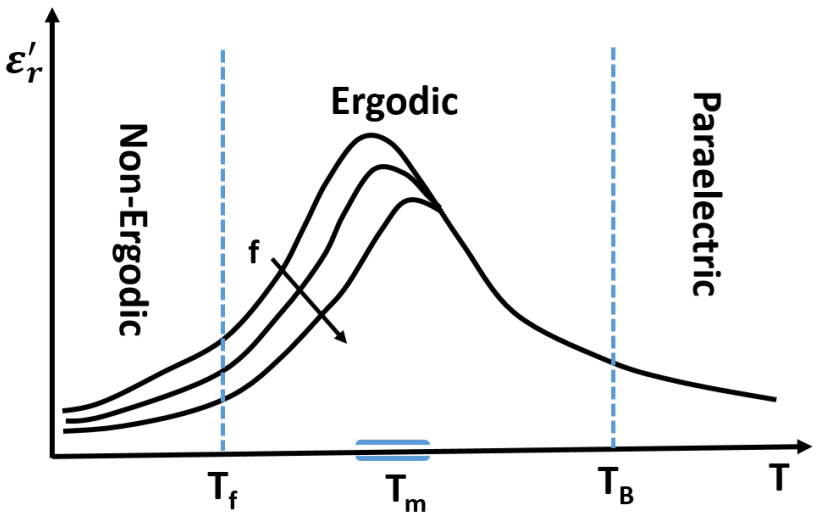

Figure 2.11: Prototypical response of a canonical relaxor

The microscopic origins of PNRs are still not understood, though several models [21-29] have been proposed. Details of these models is out of the scope of this work but in general models are based on two different approaches. The first considers PNRs as local frustrations embedded into a cubic matrix (Figure 2.12 (a)). The second approach is to consider PNRs as nano-domains separated by domain wall and not by regions of cubic symmetry as shown in Figure 2.12 (b) [19].

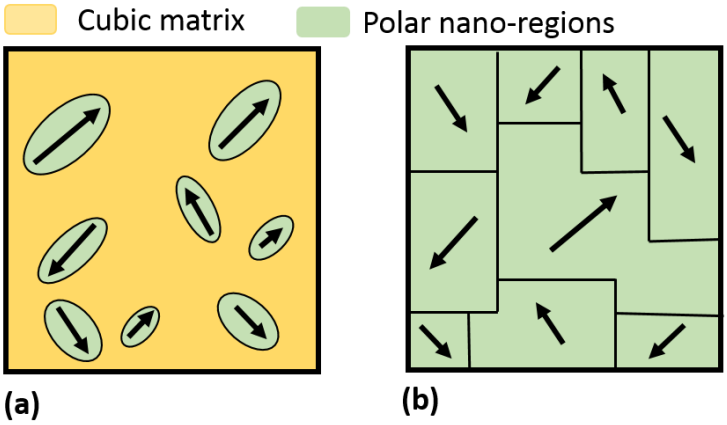

Figure 2.12: (a) PNRs embedded in a cubic matrix; (b) nano-domains separated by domain walls. Arrows indicate polarisation directions (redrawn after [19]).

2.1.5 Basic tensor properties of piezoelectric materials

The application of stress on an elastic object results in strain, which in linear region can be approximated by Hook's law given in equation 2.06.

$$\boldsymbol{x_{ij}} = \boldsymbol{s_{ijkl}X_{kl}} \qquad \text{Equation 2.06,}$$

where $\boldsymbol{s_{ijkl}}$ (elastic compliance) is a fourth rank tensor that relates second rank tensors $\boldsymbol{x_{ij}}$ (strain) and $\boldsymbol{X_{kl}}$ (stress). In piezoelectric materials, in addition to strain, the applied stress can result in a charge density (D), which is called the direct effect and can be expressed by the linear relationship given below.

$$\boldsymbol{D_i} = \boldsymbol{d_{ijk}X_{jk}} \qquad \text{Equation 2.07,}$$

Similarly the inverse phenomenon, where an electric field (E) results in strain (x) can be expressed by the linear relationship,

$$\boldsymbol{x_{ij}} = \boldsymbol{d_{kij}E_k} \qquad \text{Equation 2.08,}$$

$\boldsymbol{d_{ijk}}$ (pC/N) in equation 2.07 and $\boldsymbol{d_{kij}}$ (pm/v) in equation 2.08 are third rank tensors known as piezoelectric co-efficients [7]. Generally speaking, a tensor of order n has 3^n elements.

Therefore, the 3rd rank tensor *d* in this case should have 27 elements as shown in the arrays below.

$$i = 1, \qquad i = 2, \qquad i = 3$$

$$\begin{bmatrix} d_{111} & d_{112} & d_{113} \\ d_{121} & d_{122} & d_{123} \\ d_{131} & d_{132} & d_{133} \end{bmatrix} \begin{bmatrix} d_{211} & d_{212} & d_{213} \\ d_{221} & d_{222} & d_{223} \\ d_{231} & d_{232} & d_{233} \end{bmatrix} \begin{bmatrix} d_{311} & d_{312} & d_{313} \\ d_{321} & d_{322} & d_{323} \\ d_{331} & d_{332} & d_{333} \end{bmatrix}$$

Both stress and strain are symmetric tensors, i.e. $d_{ijk} = d_{ikj}$, therefore the number of elements are reduced to 18. However the tensor notation introduced in equations 2.06 and 2.07 are rarely used and the suffixes are reduced by introducing matrix notations given in table 2.1 [6].

Table 2.1: Conversion of full tensor notation to reduced (1-6) matrix notations

Tensor Notation	**11**	**22**	**33**	**23,32**	**31,13**	**12,21**
Matrix Notation	1	2	3	4	5	6

The number N=18 refer to the case of triclinic symmetry with point group 1. N can be significantly reduced as we go to high symmetry crystals following Neumann principle, which states "*the symmetry elements of any physical property of a crystal must include all the symmetry elements of the point group of the crystal"* e.g. in case of tetragonal 4mm, there are only three independent non-zero piezoelectric charge components as shown in the array below [30].

$$\begin{bmatrix} 0 & 0 & 0 & 0 & d_{15} & 0 \\ 0 & 0 & 0 & d_{15} & 0 & 0 \\ d_{31} & d_{31} & d_{33} & 0 & 0 & 0 \end{bmatrix}$$

In matrix notation, the first subscript correspond to the direction of electrical field/displacement, while the second refers to direction of stress or strain [31]. Direction 3 by convention is considered as the poling direction. Hence d_{31} relates field along the

polar axis to the strain produced perpendicular. In case of d_{33}, strain is measured along the polar axis. In case of d_{15} the field perpendicular to polar axis is related to a shear strain. The *d* co-efficients introduced in equation 2.06 and 2.07 can be proved to be thermodynamically equal ($d_{direct} = d_{inverse)}$ and is an important figure of merit for piezoelectric materials commonly known as small signal piezoelectric co-efficient [32].

2.1.6 Electrostrictors

A phenomenon closely related to piezoelectric effect is electrostriction. Electrostriction can be defined as mechanical deformation of a material under application of electric field, where the induced strain *x* varies proportional to the square of polarisation/electric field (*P*/*E*) as expressed in the following equations.

$$\boldsymbol{x_{ij} = Q_{ijkl} P_k P_l} \qquad \text{Equation 2.09,}$$

$$\boldsymbol{x_{ij} = M_{ijkl} E_k E_l} \qquad \text{Equation 2.10,}$$

Where $\boldsymbol{Q_{ijkl}}$ and $\boldsymbol{M_{ijkl}}$ are fourth rank tensors of electrostrictive coefficients [33]. Similar to piezoelectric co-efficients, electrostrictive co-efficients are also commonly written in matrix notation, introduced in the preceding section. Note that the effect is quadratic and not linear as in case of piezoelectric effect (equation 2.08). Though, in the literature sometimes, the title "piezoelectric ceramic[$]" is used for both piezoelectric and electrostrictive ceramics but the differences between both effects are well known [34]. Electrostriction has no corresponding direct effect and hence can be only used for conversion of electrical energy to mechanical energy.

[$] In this thesis, if not explicitly mentioned "piezoelectric materials" refers to both piezoelectric and electrostrictive materials.

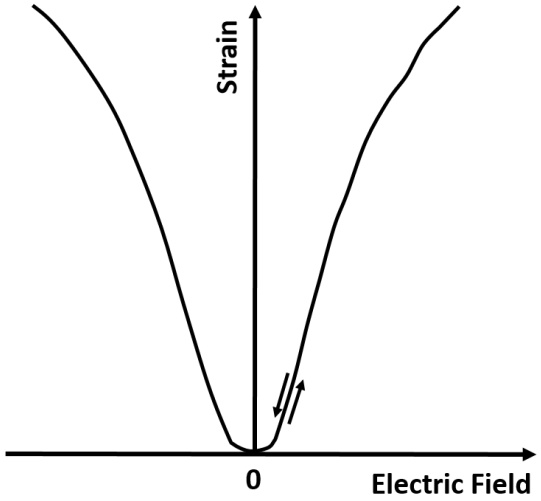

Figure 2.13: Typical electrostrictive *S-E* response of a PMN-based ceramic. redrawn after [6]

This phenomenon is not constrained by crystallographic symmetry and can be observed in all dielectrics. The induced strain does not depend on polarity and is always positive regardless the direction of electric filed [32]. Typical *S-E* response in electrostrictive material is shown in Figure 2.13. Magnitude of electrostrictive strain is usually very small as compare to piezoelectric strain, however in relaxor ferroelectrics such as PMN, electrostrictive strains can be sufficiently large to be utilized for commercial applications. In situations where excellent displacement accuracy is required, electrostrictive materials are preferred because they don't suffer from hysteresis [33]. In addition, electrostrictive ceramics don't have any remanent strain and hence the devices fabricated from these materials will have no substantial residual stress, which is a problem in piezoelectric materials [35].

2.2 Strategies to enhance electromechanical coupling

Enhancement of electromechanical response in piezoelectric materials is either achieved via structural engineering or via compositional engineering. Structural engineering focuses on optimisation of structure at micro and/or nano level without changing composition of the material [36]. Significant enhancements in electromechanical responses have been achieved through structural engineering techniques such as domain engineering [37,38], grain size optimisation [39] and texturing [40]. However traditionally, compositional engineering has been more popular for enhancement of electromechanical responses and is the subject of this study. Compositional engineering means, optimising the properties of a solid solution by finding the composition near to a structural instability such as morphotropic phase boundary (MPB) or polymorphic phase transition (PPT). MPB is compositionally driven phase boundary and is almost temperature independent, while PPT is driven by thermodynamic variables and hence significantly dependent on temperature. A schematic diagram showing MPB and PPT between two perovskites A and B is shown in Figure 2.14.

Figure 1 in reference [36]

Figure 2.14. Characteristic (hypothetical) phase diagrams for perovskite solid solutions exhibiting either a (a) morphotropic phase boundary (MPB); (b) orthorhombic to tetragonal (O–T) polymorphic phase transition (PPT). The resulting temperature dependence of the piezoelectric coefficient (c) for hypothetical MPB and PPT materials with the same room-temperature piezoelectric coefficient and same Curie temperature (T_C), where dotted trend lines indicate degradation of piezoelectric properties due to depolarization at temperatures near $T_{O–T}$ and T_C [36].

Enhancement in electromechanical responses at interferroelectric phase boundaries is attributed to (i) the existence of large number of equivalent polarisation directions due to the co-existence of phases with different symmetries, which facilitates alignment of ferroelectric domains and (ii) softening of the crystal lattice at the phase boundary [36]. Crystal softening refers to a phenomenon, where frequency of a phonon approaches to

zero at the transition point. Consequently, restoring force is reduced which allows the ions to condense into a lower symmetry accompanied by enhancement in dielectric and piezoelectric properties [41]. Though enhancement in properties can be achieved in both PPT and MPB, the latter is more attractive for technological applications due to its temperature independent behavior as in case of $Pb(Zr,Ti)O_3$ (PZT). PZT refers to solid solution between antiferroelectric $PbZrO_3$ (PZ) and ferroelectric $PbTiO_3$ (PT). A MPB exist at 48 % PT as shown in the phase diagram in Figure 2.15 (a) [34].

(a) Figure 7.1 in reference [34] and (b) Figure 6 in reference [42]

Figure 2.15: (a) Phase diagram of PZT system. Paraelectric cubic phase (P_C), ferroelectric high temperature R phase ($F_{R(HT)}$), ferroelectric low temperature R phase ($F_{R(LT)}$), Antiferroelectric orthorhombic phase (A_O), ferroelectric T phase (F_T) [34]; (b) New PZT phase diagram. Diagonal lines represent monoclinic (M) region. Horizontal lines superimposed on diagonal lines represents tetragonal-monoclinic (M+T) coexistence region, cubic phase; (C), high temperature R phase (R_{HT}), low temperature R phase (R_{LT}) [42].

Noheda et al. [42] reported that an intermediate monoclinic phase exist between the rhombohedral (R) and tetragonal phase (T) at low temperatures as illustrated in Figure 2.15 (b). A monoclinic phase has 24 possible polarisation directions and will hence allow easy re-orientation of polarisation vector leading to enhancement in piezoelectric properties. Researchers are therefore trying to mimic the MPB in PZT in lead free ceramics by testing solid solutions between endmembers of different symmetries.

2.3 Literature review

2.3.1 Piezoelectric materials

The first practical application of piezoelectrics came in the First World War (1917) when Paul Lengvin used Quartz as a transducer to send and receive ultrasonic waves in sonars. However natural materials did not find many further applications because of their low piezoelectric properties. During WW II, the discovery of ferroelectric ceramic $BaTiO_3$ (BT) opened a new window for piezoelectric materials to be used in many applications for sensing and actuation. About 10 years later $Pb(Zr,Ti)O_3$ (PZT) was discovered which virtually replaced BT for all piezoelectric applications [1]. To date, PZT-based ceramics are the most popular materials for piezoelectric applications because of their high piezoelectric co-efficients, low cost and ease of reproducibility but growing legislation against use of toxic lead in electronics [43,44] has triggered intensive research to find alternatives to PZT. In addition to PZT other materials which are of significant interest to practical applications are those exhibiting high electrostrictive strains. Unfortunately materials such as $Pb(Mg_{1/3}Nb_{2/3})O_3–PbTiO_3$ also contain a significant amount of lead [45]. Research in lead-free piezoelectrics and electrostrictors is therefore of great scientific and potentially commercial interest.

2.3.2 Lead-free piezoelectric materials

More than a decade of active research in lead-free piezoelectrics has initiated some interesting results. Amongst the many systems investigated BT, $Na_{1/2}Bi_{1/2}TiO_3$ (NBT) and $(K,Na)NbO_3$ (KNN)-based systems are the most promising lead-free ceramics. In 2009, Liu et al. [46] reported d_{33} = 620 pC/N and a strain of 0.057 % at 0.5 kV/mm (d^*_{33}= 1140 pm/V) in pseudo-binary system $Ba(Ti_{0.8}Zr_{0.2})O_3–(Ba_{0.7}Ca_{0.3})TiO_3$ (BZT-BCT). BZT-BCT ceramics consist of highly stable oxides and require significantly higher sintering temperatures (~1500 °C) but the absence of volatile elements makes them comparatively easier to be reproduced on larger scales. These materials, however cannot be used in high temperature regimes due to their low T_C (< 100 °C). Nonetheless, BZT-BCT has attracted a lot of attention because of its potential to replace PZT-based ceramics in devices

operating near room temperature (RT). Interest in NBT-based ceramics was stimulated, when Zhang et al. (2007) [47] reported a giant strain of 0.45 % at 8 kV/mm d^*_{33} = 562 pm/V in the ternary system of (0.94-*x*)$Bi_{0.5}Na_{0.5}TiO_3$-0.06$BaTiO_3$-*x*$K_{0.5}Na_{0.5}NbO_3$. The giant strain is very attractive for actuator applications but the down side of these materials is the large hysteresis and high driving field. The giant strains were subsequently shown to be temperature dependent, which impedes the use of these materials in high temperature applications [48]. Research in KNN-based ceramics was triggered by Saito et al. (2004) [49], when they reported a d_{33} = 416 pC/N and a strain of 0.15 % at 2 kV/mm (d^*_{33}= 750 pm/v) in textured $(K_{0.44}Na_{0.52}Li_{0.04})(Nb_{0.86}Ta_{0.10}Sb_{0.04})O_3$. A complex texturing process was used by Saito et al. to achieve these properties; however many subsequent studies showed high piezoelectric properties can also be achieved through conventional solid state methods [50-52]. Despite many issues (discussed in section 2.3.5.3) KNN is still widely considered as a possible replacement of PZT. As discussed in chapter 1 the inspiration of this study was to develop lead free materials for high temperature applications, therefore for this study, we selected high T_C perovskites BF, KBT and KNN, which are reviewed in subsequent sections.

2.3.3 Bismuth ferrite (BF)

2.3.3.1 Structure of BF

BF is a rhombohedrally distorted perovskite (ABO_3) type structure (space group *R*3*c*). At room temperature, the lattice parameters are a = 5.6343 Å and α = 59.438° with ferroelectric polarisation along the [111] axes [53]. The unit cell can also be expressed in hexagonal settings with the hexagonal c-axis $[001]_{hexagonal}$ parallel to the diagonal $[111]_{pseudocubic}$ axis, with lattice parameters a = 5.58 Å and c = 13.90 Å. Bi^{3+} is on a 12 co-ordinated, cubo-octahedral A site and Fe^{3+} lies on 6 co-ordinated octahedral B site [54,55]. The tolerance factor calculated for BF using Shannon radii[$] is 0.88 [56]. We recall that for t < I the oxygen octahedra has to tilt in order to fit into the unit cell. The tilt system for BF is $a^-a^-a^-$ indicating an antiphase rotation of FeO_6 octahedra along $[111]_{pseudocubic}$ axis, schematically shown in Figure 2.16.

.

Adopted from Figure 1 in reference [57].

Figure 2.16: Schematic diagram of BF crystal structure, with polarisation along [111] axis indicated by bold arrow [57].

””

[$] ionic radii of 8-fold coordination is used for Bi^{3+} (12-fold values are not reported). For Fe^{3+} ionic radii of 6-fold with high spin is used.

2.3.3.2 Processing of BF

Processing single phase BF is notoriously difficult and the final ceramic is often accompanied by secondary phases such as sillenite $Bi_{25}FeO_{39}$ (Bi:Fe = 25:1) and mullite $Bi_2Fe_4O_9$ (Bi:Fe = 1:2) [58]. In addition to conventional solid state sintering many other processing methods have been tried to achieve a single phase BF. These processing methods include spark plasma sintering [59], hydrothermal synthesis [60], precipitation method [61], sol–gel synthesis [62], combustion synthesis [63], high-pressure synthesis [64] and mechanochemical synthesis [65]. Some of these methods have successfully produced single phase BF ceramics. However only solid state synthesis is relevant to this work and other methods will not be discussed. Though difficulties of processing BF into single phase still prevail, significant advancement has been made to understand the origins of secondary phases formed during processing of BF. Selbach et al. [66] used thermodynamic data reported by Phapale et al. [67] and showed that Gibbs free energy ($\Delta_{r,(1)}\boldsymbol{G}_{\boldsymbol{m}}^{\circ}$) for BF is slightly higher than zero between temperatures from 447 to 767 °C as shown in Figure 2.17 (a). This means that parasitic phases (sillenite and mullite) in this region are thermodynamically more stable than the perovskite phase. These results were in agreement with experimental data shown in Figure 2.17 (b). Secondary phases clearly appear, when a BF ceramic with small amount of secondary phases was annealed at 700 °C. The BF phase starts to reappear when the ceramics are annealed at higher temperatures 775 and 850 °C as illustrated in Figure 2.17 (b). In addition to thermodynamics, kinetics of Bi_2O_3-Fe_2O_3 reaction are also addressed in the literature. Diffusion behaviour of the binary system Bi_2O_3-Fe_2O_3, studied through the technique called diffusion coupling revealed that the diffusion of Bi^{3+} is activated before Fe^{3+} ions and hence it was proposed that formation of BF phase is governed by diffusion of Bi^{3+} ion into the Fe_2O_3 grains [68]. Bernardo et al. [68] proposed a model (Figure 2.18) to explain the reaction path ways in solid state synthesis of BF. According to the model, a perovskite phase is initially formed between the sillenite (bismuth rich) and mullite (bismuth poor) phases. In hypothetical conditions, the bismuth rich and bismuth poor phases should decompose and form entirely a single BF phase; however in reality this process does not occur. Crystallisation of the mullite phase blocks the diffusion process and hence results in co-existence of three different phases in the final ceramic. Onset of densification in BF is ~ 800 °C [58], hence

calcination temperatures should be lower to avoid coarsening of powders. So the calcination step will usually fall in the thermodynamically unstable region (Figure 2.17 (a)) of BF. Another important issue is the volatility of bismuth. The peritectic point of the sillenite phase is ~ 790 °C [69], which is even lower than melting point for Bi_2O_3 (~ 825 °C) [70], and hence the decomposition of this phase may result in uncontrolled loss of Bi_2O_3. Processing undoped BF into a single phase dense ceramic via ordinary solid state method is therefore extremely difficult. However with suitable dopants, not only can the properties and structure of BF be tailored but obtaining single phase, dense ceramics becomes more feasible.

Figure 1 in reference [58]

Figure 2.17: (a) Calculated temperature dependence of the Gibbs free energy ($\Delta_{r,(1)}G_m^{\circ}$) of the equilibrium reaction between $BiFeO_3$ and the Bi- and Fe-rich phases [58]; (b) X-ray diffraction (XRD) patterns of $BiFeO_3$ at room temperature (25°C) and after isothermal annealing at 700°C, 775°C, and 850°C, showing firstly the decomposition of $BiFeO_3$ into $Bi_{25}FeO_{39}$ and Bi_2Fe4O_9 at 700°C, followed by the disappearance of these secondary phases (i.e., the reappearance of $BiFeO_3$) at T ≥ 775°C [66].

Figure 6 in reference [68]

Figure 2.18: Schematic diagram of the reaction paths in the solid state synthesis of BiFeO3. (a) Hypothetical end of reaction and (b) experimental situation [68].

2.3.3.3 Properties of BF

BF is one of the most extensively researched perovskite compounds because of its room temperature multiferroic properties. It is simultaneously ferroelectric (FE) with a T_C ~825 °C [71] and antiferromagnetic (AFM) with a Neel temperature (T_N) of 370 °C [72]. The magnetic ordering is G-type with a weak canting moment with a 62nm spin cycloid [73]. As a room temperature multiferroic, BF is an obvious choice for applications such as multiple state memory elements, electric field controlled magnetic resonance devices, and

transducers with magnetically modulated piezoelectricity [74]. The polarisation of BF is reported to be very large (ca.90–100 μC/cm^2) [75,76], and hence it has attracted considerable attention for potential use in next generation lead-free ferroelectric memories [55]. However, relevant to this work are piezoelectric properties of BF, which will be addressed in detail. Three main properties make BF an interesting candidate for piezoelectric applications. The very first reason of interest in BF is the non-toxic behavior of the heavy metal bismuth; a likely replacement for lead due to similar electronic structure. The second eye catching property for piezoelectric community is the high T_C (825 °C), which makes it very attractive for high temperature applications. Thirdly, the rhombohedral symmetry of BF makes it an important endmember for constructing MPB similar to that of PZT by combining it with an endmember of tetragonal symmetry, such as PT, BT and KBT. The d_{33} values of undoped BF reported in literature range from 4 pC/N [59] to 45 pC/N [77]. This variation in values can be attributed to insufficient poling due to high conductivities in BF ceramics. High conductivities in BF ceramics are usually linked to (i) the presence of secondary phases [78] (ii) the reduction of Fe^{3+} ion to Fe^{2+} during processing [79]. In most of the literature unsaturated *P-E* loops are reported because the breakdown strength of the processed ceramics is usually smaller than the coercive fields. In some cases pinched *P-E* loops are reported [78,80,81]. The pinching behavior is attributed to domain wall pinning arising due to defects [80]. The unfortunate combination of high coercive fields (~10 kV/mm) with high conductivities has therefore resulted in poor documentation of the piezoelectric properties in undoped BF. However, in some nicely processed ceramics, where high fields were applied, BF has shown the potential to be considered as a lead-free candidate. E.g. Rojac et al. [82] reported a high strain of 0.36 % (peak to peak) at low frequency of 0.1 Hz and a high driving field of 14 kV/mm in mechanochemically synthesized BF shown in Figure 2.19. The high strain was attributed to the switching of non 180° domain walls.

Figure 1 in reference [82]

Figure 2.19: *S-E* hysteresis loop of $BiFeO_3$ measured at 0.1 Hz and electric field amplitude of 14 kV/mm [82].

2.3.3.3.1 Doped BF

Difficulties in processing and high conductivities are largely been addresses by doping BF on both A and B sites. Amongst the A-site isovalent dopants, rare earth (RE) elements have attracted the greatest attention. The B-site is usually doped with a donor ion to control the high conductivities.

2.3.3.3.1.1 A-site doping in BF

Partial substitution of RE ions on A site has been extensively studied by many research groups. Most of these studies are driven by the multiferroic nature of BF but within this study the magnetic properties of BF will not be addressed. There is a general agreement that doping RE ions like La^{3+} [83-86], Nd^{3+} [87,88] and Sm^{3+} [89], Gd^{3+} [90] eliminates the secondary phases and single phase ceramics can be processed via conventional solid state synthesis. Improvement in dielectric [83] and piezoelectric properties [91], along with reduction in leakage current [86] are also reported for La^{3+} doped compounds. Nd^{3+} doped compounds are reported to have large piezoelectric coefficients (28 pC/N) and reduced leakage current [92]. Large piezoelectric coefficient (29 pC/N) and high remanent polarisations (15 μc/cm^2) are reported for Sm^{3+} doped compounds [93]. Apart from REs other dopants are also used for partial replacement of Bi. Mishra et al. [94] investigated Y^{3+} (non-rare earth but similar in size) as A-site dopant and reported structural changes followed by reduction in secondary phases and improvement of ferroelectric and dielectric properties of BF. Substitution of A-site ion by another ion of same valence but different size induces a chemical pressure on the crystal lattice and may result in crystal phase transition. Transformation from rhombohedral phase to that of orthoferrite with doping of RE is well known, reported in early phase diagrams for $Bi_{1-x}La_xFeO_3$ by Polomska et al. [95]. Karimi et al. [96,97] reported an antipolar $PbZrO_3$ (PZ)-like structure (*Pbam*) stabilised between the ferroelectric (*R*3*c*) and paraelectric (*Pnma*) for RE doped BF illustrated in Figure 2.20.

Figure 16 in reference [97]

Figure 2.20: Preliminary phase diagrams for RE doped BF 100x derived using combination of XRD, DSC, Raman and TEM data [97].

2.3.3.3.1.2 B-site doping in BF

Although A-site dopants have reduced secondary phases and improved dielectric and piezoelectric properties, they do not significantly decrease the leakage current. Several authors have proposed that high conductivities in BF arise due to reduction of Fe^{3+} ion into Fe^{2+}, which results in formation of oxygen vacancies according to the equation $Bi^{3+}Fe^{3+}_{1-y}Fe^{2+}_{y}O_{3y/2}$. In such a case, it is intuitive to deplete oxygen vacancies by doping the B-site of BF with donor dopant of suitable size such as Ti^{4+}, Nb^{5+} and V^{+5}. Kumar et al. [98] reported an increase in electric resistivity by six order of magnitude and decrease in tan δ in Ti doped BF. Similarly Jun et al. [99] reported an increase in resistivity by six orders of magnitude by doping Nb in BF despite the presence of secondary phases present in their processed ceramics. Kazutomo et al. [100] reported effective reduction in leakage current by doping Sn^{4+}, Zr^{4+} and Ti^{4+} on B-site of BF. Benfang et al. [101] reported that leakage current and tan δ decreased in $La^{3+}$and V^{5+} co-doped $Bi_{0.85}La_{0.15}Fe_{1-x}V_xO_3$ as x increased from 0 to 0.1. Kalantari et al. [102] investigated $Bi_{0.85}Nd_{0.15}Fe_{1-y}Ti_yO_3$ ($0 \leq y \leq 0.1$) ceramics and reported PZ-like structure for $y \leq 0.05$. Ti doping effectively reduced tan δ from > 0.3 to < 0.04, decreased bulk conductivity from ~ 1 mS cm^{-1} to < 1μS cm^{-1} accompanied by an increase in bulk activation energy for conduction from 0.29 to >1 eV. At low concentrations (Ti < 3%) the decrease in conduction was attributed to elimination of oxygen vacancies by donor dopant Ti^{4+}, however the mechanism for Ti > 3% was unclear because of non-linear relationship between T_C and Ti concentration. The authors assumed that the compensation mechanism in higher concentrations could be related to formation of V_{Bi}''' based on analogy with V_{Pb}''' formation in Pb based perovskites [103]. In a subsequent study Reaney et al. [104] investigated $Bi_{0.85}Nd_{0.15}Fe_{0.9}Ti_{0.1}O_3$ ceramics to clarify the ionic compensation mechanisms in higher concentration (Ti > 3%) using aberration corrected scanning transmission electron microscope. The authors found periodic distribution of Nd-rich precipitates in lattice, concluding that Ti donor doping is

compensated by V_{Nd}''' instead of V_{Bi}''' and V_{Fe}'''. They suggested two ionic compensation mechanisms to explain the change in conductivity and non-linear behaviour of T_C with Ti concentration. At lower concentrations Ti^{4+} replaces Fe^{2+} resulting in $\frac{2}{3}V_{Nd}'''$ and at higher concentrations (when all Fe^{2+} ions are compensated) Ti^{4+} replaces Fe^{3+} resulting in $\frac{1}{3}V_{Nd}'''$. Based on the findings of Reaney et al. we suggest that homogenous and electrically resistive ceramics could be fabricated in the solid solution $BiFeO_3$-$RE_{2/3}TiO_3$. Exploration of these solid solutions for possible piezoelectric applications is the subject of chapter 5. We also note that the problem of high conductivity persist in BF-based solid solutions, such as BF-BT [105,106] and BF-KBT [107]. We therefore suggest that the compound $BiFeO_3$-$RE_{2/3}TiO_3$ can also serve as a useful endmembers to form solid solutions with low conductivities.

2.3.4 $K_{1/2}Bi_{1/2}TiO_3$ (KBT)[$]

2.3.4.1 Structure of KBT

KBT was first fabricated in1959 by Smolenskii et al. [17]. It is a typical ABO_3 type material with K^+ and Bi^{3+} on A site and Ti^{4+} on B site. X-ray analysis on KBT by Ivanova et al. [108] showed that the crystal structure of KBT is tetragonal (*P4mm*) at room temperature with c/a = ~1.018. They further reported that KBT transforms to a pseudocubic structure around 270 °C and becomes completely cubic ($Pm\bar{3}m$) around 410 °C as shown in Figure 2.21.

Figure 1 in reference [111]

Figure 2.21: Temperature dependence of lattice constants (a and c), and volume (V) of (KBT=BKT) ceramics reported by Ivanova et al. [108].

In-situ TEM analysis by Otoničar et al. [109] showed that some regions starts to transform to cubic phase at ~280 °C, while in others, the domain structure persists until ~ 400 °C, confirming that the pseudocubic phase identified by Ivonova et al. is actually the region where tetragonal and cubic phase co-exists. The dielectric profile of KBT shows a frequency dependent broad maximum ~ 380 °C [110], indicative of weak relaxation behavior. The observed relaxation behavior is attributed to compositional disorder of K^+ and Bi^{3+} cations on the A-site [111,112].

[$] note that KBT is a stoichiometric compound and not a solid solution. For sake of differentiation the subscript is written as whole fractions (1/2) instead of decimal number (0.5) and the same format will be used throughout the text.

2.3.4.2 Processing of KBT

Processing KBT into a single phase dense ceramic is very challenging. Low densities and secondary phases, such as $K_2Ti_6O_{13}$ [113], $K_4Ti_3O_8$ [114] and $K_2Ti_4O_9$ [115] are reported to exist in ceramics fabricated via conventional solid state route. Investigation by König et al. [115] revealed that $K_2Ti_4O_9$ forms during calcination at temperatures < 1000 °C, which transforms to $K_2Ti_6O_{13}$ during sintering at > 1000 °C. Generally, the difficulties in processing are attributed to volatility of both K_2CO_3 [116] and Bi_2O_3 [112] during high temperature treatment. Hiruma el al. [113] reported that KBT melts at 1070 °C but according to König et al. [115] the melting point is 1040 °C. The low melting point of KBT limits the sintering window and hence the sintering temperature needs to be very carefully selected and then performed in accurately controlled furnaces. Another issue is the hygroscopic nature of K_2CO_3. The content of moisture in raw material can affect the stoichiometry, which can dramatically influence the electrical properties [117]. The transformation of $K_2Ti_4O_9$ to $K_2Ti_6O_{13}$ during sintering is accompanied by formation of potassium rich phase [118], which is responsible for the highly hygroscopic nature of KBT ceramics. Recently König et al. [119] showed that the potassium rich phase in the final ceramic can be suppressed by 20-40 h prolonged sintering. Due to difficulties in processing, studies on the KBT are scarce in comparison to the sodium analogue.

2.3.4.3 Properties of KBT

KBT is ferroelectric material with high T_C of ~380 °C. The d_{33} values of undoped KBT reported in literature range from 31 pC/N [120] to 120 pC/N [119]. This large inconsistency in piezoelectric coefficients can be attributed to the quality of processed samples. KBT are hard piezoelectrics with a high coercive field of ~ 6 kV/mm [119]. Hence, well-defined *P-E* loops cannot be obtained in poorly sintered ceramics due to large conductivity primarily arising from adsorbed moisture. A comparison of two contrasting *P-E* loops reported for KBT is shown in Figure 2.22.

Adopted from Figure 11 in reference [119] (b) Figure 8 in reference [122]

Figure 2.22: (a) saturated *P-E* loops for undoped KBT reported by [119]; (b) Rounded *P-E* loops showing high conductivities for undoped KBT reported by [122].

Despite challenges in processing KBT has attracted attention because of its (i) high T_C and (ii) tetragonal symmetry at room temperature. The later allows construction of an MPB by combining materials of other symmetries with KBT, especially those with rhombohedral symmetry such as NBT and BF. The mostly widely studied MPB is the one that occurs in solid solution (1-x)NBT-xKBT at x = 0.18.The NBT rich system has the disadvantage of lower T_d (<200 °C) and will not be discussed [121]. Amongst others, one of the most important solid solution is (1-x)BF-xKBT. Matsuo et al. [123] reported the formation of MPB between rhombohedral and pseudocubic phases at $0.4<x<0.43$. Ceramics with x = 0.4 exhibited a k_{33} of 0.36, which was reported to stable up to 300 °C. At x =0.5 ceramics exhibited a high strain d_{33}^{*} = 230 pm/V (10 kV/mm$^{\$}$). Studies by Morozov et al. [124,125] revealed that the system (1-x)BF-xKBT exhibits a high strain d_{33}^{*} = 250 pm/V (E = 5 kV/mm) at x = 0.75. A large increase ~ 48 % in strain was observed as temperature was increase from RT to 100 °C. Piezoelectric coefficients of KBT-based binary and ternary systems are summarized in Table 2.2 excluding those containing lead. The summary in Table 2.2 reveals that KBT-based system do not exhibit very high d_{33} co-efficients and in most cases the relaxor behavior is promoted by addition of other endmembers and an enhancement in strain (d_{33}^{*}) is often reported. High depolarization temperatures compared to NBT-KBT and their ternary derivatives [126] with the potential to yield high strains makes KBT-based materials interesting candidates for high temperature actuator applications. In this study we intend to combine KBT with low loss materials developed in the system $BiFeO_3$-$REFeO_3$-$RE_{2/3}TiO_3$. We expect to have better control over processing and conductivities using a well behaved endmember from the system $BiFeO_3$-$REFeO_3$-$RE_{2/3}TiO_3$ instead of the problematic BF. This work is the subject of chapter 6.

$^{\$}$ The value in parenthesis shows the maximum driving electric field

Table 2.2: Survey of piezoelectric coefficients in KBT-based ceramics along with their temperature stabilities (when reported). Strain values are recorded in frequency range from 0.25 to 10 Hz. ΔS % = percentage variation in d^*_{33} within inspected temperature range.

Composition	d_{33}	d_{33}^*	ΔS (%)	Ref.
$K_{1/2}Bi_{1/2}TiO_3$ **(Hot Pressed)**	69.8 pC/N	135 pm/V	N/R (not reported)	[113]
$0.75K_{1/2}Bi_{1/2}TiO_3$ -0.25$BiFeO_3$	N/R	250 pm/V	48 % (RT-100 °C)	[125]
$0.50K_{1/2}Bi_{1/2}TiO_3$ -0.50$BiFeO_3$ **(prepared from nano-sized powders)**	~ 65 pm/V	230 pm/V	N/R	[123]
0.40 $K_{1/2}Bi_{1/2}TiO_3$ -0.60$BiFeO_3$ **(prepared from nano-sized powders)**	~ 130 pm/V	250 pm/V	N/R	[123]
0.99 $K_{1/2}Bi_{1/2}TiO_3$ - 0.01$Bi(Mg_{2/3}Nb_{1/3})$ O_3	96 pC/N	135 pm/V	58% (40-160 °C)	[127]
0.94 $K_{1/2}Bi_{1/2}TiO_3$ - 0.06$Bi_{1/2}Mg_{1/2}TiO_3$	N/R	600 pm/V	N/R	[126]
0.94 $K_{1/2}Bi_{1/2}TiO_3$- 0.06$Bi_{1/2}Ni_{1/2}TiO_3$	126 pC/N	N/R	N/R	[128]
0.9 $K_{1/2}Bi_{1/2}TiO_3$ - 0.1$Bi_{1/2}Na_{1/2}ZrO_3$	N/R	133 pm/V	N/R	[129]
0.9 $K_{1/2}Bi_{1/2}TiO_3$-0.1$Ba(Ti_{0.8}$ $Zr_{0.2})O_3$	N/R	200 pm/V	N/R	[130]
0.9 $K_{1/2}Bi_{1/2}TiO_3$ - 0.1$Bi(Zn_{1/2}Ti_{1/2})$O3	N/R	235 pm/V	N/R	[131]
0.05$Bi(Zn_{1/2}Ti_{1/2})O_3$–0.4 $K_{1/2}Bi_{1/2}TiO_3$ - 0.55$(Bi_{1/2}Na_{1/2})TiO_3$	N/R	547	N/R	[132]

2.3.5 (K, Na)NbO_3 (KNN)

2.3.5.1 Structure of KNN

(KNN refers to solid solution between $KNbO_3$ (KN) and $NaNbO_3$ (NN). The phase diagram of (K,Na)NbO_3 is introduced in Figure 2.23.

Figure 2 in reference [133]

Figure 2.23: Phase diagram for the system $KNbO_3$-$NaNbO_3$. L=liquid, S=solid, P_C= paraelectric cubic, P_{TM} = paraelectric tetragonal, P_{TM2} = paraelectric pseudotetragonal, P_{TM3} = paraelectric pseudotetragonal, P_{OM} = paraelectric orthorhombic, A_O = antiferroelectric orthorhombic, F_{T1} = ferroelectric tetragonal with high potassium, F_{T2} = ferroelectric tetragonal, F_{TM} = ferroelectric tetragonal obtained with additives, F_{O1}=ferroelectric orthorhombic, F_{O2} = ferroelectric orthorhombic, F_{OM1} = ferroelectric orthorhombic field enforced in $NaNbO_3$, F_{OM2} = ferroelectric orthorhombic, F_R = ferroelectric rhombohedral, F_{MON} = ferroelectric monoclinic. Reprinted from reference [133], original data from reference [34].

An MPB is reported to exist between two orthorhombic phases F_{O1} and F_{O2} at $x \approx 0.5$ ($K_{0.5}Na_{0.5}NbO_3$) [134]. Although the MPB is controversial [135], it is unanimously agreed that a broad maximum in piezoelectric coefficients is observed in vicinity of the $K_{0.5}Na_{0.5}NbO_3$ composition. It should be noted that there are reports [136,137] stressing that the orthorhombic phase of $K_{0.5}Na_{0.5}NbO_3$ is actually monoclinic, but here we refer to orthorhombic symmetry throughout the text. From the phase diagram one can clearly see that $K_{0.5}Na_{0.5}NbO_3$ goes through a series of phase transitions as a function of temperature, more clearly illustrated in Figure 2.24.

Figure 13 in reference [138]

Figure 2.24: Structure phase transitions of $K_{0.5}Na_{0.5}NbO_3$. re-printed from reference [138].

2.3.5.2 Processing of KNN

KNN can be processed using conventional solid state route according to the reaction below.

$$K_2CO_3 + Na_2CO_3 + 2\ Nb_2O_5 \rightarrow 4K_{0.5}Na_{0.5}NbO_3 + 2CO_2$$

The precursors K_2CO_3 and Na_2CO_3 are both hygroscopic, hence ensuring correct stoichiometry is challenging. However, more of a problem is the volatility of the A-site alkali metals. Wang et al. [139] showed that serious volatility starts at temperature < 1000 °C in KNN-based ceramics as shown in Figure 2.25.

Adopted from Figure 6 in reference [139]

Figure 2.25: Weight loss of alkali metals in KNN- based ceramics as a function of sintering temperature [139].

Normally for piezoelectric material it is imperative to get the highest possible density, however studies by Li et al. [140] and others [139,141] have shown that in KNN-based materials highest piezoelectric properties are obtained at densities lower than the optimal density. The situation was rationalised by proposing that a liquid phase is formed at higher temperature which helps densification but at the same time accelerates volatilizations of alkali components. The sintering window is very narrow [142,143] and temperatures needs to be carefully adjusted to achieve a decent density without drastic volatility. Volatility is a serious issue and can only be reduced by lowering the sintering temperatures. Techniques such as (i) reducing particle size of calcined powders [144,145] (ii) hot pressing [146] (iii) addition of excess alkali carbonates [147,148] and (iv) the use sintering aids such as CuO [149,150], ZnO [151] and MnO_2 [152,153] are utilized to get dense stoichiometric compounds in KNN. Spark plasma sintering (SPS) is another technique, which can sinter ceramics at lower temperature than conventional solid state sintering making them very attractive for KNN-like materials [154]. Many studies [155-157] have shown superior properties for KNN in comparison to that fabricated by conventional sintering. However conventional sintering is preferred due to ease of large scale production with low cost in comparison to SPS.

2.3.5.3 Properties of KNN

Piezoelectricity in KNN was known since 1950s [158], however it was not the focus of significantly research until recently due to superior properties available in PZT. The recent interest in KNN is stimulated by growing legislation against use of lead [43,44]. Undoped $K_{0.5}Na_{0.5}NbO_3$ has a high T_C of ~ 410 °C and exhibits a d_{33} of ~80 pC/N [158] to 125 pC/N [159] in conventionally sintered ceramics. Though the piezoelectric properties in undoped $K_{0.5}Na_{0.5}NbO_3$ are moderate, it has been shown that through compositional engineering KNN can be tailored to exhibit very high d_{33}s ranging from 200 pC/N [160,161] to 490 pC/N [162,163]. On classic d_{33} vs. T_C plot KNN is clear winner amongst the top three candidates for lead free piezoelectrics as shown in Figure 2.26. KNN-based materials do not exhibit giant strains as compared to NBT-based ceramics but moderately large strains can be obtained at very low driving fields.

Figure 7 b in reference [138]

Figure 2.26: d_{33} vs. T_C for leading lead free materials [138].

Lv et al. reported a large unipolar strain of 0.18 % at a very low field of 1.8 kV/mm corresponding to a d^*_{33} of ~ 833 pm/V in KNN-based ceramics [164]. Low driving field is a major advantage in actuators where application of high electric fields in not feasible. Key to easy compositional engineering of $K_{0.5}Na_{0.5}NbO_3$ is presence of various polymorphs as introduced in Figure 2.24. The general strategy is to shift the orthorhombic-tetragonal transition ($T_{O\text{-}T}$) to room temperature through various dopants. Piezoelectric properties are enhanced due to the presence of the $T_{O\text{-}T}$ phase boundary, as discussed in section 2.2. In analogy to $T_{O\text{-}T}$, researchers [165-167] have also tried to push the rhombohedral to orthorhombic ($T_{R\text{-}O}$) phase boundary towards room temperature. The $T_{R\text{-}O}$ in general has shown inferior piezoelectric properties to that of $T_{O\text{-}T}$ but nonetheless enhancements in piezoelectric coefficients were achieved [165,166]. The major bottle neck impeding the use of KNN-based ceramics in practical applications is the fact that both $T_{O\text{-}T}$ and $T_{R\text{-}O}$ are temperature driven phase boundaries and piezoelectric properties seriously degrade with increase in temperature as confirmed by many studies [168-171].

To counter the problem, it was proposed that a rhombohedral-tetragonal phase boundary ($T_{R\text{-}T}$), could be formed by shifting rhombohedral and tetragonal phases simultaneously towards room temperature via compositional engineering [172,173,51]. The idea was to mimic the MPB in PZT, which could would solve the issue of temperature stability. Though the strategy was useful in enhancing the piezoelectric coefficients, the issue of temperature stability still persists. Wang et al. [174] showed that the so called $T_{R\text{-}T}$ does not show MPB-like behaviour and is temperature sensitive. To the best of author's knowledge none of the phase boundary in KNN-based material has been proved to behave like a MPB. While d_{33} still remains strongly temperature dependent, successful efforts have been made to improve stability of d^*_{33} giving hope that KNN-based materials can be used for high temperature actuators. Saito et al. [49] showed that temperature stability of d^*_{33} can be improved through texturing. However, the complex process of texturing is not very attractive for industrial applications. Recently Yao et al. [175] showed that improved temperature stability can be achieved in presence of a PPT in $CaZrO_3$ modified KNN ceramics. However, this stability is electric field dependent and only achieved when significantly high electric fields are applied as shown in Figure 2.27.

Figure 2 a in reference [175]

Figure 2.27: Temperature dependence of d_{33}* normalized to its room temperature value d_{33RT}^* of $CaZrO_3$ modified KNN ceramics under electric fields ranging from 0.01 to 5 kV/mm [175].

The application of large electric fields kills the advantage of fabricating actuators operating at low voltages. With KNN-based materials compromise is required between temperature stability and enhanced piezoelectric coefficient. Realizing this fact, we focus to exploit the large tetragonal region by shifting the $T_{O\text{-}T}$ to sub-ambient temperatures with addition of $BiFeO_3$-$REFeO_3$-$RE_{2/3}TiO_3$ in KNN. Shifting $T_{O\text{-}T}$ to sub ambient temperatures will result in relative lower d^*_{33} but there is a possibility to fabricate a lead free material capable of yielding a temperature stable strain in a wide range due to absence of phase transitions from RT to T_C.

2.4 References

[1] J. Holterman and P. Groen, *An Introduction to Piezoelectric Materials and Applications*. Stiching Applied Piezo, 2013.

[2] R. C. Buchanan, "Ceramic Insulators," in *Ceramic Materials for electronics*, 3rd ed., R. C. Buchanan, Ed. 2004, p. 11.

[3] M. Acosta, "Strain Mechanisms in Lead-Free Ferroelectrics for Actuators," Technische Universität Darmstadt, 2015.

[4] K. C. Kao, *Dielectric Phenomenon in Solids*. Elsevier Academic Press, 2004.

[5] N. A. Spaldin, "Analogies and Differences between Ferroelectrics and Ferromagnets," in *Physics of Ferroelectrics: A Modern Perspective*, Berlin, Heidelberg: Springer Berlin Heidelberg, 2007, pp. 175–218.

[6] K. Uchino, *Ferroelectric Devices*. Marcel Dekker Inc., 2000.

[7] D. Damjanovic, "Ferroelectric, dielectric and piezoelectric properties of ferroelectric thin films and ceramics," *Reports Prog. Phys.*, vol. 61, no. 9, p. 1267, 1998.

[8] G. H. Haertling, "Ferroelectric Ceramics: History and Technology," *J. Am. Ceram. Soc.*, vol. 82, p. 797, 1999.

[9] I. Sterianou, "Bismuth-based Perovskites for High Temperature Piezoelectric Applications," University of Sheffield, 2007.

[10] V. M. Goldschmidt, "Die Gesetze der Krystallochemie," *Naturwissenschaften*, vol. 14, no. 21, pp. 477–485, 1926.

[11] C. A. Randall, A. S. Bhalla, T. R. Shrout, and L. E. Cross, "Classification and consequences of complex lead perovskite ferroelectrics with regard to B-site cation order," *J. Mater. Res.*, vol. 5, no. 4, pp. 829–834, 1990.

[12] A. G. H. Smith, "Structural and Defect Properties of Strontium Titanate," University College London, 2011.

[13] N. A. Benedek and C. J. Fennie, "Why are there so few perovskite ferroelectrics?," *J. Phys. Chem. C*, vol. 117, no. 26, pp. 13339–13349, 2013.

[14] B. B. Van Aken, T. T. M. Palstra, A. Filippetti, and N. A. Spaldin, "The origin of ferroelectricity in magnetoelectric $YMnO_3$," *Nat. Mater.*, vol. 3, no. 3, pp. 164–170, 2004.

[15] W. N. Sharpe, *Hand Book of Experimental Solid Mechanics*. Springer Science+Business Media LLC New York, 2008.

[16] A. A. Bokov and Z. G. Ye, "Phenomenological description of dielectric permittivity peak

in relaxor ferroelectrics," *Solid State Commun.*, vol. 116, no. 2, pp. 105–108, 2000.

[17] G. A. Smolenskii and A. I. Agranovskaya, "Dielectric polarization of a number of complex compounds," *Sov. Physics-Solid State*, vol. 1, no. 10, pp. 1429–1437, 1959.

[18] L. E. Cross, *Piezoelectricity*. Springer Berlin Heidelberg, 2008.

[19] A. A. Bokov and Z.-G. Ye, "Recent progress in relaxor ferroelectrics with perovskite structure," *J. Mater. Sci.*, vol. 41, no. 1, pp. 31–52, 2006.

[20] A. A. Bokov and Z.-G. Ye, "Dielectric Relaxation in Relaxor Ferroelectrics," *J. Adv. Dielectr.*, vol. 02, no. 02, p. 1241010, 2012.

[21] P. N. Timonin, "Griffiths' phase in dilute ferroelectrics," *Ferroelectrics*, vol. 199, no. 1, pp. 69–81, 1997.

[22] V. M. Ishchuk, "Was it necessary to introduce the notion 'relaxor ferroelectrics'? - the problem of phase transitions in $(Pb,Li_{1/2}\text{-}La_{1/2})(Zr,Ti)O_3$, $(Pb,La)(Zr,Ti)O_3$, $Pb(Mg_{1/3}Nb_{2/3})O_3$, $Pb(In_{1/2}Nb_{1/2})O_3$ and related materials. 1. model conceptions," *Ferroelectrics*, vol. 255, no. 1, pp. 73–109, 2001.

[23] G. A. Smolenskii, "Physical phenomena in ferroelectrics with diffused phase transition," *J. Phys. Soc. Jpn*, vol. 28, no. 1, pp. 26–37, 1970.

[24] A. A. Bokov, "The nature of ferroelectric phase transition diffusion in disordered crystals," *Solid State Commun.*, vol. 90, no. 10, pp. 687–691, 1994.

[25] M. D. Glinchuk and R. Farhi, "A random field theory based model for ferroelectric relaxors," *J. Phys. Condens. Matter*, vol. 8, no. 37, pp. 6985–6996, 1996.

[26] V. Westphal, W. Kleemann, and M. Glinchuk, "Diffuse phase transitions and random-field-induced domain states of the 'relaxor' ferroelectric $Pb(Mg_{1/3}Nb_{2/3}O_3$.," *Phys. Rev. Lett.*, vol. 68, no. 6, pp. 847–850, Feb. 1992.

[27] D. Viehland, S. J. Jang, L. E. Cross, and M. Wuttig, "Freezing of the polarization fluctuations in lead magnesium niobate relaxors," *J. Appl. Phys.*, vol. 68, no. 6, p. 2916, 1990.

[28] W. Kleemann, J. Dec, S. Miga, and R. Pankrath, "Relaxor Ferroelectrics—From Random Field Models to Domain State Physics," *Ferroelectrics*, vol. 302, no. 1, pp. 247–252, 2004.

[29] A. K. Tagantsev and A. E. Glazounov, "Mechanism of polarization response in the ergodic phase of a relaxor ferroelectric," *Phys. Rev. B*, vol. 57, no. 1, pp. 18–21, 1998.

[30] A. L. Kholkin, N. A. Pertsev, and A. V. Goltsev, "Piezoelectricity and crystal symmetry," in *Piezoelectric and Acoustic Materials for Transducer Applications*, A. Safari and E. Akdogan, Eds. Springer Science+Business Media LLC, 2008, pp. 17–38.

[31] E. R. Newnham, *Structure-Property Relations*. Springer Berlin Heidelberg, 1975.

[32] W. R. Schwartz, J. Ballato, and H. G. Haertling, "Pizoelectric and Electro-optic Ceramics," in *Ceramic Materials for Electronics*, 3rd ed., R. C. Buchanan, Ed. Marcel Dekker Inc., 2004.

[33] F. Li, L. Jin, Z. Xu, and S. Zhang, "Electrostrictive effect in ferroelectrics: An alternative approach to improve piezoelectricity," *Appl. Phys. Rev.*, vol. 1, no. 1, pp. 653–661, 2014.

[34] B. Jaffe, W. R. Cook and H. Jaffe, *Piezoelectric Ceramics*. Acadamic Press (London) Inc. Ltd., 1971.

[35] S.-T. Zhang, A. B. Kounga, W. Jo, C. Jamin, K. Seifert, T. Granzow, J. Rödel, and D. Damjanovic, "High-strain lead-free antiferroelectric electrostrictors," *Adv. Mater.*, vol. 21, no. 46, pp. 4716–4720, 2009.

[36] S. O. Leontsev and R. E. Eitel, "Progress in engineering high strain lead-free piezoelectric ceramics," *Sci. Technol. Adv. Mater.*, vol. 11, no. 4, p. 044302, 2010.

[37] S. Wada, K. Yako, H. Kakemoto, T. Tsurumi, and T. Kiguchi, "Enhanced piezoelectric properties of barium titanate single crystals with different engineered-domain sizes," *J. Appl. Phys.*, vol. 98, no. 1, 2005.

[38] S. Wada, T. Muraishi, K. Yokoh, K. Yako, H. Kamemoto, and T. Tsurumi, "Domain Wall Engineering in Lead-Free Piezoelectric Crystals," *Ferroelectrics*, vol. 73, pp. 11-27, 2008.

[39] C. A. Randall, N. Kim, J.-P. Kucera, W. Cao, and T. R. Shrout, "Intrinsic and Extrinsic Size Effects in Fine-Grained Morphotropic-Phase-Boundary Lead Zirconate Titanate Ceramics," *J. Am. Ceram. Soc.*, vol. 81, no. 3, pp. 677–688, 1998.

[40] G. L. Messing, S. Trolier-McKinstry, E. M. Sabolsky, C. Duran, S. Kwon, B. Brahmaroutu, P. Park, H. Yilmaz, P. W. Rehrig, K. B. Eitel, E. Suvaci, M. Seabaugh, and K. S. Oh, *Templated Grain Growth of Textured Piezoelectric Ceramics*, vol. 29. 2004.

[41] N. Nakanishi, A. Nagasawa, and Y. Murakami, "Lattice stability and soft modes," *J. Phys. Colloq.*, vol. 43, no. C4, pp. C435-C455, 1982.

[42] B. Noheda, D. E. Cox, G. Shirane, R. Guo, B. Jones, and L. E. Cross, "Stability of the monoclinic phase in the ferroelectric perovskite $PbZr_{(1-x)}Ti_xO_3$," *Phys. Rev. B*, vol. 63, p. 014103, 2000.

[43] "EU-Directive 2002/96/EC, 'Waste Electrical and Electronic Equipment (WEEE),' Off. J. Eur. Union, 46 [L37] 24–38 (2003)."

[44] "EU-Directive 2002/95/EC: Restriction of the Use of Certain Hazardous Substances in Electrical and Electronic Equipment (RoHS). Off. J. Eur. Union 2003, 46 (L37), 19."

[45] D. Damjanovic, N. Klein, J. Li, and V. Porokhonskyy, "What Can Be Expected From

Lead-Free Piezoelectric Materials?," *Funct. Mater. Lett.*, vol. 03, no. 01, pp. 5–13, 2010.

[46] W. Liu and X. Ren, "Large piezoelectric effect in Pb-free ceramics," *Phys. Rev. Lett.*, vol. 103, no. 25, pp. 1–4, 2009.

[47] S.-T. Zhang, A. B. Kounga, E. Aulbach, H. Ehrenberg, and J. Rödel, "Giant strain in lead-free piezoceramics $Bi_{0.5}Na_{0.5}TiO_3$–$BaTiO_3$–$K_{0.5}Na_{0.5}NbO_3$ system," *Appl. Phys. Lett.*, vol. 91, no. 11, p. 112906, 2007.

[48] S.-T. Zhang, A. B. Kounga, E. Aulbach, W. Jo, T. Granzow, H. Ehrenberg, and J. Rödel, "Lead-free piezoceramics with giant strain in the system $Bi_{0.5}Na_{0.5}TiO_3$–$BaTiO_3$–$K_{0.5}Na_{0.5}NbO_3$. II. Temperature dependent properties," *J. Appl. Phys.*, vol. 103, no. 3, p. 34107, 2008.

[49] Y. Saito, H. Takao, T. Tani, T. Nonoyama, K. Takatori, T. Homma, T. Nagaya, and M. Nakamura, "Lead-free piezoceramics," *Nature*, vol. 432, pp. 84-87, 2004.

[50] J. Fu, R. Zuo, X. Fang, and K. Liu, "Lead-free ceramics based on alkaline niobate tantalate antimonate with excellent dielectric and piezoelectric properties," *Mater. Res. Bull.*, vol. 44, no. 5, pp. 1188–1190, 2009.

[51] X. Cheng, J. Wu, X. Lou, X. Wang, X. Wang, D. Xiao, and J. Zhu, "Achieving Both Giant d_{33} and High T_C in Potassium Sodium Niobate Ternary System," *ACS Appl. Mater. & Interface*, vol. 6, pp. 750-756, 2014.

[52] R. Zuo, J. Fu, and D. Lv, "Phase Transformation and Tunable Piezoelectric Properties of Lead-Free $(Na_{0.52}K_{0.48-x}Li_x)(Nb_{1-x-y}Sb_yTa_x)O_3$ System," *J. Am. Ceram. Soc.*, vol. 92, no. 1, pp. 283–285, 2009.

[53] F. Kubel and H. Schmid, "Structure of a ferroelectric and ferroelastic monodomain crystal of the pervoskite $BiFeO_3$," *Acta cryst. Sect B*, vol. B46, pp. 698–702, 1990.

[54] J. M. Moreau, C. Michel, R. Gerson, and W. J. J. James, "Ferroectric $BiFeO_3$ X-ray and neutron diffraction study," *J. Phys. C Solid State Phys.*, vol. 32, pp. 1315–1320, 1971.

[55] G. Catalan and J. F. Scott, "Physics and Applications of Bismuth Ferrite," *Adv. Mater.*, vol. 21, no. 24, pp. 2463–2485, 2009.

[56] R. D. Shannon, "Revised Effective Ionic Radii and Systematic Studies of Interatomic Distances in Halides and Chalcogenides," *Acta Crystallogr. Sect. A*, vol. 32, p. 751, 1976.

[57] T. Zhao, A. Scholl, F. Zavaliche, K. Lee, M. Barry, A. Doran, M. P. Cruz, Y. H. Chu, C. Ederer, N. A. Spaldin, R. R. Das, D. M. Kim, S. H. Baek, C. B. Eom, and R. Ramesh, "Electrical control of antiferromagnetic domains in multiferroic $BiFeO_3$ films at room temperature.," *Nat. Mater.*, vol. 5, no. 10, pp. 823–829, 2006.

[58] T. Rojac, A. Benčan, B. Malič, G. Tutuncu, J. L. Jones, J. E. Daniels, D. Damjanovic,

and A. Bencan, “BiFeO3 ceramics: Processing, electrical, and electromechanical properties,” *J. Am. Ceram. Soc.*, vol. 97, no. 7, pp. 1993–2011, 2014.

[59] Z. Dai and Y. Akishige, “Electrical properties of multiferroic $BiFeO_3$ ceramics synthesized by spark plasma sintering,” *J. Phys. D. Appl. Phys.*, vol. 43, no. 44, p. 445403, 2010.

[60] C. Chen, J. Cheng, S. Yu, L. Che, and Z. Meng, “Hydrothermal synthesis of perovskite bismuth ferrite crystallites,” *J. Cryst. Growth*, vol. 291, pp. 135–139, 2006.

[61] M. Muneeswaran, P. Jegatheesan, and N. V Giridharan, “Synthesis of nanosized $BiFeO_3$ powders by co-precipitation method,” *J. Exp. Nanosci.*, vol. 8, no. 3, pp. 341–346, 2013.

[62] J. K. Kim, S. S. Kim, and W. J. Kim, “Sol-gel synthesis and properties of multiferroic $BiFeO_3$,” *Mater. Lett.*, vol. 59, pp. 4006–4009, 2005.

[63] S. Farhadi and M. Zaidi, “Bismuth ferrite ($BiFeO_3$) nanopowder prepared by sucrose-assisted combustion method: A novel and reusable heterogeneous catalyst for acetylation of amines, alcohols and phenols under solvent-free conditions,” *J. Mol. Catal. A Chem.*, vol. 299, no. 1, pp. 18–25, 2009.

[64] L. Zhai, Y. G. Shi, J. L. Gao, S. L. Tang, and Y. W. Du, “Ferroelectric and magnetic properties in high-pressure synthesized $BiFeO_3$ compound,” *J. Alloys Compd.*, vol. 509, no. 28, pp. 7591–7594, 2011.

[65] I. Szafraniak, M. Polomska, B. Hilczer, A. Pietraszko, and L. Kepinski, “Characterization of $BiFeO_3$ nanopowder obtained by mechanochemical synthesis,” *J. Eur. Ceram. Soc.*, vol. 27, pp. 4399–4402, 2007.

[66] S. M. Selbach, M.-A. Einarsrud, and T. Grande, “On the Thermodynamic Stability of $BiFeO_3$,” *Chem. Mater.*, vol. 21, no. 1, pp. 169–173, 2008.

[67] S. Phapale, R. Mishra, and D. Das, “Standard enthalpy of formation and heat capacity of compounds in the pseudo-binary Bi_2O_3-Fe_2O_3 system,” *J. Nucl. Mater.*, vol. 373, no. 1–3, pp. 137–141, 2008.

[68] M. S. Bernardo, T. Jardiel, M. Peiteado, A. C. Caballero, and M. Villegas, “Reaction pathways in the solid state synthesis of multiferroic $BiFeO_3$,” *J. Eur. Ceram. Soc.*, vol. 31, no. 16, pp. 3047–3053, 2011.

[69] A. Maître, M. François, and J. C. Gachon, “Experimental Study of the Bi_2O_3-Fe_2O_3 Pseudo-Binary System,” *J. Phase Equilibria Diffus.*, vol. 25, no. 1, pp. 59–67, 2004.

[70] F. Schröder, N. Bagdassarov, F. Ritter, and L. Bayarjargal, “Temperature dependence of Bi_2O_3 structural parameters close to the α–δ phase transition,” *Phase Transitions*, vol. 83, no. 5, pp. 311–325, 2010.

[71] D. Arnold, K. Knight, F. Morrison, and P. Lightfoot, “Ferroelectric-Paraelectric

Transition in $BiFeO_3$: Crystal Structure of the Orthorhombic β Phase," *Phys. Rev. Lett.*, vol. 102, no. 2, 2009.

[72] P. Fischerl, M. PoIomska, I. Sosnowska, and M. Szymanski, "Temperature dependence of the crystal and magnetic structures of $BiFeO_3$," *J. Phys. C Solid State Phys.*, no. 13, pp. 1931–1940, 1980.

[73] I. Sosnowska, T. P. Neumaier, and E. Steichele, "Spiral magnetic ordering in bismuth ferrite," *J. Phys. C Solid State Phys.*, vol. 15, pp. 4835–4846, 1982.

[74] M. Fiebig, "Revival of the magnetoelectric effect," *J. Phys. D. Appl. Phys.*, vol. 38, no. 8, pp. R123–R152, 2005.

[75] J. B. Neaton, C. Ederer, U. V. Waghmare, N. A. Spaldin, and K. M. Rabe, "First-principles study of spontaneous polarization in multiferroic $BiFeO_3$," *Phys. Rev. B*, vol. 71, no. 1, p. 014113, 2005.

[76] V. V. Shvartsman, W. Kleemann, R. Haumont, and J. Kreisel, "Large bulk polarization and regular domain structure in ceramic $BiFeO_3$," *Appl. Phys. Lett.*, vol. 90, no. 17, pp. 2005–2008, 2007.

[77] Y. Yao, B. Ploss, C. L. Mak, and K. H. Wong, "Pyroelectric properties of $BiFeO_3$ ceramics prepared by a modified solid-state-reaction method," *Appl. Phys. A Mater. Sci. Process.*, vol. 99, no. 1, pp. 211–216, 2010.

[78] G. L. Yuan, S. W. Or, Y. P. Wang, Z. G. Liu, and J. M. Liu, "Preparation and multi-properties of insulated single-phase $BiFeO_3$ ceramics," *Solid State Commun.*, vol. 138, no. 2, pp. 76–81, 2006.

[79] X. Qi, J. Dho, R. Tomov, M. G. Blamire, and J. L. MacManus-Driscoll, "Greatly reduced leakage current and conduction mechanism in aliovalent-ion-doped $BiFeO_3$," *Appl. Phys. Lett.*, vol. 86, no. 6, p. 62903, 2005.

[80] T. Rojac, M. Kosec, B. Budic, N. Setter, and D. Damjanovic, "Strong ferroelectric domain-wall pinning in $BiFeO_3$ ceramics," *J. Appl. Phys.*, vol. 108, no. 7, p. 074107, 2010.

[81] F. Chen, Q. F. Zhang, J. H. Li, Y. J. Qi, C. J. Lu, X. B. Chen, X. M. Ren, and Y. Zhao, "Sol-gel derived multiferroic $BiFeO_3$ ceramics with large polarization and weak ferromagnetism," *Appl. Phys. Lett.*, vol. 89, no. 9, p. 0092910, 2006.

[82] T. Rojac, M. Kosec, and D. Damjanovic, "Large electric-field induced strain in $BiFeO_3$ ceramics," *J. Am. Ceram. Soc.*, vol. 94, no. 12, pp. 4108–4111, 2011.

[83] V. L. Mathe, K. K. Patankar, M. B. Kothale, S. B. Kulkarni, P. B. Joshi, and S. A. Patil, "Preparation, structural analysis and dielectric properties of $Bi_xLa_{1-x}FeO_3$ perovskite," *Pramana-Journal Phys.*, vol. 58, pp. 1105–1113, 2002.

[84] S.-T. Zhang, L.-H. Pang, Y. Zhang, M.-H. Lu, and Y.-F. Chen, "Preparation, structures, and multiferroic properties of single phase $Bi_xLa_{1-x}FeO_3$ (x = 0–0.40) ceramics," *J. Appl. Phys.*, vol. 100, no. 11 p. 114108, 2006.

[85] S. R. Das, R. N. P. Choudhary, P. Bhattacharya, R. S. Katiyar, P. Dutta, A. Manivannan, and M. S. Seehra, "Structural and multiferroic properties of La-modified BiFeO3 ceramics," *J. Appl. Phys.*, vol. 101, no. 3, p. 34104, 2007.

[86] Z. X. Cheng, X. L. Wang, A. H. Li, X. L. Wang, S. X. Dou, K. Ozawa, H. Kimura, S. J. Zhang, and T. R. Shrout, "Structure, ferroelectric properties, and magnetic properties of the La-doped bismuth ferrite," *J. Appl. Phys.*, vol. 103, no. 7 p. 07E507, 2008.

[87] V. L. Mathe, K. K. Patankar, R. N. Patil, and C. D. Lokhande, "Synthesis and dielectric properties of $Bi_{1-x}Nd_xFeO_3$ perovskites," *J. Magn. Magn. Mater.*, vol. 270, no. 3, pp. 380–388, 2004.

[88] P. Pandit, S. Satapathy, P. K. Gupta, and V. G. Sathe, "Effect of coalesce doping of Nd and La on structure, dielectric, and magnetic properties of $BiFeO_3$," *J. Appl. Phys.*, vol. 106, no. 11 p. 114105, 2009.

[89] K. S. Nalwa, A. Garg, and A. Upadhyaya, "Effect of samarium doping on the properties of solid-state synthesized multiferroic bismuth ferrite," *Mater. Lett.*, vol. 62, pp. 878–881, 2008.

[90] C. Fanggao, S. Guilin, F. Kun, Q. Ping, and Z. Qijun, "Effect of Gadolinium Substitution on Dielectric Properties of Bismuth Ferrite," *J. Rare Earths*, vol. 24, pp. 273–276, 2006.

[91] G. L. Yuan, S. W. Or, and H. L. W. Chan, "Structural transformation and ferroelectric–paraelectric phase transition in $Bi_{1-x}La_xFeO_3$ (x = 0–0.25) multiferroic ceramics," *J. Phys. D. Appl. Phys.*, vol. 40, pp. 1196–1200, 2007.

[92] G. L. Yuan and S. W. Or, "Enhanced piezoelectric and pyroelectric effects in single-phase multiferroic $Bi_{1-x}Nd_xFeO_3$ (x=0–0.15) ceramics," *Appl. Phys. Lett.*, vol. 88, no. 6, p. 62905, 2006.

[93] G. L. Yuan and S. W. Or, "Multiferroicity in polarized single-phase $Bi_{0.875}Sm_{0.125}$ FeO_3 ceramics," *J. Appl. Phys.*, vol. 100, no. 2, p. 24109, 2006.

[94] R. K. Mishra, D. K. Pradhan, R. N. P. Choudhary, and A. Banerjee, "Effect of yttrium on improvement of dielectric properties and magnetic switching behavior in $BiFeO_3$," *J. Phys. Condens. Matter*, vol. 20, p. 45218, 2008.

[95] M. Polomska, W. Kaczmarek, and Z. Pajak, "Electric and Magnetic Properties of $(Bi_{1-x}La_x)FeO_3$ Solid Solutions," *Phys. Stat. Sol.*, vol. 23, p. 567, 1974.

[96] S. Karimi, I. M. Reaney, I. Levin, and I. Sterianou, "Nd-doped $BiFeO_3$ ceramics with antipolar order," *Appl. Phys. Lett.*, vol. 94, no. 11 p. 112903, 2009.

[97] S. Karimi, I. M. Reaney, Y. Han, J. Pokorny, and I. Sterianou, "Crystal chemistry and domain structure of rare-earth doped $BiFeO_3$ ceramics," *J. Mater. Sci.*, vol. 44, no. 19, pp. 5102–5112, 2009.

[98] M. Kumar and K. L. Yadav, "Study of room temperature magnetoelectric coupling in Ti substituted bismuth ferrite system," *J. Appl. Phys.*, vol. 100, no. 7, p. 74111, 2006.

[99] Y. K. Jun, W. T. Moon, C. M. Chang, H. S. Kim, H. S. Ryu, J. W. Kim, K. H. Kim, and S. H. Hong, "Effects of Nb-doping on electric and magnetic properties in multi-ferroic $BiFeO_3$ ceramics," *Solid State Commun.*, vol. 135, no. 1–2, pp. 133–137, 2005.

[100] K. Abe, N. Sakai, J. Takahashi, H. Itoh, N. Adachi, and T. Ota, "Leakage current properties of cation-substituted $BiFeO_3$ ceramics," *Jpn. J. Appl. Phys.*, vol. 49, no. 9 Part 2, 2010.

[101] B. Yu, M. Li, J. Wang, L. Pei, D. Guo, and X. Zhao, "Enhanced electrical properties in multiferroic $BiFeO_3$ ceramics co-doped by $La^{3+}$and V^{5+}," *J. Phys. D. Appl. Phys.*, vol. 41, no. 18, p. 185401, 2008.

[102] K. Kalantari, I. Sterianou, S. Karimi, M. C. Ferrarelli, S. Miao, D. C. Sinclair, and I. M. Reaney, "Ti-Doping to Reduce Conductivity in $Bi_{0.85}Nd_{0.15}FeO_3$ Ceramics," *Adv. Funct. Mater.*, vol. 21, pp. 3737–3743, 2011.

[103] K. H. Härdtl and D. Hennings, "Distribution of A-Site and B-Site Vacancies in $(Pb,La)(Ti,Zr)O_3$ Ceramics," *J. Am. Ceram. Soc.*, vol. 55, no. 5, pp. 230–231, 1972.

[104] I. M. Reaney, I. MacLaren, L. Wang, B. Schaffer, A. Craven, K. Kalantari, I. Sterianou, S. Miao, S. Karimi, and D. C. Sinclair, "Defect chemistry of Ti-doped antiferroelectric $Bi_{0.85}Nd_{0.15}FeO_3$," *Appl. Phys. Lett.*, vol. 100, no. 18, p. 182902, 2012.

[105] M. M. Kumar, A. Srinivas, and S. V. Suryanarayana, "Structure property relations in $BiFeO_3/BaTiO_3$ solid solutions," *J. Appl. Phys.*, vol. 87, no. 2, p. 855, 2000.

[106] S. O. Leontsev and R. E. Eitel, "Dielectric and Piezoelectric Properties in Mn-Modified $(1-x)BiFeO_3$-$xBaTiO_3$ Ceramics," *J. Am. Ceram. Soc.*, vol. 92, no. 12, pp. 2957–2961, 2009.

[107] M. I. Morozov, M. A. Einarsrud, and T. Grande, "Control of conductivity and electric field induced strain in bulk $Bi_{0.5}K_{0.5}TiO_3$-$BiFeO_3$ ceramics," *Appl. Phys. Lett.*, vol. 104, no. 12, p. 122905, 2014.

[108] V. V Ivanova, A. G. Kapyshev, Y. N. Venevtsev, and G. S. Zhdanov, "X-ray determination of the symmetry of elementary cells of the ferroelectric materials $(K_{0.5}Bi_{0.5})TiO_3$ and $(Na_{0.5}Bi_{0.5})TiO_3$ and of high-temperature phase transitions in $(K_{0.5}Bi_{0.5})TiO_3$," *Izv. Akad. Nauk SSSR*, vol. 26, pp. 354–356, 1962.

[109] M. Otoničar, S. D. Škapin, B. Jančar, R. Ubic, and D. Suvorov, "Analysis of the Phase Transition and the Domain Structure in $K_{0.5}Bi_{0.5}TiO_3$ Perovskite Ceramics by In Situ

XRD and TEM," *J. Am. Ceram. Soc.*, vol. 93, no. 12, pp. 4168–4173, 2010.

[110] O. Elkechai, M. Manier, and J. P. Mercurio, "$Na_{0.5}Bi_{0.5}TiO_3$ –$K_{0.5}Bi_{0.5}TiO_3$ (NBT-KBT) system: A structural and electrical study," *Phys. Status Solidi A*, vol. 157, no. 2, pp. 499–506, 1996.

[111] Y. Hiruma, A. Rintaro, H. Nagata, and T. Takenaka, "Ferroelectric and Piezoelectric Properties of $(Bi_{1/2}K_{1/2})TiO_3$ Ceramics," *Jpn. J. Appl. Phys.*, vol. 44, no. 7A, pp. 5040–5044, 2005.

[112] Z. F. Li, C. L. Wang, W. L. Zhong, J. C. Li, and M. L. Zhao, "Dielectric relaxor properties of $K_{0.5}Bi_{0.5}TiO_3$ ferroelectrics prepared by sol–gel method," *J. Appl. Phys.*, vol. 94, no. 4, p. 2548, 2003.

[113] Y. Hiruma, R. Aoyagi, H. Nagata, and T. Takenaka, "Ferroelectric and Piezoelectric Properties of $(Bi_{1/2}K_{1/2})TiO_3$ Ceramics," *Jpn. J. Appl. Phys.*, vol. 44, no. 7A, pp. 5040–5044, 2005.

[114] S. Zhao, G. Li, A. Ding, T. Wang, and Q. Yin, "Ferroelectric and piezoelectric properties of $(Na,K)_{0.5}Bi_{0.5}TiO_3$ lead free ceramics," *J. Phys. D. Appl. Phys.*, vol. 39, no. 10, p. 2277, 2006.

[115] J. König, M. Spreitzer, B. Jančar, D. Suvorov, Z. Samardžija, and A. Popovič, "The thermal decomposition of $K_{0.5}Bi_{0.5}TiO_3$ ceramics," *J. Eur. Ceram. Soc.*, vol. 29, no. 9, pp. 1695–1701, 2009.

[116] T. Wada, K. Toyoike, K. Matsuo, K. Yoshihiro, and Y. Imanaka, "Dielectric and Piezoelectric Properties of $(A_{0.5}Bi_{0.5})TiO_3$ – $ANbO_3$ (A = Na , K) Systems," *Jpn. J. Appl. Phys.*, vol. 40, pp. 5703–5705, 2001.

[117] M. Li, H. Zhang, S. N. Cook, L. Li, J. A. Kilner, I. M. Reaney, and D. C. Sinclair, "Dramatic influence of A-site nonstoichiometry on the electrical conductivity and conduction mechanisms in the perovskite oxide $Na_{0.5}Bi_{0.5}TiO_3$," *Chem. Mater.*, vol. 27, no. 2, pp. 629–634, 2015.

[118] N. Bao, X. Feng, X. Lu, and Z. Yang, "Study on the formation and growth of potassium titanate whiskers," *J. Mater. Sci.*, vol. 37, no. 14, pp. 3035–3043, 2002.

[119] J. König and D. Suvorov, "Evolution of the electrical properties of $K_{0.5}Bi_{0.5}TiO_3$ as a result of prolonged sintering," *J. Eur. Ceram. Soc.*, vol. 35, no. 10, pp. 2791–2799, 2015.

[120] J. M. Kim, Y. S. Sung, J. H. Cho, T. K. Song, M. H. Kim, H. H. Chong, T. G. Park, D. Do, and S. S. Kim, "Piezoelectric and Dielectric Properties of Lead-Free (1-x)$(Bi_{0.5}K_{0.5})TiO_3$-x$BiFeO_3$ Ceramics," *Ferroelectrics*, vol. 404, no. 1, pp. 88–92, 2010.

[121] Y. Hiruma, H. Nagata, and T. Takenaka, "Phase diagrams and electrical properties of $Bi_{1/2}Na_{1/2}TiO_3$-based solid solutions," *J. Appl. Phys.*, vol. 104, no. 12, p. 124106, 2008.

[122] P. V. B. Rao and T. B. Sankaram, “Impedance spectroscopy studies of $K_{0.5}Bi_{0.5}TiO_3$,” *J. Electroceramics*, vol. 25, no. 1, pp. 60–69, 2010.

[123] H. Matsuo, Y. Noguchi, M. Miyayama, M. Suzuki, A. Watanabe, S. Sasabe, T. Ozaki, S. Mori, S. Torii, and T. Kamiyama, “Structural and piezoelectric properties of high-density $Bi_{0.5}K_{0.5}TiO_3$–$BiFeO_3$ ceramics,” *J. Appl. Phys.*, vol. 108, no. 10, p. 104103, 2010.

[124] M. I. Morozov, M. A. Einarsrud, T. Grande, and D. Damjanovic, “Lead-Free Relaxor-Like $0.75Bi_{0.5}K_{0.5}TiO_3$– $0.25BiFeO_3$ Ceramics with Large Electric Field-Induced Strain,” *Ferroelectrics*, vol. 439, no. 1, pp. 88–94, 2012.

[125] M. I. Morozov, M.-A. Einarsrud, and T. Grande, “Polarization and strain response in $Bi_{0.5}K_{0.5}TiO_3$-$BiFeO_3$ ceramics,” *Appl. Phys. Lett.*, vol. 101, no. 25, p. 252904, 2012.

[126] A. Zeb and S. J. Milne, “Large Electromechanical Strain in Lead-Free Binary System $K_{0.5}Bi_{0.5}TiO_3$- $Bi(Mg_{0.5}Ti_{0.5})O_3$,” *J. Am. Ceram. Soc.*, vol. 97, no. 8, pp. 2413–2415, 2014.

[127] Z. Pan, Q. Wang, J. Chen, C. Liu, L. Fan, L. Liu, L. Fang, and X. Xing, “Enhanced Piezoelectric Properties of Tetragonal $(Bi_{1/2}K_{1/2})TiO_3$ Lead-Free Ceramics by Substitution of Pure Bi-Based $Bi(Mg_{2/3}Nb_{1/3})O_3$,” *J. Am. Ceram. Soc.*, vol. 98, no. 1, pp. 104–108, 2015.

[128] W. Zhao and R. Zuo, “Morphotropic phase boundary and electrical properties of lead-free $(K_{0.5}Bi_{0.5})TiO_3$–$Bi(Ni_{0.5}Ti_{0.5})O_3$ relaxor ferroelectric ceramics,” *Ceram. Int.*, vol. 39, no. 8, pp. 9121–9124, 2013.

[129] E. T. Wefring, M. I. Morozov, M.-A. Einarsrud, and T. Grande, “Solid-State Synthesis and Properties of Relaxor (1− x)BKT- x BNZ Ceramics,” *J. Am. Ceram. Soc.*, vol. 97, pp. 2928–2935, 2014.

[130] A. Zeb, S. J. Milne, and S. Zhang, “Dielectric and Piezoelectric Properties of $(1-x)K_{0.5}Bi_{0.5}TiO_3$-$xBa(Ti_{0.8}Zr_{0.2})O_3$ Ceramics,” *J. Am. Ceram. Soc.*, vol. 96, no. 10, pp. 3089–3093, 2013.

[131] C.-C. Huang, N. Vittayakorn, and D. P. Cann, “Structure and Ferroelectric Properties of $Bi(Zn_{1/2}Ti_{1/2})O_3$-$(Bi_{1/2}K_{1/2})TiO_3$ Perovskite Solid Solutions,” *Trans. Ultrason. Ferroelectr. Freq. Control*, vol. 56, no. 7, pp. 1304–1308, 2009.

[132] E. A. Patterson, D. P. Cann, J. Pokorny, and I. M. Reaney, “Electromechanical strain in $Bi(Zn_{1/2}Ti_{1/2})O_3$–$(Bi_{1/2}Na_{1/2})TiO_3$–$(Bi_{1/2}K_{1/2})TiO_3$ solid solutions,” *J. Appl. Phys.*, vol. 111, no. 9, p. 094105, 2012.

[133] J. F. Li, K. Wang, F. Y. Zhu, L. Q. Cheng, and F. Z. Yao, “$(K,Na)NbO_3$-based lead-free piezoceramics: Fundamental aspects, processing technologies, and remaining challenges,” *J. Am. Ceram. Soc.*, vol. 96, no. 12, pp. 3677–3696, 2013.

[134] V. J. Tennery, “Thermal and X-Ray Diffraction Studies of the $NaNbO_3$-$KNbO_3$ System,” *J. Appl. Phys.*, vol. 39, no. 10, p. 4749, 1968.

[135] Y.-J. Dai, X.-W. Zhang, and K.-P. Chen, "Morphotropic phase boundary and electrical properties of $K_{1-x}Na_xNbO_3$ lead-free ceramics," *Appl. Phys. Lett.*, vol. 94, no. 4, p. 042905, 2009.

[136] J. Tellier, B. Malic, B. Dkhil, D. Jenko, J. Cilensek, and M. Kosec, "Crystal structure and phase transitions of sodium potassium niobate perovskites," *Solid State Sci.*, vol. 11, no. 2, pp. 320–324, 2009.

[137] D. W. Baker, P. A. Thomas, N. Zhang, and A. M. Glazer, "A comprehensive study of the phase diagram of $K_xNa_{1-x}NbO_3$," *Appl. Phys. Lett.*, vol. 95, no. 9, p. 91903, 2009.

[138] J. Wu, D. Xiao, and J. Zhu, "Potassium-sodium niobate lead-free piezoelectric materials: Past, present, and future of phase boundaries," *Chem. Rev.*, vol. 115, no. 7, pp. 2559–2595, 2015.

[139] K. Wang and J.-F. Li, "$(K,Na)NbO_3$-based lead-free piezoceramics: Phase transition, sintering and property enhancement," *J. Adv. Ceram.*, vol. 1, no. 1, pp. 24–37, 2012.

[140] J. F. Li, Y. Zhen, B. P. Zhang, L. M. Zhang, and K. Wang, "Normal sintering of $(K, Na)NbO_3$-based lead-free piezoelectric ceramics," *Ceram. Int.*, vol. 34, no. 4, pp. 783–786, 2008.

[141] Y. Zhen and J. F. Li, "Normal sintering of $(K,Na)NbO_3$-based ceramics: Influence of sintering temperature on densification, microstructure, and electrical properties," *J. Am. Ceram. Soc.*, vol. 89, no. 12, pp. 3669–3675, 2006.

[142] M. Kosec and D. Kolar, "On Activated Sintering and Electrical Properties of $NaKNbO_3$," *Mat. Res. Bull*, vol. 10, no. 1974, pp. 335–340, 1975.

[143] P. Zhao, B.-P. Zhang, and J.-F. Li, "High piezoelectric d_{33} coefficient in Li-modified lead-free $(Na,K)NbO_3$ ceramics sintered at optimal temperature," *Appl. Phys. Lett.*, vol. 90, no. 24, p. 242909, 2007.

[144] R. Zuo, J. Rödel, R. Chen, and L. Li, "Sintering and Electrical Properties of Lead-Free $Na_{0.5}K_{0.5}NbO_3$ Piezoelectric Ceramics," *J. Am. Ceram. Soc.*, vol. 89, no. 6, pp. 2010–2015, 2006.

[145] S.-G. Bae, H-G. Shin, K.-H. Chung, J.-H. Yoo, and I.-H. Im, "Effect of Particle Size on the Dielectric and Piezoelectric Properties of $0.95(K_{0.5}Na_{0.5})NbO_3$-$0.05BaTiO_3$ Lead-free Piezoelectric Ceramics," *Trans. Electr. Electron. Mater.*, vol. 16, no. 4, pp. 179-182, 2015.

[146] E. Jaeger R.E L., "Hot Pressing of Potassium-Sodium Niobates," *J. Am. Ceram. Soc.*, vol. 45, no. 5, pp. 209–213, 1962.

[147] K. Wang and J.-F. Li, "Low-Temperature Sintering of Li-Modified $(K,Na)NbO_3$ Lead-Free Ceramics: Sintering Behavior, Microstructure, and Electrical Properties," *J. Am. Ceram. Soc.*, vol. 93, no. 4, pp. 1101–1107, 2010.

[148] T. A. M. Skidmore S. J., "Phase development during mixed-oxide processing of a $[Na_{0.5}K_{0.5}NbO_3]_{1-x}$–$[LiTaO_3]_x$ powder," *J. Mater. Res.*, vol. 22, no. 08, pp. 2265–2272, 2011.

[149] I. T. Seo, K. H. Cho, H. Y. Park, S. J. Park, M. K. Choi, S. Nahm, H. G. Lee, H. W. Kang, and H. J. Lee, "Effect of CuO on the sintering and piezoelectric properties of $0.95(Na_{0.5}K_{0.5})NbO_3$-$0.05SrTiO_3$ lead-free piezoelectric ceramics," *J. Am. Ceram. Soc.*, vol. 91, no. 12, pp. 3955–3960, 2008.

[150] J. Wu, "High piezoelectricity in low-temperature sintering potassium–sodium niobate-based lead-free ceramics," *RSC Adv.*, vol. 4, no. 96, pp. 53490–53497, 2014.

[151] F. Rubio-Marcos, J. J. Romero, M. G. Navarro-Rojero, and J. F. Fernandez, "Effect of ZnO on the structure, microstructure and electrical properties of KNN-modified piezoceramics," *J. Eur. Ceram. Soc.*, vol. 29, no. 14, pp. 3045–3052, 2009.

[152] C. W. Ahn, S. Nahm, M. Karmarkar, D. Viehland, D. H. Kang, K. S. Bae, and S. Priya, "Effect of CuO and MnO_2 on sintering temperature, microstructure, and piezoelectric properties of $0.95(K_{0.5}Na_{0.5})NbO_3$-$0.05BaTiO_3$ ceramics," *Mater. Lett.*, vol. 62, no. 20, pp. 3594–3596, 2008.

[153] H. E. Mgbemere, R. P. Herber, and G. A. Schneider, "Effect of MnO_2 on the dielectric and piezoelectric properties of alkaline niobate based lead free piezoelectric ceramics," *J. Eur. Ceram. Soc.*, vol. 29, no. 9, pp. 1729–1733, 2009.

[154] T. Hungría, J. Galy, and A. Castro, "Spark plasma sintering as a useful technique to the nanostructuration of piezo-ferroelectric materials," *Adv. Eng. Mater.*, vol. 11, no. 8, pp. 615–631, 2009.

[155] J. F. Li, K. Wang, B. P. Zhang, and L. M. Zhang, "Ferroelectric and piezoelectric properties of fine-grained $Na_{0.5}K_{0.5}NbO_3$ lead-free piezoelectric ceramics prepared by spark plasma sintering," *J. Am. Ceram. Soc.*, vol. 89, no. 2, pp. 706–709, 2006.

[156] K. Wang, B.-P. Zhang, J.-F. Li, and L.-M. Zhang, "Lead-free $Na_{0.5}K_{0.5}NbO_3$ piezoelectric ceramics fabricated by spark plasma sintering: Annealing effect on electrical properties," *J. electroceramics*, vol. 21, no. 1–4, pp. 251–254, 2008.

[157] Z.-Y. Shen, J.-F. Li, K. Wang, S. Xu, W. Jiang, and Q. Deng, "Electrical and Mechanical Properties of Fine-Grained Li/Ta-Modified $(Na,K)NbO_3$-Based Piezoceramics Prepared by Spark Plasma Sintering," *J. Am. Ceram. Soc.*, vol. 93, no. 5, pp. 1378–1383, 2010.

[158] L. Egerton and M. D. Dillon, "Piezoelectric and Dielectric Properties of Ceramics in the System Potassium-Sodium Niobate," *Mater. Sci.*, vol. 42, no. 9, pp. 438–442, 1959.

[159] L. Wu, J. L. Zhang, C. L. Wang, and J. C. Li, "Influence of compositional ratio K/Na on physical properties in $(K_xNa_{1-x})NbO_3$ ceramics," *J. Appl. Phys.*, vol. 103, no. 8, p. 084116, 2008.

[160] Y. Guo, K. Kakimoto, and H. Ohsato, "Phase transitional behavior and piezoelectric properties of $(Na_{0.5}K_{0.5})NbO3–LiNbO_3$ ceramics," *Appl. Phys. Lett.*, vol. 85, no. 18, p. 4121, 2004.

[161] K. Wang and J. F. Li, "Analysis of crystallographic evolution in $(Na,K)NbO_3$ -based lead-free piezoceramics by x-ray diffraction," *Appl. Phys. Lett.*, vol. 91, no. 26, p. 262902, 2007.

[162] J. Wu, Y. Wang, and H. Wang, "Phase boundary, poling conditions, and piezoelectric activity and their relationships in $(K_{0.42}Na_{0.58})(Nb_{0.96}Sb_{0.04})O_3 –(Bi_{0.5}K_{0.5})_{0.90}Zn_{0.10}$," *RSC Adv.*, vol. 4, no. 110, pp. 64835–64842, 2014.

[163] J. W. Ting Zheng Dingquan Xiao, Jianguo Zhu, Xiangjian Wang and Xiaojie Lou, "Potassium–sodium niobate lead-free ceramics: modified strain as well as piezoelectricity," *J. Matter. Chem. A*, vol. 3, 2015.

[164] X. Lv, J. Wu, D. Xiao, Y. Yuan, H. Tao, J. Zhu, X. Wang, and X. Lou, "High unipolar strain in samarium-doped potassium–sodium niobate lead-free ceramics," *RSC Adv.*, vol. 5, no. 49, pp. 39295–39302, 2015.

[165] R. Zuo, C. Ye, and X. Fang, "Dielectric and Piezoelectric Properties of Lead Free $Na_{0.5}K_{0.5}NbO_3–BiScO_3$ Ceramics," *Jpn. J. Appl. Phys.*, vol. 46, no. 10A, pp. 6733–6736, 2007.

[166] R. Zuo, J. Fu, D. Lv, and Y. Liu, "Antimony tuned rhombohedral-orthorhombic phase transition and enhanced piezoelectric properties in sodium potassium niobate," *J. Am. Ceram. Soc.*, vol. 93, no. 9, pp. 2783–2787, 2010.

[167] J. Wu, H. Tao, Y. Yuan, X. Lv, X. Wang, and X. Lou, "Role of antimony in the phase structure and electrical properties of potassium–sodium niobate lead-free ceramics," *RSC Adv.*, vol. 5, no. 19, pp. 14575–14583, 2015.

[168] E. K. Akdogan, K. Kerman, M. Abazari, and A. Safari, "Origin of high piezoelectric activity $(K_{0.44}Na_{0.52}Li_{0.04})$-$(Nb_{0.84}Ta_{0.1}Sb_{0.06})O_3$ ceramics," *Appl. Phys. Lett.*, vol. 92, no. 11, p. 112908, 2008.

[169] S. Zhang, R. Xia, and T. R. Shrout, "Modified $(K_{0.5}Na_{0.5}NbO_3$ based lead-free piezoelectrics with broad temperature usage range," *Appl. Phys. Lett.*, vol. 91, no. 13, p. 132913, 2007.

[170] S. Zhang, R. Xia, T. R. Shrout, G. Zang, and J. Wang, "Piezoelectric properties in perovskite $0.948K_{0.5}Na_{0.5}NbO_3 –0.052LiSbO_3$ lead-free ceramics," *J. Appl. Phys.*, vol. 100, no. 10, p. 104108, 2006.

[171] E. Hollenstein, D. Damjanovic, and N. Setter, "Temperature stability of the piezoelectric properties of Li-modified KNN ceramics," *J. Eur. Ceram. Soc.*, vol. 27, no. 13–15, pp. 4093–4097, 2007.

[172] J. Wu, J. Xiao, T. Zheng, X. Wang, X. Cheng, B. Zhang, D. Xiao, and J. Zhu, "Giant piezoelectricity of (K,Na)(Nb,Sb)O_3-(Bi,Na,K,Pb)ZrO_3 ceramics with rhombohedral-tetragonal (R-T) phase boundary," *Scr. Mater.*, vol. 88, pp. 41–44, 2014.

[173] X. Wang, J. Wu, D. Xiao, J. Zhu, X. Cheng, T. Zheng, B. Zhang, X. Lou, and X. Wang, "Giant piezoelectricity in potassium-sodium niobate lead-free ceramics," *J. Am. Chem. Soc.*, vol. 136, no. 7, pp. 2905–2910, 2014.

[174] D. Wang, F. Hussain, A. Khesro, A. Feteria, Y. Tian, Q. Zhao and I. M. Reaney, "Composition and temperature dependence of piezoelectricity in (1-x)($K_{1-y}Na_y$)NbO_3-x($Bi_{1/2}Na_{1/2}ZrO_3$) lead-free ceramics." *J. Am. Ceram. Soc.,* 2016 (accepted)

[175] F.-Z. Yao, K. Wang, W. Jo, K. G. Webber, T. P. Comyn, J.-X. Ding, B. Xu, L.-Q. Cheng, M.-P. Zheng, Y.-D. Hou, and J.-F. Li, "Diffused Phase Transition Boosts Thermal Stability of High-Performance Lead-Free Piezoelectrics," *Adv. Funct. Mater.*, vol. 26, pp. 1217–124, 2016.

Chapter 3: Characterisation Techniques

3.1 Introduction

This chapter will discuss the techniques used to characterise raw materials, powders during processing and final fabricated ceramics.

3.2 Particle size analysis

Particle size analysis (PSA) was performed on raw materials, mixed precursors and calcined powders prior to sintering. A MASTERSIZER 3000 (Malvern Instrument Ltd.) attached with a Hydro dispersion unit (MAZ3300) was used to study particle size distributions of the samples.

A suspension of particles was created by stirring a small amount of powder (< 1 g) in distilled water using Hydro dispersion unit. The suspension was further optimised by ultarasonication. The equipment measures particle size distribution from angular variations in intensity of scattered laser beam as it passes through the suspension of particles.

3.3 Density measurements

3.3.1 Archimedes' density

Archimedes' densities of sintered ceramics were measured using Mettler Toledo model MS104S digital densitometer. The equipment calculates apparent density by comparing weights in air with weight in water using equation 3.1.

$$\rho = \frac{A}{A-B}(\rho_L - d) + d \qquad \text{Equation 3.1,}$$

where, ρ is density of sample, A is weight of sample in air, B is weight of sample in water, ρ_L is density of water at measurement temperature and d is density of air (~ 0.001 g/cm^3). Archimedes' method gives very precise results for dense samples, however in case of less dense samples which contain open pores, the densitometer shows higher density than

actual. This happens because water seeps into the sample and hence the volume of pores filled with water is not taken into account.

3.3.2 Geometric density

Geometric densities were also calculated for each sample according to equation 3.2.

$$\rho = \frac{m}{V} \qquad \text{Equation 3.2,}$$

where 'm' is mass and 'V' is volume of the sample. Mass of sample was measured using a digital balance with accuracy of ± 1 mg. Volume was calculated by finding diameter and thickness of the sample using a digital Vernier Calliper with an accuracy of ± 0.05 mm. For dense samples the difference between two methods was ~ 2 % and measurement of densitometer was considered more accurate. For less dense samples this difference can be > 10 % and hence the density calculated from the geometric method was considered to be more accurate.

3.3.3 Theoretical density

Theoretical densities were calculated using the following formula.

$$\boldsymbol{\sigma_{th}} = \frac{\boldsymbol{M.n}}{\boldsymbol{N_A V_{cell}}} \times \mathbf{10^{27}} \qquad \text{Equation 3.3,}$$

where σ_{th} is theoretical density (kg/m^3), M is molecular weight (g), 'n' is number of formula units per unit cell, 'V_{cell}' is volume of unit cell (Å^3) and 'N_A' is Avogadro number (6.022141×10^{23} mol.$^{-1}$). The volume of cell was calculated from X-ray diffraction (XRD) data as discussed in the next section.

3.4 Structural and microstructural analysis

3.4.1 X-ray diffraction (XRD)

X-rays are high energy electromagnetic radiation with a wavelength between ultraviolet and Gamma radiations**.** In laboratory x-rays are conventionally produced in an evacuated tube usually called an X-ray tube. Within the X-ray tube a filament is heated to emit electrons. These electrons are then accelerated towards a suitable target material by application of high electric field. A schematic of X-ray tube is shown in Figure 3.1.

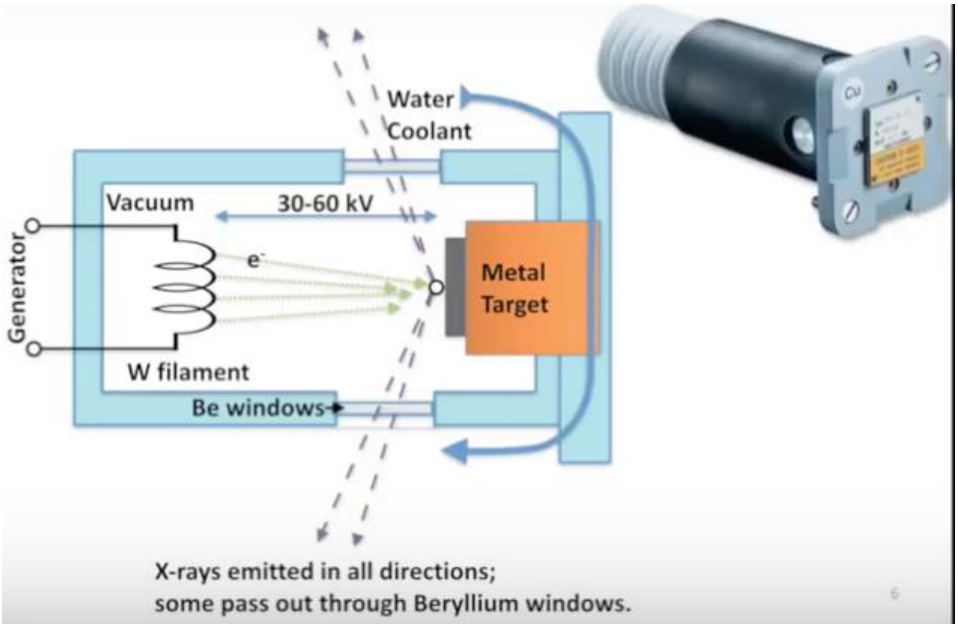

Figure 3.1: Schematic of an X-ray tube. (Re-printed from Lecture by Dr. Nek Reeves Maclaren, University of Sheffield)

Upon collision with the target material, X-rays are generated, however the process is very inefficient and approximately 98 % of the kinetic energy of the incident electron beam is converted to into heat and hence a cooling system is required. The X-rays generated are of two types (i) continuous X-rays and (ii) characteristic X-rays. Continuous X-rays arise from deceleration of electrons while characteristic X-rays arise from inner shell transitions and have therefore a specific wavelength. To choose amongst different kind of

wavelengths, filters are used and hence a monochromatic beam is obtained. Usually, $\boldsymbol{k_\alpha}$ radiations are utilised which correspond to a transition from L-shell to K shell. Since L shell can have sub shells and therefore transitions from each L-subshell to K shell are slightly different in wavelengths, represented by $\boldsymbol{k_{\alpha 1}}$ and $\boldsymbol{k_{\alpha 2}}$. However no filters were used to remove $\boldsymbol{k_{\alpha 2}}$ radiations and an average wavelength is considered for calculation purposes. For Cu target material, the intensity of $\boldsymbol{k_{\alpha 1}}$ is twice to that of $\boldsymbol{k_{\alpha 1}}$.

The wavelength of x-rays is comparable to inter planar spacing between the planes of crystals. Hence a crystal can serve as a diffraction grating for an incident X-ray radiation. Bragg's Law given in equation 1 was derived in 1913 by W.L Bragg, which gives a relation between wavelength (λ), inter planar spacing (d) and angle of diffraction (θ).

$$n\lambda = 2dsin\theta \qquad \text{Equation 3.4;}$$

In an XRD experiment usually a powder sample is exposed to a monochromatic x-ray radiation. Powders are polycrystalline materials with random orientations, the incident beam at certain angles will satisfy diffraction conditions for a particular set of planes and hence a diffraction pattern is observed [1,2].

In this study, XRD was performed to establish crystal structure and phase assemblage of raw materials, phase formation and assemblage of calcined powders and final sintered ceramics. Room temperature (RT) XRD data were collected using either Siemens D5000 or Bruker D2 Phaser with CuKα (λ = 1.5418 Å) source in the range 20 to 70 degrees 2θ at a step size of 0.02˚-0.05° operated at 40kV and 30mA. *In-situ* XRD was performed for selected samples in the temperature range 30–500 °C using a Siemens D5000 HTXRD, with CuKα source in the range 20 to 70 degrees 2θ at a step size of 0.05° operated at 40kV and 30mA.

Sintered samples were annealed at 500°C for 6 h to reduce the mechanical stresses produced during polishing or grinding.

Phase analysis was performed using an up-to-date data base from the International Center for Diffraction Data (ICDD). Lattice parameters were calculated from XRD data using

WinXpow software, utilizing least square fit method. Before lattice parameter calculations peak positions of the observed data were corrected using Si as a standard.

3.4.2 Raman spectroscopy

Raman spectroscopy is sensitive to local structure and is therefore very useful to understand the short range structural order, invisible to XRD. Raman spectroscopy relies Raman scattering, which refers to inelastic scattering of light from a material. This inelastic scattering causes a shift in the wave length of incident light, which can then be used to deduce information about the sample.

Usually a monochromatic laser beam is used as light source. Since light is an electromagnetic wave, the electric field E of the incident wave can excite a molecule with an oscillating dipole moment. When the excited molecule goes back to the its basic vibration state, a photon is released which can have three different types of frequencies.

1. Rayleigh scattering: The emitted photon has same frequency as that of incident photon.
2. Stokes Raman scattering: The emitted photon has lesser frequency than of incident photon.
3. Anti-Stokes Raman scattering: The emitted photon has higher frequency than that of incident photon.

The situation is schematically shown in Figure 3.2

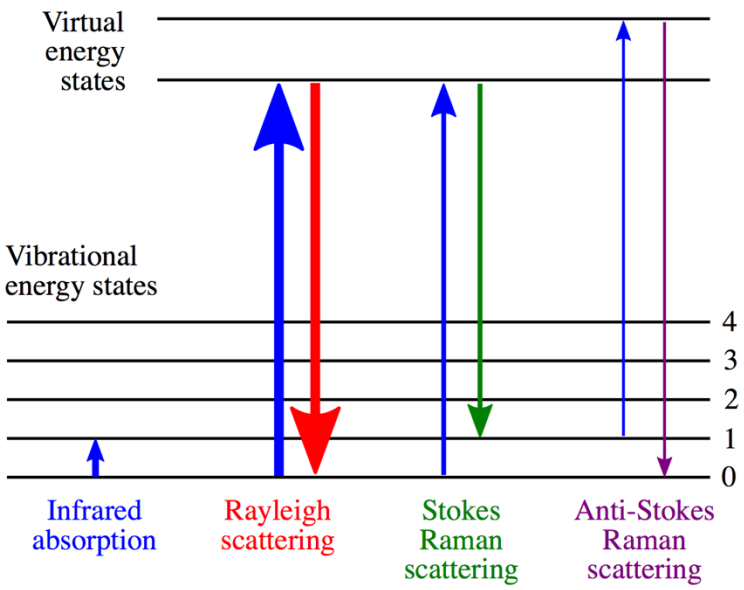

Figure 3.2: Energy level diagram showing the states involved in Raman spectra (re-printed from [3])

Only Stokes and Anti-Stokes scatterings (inelastic) can yield useful information about the sample under observation. Rayleigh scattering is completely useless for characterisation purposes. However, it should be noted that 99.999% of the all incident photons undergo Rayleigh scattering and therefore special arrangements are made to separate the useful signal from the intense Rayleigh signal [4].

A green LASER with wavelength of 514.5 nm and a power of 20 mW was focused on a ~2 μm spot and unpolarised Raman spectra were excited and recorded in back scattering geometry using Renishaw InVia micro-Raman spectrometer. A THMS600 stage (Linkam Scientific Instrument limited England) was used to record in-situ Raman spectra. The temperature was controlled by a TMS94 temperature controller with an accuracy of ±1 °C.

3.4.3 Differential scanning calorimetry (DSC)

DSC is a thermal analysis technique which works on the principle of heat flow. The measuring cell of DSC consist of a furnace and two pans with an integrated sensor. One pan is empty (reference) and the second one contains the sample. The furnace is subjected to a controlled temperature program. A thermocouple is connected to sensor area which can measure difference of temperature between the two pans. Since the reference pan is empty, it heats slightly faster than the sample pan. At constant heat rate both pans will show a linear increase in temperature unless phase transition occurs in the sample. At the onset of phase change the DSC curve of the sample pan will show an anomaly whilst that of the reference remains unaffected. As the transition is completed the sample again starts a linear increase in temperature. DSC curve for the sample is obtained from differential signal (ΔT) between the two pans. The area of the peak can be used to quantify heat content of transition [5].

To investigate phase transitions in selected samples, about 30 mg of crushed pellet powders were analysed using a Netzsh Proteus software controlled Netzch DSC 404 C Pegasus at heating/cooling rate of 10˚/min. Alumina crucibles were used for these measurements. To ensure that there are no anomalies associated with adsorbed volatiles each measurement was taken twice.

3.4.4 Dilatometry

Dilatometry measures linear thermal expansion or shrinkages in a sample during hearing or cooling. Samples are connected to push rod inside the furnace. The push rod is connected to an inductive displacement transducer (LVDT system), which measures the expansions/contractions in the sample as temperature is increased [6]. Samples prepared for dilatometry were cylindrical in shape with length of ~6 mm. A NETZSCH DIL 402 C was used to perform the experiments. Dilatometry was performed on samples between RT to 700°C with a heating rate of 10 °C/min.

3.4.5 Scanning electron microscopy (SEM)

In scanning electron microscope (SEM), a sample is scanned by a highly energetic electron beam. Electrons are produced by an electron gun through thermionic emission which are then accelerated in vacuum by application of high electric field. When an electron beam interacts with a specimen, it can give rise to several phenomenon including secondary electron emissions, back scattering and emission of characteristic X-rays. Secondary electrons (SEs) are electron from the specimen, ejected by primary electrons. Depending on the type of bonding SEs can be classified into (i) slow SEs (loosely bound) (ii) Fast SEs (strongly bound) and (iii) Auger electrons (outer electrons emitted in place of characteristic X-rays). Slow electrons are emitted from regions near the surface and are very abundant. Almost each primary electron can result in ejection of a secondary electron. These electrons contain negligible elemental information (not from specific atom) but are very useful for high resolution imaging. Typical SEM imaging is done by utilizing slow SEs and the image is usually referred to as secondary electron image. Fast electrons are usually not desired as they can travel along way in the specimen and give rise to emission of further characteristic detrimental to resolution and chemical analysis. Auger electrons can be used for Auger spectroscopy not relevant to this study.

Primary electrons which are scattered by the nucleus at angles approaching 180° are known as back scattered electrons. The intensity of backscatter electrons is proportional to the atomic number of the atom. Hence backscatter electrons can be used to study chemical variation across the sample surface. Since the characteristic X-rays have specific wavelengths, they can be collected to deduce useful elemental information. However, it is difficult to detect element with low concentration or very low atomic number (below Na) [2,7]. For reliable chemical or elemental analysis samples ceramic samples require high quality polishing. For revealing feature such as grains and grain boundaries in SE image, the polished samples need to be etched either chemically or thermally.

In this study an Inspect F microscope operating at 5 kV at working distance of 10 mm was used to study microstructure of sintered samples. The samples were mounted on aluminium stub and then gold coated using a sputter coater to avoid accumulation of charges on surface of sample.

3.4.6 Transmission electron microscopy (TEM)

In transmission electron microscopy (TEM) a thin sample is exposed to an energetic beam of electrons. Electrons can interact in different ways with the sample (as discussed in preceding section), which can be used for imaging and compositional analysis. The conventional imaging mode in TEM is bright field imaging, where a high resolution images can be obtained from the transmitted (un-diffracted) electron beam. In bright field imaging thicker regions or areas with higher densities will appear darker due to greater weakening in the intensity of the transmitted beam. However, the diffracted beam can also be used for imaging purposes, known as dark field imaging. Since the diffracted beam has interacted strongly with specimen useful features such as planar defects and stalking faults can be observed in a dark field image [8].

In addition, electron diffraction (ED) data can be obtained to study crystal symmetry. ED data are invaluable to study local structure of crystals especially in case of tilted perovskite. X rays interacts very poorly with oxygen and thus information from oxygen sub lattice is limited in XRD. In ED a single crystal can be easily studied and the sensitivity of electrons to oxygen and short coherent lengths can help in the unambiguous interpretation of crystal symmetry [9].

TEM was performed to characterise domain structure and crystal structure for selected samples. Samples for TEM were prepared by mounting a section of sintered ceramic on Gatan Disk Grinder and were then mechanically ground to a thickness of ~30μm using silicon carbide paper. An (Epoxy resin, Wellingbrough, UK) glue was used to stick the samples to 3 mm copper support rings with an aperture of 1 mm. A Gatan DuoMill (Pleasanton, California, USA) was used to accelerate Argon ions at 6 kV. The accelerated ion beam was made incident on the sample at 12-15°. The samples were ion milled until perforation. Electron diffraction patterns and images were taken by Dr. Rebecca Boston using a JEOL-2010F TEM, operating at 200 kV.

3.5 Electrical measurements

3.5.1 Capacitance and dielectric loss measurements

Capacitance and dielectric loss (tanδ) versus temperature can be measured using an LCR (L=Inductance; C =Capacitance and R = Resistance) meter. The LCR meter used in this study works on principal of "automatic balancing bridge method" shown in Figure 3.3. An amplifier automatically keeps the current (I_2) passing through resister R_2 the same to current (I) passing through device under test (DUT). In diagram V_1 is input voltage and V_2 is output voltage. The lower potential of DUT (L) is at virtual ground i.e. V = 0.

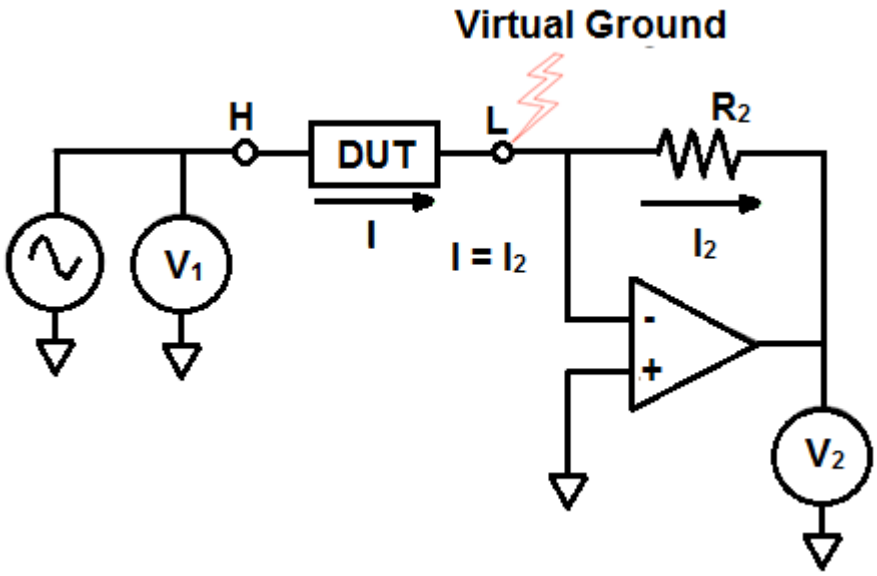

Figure 3.3: Schematic diagram of Automatic Balancing Bridge.

By measuring V_2, impedance can be calculated using the following formula.

$$Z = R_2 \frac{V_1}{V_2} \qquad \text{Equation 3.5,}$$

At the same time phase angles are also calculated which in combination with the impedance values are used to determine tan δ and capacitance for sample under test and

are displayed on the screen [10]. The computer connected to the LCR meter, records capacitance and tan δ values measured during the experiment. Dielectric constant can be calculated from capacitance using the following formula

$$\varepsilon_r = \frac{C.d}{\varepsilon_o.A} \qquad \text{Equation 3.6,}$$

where, C is capacitance (F), d is thickness of the sample (m), A is area of face of the pellet (m^2), ε_o is permittivity of free space, 8.854×10^{-12}(F/m) and ε_r is relative permittivity or dielectric constant.

Capacitance and dielectric loss (tanδ) versus temperature was measured at 1 kHz, 10 kHz, 100 kHz, 250 kHz and 1 MHz using an LCR (L=Inductance; C =Capacitance and R = Resistance) meter (Model 4284A, Hewlett Packard) connected to a computer through CP-IB interface. The sample was loaded into a conductivity jig and placed in a tube furnace. An extra thermocouple was present near the sample for accurate measurement of temperature.

3.5.2 Impedance spectroscopy

Electrical microstructure of a sample can be interpreted by using impedance spectroscopy over a wide range of frequencies (10^{-2} to 10^7 Hz). Impedance spectroscopy can be carried out using an impedance analyser (LCR meter), which can measure impedance using automatic balancing bridge, explained in the preceding section.

The obtained complex impedance (Z) can be related to three other complex formalism namely, admittance (Y), permittivity (ε) and electric modulus (M) and hence four different formalisms can be used to analyse impedance spectroscopy data. The mathematical relations for these formalisms are given below.

$$Z = Z' - jZ'' \qquad \text{Equation 3.7,}$$

$$Y = \frac{1}{Z} = \frac{1}{Z' - jZ''} = \frac{Z' + jZ''}{(Z')^2 + (Z'')^2}$$
$$Y' = \frac{Z'}{(Z')^2 + (Z'')^2}$$
$$Y'' = \frac{Z''}{(Z')^2 + (Z'')^2}$$

Equations 3.8,

$$M = j\omega C_0 Z = \omega C_0 (Z' - jZ'') = \omega C_0 Z'' + j\omega C_0 Z'$$
$$M' = \omega C_0 Z''$$
$$M'' = \omega C_0 Z'$$
$$C_0 = \varepsilon_0 \frac{A}{d}$$

Equations 3.9,

$$\varepsilon = \frac{1}{M} = \frac{1}{M' + jM''} = \frac{1}{\omega C_0} \cdot \frac{Z'' - jZ'}{(Z')^2 + (Z'')^2}$$
$$\varepsilon' = \frac{1}{\omega C_0} \cdot \frac{Z''}{(Z')^2 + (Z'')^2}$$
$$\varepsilon'' = \frac{1}{\omega C_0} \cdot \frac{Z'}{(Z')^2 + (Z'')^2}$$

Equations 3.10,

Where Z' and Z'' are respectively real and imaginary parts of complex impedance, $j = \sqrt{-1}$, $\omega = 2\pi f$ is angular frequency and C_o is capacitance of vacuum in the measuring cell.

M or ε are can be used to calculated capacitance directly and resistance can be calculated indirectly from relation $\omega RC = 1$. Similarly, resistance can be calculated directly from Z or Y and then capacitance can be calculated indirectly from relation, $\omega RC = 1$. A model equivalent circuit is required to analyse the impedance data. An ideal dielectric can be modelled electrically as a capacitor. However, all real materials have some leakage current (long range conduction) associated with it, for which a resistor is introduced in parallel. In Z and M formalism a parallel RC circuit gives a single semi-circle. Complex plane plot for a single RC circuit is shown in Figure 3.4.

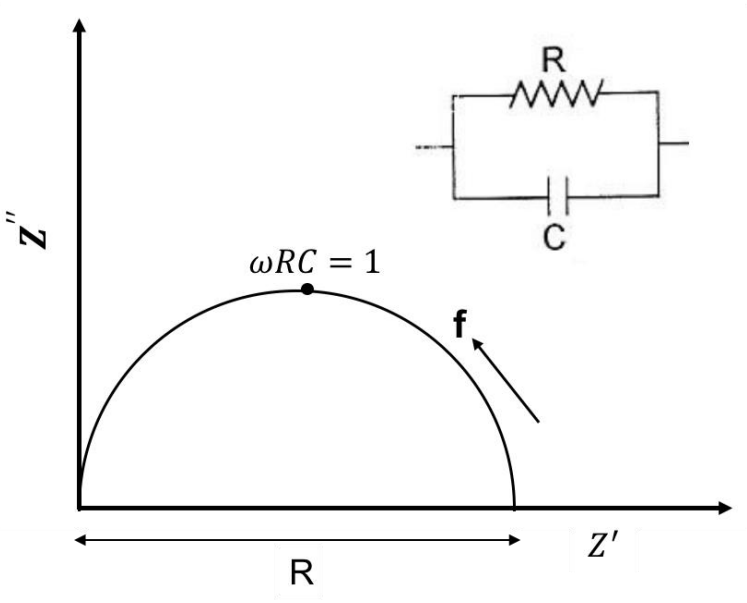

Figure 3.4: Possible equivalent circuit for an electrically homogenous dielectric in complex plane plot of impedance formalism.

If a material has more than one electro-active parts such as grain and grain boundary, then another parallel RC circuit can be introduced in series. Complex plane plot for two parallel RC elements connected in series is shown in Figure 3.5.

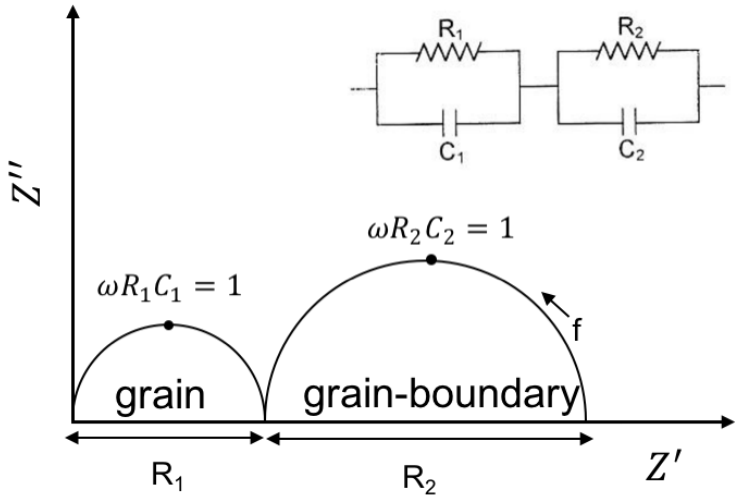

Figure 3.5: Possible equivalent circuit for a dielectric with different responses from grain and grain boundary in complex plane plot of impedance formalism.

where, R_1 is resistance of the grain and R_2 is resistance of gran boundary. Grain boundaries are generally more resistive than grains due to voids, secondary phases and crystal anisotropy etc. The total resistance of material in such case is

$$R_{total} = R_{grain} + R_{grain-boundary} \quad \text{Equation 3.11,}$$

Since capacitance depends on geometry; its magnitude is generally a good indicator of differentiating between different electro-active regions. For example, a grain boundary will have high capacitance because it has very small thickness in comparison to the grain. Capacitance values and their possible interpretations are given in Table 3.1 [11,12].

Table 3.1: Capacitance values and their possible interpretation.

Capacitance (F)	Phenomenon
10^{-12}	bulk
10^{-11}	secondary phase(s)
10^{-11} – 10^{-8}	grain boundary
10^{-10}-10^{-9}	bulk ferroelectric
10^{-9} – 10^{-7}	surface layers
10^{-7}-10^{-5}	sample-electrode interface
10^{-4}	electrochemical reaction

Normally impedance measurements are taken at different temperatures which can be used to determine activation energies of conduction by using Arrhenius equation given below.

$$\sigma = \sigma_o \, e^{\frac{E_a}{KT}} \quad \text{Equation 3.12,}$$

where, σ is conductivity, σ_o is pre-exponential constant, E_a is activation energy, K is Boltzmann constant (8.6173324 x 10^{-5} eV.K^{-1}) and T is temperature.

From equation 3, E_a can be written as

$$E_a = -m\,(0.19842) \qquad \text{Equation 3.13,}$$

where, m is slope of the linear fit obtained by plotting log(σ) vs. $\frac{1000}{T}$.

For impedance spectroscopy, samples were loaded into a conductivity jig and placed in a tube furnace similar to that of LCR measurements. Impedance measurements were taken at various temperatures ranging from 25 to 750 °C using either HP4192A (5 Hz-13MHz) or Agilent E4980A (20 Hz- 2 MHz) precision LCR meter. The applied voltage was 0.1 V and data were corrected for geometry using ZView™ software (Scribner Associates Inc, USA).

3.5.3 Piezoelectric measurements

Depending on the input signal piezoelectric characterisation can be classified into two categories (i) small signal characterisation (ii) large signal characterisation. Large signal refers to driving fields large enough in amplitude to switch the ferroelectric domains. Small signal on the hand refer to sub coercive fields where linear relation is observed between applied electric field and induce strain.

3.5.3.1 Small signal dynamic measurements (Resonance method)

All elastic materials show numerous mechanical resonances. Mechanical resonance refers to a phenomenon in which a vibrating body shows maximum amplitude at a particular driving frequency. A piezoelectric material has the ability to excite elastic waves electrically and therefore provides a method of studying electromechanical coefficients. At resonance, a piezoelectric vibrator can be modelled by an equivalent circuit, which combines electric components L, C and R in series as shown in Figure 3.6. C_p is

capacitance of the sample in absence of mechanical deformation at resonant frequency [13].

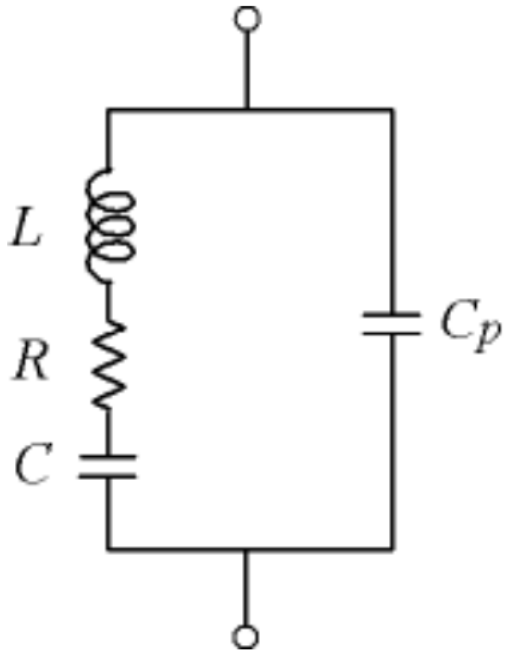

Figure 3.6: Equivalent circuit for a piezoelectric vibrator at the resonance state [13].

Resistance is frequency independent, while reactance of capacitor and inductor depends on frequency according to the following equations.

$$X_L = 2\pi f L \qquad \text{Equation 3.14,}$$

$$X_C = \frac{1}{2\pi f C} \qquad \text{Equation 3.15,}$$

Where X_L and X_C are respectively reactance of inductor and capacitor.

Dependence of resistance and reactance as a function of frequency is show in Figure 3.7.

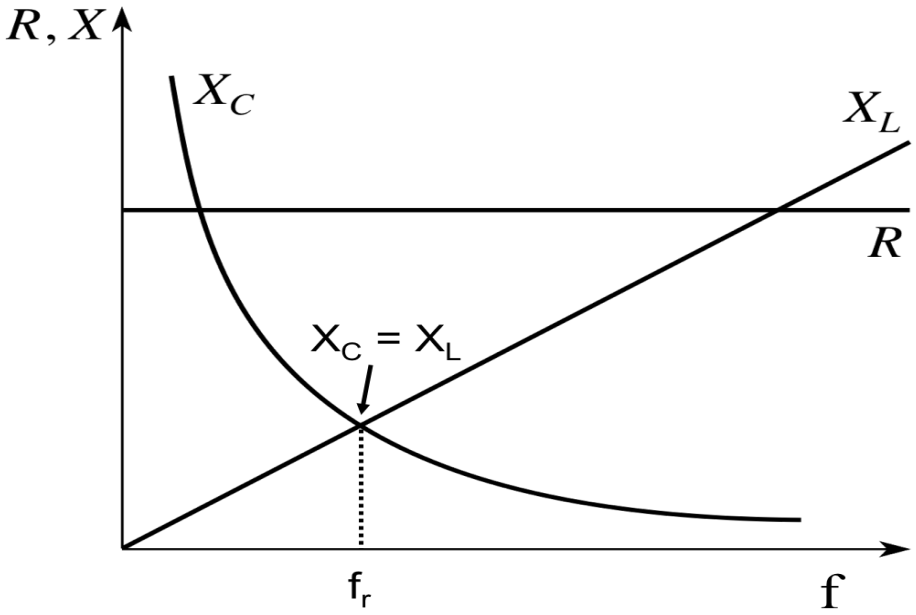

Figure 3.7: Resistance and reactance as a function of frequency.

The frequency at which $X_C = X_L$ is known as resonant frequency (f_r). Since X_C and X_L are out of phase by 180°, the total reactance at f_r is effectively zero leading to a minimum in impedance.

As the name suggest antiresonance is opposite phenomenon to resonance and hence correspond to a minimum amplitude for a vibrating body. Therefore, in electrical context discussed here, it corresponds to maximum in impedance. The above discussion concludes that resonance and ant antiresonance peaks can be experimentally found by performing impedance spectroscopy over a wide range of frequency. Typical impedance curve for a piezoelectric material is shown in Figure 3.8.

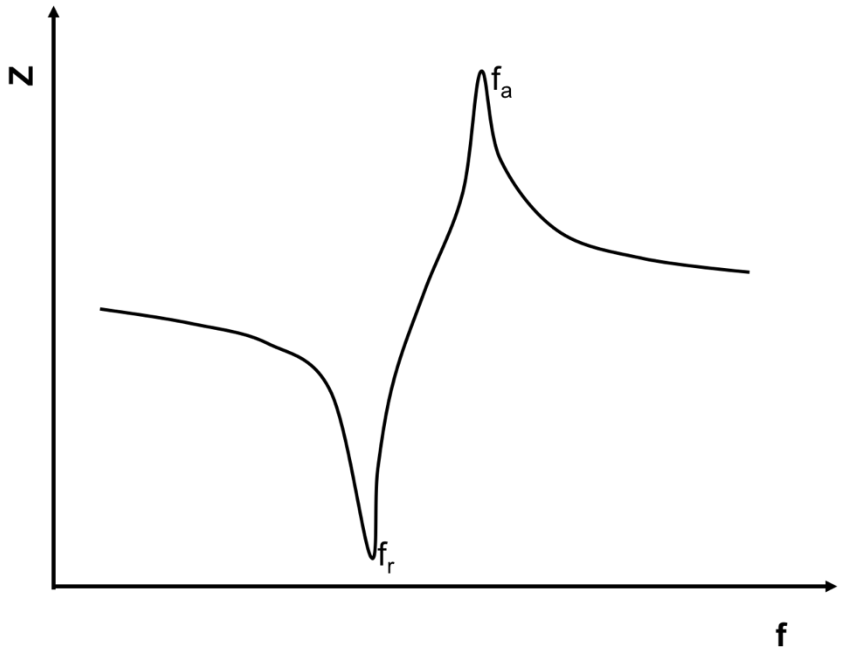

Figure 3.8: Impedance curve for a piezoelectric material.

The values of resonance and antiresonance frequencies in addition to values of capacitance and tanδ can be used to determine piezoelectric, dielectric and elastic constants, if experiments are performed on samples of suitable geometry and theory for mode of operation in the sample is known. e.g. The planar electromechanical coupling factor (k_p) can be estimated from the resonance (f_r) and antiresonance (f_a) frequencies using Onoe's formula, given below [14].

$$\frac{1}{k_p^2} = 0.398\ \frac{f_r}{f_a - f_r} + 0.579 \qquad \text{Equation 3.16,}$$

A complete set of equations and procedures to find various piezoelectric constants can be found in IEEE standards [15]. Standardised geometries for fundamental vibration modes are shown Figure 3.9.

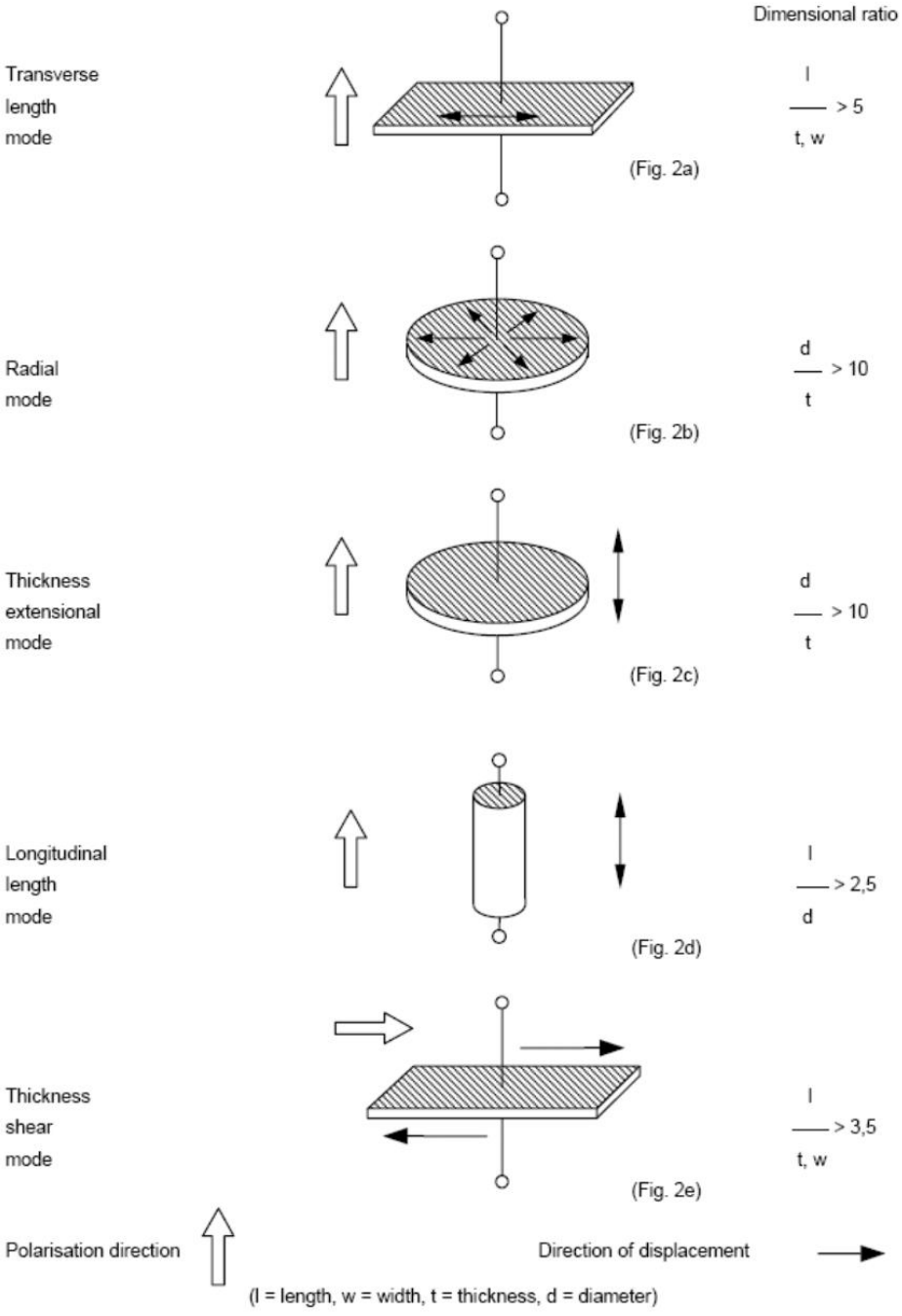

Figure 3.9: Fundamental vibration modes for piezoelectric resonators [16].

The values for f_a and f_r in this study were measured by using an Agilent 4294A Impedance analyzer (40 Hz to 110 MHz). Temperature dependence of k_p was measured by placing the sample between two platinum wires in a conductivity jig placed in a furnace attached

to the impedance analyser. Similar to the LCR measurements an extra thermocouple was placed near the sample to get accurate temperature readings.

3.5.3.2 Small signal quasi-static measurements (Berlincourt method)

Piezoelectric charge constant (d_{33}) was measured using "Berlincourt" method. It is a simple test to measure the direct piezoelectric effect. In this type of measurement, a cyclic stress is applied on the sample by sandwiching it in between two vibrating metal parts. A piezoelectric material generates electric current due to applied pressure, which charges a capacitor connected in parallel to it. Measurement of the voltage on capacitor is used to calculate d_{33} of the sample under test [17]. The test is performed at low frequency (< 1 kHz), hence it is also termed as quasi-static measurement. Although the testing frequency is much lower than resonance method, it is high enough to complete the test within few seconds. Note that d_{33} can also be measured using equation 2.08 by measuring strain at small signals.

d_{33} in this study was measured using (Piezotest. Model PM300, London, UK) piezoelectric meter after DC poling. An optimised poling field was considered to be where a further increase in electric field did not result in an increase in d_{33} by more than 5 %. A dynamic force of 0.25 N with frequency of 110 Hz was applied to take these measurements.

3.5.3.3 Large signal quasi-static measurements

Polarisation under large signals are conventionally measured using a Sawyer-Tower circuit, in which a large integrating capacitance is placed in series with the sample. By measuring the voltage across capacitor, charge on capacitor can be measured, which is equivalent of charge on the test sample. However, the system routinely used during this study determines charge on the sample by detecting current (I) through the sample by a feedback method. Polarisation (P) is then calculated by first calculating, charge (Q) and dielectric displacement through following set of equations.

$$Q_{(t)} = \int_{t_1}^{t_2} I \ dt \qquad \text{Equation 3.17,}$$

$$D_{(t)} = \frac{Q_{(t)}}{A} \qquad \text{Equation 3.18,}$$

$$P_{(t)} = D_{(t)} - \varepsilon_o E_{(t)} \qquad \text{Equation 3.19,}$$

where, A is area of the sample and E is applied electric field.

Since polarisation is coupled with strain, therefore strain is routinely measured simultaneously with polarisation using one of the four techniques listed below.

1. Capacitance probe
2. Fiber optic probe
3. Strain gauges
4. Laser interferometry

In this study laser interferometry was used, which has probably the highest resolution amongst all four techniques. This technique mostly relies on Michelson interference in which the path difference between a reference beam (fixed path) and a beam reflected from the sample is used to measure the displacement [18].

For polarisation (*P*) and bipolar strain (*S*) vs. electric field (*E*) measurements samples were thinned to ~ 0.7 mm and then silver electroded on both sides. The measurements were taken using an aix-ACCT TF2000FE- HV ferroelectric test unit (aix-ACCT Inc., Germany).

The sample holder has an integrated heating unit and is coupled with a laser beam interferometer. Hence, simultaneous acquisition of polarisation and electromechanical strain data over a wide range of temperature can be performed. For *S*-*E* and *P*-*E* data with temperature, samples were given sufficient time to achieve thermal equilibrium within ± 0.2 °C. The sample holder was filled with silicon oil to increase range of applied voltage without any electric arcing. All measurements were taken at a fixed frequency of 1 Hz using a triangular wave form.

To study the fatigue behaviour, samples were exposed to a triangular bipolar loading of ~$3E_c$ for 10^6 cycles at a frequency of 5-10 Hz using the same system. All measurements were done at Christian Doppler Laboratory on Advanced Ferroic Oxides, Sheffield Hallam University (SHU), Sheffield. To validate the results obtained in SHU, room temperature *S-E* measurement on some samples, under same conditions were performed by Dr. Dawei Wang at Material Research Institute (MRI) Penn State University USA using a modified Sawyer Tower Circuit driven by a lock in amplifier (Stanford Research system, Sunnyvale, CA, Model SR830).

3.6 References

[1] E. Lifshin, *X-ray Characterization of Materials*. 1999.

[2] A. R. West, *Solid State Chemistry and its Applications*, 2nd ed. Jhon Wiley & Sons Ltd, 2014.

[3] "https://commons.wikimedia.org/wiki/File:Raman_energy_levels.svg." visited 0n 03-01-17

[4] A. Long, *Raman spectroscopy*. Springer Berlin Heidelberg, 2003.

[5] "https://www.netzsch-thermal-analysis.com/en/landing-pages/principle-of-a-heat-flux-dsc/." visited on 03-01-17

[6] "http://www.paralab.pt/sites/default/files/pdf/DIL%20402%20E%207%20PURO.pdf." visited on 03-01-17.

[7] J. I. Goldstein, D. E. Newbury, P. Echlin, D. C. Joy, C. E. Lyman, E. Lifshin, L. Sawyer, and J. R. Michael, *Scanning Electron Microscopy and X-ray Microanalysis*. Boston, MA: Springer US, 2003.

[8] D. B. Williams and C. B. Carter, *The Transmission Electron Microscope*. Boston, MA: Springer US, 2009.

[9] D. I. Woodward and I. M. Reaney, "Electron diffraction of tilted perovskites," *Acta Crystallogr. Sect. B Struct. Sci.*, vol. 61, no. 4, pp. 387–399, 2005.

[10] "http://kripton2035.free.fr/Resources/Impedance%20Measurement%20Basic.pdf." visited on 03-01-17.

[11] A. R. WEST, D. C. SINCLAIR, and N. HIROSE, "Characterization of Electrical Materials, Especially Ferroelectrics, by Impedance Spectroscopy," *J. Electroceramics*, vol. 1, no. 1, pp. 65–71, 1997.

[12] J. T. S. Irvine, D. C. Sinclair, and A. R. West, "Electroceramics: characterization by impedance spectroscopy," *Adv. Mater.*, vol. 2, no. 3, pp. 132–138, 1990.

[13] W. R. C. J. B. Jaffe H. Jaffe and B. Jaffe, *Piezoelectric Ceramics*. Acadamic Press (London) Inc. Ltd., 1971.

[14] S. Zhang, E. F. Alberta, R. E. Eitel, C. A. Randall, and T. R. Shrout, "Characterization of Modified $BiScO_3$ –$PbTiO_3$ Ceramics," *IEEE Trans. Ultrason. Ferroelectr. Freq. Control*, vol. 52, no. 11, pp. 2131–2139, 2005.

[15] A. American and N. Standard, "An American National Standard IEEE standard on piezoelectricity," pp. 8–10, 1988.

[16] I. Sterianou, “Bismuth-based Pervoskites for High Temperature Piezoelectric Applications,” The University of Sheffield, 2007.

[17] M. Stewart and M. G. Cain, “Direct Piezoelectric Measurement: The Berlincourt Method,” in *Characterisation of Ferroelectric Bulk Materials and Thin Films*, M. G. Cain, Ed. Dordrecht: Springer Netherlands, 2014, pp. 37–64.

[18] M. Stewart, M. G. Cain, and D. Hall, “Ferroelectric Hysteresis Measurement & Analysis,” *NPL Rep. C.*, no. May, pp. 1–57, 1999.

Chapter 4: Processing of Materials

4.1 Introduction

All ceramics studied in this project (listed in Table 4.1) were fabricated using a solid state synthesis route. This chapter will explain in detail the processing of ceramics from characterisation of raw materials to fabrication of the final ceramic body.

Table 4.1: List of compositions studied in this project

S.No.	Series	*x* (mol. %)
	$BiFeO_3$ (BF)-based (Chapter 5)	
1	(1-*x*)$BiFeO_3$- *x*$Nd_{2/3}TiO_3$	0, 0.05, 0.10, 0.15
2	(0.97-*x*)$BiFeO_3$-*x*$NdFeO_3$-0.03$Nd_{2/3}TiO_3$	0.05, 0.10, 0.15
3	(0.95-*x*)$BiFeO_3$-*x*$LaFeO_3$-0.05$La_{2/3}TiO_3$	0, 0.05, 0.10, 0.15, 0.20, 0.25, 0.30, 0.35
	$K_{1/2}Bi_{1/2}TiO_3$ (KBT)-based (Chapter 6)	
4	(1-*x*)$K_{1/2}Bi_{1/2}TiO_3$ – *x*(0.8$BiFeO_3$-0.15$LaFeO_3$-0.05$La_{2/3}TiO_3$)	0, 0.02, 0.04, 0.06, 0.08, 0.10, 0.12, 0.15, 0.20, 0.3, 0.4, 0.5, 0.6, 0.7
5	(1-*x*)$K_{1/2}Bi_{1/2}TiO_3$ – *x*(0.82$BiFeO_3$-0.15$NdFeO_3$-0.03$Nd_{2/3}TiO_3$)	0.03, 0.06, 0.09, 0.12, 0.15
	$K_{0.4}Na_{0.6}NbO_3$ (KNN)-based (Chapter 8)	
6	(1-*x*)$K_{0.4}Na_{0.6}NbO_3$ – *x*$BiFeO_3$	0, 0.005, 0.0075, 0.01, 0.0125, 0.015, 0.02, 0.03
7	0.99$K_{0.4-x}Li_xNa_{0.6}$NbO3- 0.01$BiFeO_3$	0.02, 0.04

A prototype multilayer actuator was fabricated based on composition in series 5 at x = 0.09. Details of multilayer processing will be given in chapter 7.

4.2 Raw materials

Raw materials with purity > 99% (listed in Table 4.2) were used to fabricate composition studied in this project.

Table 4.2: List of raw material used to fabricate ceramics given in Table 4.1

S.No.	Chemical	Purity (%)	Supplier
1	Bi_2O_3	99.9	Acros Organics
2	Fe_2O_3	99 +	Sigma Aldrich
3	Nd_2O_3	99.9	Acros Organics
4	TiO_2	99.9	Sigma Aldrich
5	La_2O_3	99.99	Stanford Materials
6	Nb_2O_5	99.5	Alfa Aesar
7	K_2CO_3	99.9	Fisher Scientific
8	Na_2CO_3	99.9	Fisher Scientific
9	Li_2CO_3	99 +	Acros Organics

4.2.1 Drying of raw materials

Electrical properties of ceramics can be hugely effected by imbalance in stoichiometry. A major source of non-stoichiometry could be the amount of adsorbed moisture and/or carbon dioxide in starting materials [1]. All raw materials listed in Table 4.2 are susceptible to take up moisture from air. Amount of moisture in a material depends on humidity in air, particle size and method of storage. Exact amount of moisture was not quantified, but all these materials may contain moisture from 0.1 % to greater than 1 %. La_2O_3, K_2CO_3 and N_2CO_3 are particularly hygroscopic and they may contain a still higher percentage. Some raw materials, such as La_2O_3 can form hydrated oxide by absorbing moisture from air at room temperature. Some raw materials, such as Nd_2O_3, form neodymium carbonate by absorbing carbon dioxide from air [2,3]. Hence, to ensure the correct stoichiometry all raw materials were dried at a temperature high enough to get rid of adsorbed moisture but well below the decomposition or melting point of raw material. The importance of this step is exemplified by comparing XRD traces obtained from La_2O_3 powders after drying them at 180 °C and 800 °C overnight as shown in Figure 4.1.

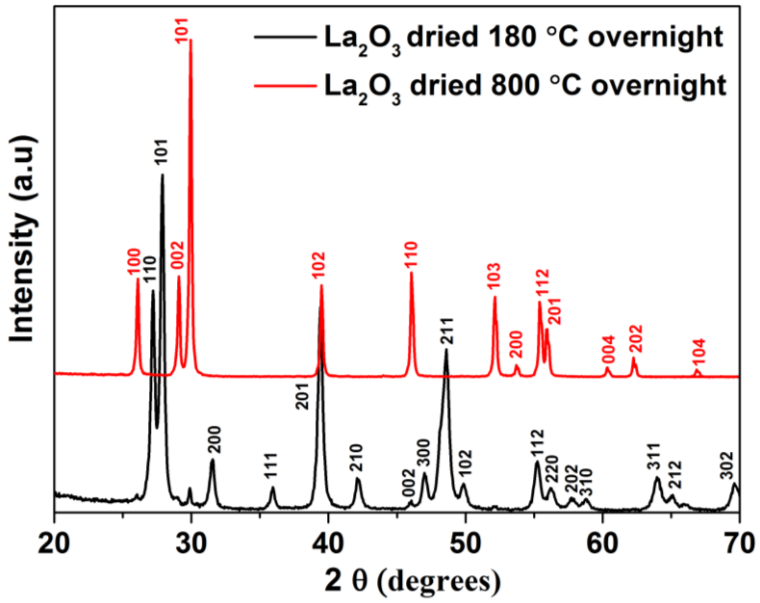

Figure 4.1: XRD plot of La_2O after drying overnight at 180 °C and 800 °C.

XRD trace of as obtained powders dried at 180 °C matched well with $La_2(OH)_3$ PDF No. 00-036-1481, while the XRD trace powders dried at 800 °C matched with La_2O_3 PDF No. 00-005-0602. All raw materials were therefore heated to the required drying temperature overnight and then cooled to 200 °C after which they were transported to sealed desiccators for cooling to room temperature. A schematic of the drying profile is shown in Figure 4.2. The drying temperatures for all raw materials are summarized in Table 4.3.

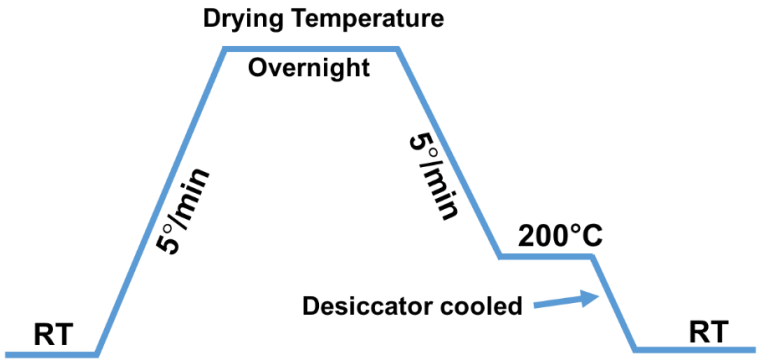

Figure 4.2: Drying profile for reagents

Table 4.3: Drying temperatures for raw materials

Chemical	Drying Temperature
Bi_2O_3, Fe_2O_3	500 °C
Nd_2O_3, TiO_2, La_2O_3	800 °C
Nb_2O_5	900 °C
K_2CO_3, Na_2CO_3	300 °C
Li_2CO_3	180 °C

4.2.2 Phase analysis of raw Materials

To confirm the crystal structure and phase assemblage, all raw materials were analysed using XRD after drying. XRD traces of all raw material from 1 to 9 were in good agreement with Powder Diffraction Files (PDF) for Bi_2O_3, Fe_2O_3, Nd_2O_3, TiO_2 (rutile), La_2O_3, K_2CO_3, Na_2CO_3 and Li_2CO_3 respectively, as shown in Figure 4.3 and 4.4.

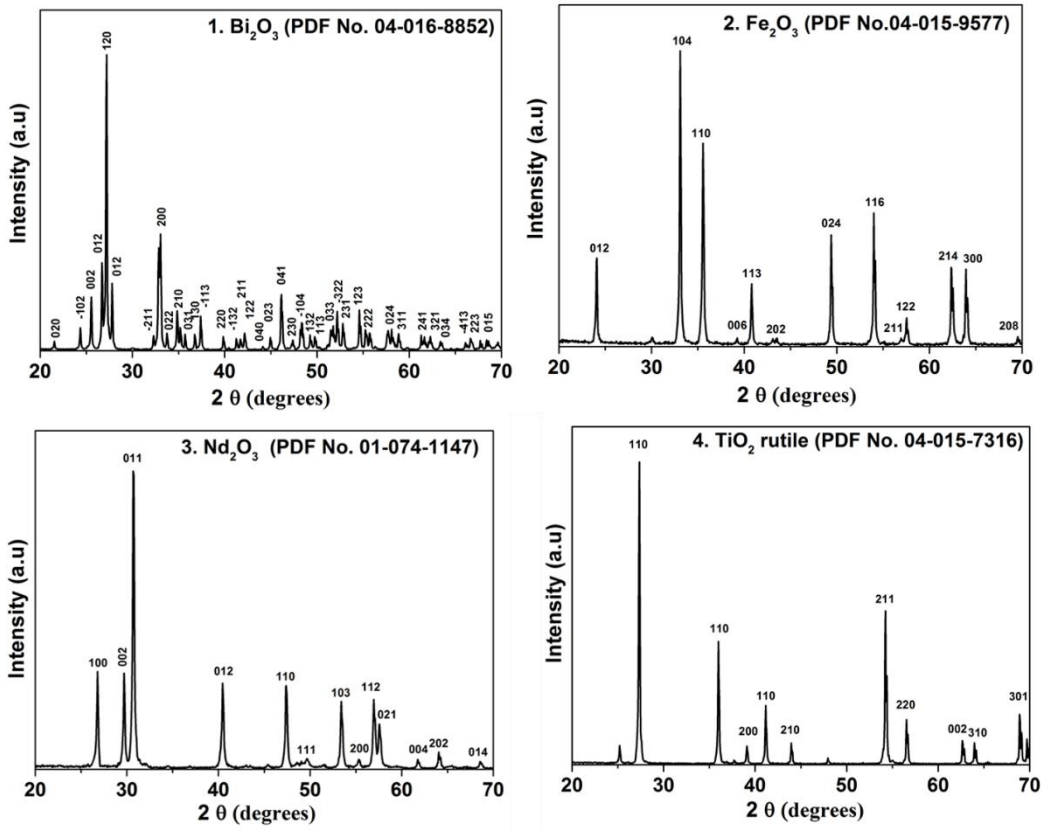

Figure 4.3: XRD traces for raw materials S. No. 1-4 matched with PDF No. 04-016-8852, 04-015-9577, 01-074-1147 and 04-015-7316 for Bi_2O_3, Fe_2O_3, Nd_2O_3, TiO_2 (rutile) respectively.

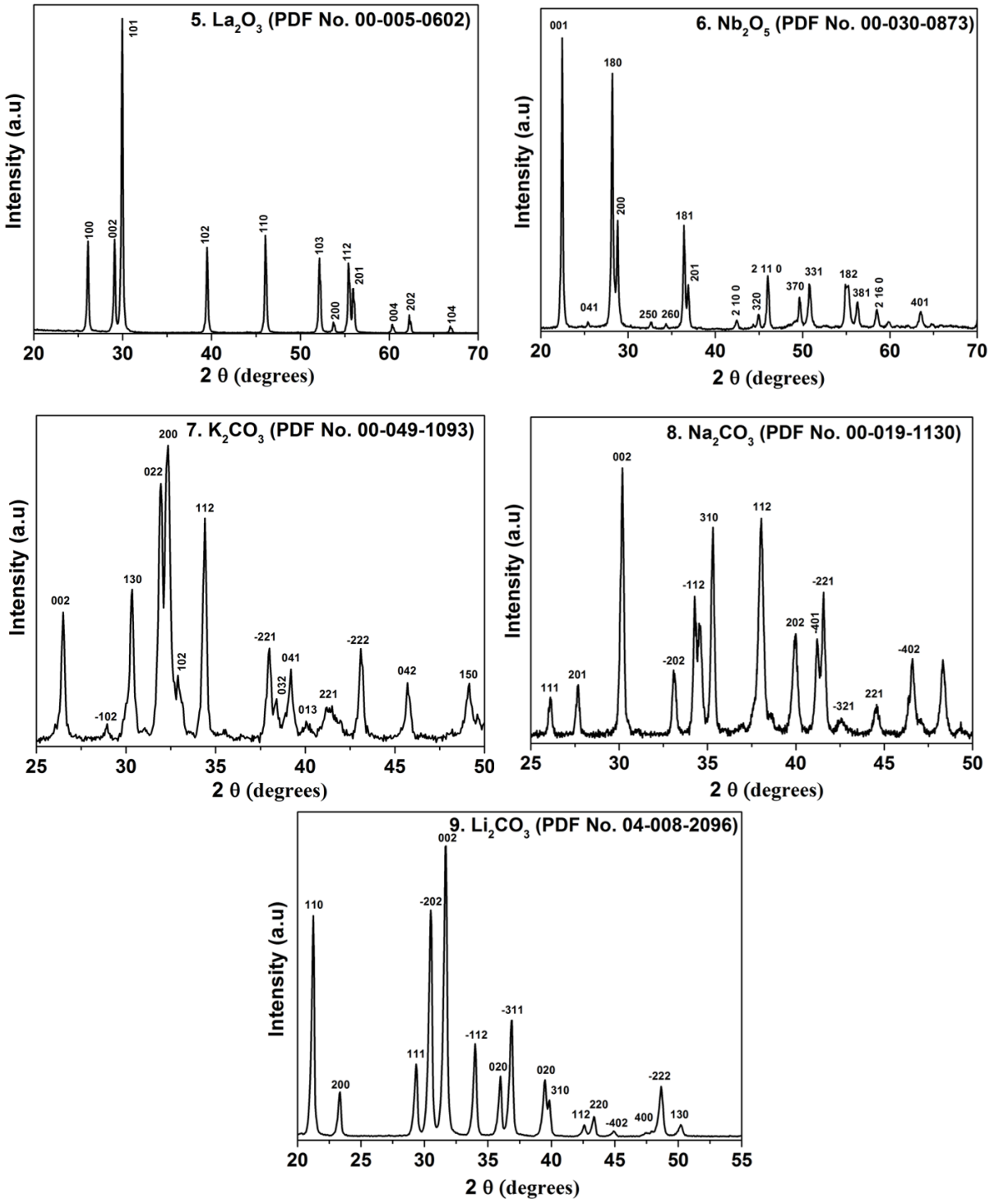

Figure 4.4: XRD traces for raw materials S. No. 5-9 matched with PDF No. 00-005-0602, 00-030-0873, 00-049-1093, 00-019-1130, 04-008-2096 for La_2O_3, Nb_2O_5 K_2CO_3, Na_2CO_3 and Li_2CO_3, respectively.

4.2.3 Particle size analysis of raw materials

Particle size distributions of oxide precursors are shown in Figure 4.5. The mean particle size for all oxides excluding Bi_2O_3 was < 6 µm. Mean particle size for Bi_2O_3 was 8.34 µm. Since the laser beam cannot differentiate between a single particle and agglomerate, the values of particle size might be affected by agglomeration. However, we expect agglomeration to be destroyed during milling prior to calcination. Carbonates used in this study don't form a suspension in water but instead get dissolved. The alkali carbonates are very reactive and are expected to form a homogenous composition when mixed well with other precursors and hence particle size analysis was not performed on as received carbonates.

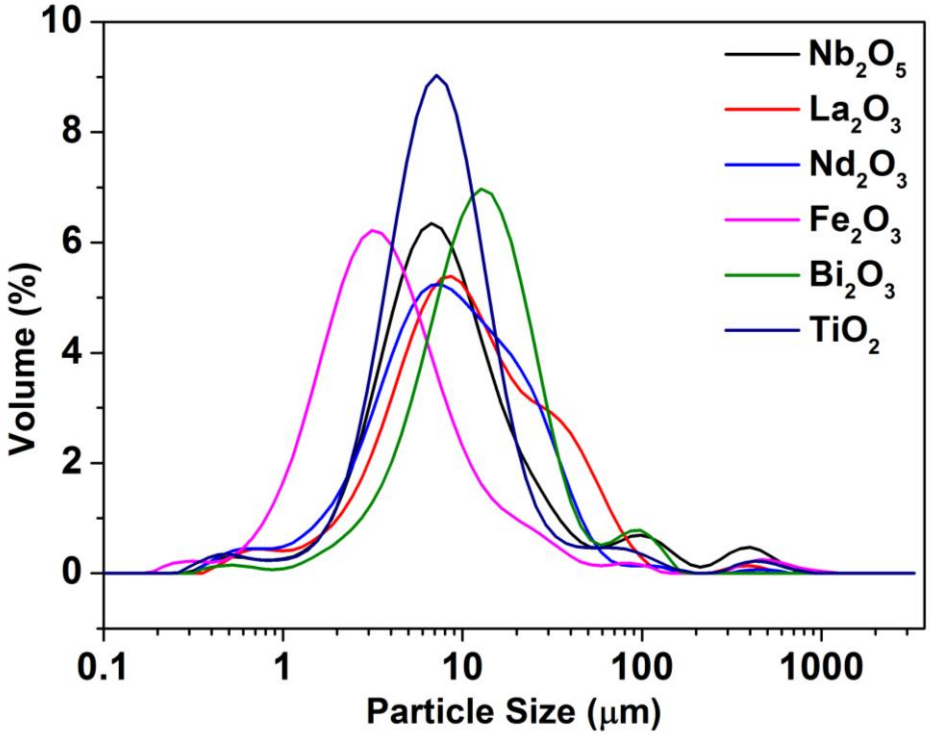

Figure 4.5: Particle size distribution of oxide precursors.

Table 4.4: Particle diameters of oxide precursors.

Reagents	D_{10} (µm)	D_{50} (µm)	D_{90} (µm)
Bi_2O_3	4.63	13.1	34.3
Fe_2O_3	1.37	3.82	14.7
Nd_2O_3	2.54	8.97	30.1
TiO_2	2.94	7.28	19.2
La_2O_3	3.13	10.7	43.7
Nb_2O_5	2.96	8.17	37.9

4.3 Processing of ceramics

4.3.1 Weighing of powders

Stoichiometric amounts of raw materials were calculated for batches 60-100 g, assuming all staring materials to be 100 % pure. The actual purity of raw materials (listed in table 4.2) is < 100 % and hence all compositions contain certain amount of impurities. All raw materials were weighed with an accuracy of ± 1 mg, immediately after drying to reduce the chances of moisture uptake. A Precisa digital balance was used for all measurements.

4.3.2 Mixing and milling of powders

For formation of a compound from raw materials, particles of the raw materials need to react and diffuse into one another. Hence, all constituents needs to be mixed homogenously. Further, the time required to complete the reaction is directly proportional to the square of particle size, hence a lower particle size is preferred for better reactivity. The reaction can be slowed down if the starting material contains aggregates rather than individual particles. So ideally the powders before calcination should be agglomerate-free. Hence it is very important to form a homogenous mixture of constituents and/or reduce the particle size prior to calcination [2].

In this study all constituents were attrition milled in isopropanol for 1 hour with 3mm diameter yttria-stabilised zirconia (YSZ) media using Union Processes Attritor (Szegvari Attritor System, Union Process, Arkon, Ohio, USA) prior to calcination. YSZ has a very low wear loss but still contamination from the media cannot be excluded. To reduce contamination across compositions different sets of media were used, one each for BF, KBT and KNN-based compounds. The slurries formed after attrition milling were dried in trays by placing them in an 80 °C oven overnight. The dried powders were then sieved through a 355 µm mesh to form free-flowing powders.

To see the effect of attrition milling, particle size analysis was performed on representative mixed-milled powders from each major system studied shown in Figure 4.6. The mean particle size prior to calcination was < 3 µm, indicating that the particle size is effectively reduced during milling and powders are ready for calcination.

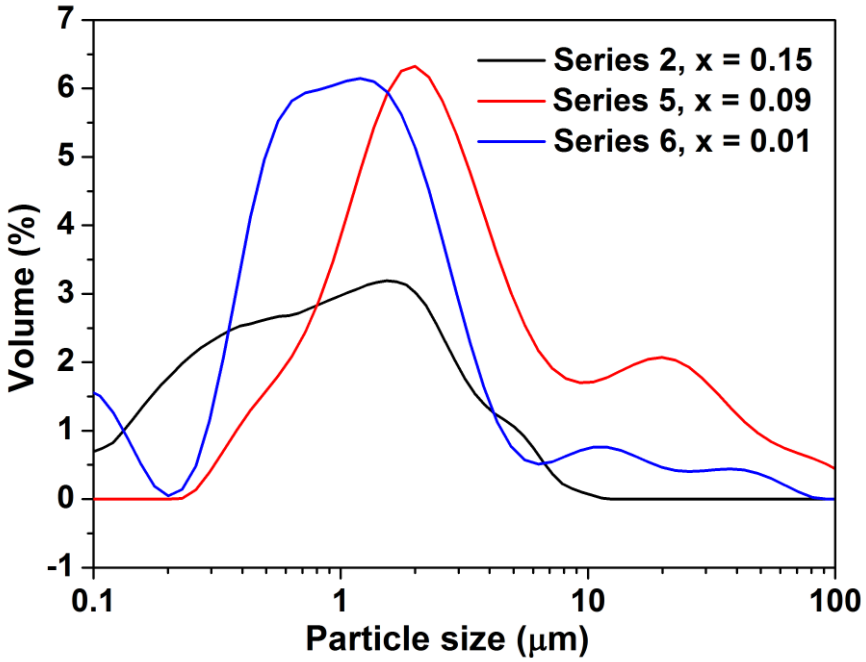

Figure 4.6: Particle size distribution of mixed milled powders.

4.3.3 Calcination

The aim of calcination is to form a homogenous single phase compound from constituents prior to sintering. The desired phase may not be always formed during calcination, however it is still an important step as the interdiffusion between ions during calcination reduces the extent of diffusion during sintering to form a homogenous compound [2].

In this study, mix-milled powders were calcined in alumina crucibles for 2-6 hours at optimum temperatures with a heating/cooling rate of 3-5°C/min using a box furnace. Reaction temperatures were optimized by trying various temperatures with a step of 50 °C on 3-4 g of mixed-milled powders. After each calcination temperature the powder was tested for phase purity using X-ray diffraction (XRD). The lowest temperature, which gave XRD trace whose peaks could be indexed as a single perovskite phase was considered to be the optimum calcination temperature. However, in some cases single phase was only obtained close to the sintering temperature. Calcined powders are usually coarser and harder than mixed milled powders and particle size generally increases with increase in calcination temperature. Calcination at temperatures closer to sintering results in partially sintered powders which are often too large for the attrition mill to break apart. Large particles leads to poor sinterability and hence are not desired.

An example of typical calcination and sintering experiments is shown for composition $0.3K_{1/2}Bi_{1/2}TiO_3 - 0.7(0.8BiFeO_3\text{-}0.15LaFeO_3\text{-}0.05La_{2/3}TiO_3)$ in series 4. Figure 4.7 shows an XRD trace of calcined powders at 800 °C and 1020 °C. Powders calcined at 800 °C shows secondary phases labelled by an asterisk (*). When the powders are calcined at 1020 °C, an almost single perovskite phase is evident in the XRD traces.

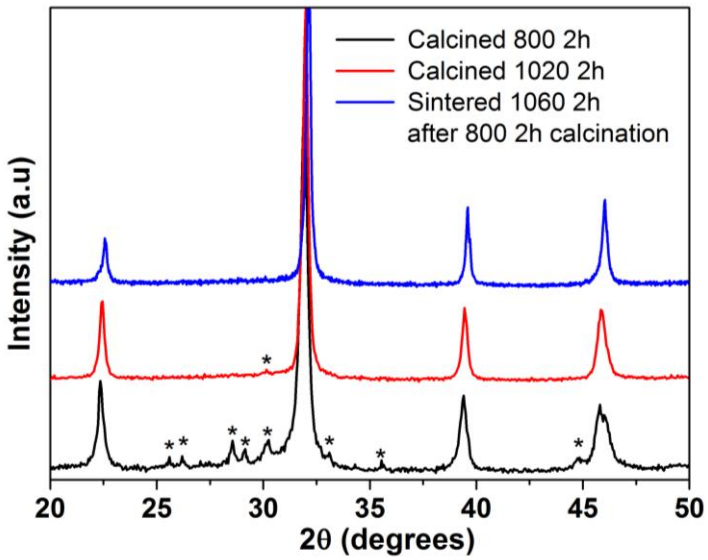

Figure 4.7: XRD traces of (Series 4, *x* = 0.7) calcined at different temperatures along with the crushed sintered pellet.

However, the powders calcined at 1020 °C were coarser due to partial sintering. A comparison between particle size distributions of powders calcined at 800 °C and 1020 °C is shown in Figure 4.8.

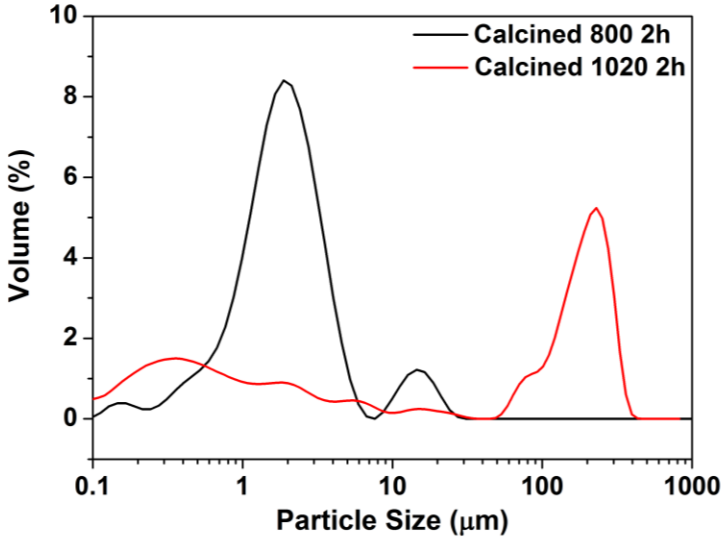

Figure 4.8: Particle size distribution, (Series 4, *x* = 0.7) calcined at different temperatures.

The powders calcined at 800 °C, formed a dense compound with an XRD trace indexed as a single perovskite phase after sintering 2h at 1060 °C, as shown in Figure 4.7. Therefore, optimum calcination temperature was chosen to be the one with the lower particle size. Calcination temperatures for studied compositions are listed in Table 4.5.

Table 4.5: Calcination temperatures of the systems studied.

System	Calcination Temperature Range
BF- based	750 °C 3 h – 950 °C 3 h
KBT-based	800 °C 2 h – 850 °C 4 h
KNN-based	800 °C 2 h – 850 °C 6 h

Calcined powders were attrition milled, dried and sieved again in same manner as mixed milled powders. Particle size analysis of representative samples is shown in Figure 4.9. The mean particle size for calcined powders was < 4 µm. Representative XRD traces of calcined powders for key compositions are shown in Figure 4.10.

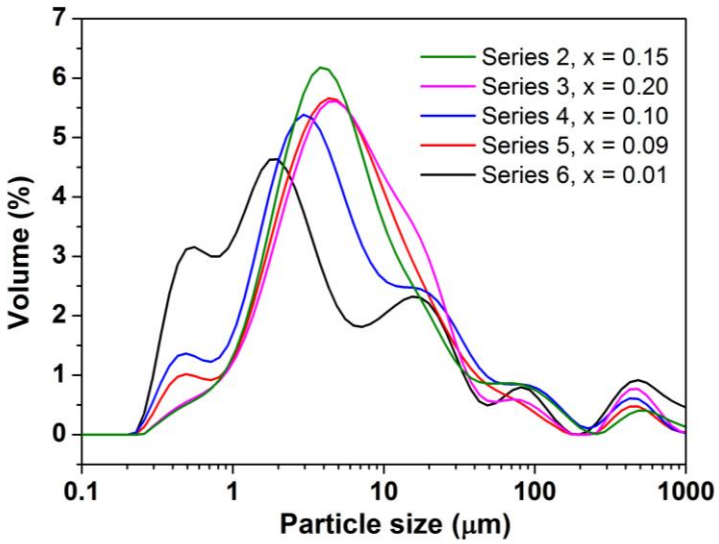

Figure 4.9: Particle size distribution of calcined powders.

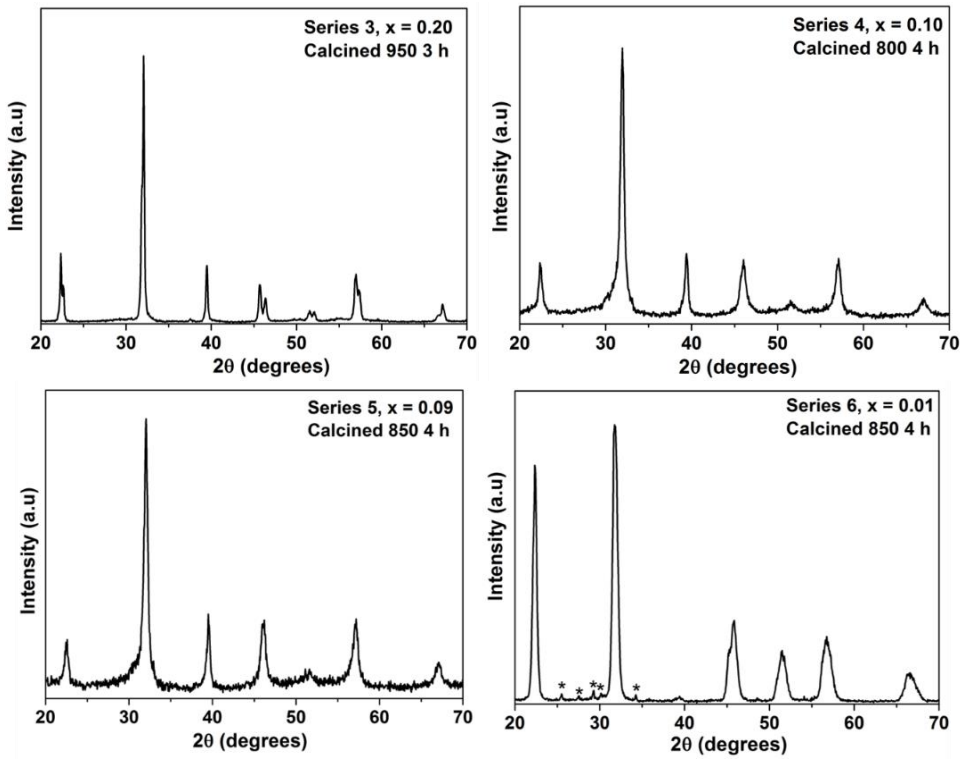

Figure 4.10: XRD traces of calcined powders for key compositions. Asterisk (*) represent secondary phase(s).

4.3.4 Compaction into green bodies

Calcined powders were pressed into 10 mm diameter and ~ 1.5 mm thick pellets using a uniaxial press. BF-based calcined powders were successfully pressed into pellets by applying a force of 0.5 tonne for 1 minute. Some BF-based powders were pressed into cylindrical bars with a length of 6 mm for dilatometry measurements. However, KBT and KNN-based calcined powders developed lateral cracks during palletization even at uniaxial forces as low as 0.1 tonne. To overcome the problem ~3 wt. % polyvinyl alcohol (PVA) binder was mixed with calcined powders using a mortar and pestle. The powders were sieved again and then successfully pressed into pellets by applying a uniaxial force of 1 tonne for 1 minute.

4.3.5 Sintering

Sintering is defined as "a process by which a powder compact is transformed to a strong, dense ceramic body upon heating" [4]. Highly dense ceramics are required for most electrical applications. Ceramics with densities < 90 % allow moisture to ingress easily, which can lead high conductivities not desirable in piezoelectric applications. Thus, two important criteria to optimize sintering temperature are phase purity and sample density. All samples characterized in this study were phase pure within the limits of in-house XRD after sintering and had relative densities from 86-97 %. The samples containing binder were given a binder burnout step at 550 °C for 3 h. All samples were sintered in alumina crucibles by firing them in air inside a box furnace. Schematics of sintering profiles are shown in Figure 4.11.

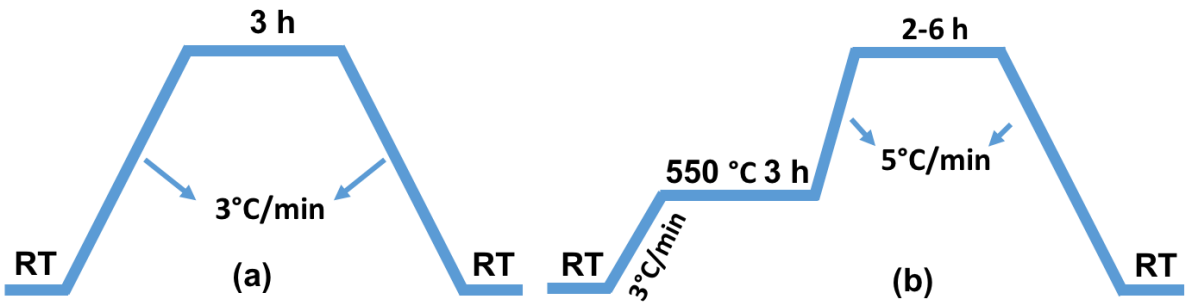

Figure 4.11: (a) Sintering profile of samples without PVA; (b) Sintering profile of samples with addition of ~3 wt. % PVA.

Some starting materials such as Bi_2O_3, K_2CO_3, Na_2CO_3 and Li_2CO_3 with melting points (< 900 °C) are susceptible to volatility during high temperature firing [3]. No attempt was made to compensate for any losses due to volatility, however, samples from all composition were sintered in a bed of their own calcined powders to minimize any potential losses.

All samples were tested to find out the temperature at which single phase ceramic with maximum density could be fabricated. Optimised sintering temperatures with corresponding relative densities are listed in Table 4.6. Apparent densities were compared with theoretical densities to find relative densities. Samples with relative densities < 90 % were dried overnight at 180 °C before electrical measurements.

Table 4.6: List of sintering temperatures and corresponding relative densities.

Compound(s)	Sintering temperature	Relative Density
Series 1 (*x* =0)	830 3 h	85 %
Series 2	980 3h to 1060 3h	95-97%
Series 3	910 3h to 950 3h	95-96%
Series 4 (*x*=0, 0.02)	1060 2h	90-91 %
Series 4 (excluding *x* =0, 0.02)	1040 2 h – 1090 2h	95-97 %
Series 5	1090 2h	96-97 %
Series 6 (*x* =0)	1130 6h	91 %
Series 6 (*x* =0.005, 0.0075, 0.1)	1105 6 h to 1120 6h	94-97 %
Series 6 (0.0125, 0.015, 0.02, 0.03)	1100 6h to1140 6h	88-90 %
Series 7	1105 6h	95-97 %

Forth coming chapters will discuss results obtained for fabricated ceramics.

4.6 References

[1] M. Li, H. Zhang, S. N. Cook, L. Li, J. A. Kilner, I. M. Reaney, and D. C. Sinclair, "Dramatic influence of A-site nonstoichiometry on the electrical conductivity and conduction mechanisms in the perovskite oxide $Na_{0.5}Bi_{0.5}TiO_3$," *Chem. Mater.*, vol. 27, no. 2, pp. 629–634, 2015.

[2] A. Moulson and J. Herbert, *Electroceramics*, 2nd ed. Wiley, 2003.

[3] P. Patnaik, *Handbook of Inorganic Chemicals*. McGraw-Hill, 2001.

[4] M. W. Barsoum, *Fundamentals Of Ceramics*. Institute of Physics Publishing, 2003.

Chapter 5: RE (La/Nd)- and Ti- co-doped $BiFeO_3$

5.1 Introduction

$BiFeO_3$ (BF) is one of the most extensively researched perovskite compounds because of its room temperature multiferroic properties. It is simultaneously ferroelectric (FE) with a T_C 825 °C [1] and antiferromagnetic (AFM) with a Néel temperature (T_N) of 370 °C [2]. However, our interest in BF is driven by its high T_C making it attractive for high temperature piezoelectric applications. Two major problems hindering use of BF in piezoelectric applications are: difficulties in processing single phase dense ceramics and high conductivities. Rare earth (RE) dopants have shown to supress secondary phases and improve piezoelectric properties [3-5]. In 2009, Karimi et al. reported [6,7] an antipolar $PbZrO_3$ (PZ)-like structure (*Pbam*) stabilised between the ferroelectric (*R*3*c*) and paraelectric (*Pnma*) for RE doped BF. The authors also noted that though the ceramics were single phase, conductivities were too high to record radio frequency measurements representative of intrinsic properties. To counter the problem Kalantari et al. [8] substituted Fe^{3+} by Ti^{4+} in (in a ratio 1:1) and showed that the room temperature bulk conductivities decreased from ~ 1 mS/cm to < 1 µS/cm for the composition $Bi_{0.85}Nd_{0.15}Fe_{0.97}Ti_{0.03}$ allowing the ceramics to withstand electric fields as large as 5 kV/mm. The authors further observed a non-linear relationship between T_C and Ti concentration, suggesting that there is more than one mechanism of charge compensation for Ti-doping. To clarify the ionic compensation mechanism, Reaney et al. [9] investigated $Bi_{0.85}Nd_{0.15}Fe_{0.9}Ti_{0.1}O_3$ ceramics using an aberration corrected scanning transmission electron microscope. The authors found periodic distribution of Nd-rich precipitates in lattice. It was proposed that at lower concentrations Ti^{4+} replaces Fe^{2+} resulting in $\frac{2}{3}\boldsymbol{V}_{\mathbf{Nd}}^{'''}$ and at higher concentrations (when all Fe^{2+} ions are compensated) Ti^{4+} replaces Fe^{3+} resulting in $\frac{1}{3}\boldsymbol{V}_{\boldsymbol{Nd}}^{'''}$, concluding that Ti donor doping is compensated by $\boldsymbol{V}_{\boldsymbol{Nd}}^{'''}$ instead of $\boldsymbol{V}_{\boldsymbol{Bi}}^{'''}$ and $\boldsymbol{V}_{\boldsymbol{Fe}}^{'''}$. Based on these findings Reaney et al. [9] suggested the appropriate tie-line for preparing single phase compositions should be based on endmember perovskites $RE_{2/3}TiO_3$ and $BiFeO_3$. This study essentially started to fabricate

stoichiometric compounds in $BiFeO_3$- $RE_{2/3}TiO_3$ (RE= Nd, La) solid solutions. However it was quickly realised that the solid solution cannot sustain a large number of A-site vacancies. Therefore a third endmember $REFeO_3$ was introduced to form stable compounds in ternary system $BiFeO_3$-$REFeO_3$-$RE_{2/3}TiO_3$ and the corresponding phase transitions and electrical properties were studied.

5.2 The (1-*x*)$BiFeO_3$-*x*$RE_{2/3}TiO_3$ (RE = Nd, La) system

XRD traces obtained for calcined powders fabricated in the system (1-*x*)$BiFeO_3$-*x*$Nd_{2/3}TiO_3$ (*x* = 0, 0.05, 0.1 and 0.15) are shown in Figure 5.1. For *x* = 0, the trace matched with *R*3*c* $BiFeO_3$ (ICDD # 71-2494) along with secondary phase of $Bi_{25}FeO_{40}$ (ICDD # 46-416). Within the detection limits of in-house XRD, apparent single phase perovskite phase was achieved for *x* = 0.05. For *x* = 0.1, the trace showed a hump arising near the main perovskite peak which developed into an unknown peak at *x* = 0.15. The absence of phase transformations of the type reported by Karimi et al. [6,7] along with appearance of the broad hump at *x* = 0.1 suggests that the limit of solid solubility is ~ *x* = 0.05.

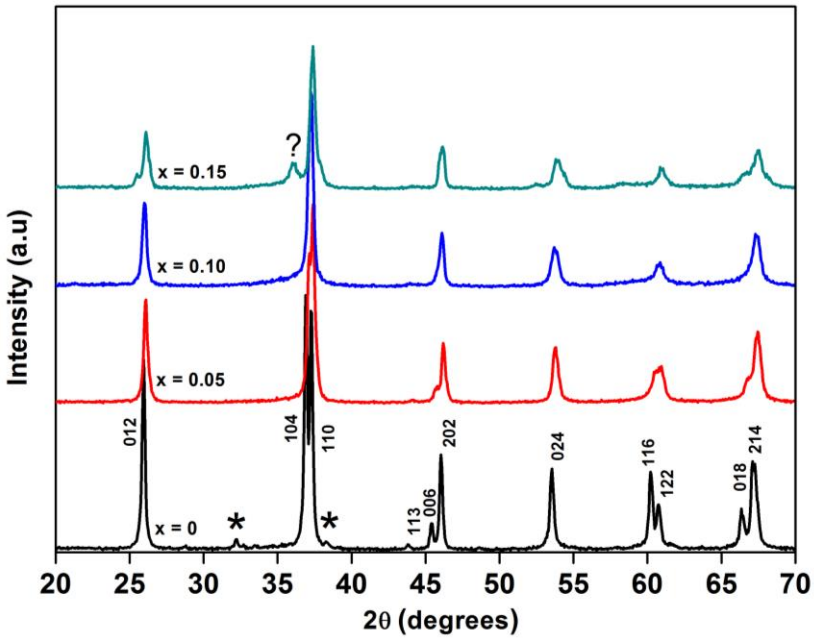

Figure 5.1: XRD traces of (1-*x*)$BiFeO_3$-*x*$Nd_{2/3}TiO_3$ for *x* = 0, 0.05, 0.1 and 0.15 (* correspond to $Bi_{25}FeO_{40}$ phase), calcined at 870 °C.

However, compositions with x = 0.05 showed significant amount of $Bi_2Fe_4O_9$ (ICDD # 74-1098) secondary phase when sintered at 920 ˚C, as shown in Figure 5.2. This implies that within the sintering regimes used, $Bi_2Fe_4O_9$ coexists thermodynamically with the perovskite phase. In an attempt to establish a broader solid solubility, Nd^{3+} was replaced by La^{3+}. La^{3+} (1.32 Å) has a similar radius to Bi^{3+} (1.35 Å) and arguably should create less strain within the structure as it substitutes for Bi^{3+}, allowing the composition to sustain a greater number of A-site vacancies. Therefore, the composition $0.95BiFeO_3$-$0.05La_{2/3}TiO_3$ was calcined and sintered at the same temperatures to its Nd analogue. $Bi_2Fe_4O_9$ secondary phases were evident in lower relative intensities than the $0.95BiFeO_3$-$0.05Nd_{2/3}TiO_3$ composition, as shown in Figure 5.3. Owing to the limited solubility in (1-x)$BiFeO_3$-$xRE_{2/3}TiO_3$, concentration of endmember $RE_{2/3}TiO_3$ was fixed at x = 0.03 for RE = Nd and x = 0.05 for RE = La but to stabilise the perovskite structure in preference to $Bi_2Fe_4O_9$ and expand the range of potential structural phase transition as function of composition, a third endmember, $REFeO_3$ was introduced to form the ternary systems (0.97-x)$BiFeO_3$-$xNdFeO_3$-$0.03Nd_{2/3}TiO_3$ (BNFT) and (0.95-x)$BiFeO_3$-$xLaFeO_3$-$0.05La_{2/3}TiO_3$ (BLFT). Structural phase transitions and electrical properties of the stoichiometric compounds BNFT and BLFT are discussed in following sections.

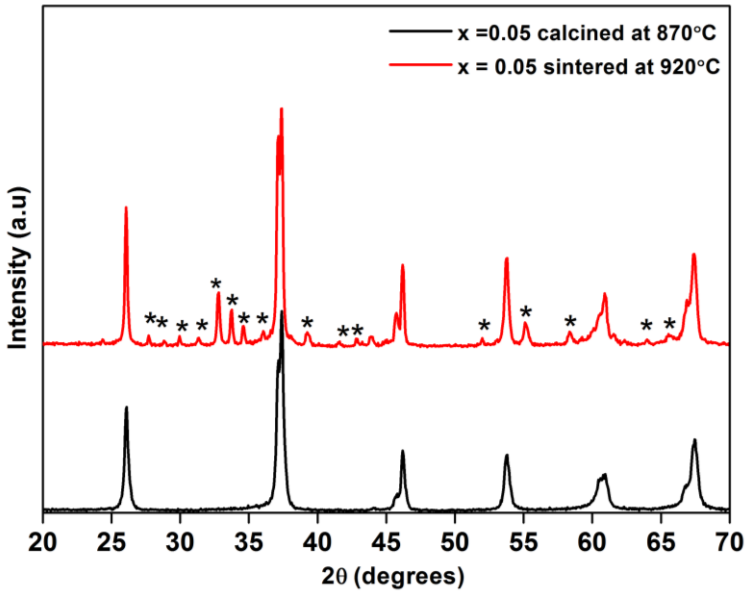

Figure 5.2: XRD traces (1-x)$BiFeO_3$-$xNd_{2/3}TiO_3$ (x = 0.05) at 870 and 920 ˚C (* correspond to $Bi_2Fe_4O_9$ phase).

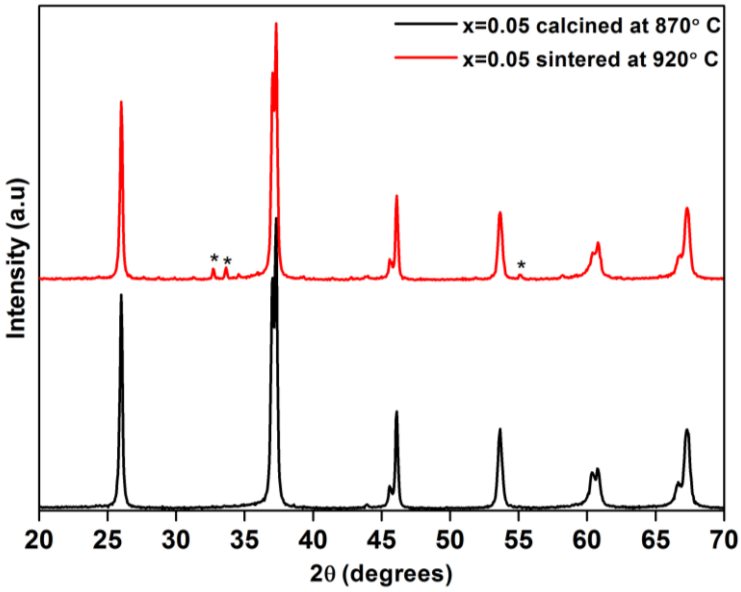

Figure 5.3: XRD traces (1-x)$BiFeO_3$-$x$$La_{2/3}TiO_3$ (x = 0.05) at 870 and 920 °C (* correspond to $Bi_2Fe_4O_9$ phase).

”””

Important Note: The XRD data in Figure 5.1 to 5.3 was taken on XRD with a cobalt source. All other XRD data in this thesis are taken by XRD with a copper source. The large mismatch in peak position in these figures with figure 5.4 onwards is a consequence of using radiations of different wavelengths and not effect of composition.

5.3 The (0.97-*x*)$BiFeO_3$-*x*$NdFeO_3$-0.03$Nd_{2/3}TiO_3$ (BNFT) system

5.3.1 Phase analysis and microstructure

XRD traces from crushed pellets of BNFT ($0.05 \leq x \leq 0.15$) are shown in Figure 5.4. All compositions were indexed according to single phase perovskite structure with no secondary peaks observed. The peaks in compositions with $x \leq 0.10$ were indexed as a ferroelectric (FE) phase with rhombohedral (*R*3*c*) symmetry. Peak splitting was observed at $x = 0.15$. This was attributed to the transformation from the FE phase to the antiferroelectric (AFE) $PbZrO_3$-like (*Pbam*) structure reported by Karimi et al. for Nd-doped $BiFeO_3$ [7]. Secondary electron images of BNFT ($0.05 \leq x \leq 0.15$) ceramics are presented in Figure 5.5. The images shows a dense microstructure with a similar grain size (< 1 µm) irrespective of the Nd concentration.

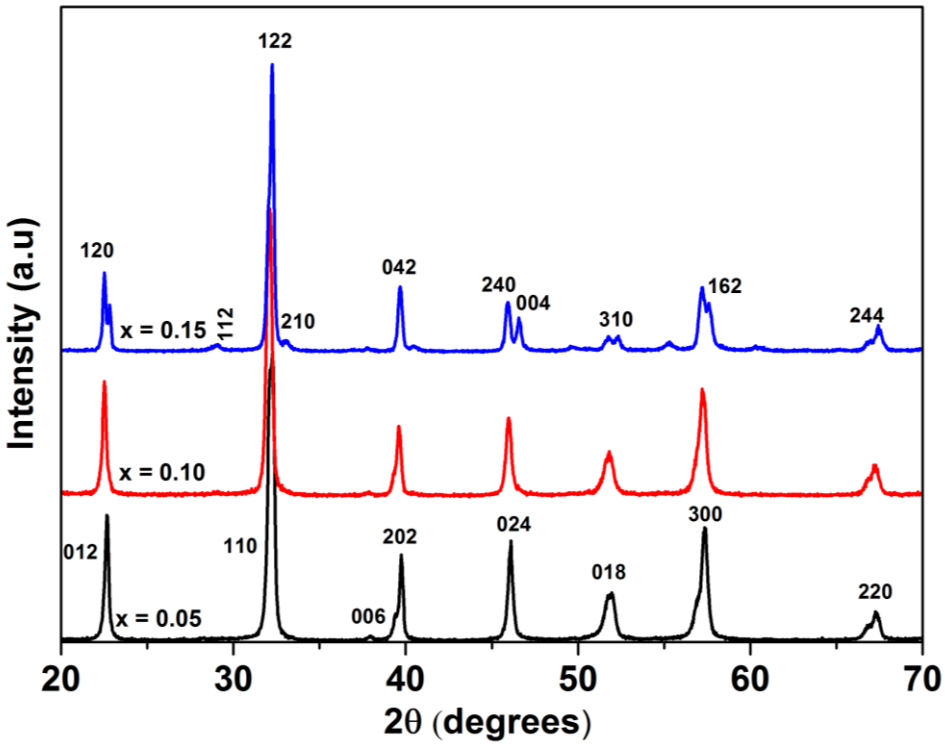

Figure 5.4: X-ray diffraction patterns of BNFT ($0.05 \leq x \leq 0.15$). $x = 0.05$ and 0.15 are, respectively, indexed as $BiFeO_3$-like (*R*3*c*), $PbZrO_3$-like (*Pbam*).

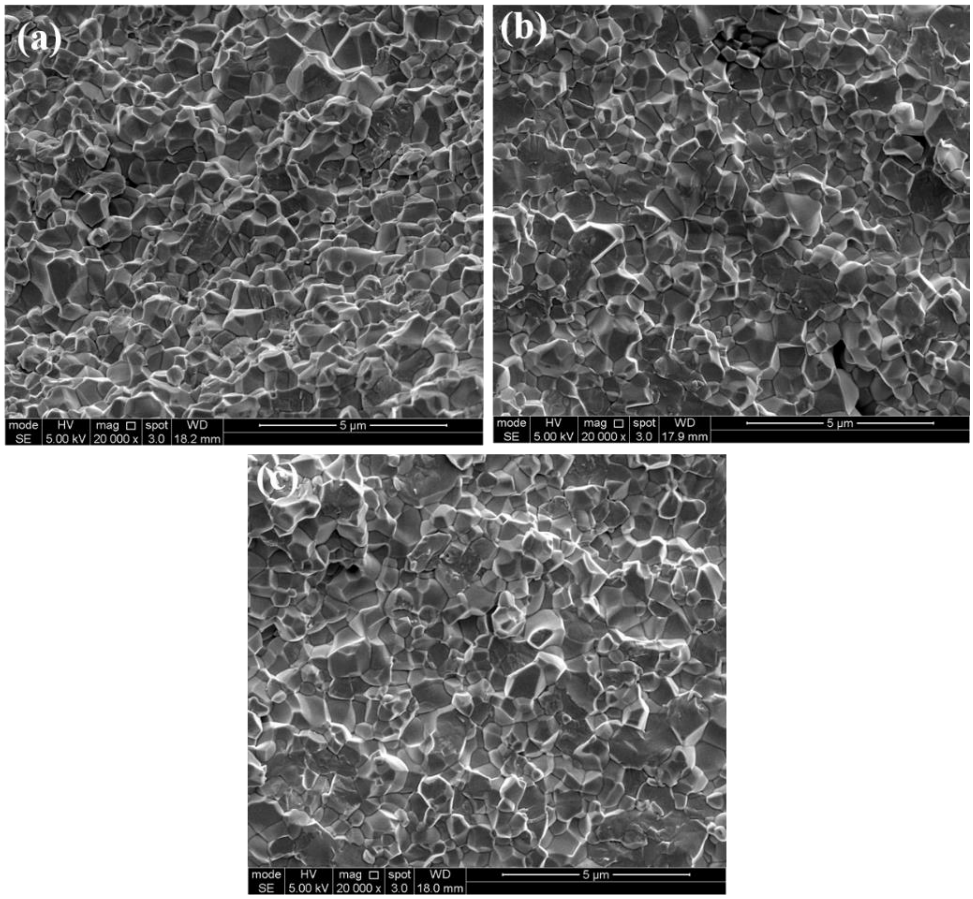

Figure 5.5: Secondary electron images of BNFT ceramics (a) x = 0.05; (b) x = 0.10 and (c) x = 0.15.

5.3.2 Structural phase transitions in BNFT ceramics

DSC curves from crushed pellets of BNFT ($0.05 \leq x \leq 0.15$) are presented in Figure 5.6. The peaks observed in these traces correspond to T_C, which is a phase transition from paraelectric (PE) to either FE or AFE phase depending on the composition. A linear decrease in T_C is observed with increase in $NdFeO_3$ concentration. Nd^{3+} has smaller ionic radii (1.27 Å) and low polarisability (5.01 $Å^3$) as compared to size (1.35 Å) and polarisability (6.12 $Å^3$) of Bi^{3+} [10,11]. As the concentration of $NdFeO_3$ is increased both tolerance factor and average A-site polarisability is decreased. This has the effect of decreasing T_C with respect to the endmember BF and also promoting an AFE rather than FE phase [6]. A weak peak is observed in all ceramics around 350 °C, which can be attributed to the paramagnetic to antiferromagnetic transition upon cooling. Figure 5.7

shows dilatometry curves obtained from BNFT ($0.05 \leq x \leq 0.15$) ceramics. A sharp decrease in volume is observed at the phase transitions consistent with the peaks observed in DSC curves. The large decrease (~2 %) at the PE-AFE phase boundary is consistent with that reported by Kalantari et al. [12] for Ti-doped $Bi_{1-x}Nd_xFeO_3$. Detailed discussion on the volume changes in these systems can be found in reports by Levin et al. [13,14].

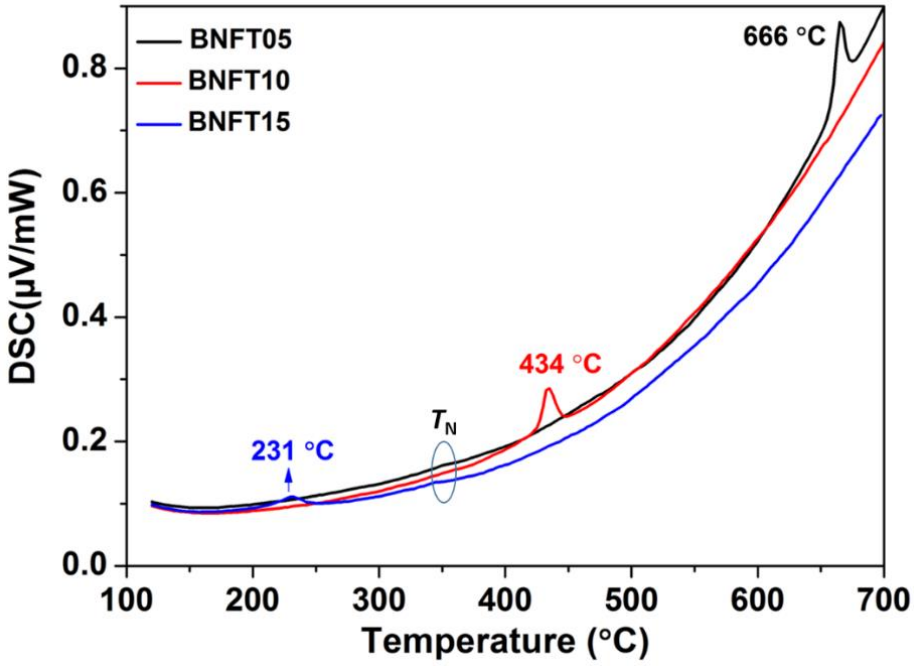

Figure 5.6: DSC curves for BNFT ($0.05 \leq x \leq 0.15$) ceramics. BNFT5 refer to composition $x = 0.05$ in BNFT series and so on.

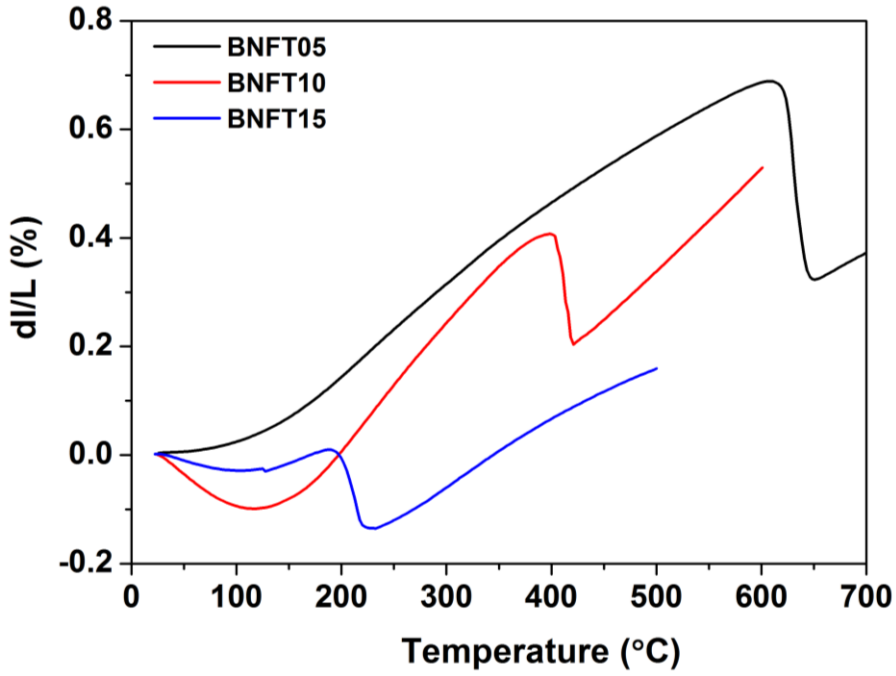

Figure 5.7: Dilatometry curves for BNFT ($0.05 \leq x \leq 0.15$) ceramics. BNFT5 refer to composition at $x = 0.05$ in BNFT series and so on.

5.3.3 Electrical properties of BNFT ceramics

Relative permitivity vs. temperature data collected for BF and BNFT ceramics is shown in Figure 5.8. All the ceramics became too conductive to record any reliable dielectric data at temperatures higher than 500 °C. Therefore transitions above 500 °C could not be observed. However the transitions below 500 °C, corresponded well to the values observed in DSC and dialotometry curves as shown in Figure 5.8 (c and d). The step like behaviour for the BNFT15 composition at PE-AFE phase boundary is similar to that observed by Kalantari et al. [12] for $Bi_{1-x}Nd_xFe_{0.97}Ti_{0.03}O_3$ compositons. It has also been shown that AFE $PbZrO_3$ also show a step like behaviour in dielectric data in presence of small impurities [15]. A strong relaxation behaviour is observed in all ceramics at a temperature around 300 °C. In BF-based ceramics, such anomalies have been previously reported [12,16,17] but their underlying cause is not yet fully understood. Here, it is intresting to note that the relaxation in dielectric data is coincident with the T_N of BNFT ceramics. Anamolies in dielectric data with magnetic ordering are also observed in many magnetic insulators such as $BiMnO_3$ [18], and Cr_2O_3 [19] etc. Park et al. [20] reported

strong coupling between magnetic and dielectric properties in antiferromagnetic $Bi_2Fe_4O_9$ single crystals. Hence, the effect of magnetic ordering on the dielectric response can not be excluded in BNFT ceramics. The losses also increase sharply at a temperature of around 300 °C and as a result of Maxwell-Wagner type relaxation, which may arise due to space-charge polarisation [21].

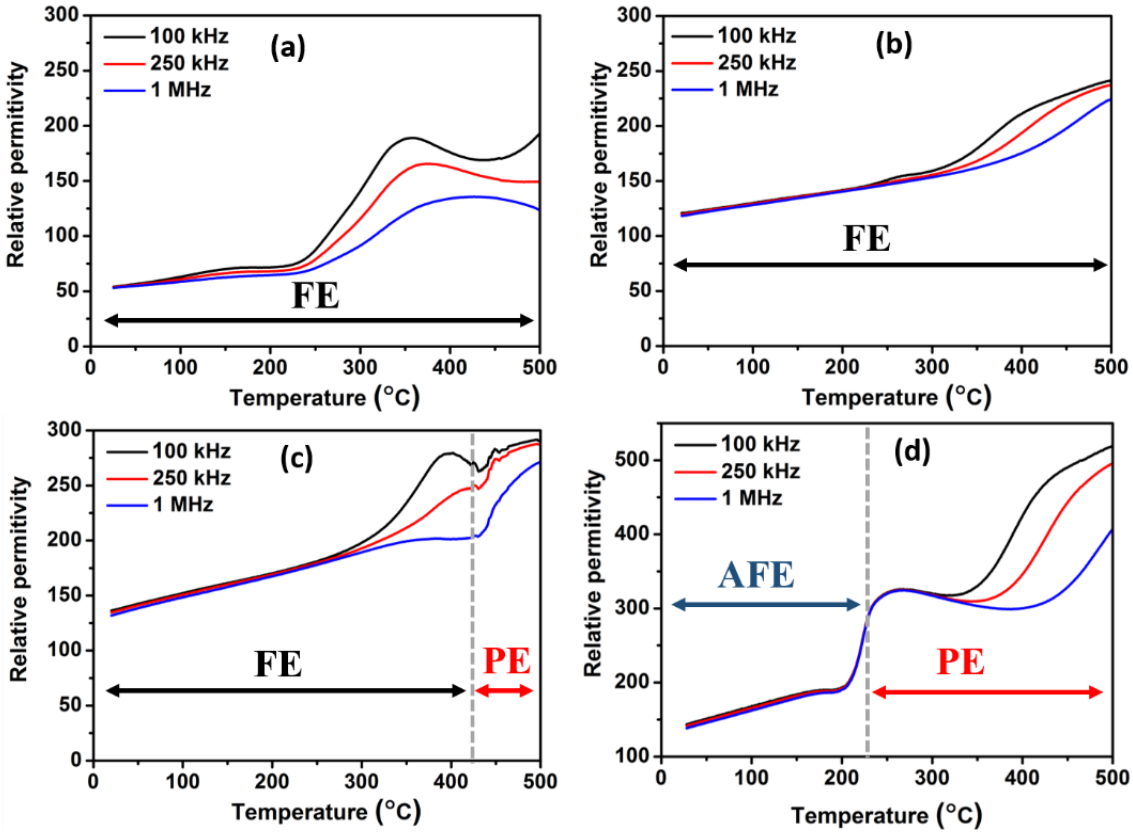

Figure 5.8: Relative permittivity vs. temperature for (a) BF; (b) BNFT (x = 0.05); (c) BNFT (x=0.10); (d) BNFT (x = 0.15). The vertical dotted line shows phase transition point from FE/AFE to PE.

The electrical microstructure and bulk conductivities of the ceramics were further investigated using impedance spectroscopy. Complex impedance (Z*) plot for BF at 270 °C is shown in Figure 5.9 (a) which gives rise to a suppressed semi-circular arc indicative of two semicircles overlapped. The peak maximum in M" is inversely proportional to capacitance and the peak maximum in Z" is directly proportional to resistance. Hence

combined spectroscopic plots can be used to differentiate the component with low capacitance (bulk) from the component with high resistance (grain boundary). Mismatch between the two peaks (Figure 5.9 (b)) confirm the electrical heterogeneous behaviour of the sample. Which means that the grain boundary has a different resistance to that of the grain and the overall resistance is dominated by the grain boundary.

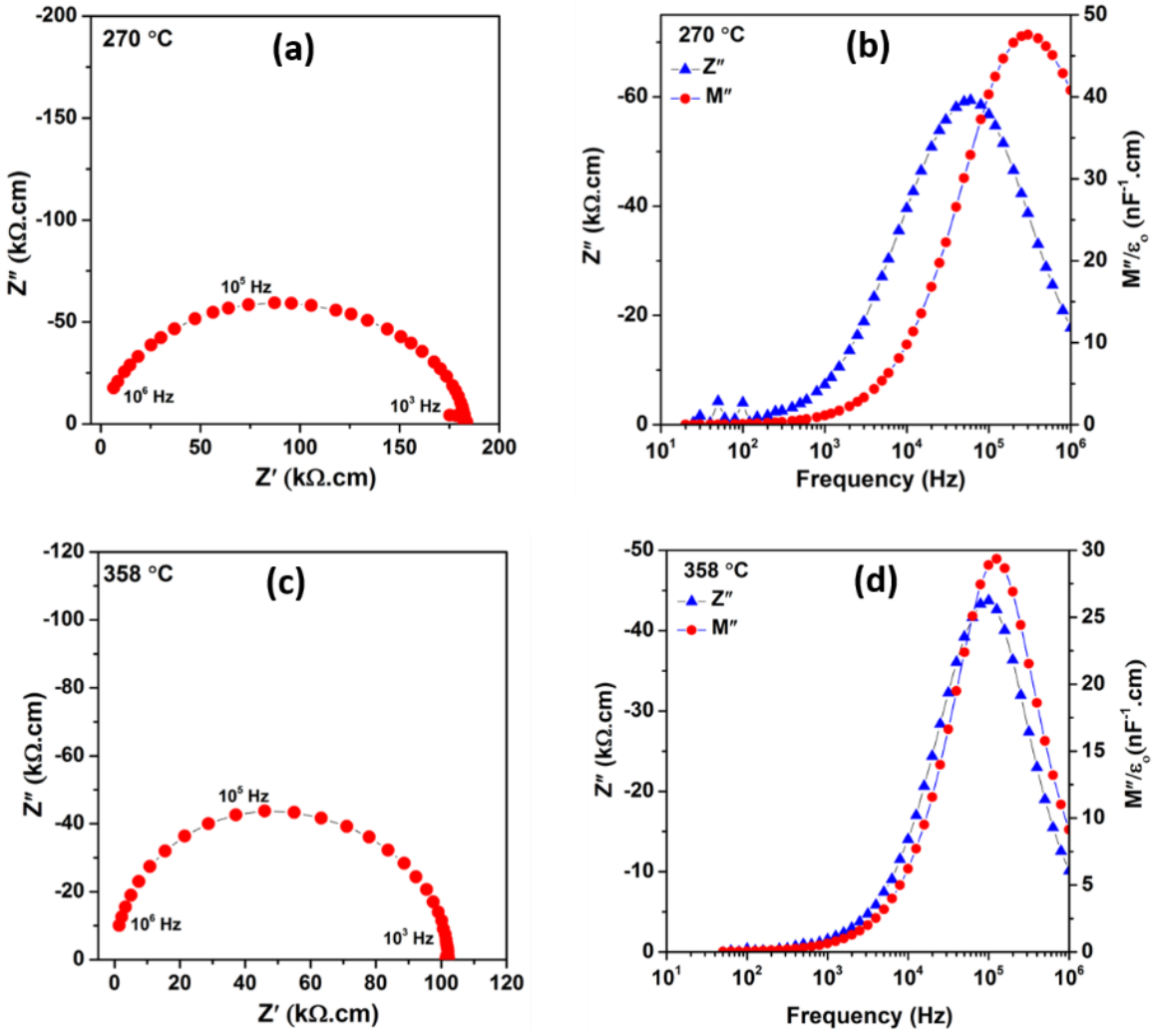

Figure 5.9: (a) complex impedance spectroscopic plot for BF at 270 °C; (b) combined Z" and M" spectroscopic plot for BF at 270 °C; (c) complex impedance spectroscopic plot for BNFT5 at 358 °C; (d) combined Z" and M" spectroscopic plot for BNFT at 358 °C.

A representative Z* for BNFT5 at 358 °C is shown in Figure 5.9 (c), which gives rise to a semicircle that could be modelled, to a first approximation, on an equivalent circuit based on a single parallel Resistor-Capacitor (RC) element. The associated capacitance of the arc was 17 pF/cm, indicating a bulk (grain) response that dominated the resistivity of the ceramic [22]. The coincidence in frequency of the peak maximum in Z" and M" spectra in Figure 5.9 (d) demonstrated the ceramic to be electrically homogenous (i.e. resistance of grain and grain-boundary is almost the same), and this feature was observed in all BNFT samples. The bulk resistivity at ~ 300 °C in BNFT ceramics is comparable to that reported by Kalantari et al. [8] for Ti doped $Bi_{0.85}Nd_{0.15}FeO_3$ and is an order of magnitude greater than the corresponding bulk conductivity for BF. The activation energies of conduction (E_a) associated with bulk were calculated from Arrhenius plots of the bulk conductivity, ($\sigma = 1/R$). A large increase in E_a from 0.61 eV for BF to >1 eV was observed for BNFT compositions as shown in Figure 5.10. This concludes that BNFT ceramics are electrically insulating, and although the conduction mechanism is unknown at this stage, the leaky behaviour displayed by undoped BF has clearly been suppressed in this series of ceramics.

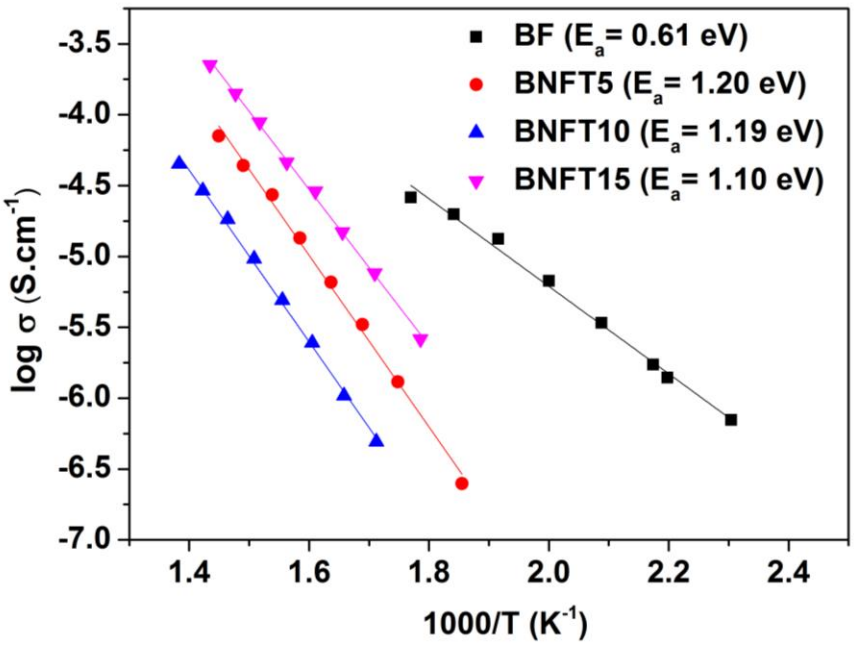

Figure 5.10: Arrhenius plots for BF and BNFT ($0.05 \leq x \leq 0.15$)

The insulating nature of BNFT ceramics is also reflected in tan δ vs. temperature plots shown in Figure 5.11, where the BNFT series show a tan δ < 0.03 from RT to > 200 °C at 100 kHz. Low insulation resistance allows application of high electric fields. A representative polarisation vs. electric field (*P*-*E*) response at RT for BNFT5 ceramic is shown in Figure 5.12. The polarisation increased linearly with an increase in applied electric field and no PE-FE/AFE switching was observed despite the large field applied (7 kV/mm) and therefore the ceramics do not yield any practically usable electromechanical strains. The coercive field for undoped BF is reported to be ~ 10 kV/mm [23] and it appears that the coercive field of BNFT ceramics is of similar order and usually sample electric break down would often occur before application of electric fields higher than 10 kV/mm. For the sake of comparison it is useful to mention that *P*-*E* loops in undoped BF could not be obtained due to low densities and high leakage currents.

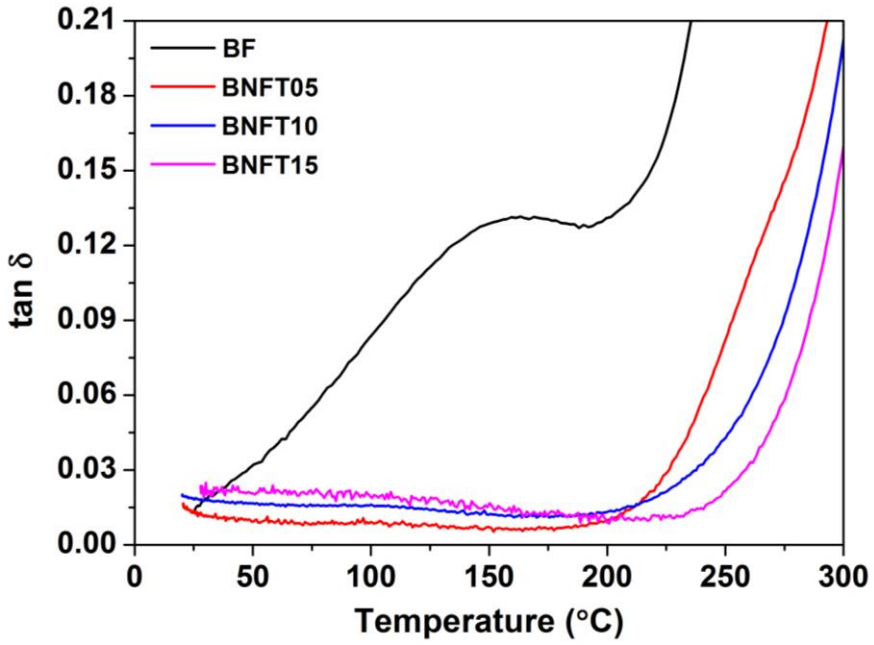

Figure 5.11: A comparison of tan δ vs. temperature between BF and BNFT ceramics at 100 kHz. BNFT5 refer to composition *x* = 0.05 in BNFT series and so on.

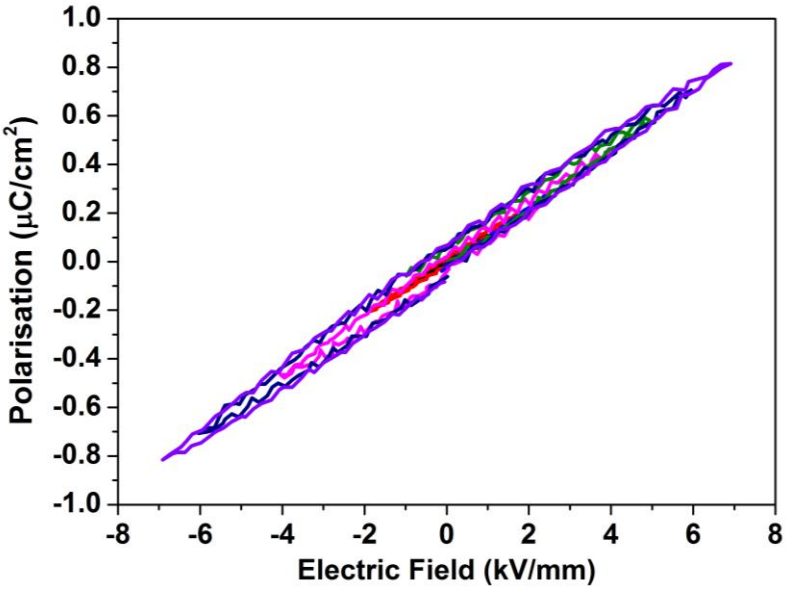

Figure 5.12: Polarisation vs. electric field response for BNFT (x = 0.05) at room temperature. Same response was observed for x = 0.10 and 0.15.

5.4 The (0.95-x)$BiFeO_3$-$x$$LaFeO_3-0.03La_{2/3}TiO_3$ (BLFT) system

5.4.1 Phase analysis and microstructure

XRD traces from crushed pellets of BLFT ($0.05 \leq x \leq 0.35$) are shown in Figure 5.13. All compositions could be indexed according to single phase perovskite structure with no secondary peaks observed. The peaks in compositions with $x \leq 0.10$ were indexed as a FE phase with rhombohedral (*R*3*c*) symmetry. Peak splitting was observed at x = 0.15 which persisted until $x \leq 0.30$. This was attributed to the transformation from the ferroelectric phase to the antiferroelectric $PbZrO_3$-like (*Pbam*) structure reported by Karimi et al. for RE-doped $BiFeO_3$ [6]. At x = 0.35, the splitting disappeared resulting in metrically cubic XRD patterns. SEM images of fractured surfaces for x = 0.05 and x = 0.15 are shown in Figure 5.14. The microstructure is similar for all compositions with a grain size < 1 μm.

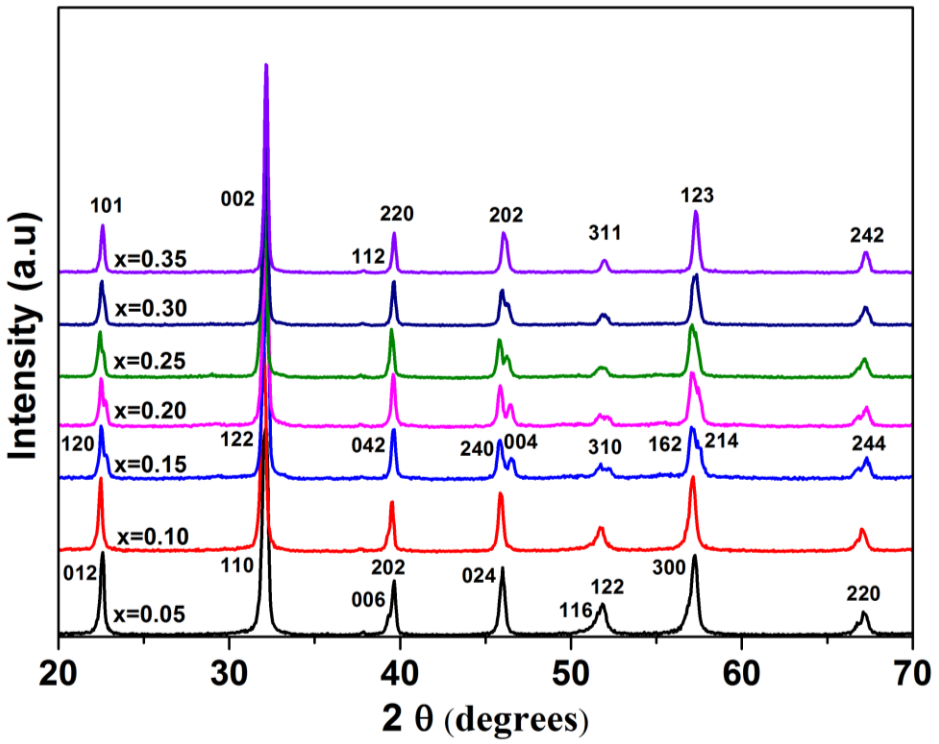

Figure 5.13: X- ray diffraction patterns of BLFT ($0.05 \leq x \leq 0.35$). x = 0.05, 0.15 and 0.35 are respectively indexed as $BiFeO_3$-like (*R*3*c*), $PbZrO_3$-like (*Pbam*) and $LaFeO_3$-like (*Pnma*).

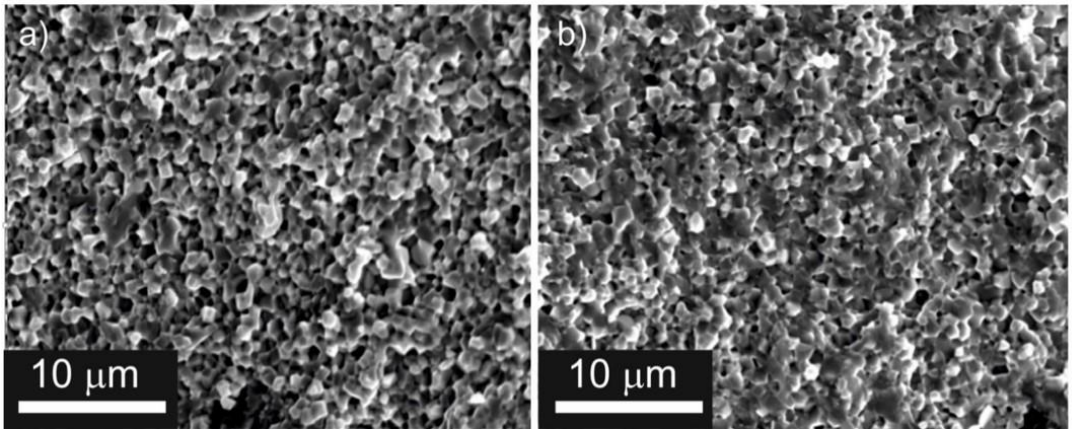

Figure 5.14: Secondary electron images of a fracture surface for a) x = 0.05 and b) x = 0.15.

5.4.2 Structural phase transitions and domain structure in BLFT ceramics

DSC data for a range of BLFT samples are shown in Figure 5.15 which reveal anomalies at ~ 715, ~ 651 and ~ 561 °C, for x = 0.05, 0.10 and 0.15, respectively. As the La concentration increases, the anomalies become broader and less intense and no discrete peaks were observed for compositions with $0.20 \leq x \leq 0.35$. The decrease in T_C and formation of AFE phase can be explained by the same reasoning discussed in section 5.3.2 for BNFT series. However, it is important to note that the T_C does not decrease at the same rate as that in BNFT series since the ionic radii and polarisability of La^{3+} (1.32 Å, 5.5 $Å^3$) are greater than those of Nd^{3+} (1.27 Å, 5.01 $Å^3$). Hence, to decrease the tolerance factor and polarisability by the same magnitude, larger concentrations of the endmember $LaFeO_3$ are required. A composition-independent anomaly at ~350 °C is observed in all DSC plots, indicating a transition from AFM ordering to a paramagnetic phase (T_N). Magnetic ordering is dominated by the B-site, and hence substituting magnetic Fe^{3+} by diamagnetic Ti^{4+} ions results in a lower value of T_N compared to pure BF [8].

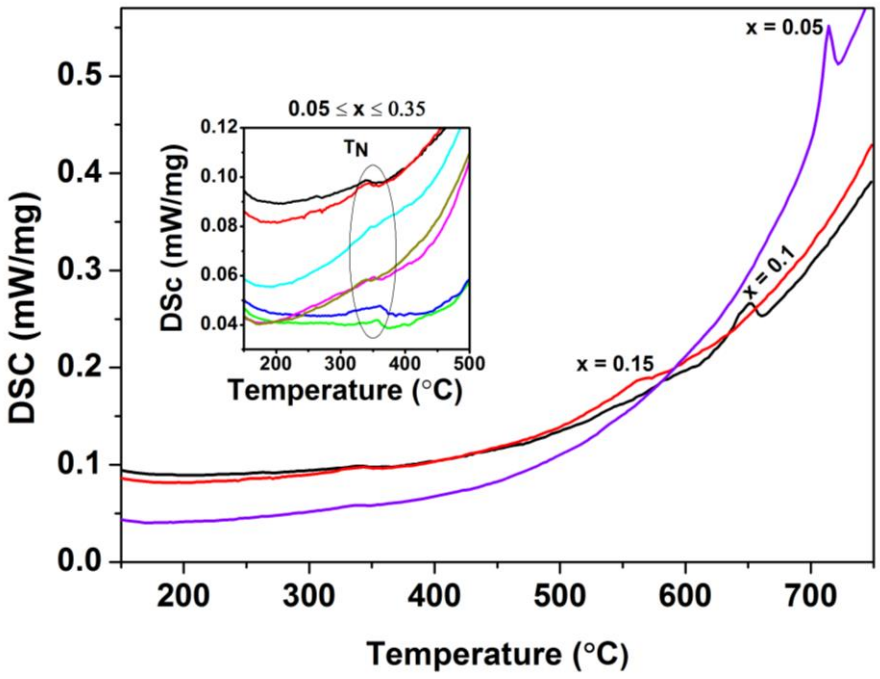

Figure 5.15: DSC data for BLFT ceramics showing Curie temperatures for x = 0.05, 0.10 and 0.15. The inset shows T_N, for $0.05 \leq x \leq 0.35$.

The relative permittivity and tan δ of samples with $0.05 \leq x \leq 0.35$ as a function of temperature is shown in Figure 5.16. BLFT ceramics also show a relaxation behaviour near T_N similar to that observed in BNFT ceramics discussed earlier. The dielectric loss at room temperature is < 0.05 for all compositions but above ~ 300 °C it rises sharply. This is attributed to an increase in conductivity, which may also account for the anomalies near T_N. Similar to BNFT ceramics the BLFT ceramics also become too conductive above 500 °C and hence the transitions observed for ($0.05 \leq x \leq 0.15$) in DSC could not be observed in dielectric data. However, composition dependent, frequency independent, broad peaks are observed in dielectric data for $x > 0.15$, which suggests they relate directly to the onset of the PE-AFE transition but further evidence is required to prove that the dielectric maxima are coincident with a change in symmetry.

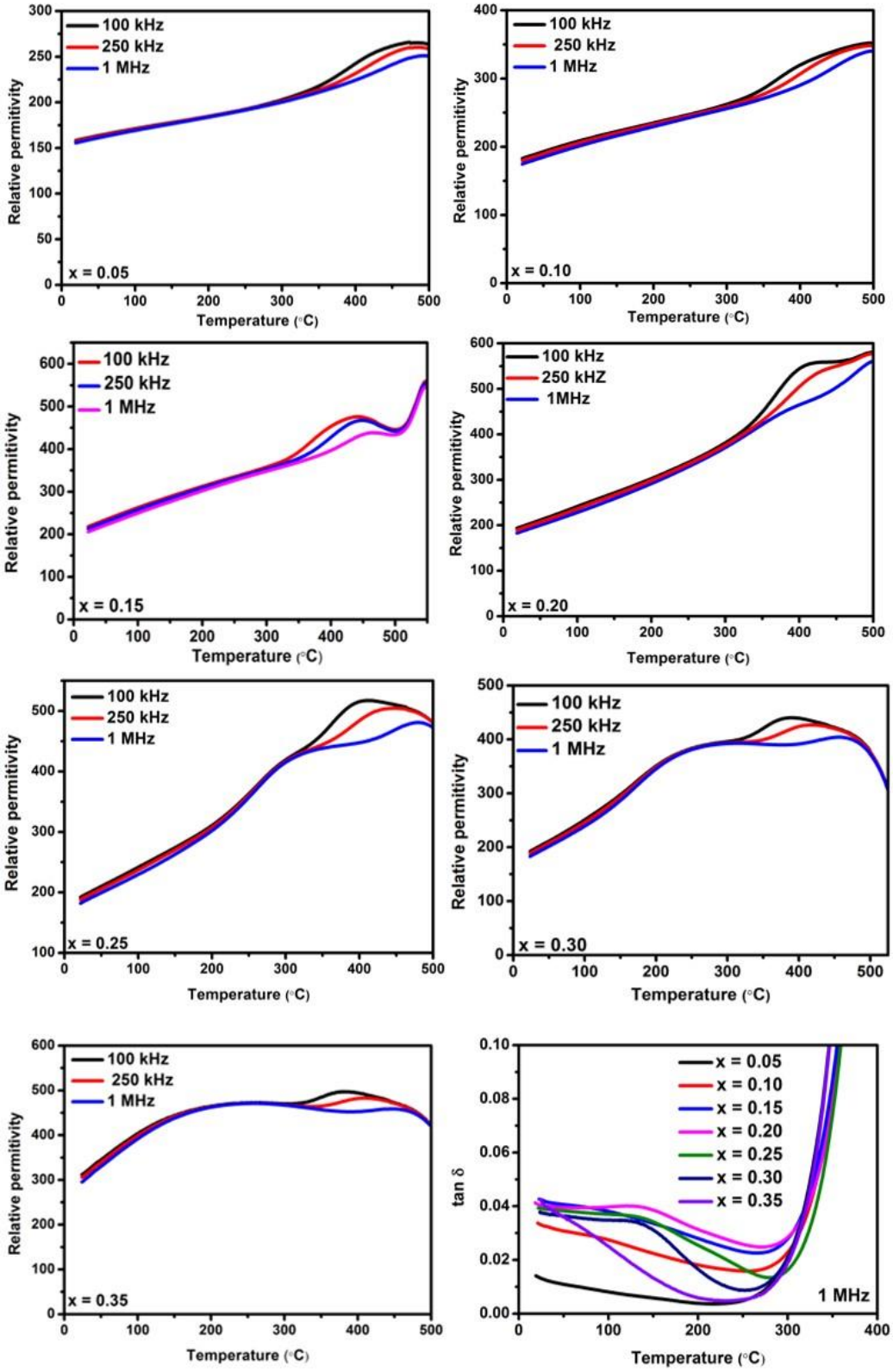

Figure 5.16: Relative permittivity and tan δ vs. temperature for BLFT $0.05 \leq x \leq 0.35$ ceramics.

In-situ XRD data for compositions $0.20 \leq x \leq 0.30$ are shown in Figure 5.17 (a-c). For x = 0.20, the peak splitting at ~ 45° 2θ starts to disappear at 300 °C and becomes undetectable by 400 °C. For x = 0.25, the peak splitting disappears at a lower temperature, between 250 and 300 °C, and similarly in x = 0.30 the peak splitting (albeit weaker) vanishes between 25 and 200 °C. *In-situ* XRD data thus confirms that the broad dielectric maxima correspond to a change in symmetry consistent with a PE-AFE transition. The PE-AFE transition for x = 0.20 is coincident with the relaxation behaviour present in all samples and hence cannot be resolved.

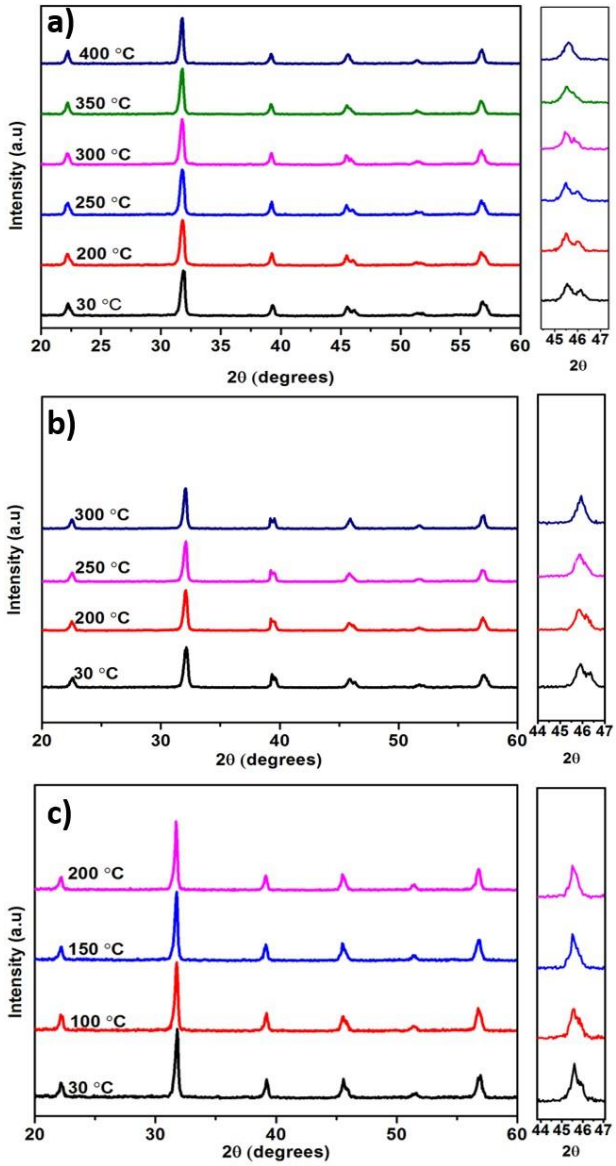

Figure 5.17: *In-situ* XRD diffractograms for a) x = 0.20; b) x = 0.25 and c) x =0.30.

TEM and electron diffraction were used to further characterise changes in domain structure and crystal structure for samples of x = 0.05, 0.20 and 0.35. A dark field image of x = 0.05, with corresponding ⟨110⟩ zone axis diffraction patterns (ZADPs) inset is shown in Figure 5.18.

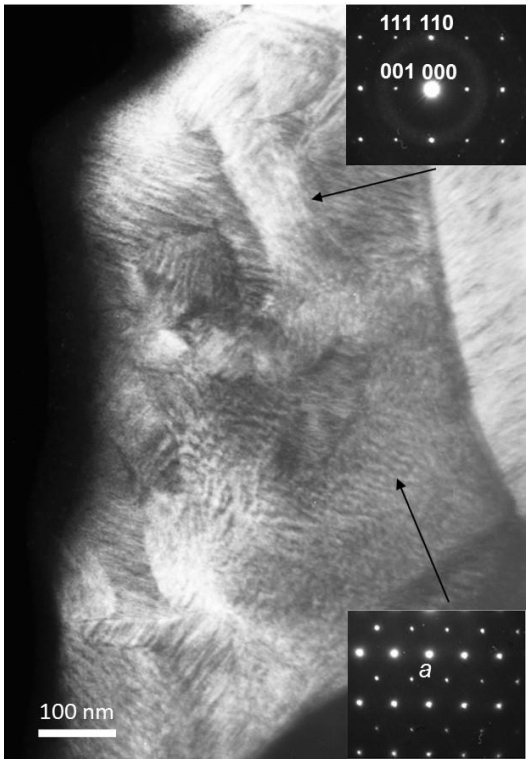

Figure 5.18: Dark field TEM illustrating the domain structure for x = 0.05 with inset ⟨110⟩ zone axis diffraction patterns from different macrodomains. Reflections indicated as '*a*' are ½{*ooo*} superstructure reflections associated with antiphase rotations of the O-octahedra.

The two patterns are from different macrodomains within the grain and reveal the variance of the ½{*ooo*} superstructure reflections which appear in 6/12 ⟨110⟩ ZADPs for *R*3*c* symmetry ($a^-a^-a^-$), according to Woodward and Reaney [24]. Figure 5.18 illustrates two domain length scales: fine scale ferroelectric/ferroelastic twin domains (10-20 nm) and larger regions (100-200 nm) which define the domain structure associated with antiphase tilting. This suggests the local directions of polarisation and strain (10-20 nm) are inconsistent with the rhombohedral distortion of the macroscopic tilt system and

symmetry. To rationalise, the observed macroscopic symmetry (*R*3*c*), macrodomain and nanodomain structure, it is proposed that each tilt domain (100-200 nm) is an amalgamation of many tens of finer scale ferroelastic/ferroelectric twins (10-20 nm) whose average polarisation vector and spontaneous strain are consistent with the symmetry of the macroscopic tilt system ($a^-a^-a^-$) but which locally have lower symmetry. The most likely symmetry based on the diffraction patterns and domain structure is monoclinic. This scenario is schematically illustrated in Figure 5.19.

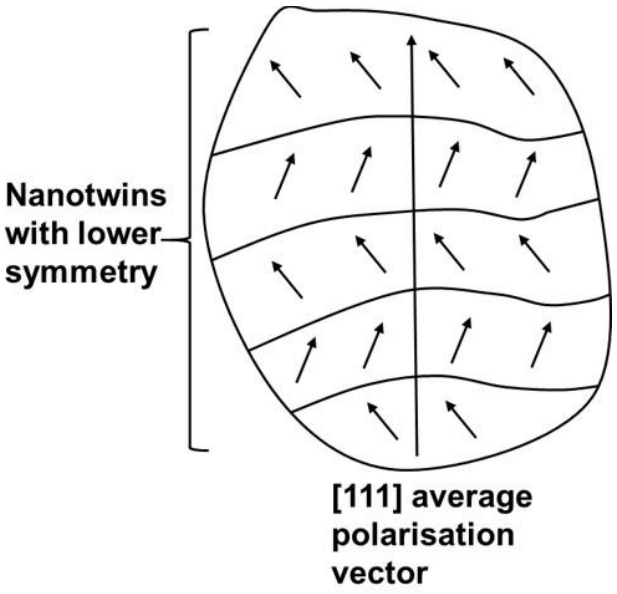

Figure 5.19: Schematic illustrating the hierarchical domain structure observed within x = 0.05.

A bright field image of a sample with x = 0.20 along with <001>, <110>, and <111> ZADPs are shown in Figure 5.20. In agreement with Karimi et al. [6] an intermediate phase is observed which is quadrupled according to the $PbZrO_3$ structure with *Pbam* symmetry. The quadrupling arises from the antipolar order of the A-site cations along <110> directions. Note however, that the ¼{*ooe*} reflections are streaked, indicating some variation in the cell dimensions in 1D, an effect discussed in detail for doped $PbZrO_3$ structured ceramics by Maclaren et al. [25]. In addition, ½{*ooo*} superstructure reflections are observed, consistent with the $a^0b^-b^-$ tilt system associated with the $PbZrO_3$-like structure [26]. Samples with x = 0.20 exhibit a typical lamellar ferroelastic domain

structure (100-200 nm) consistent with previous studies of $PbZrO_3$ structured ceramics [27] but there is no evidence of the fine scale twins observed in $x = 0.05$.

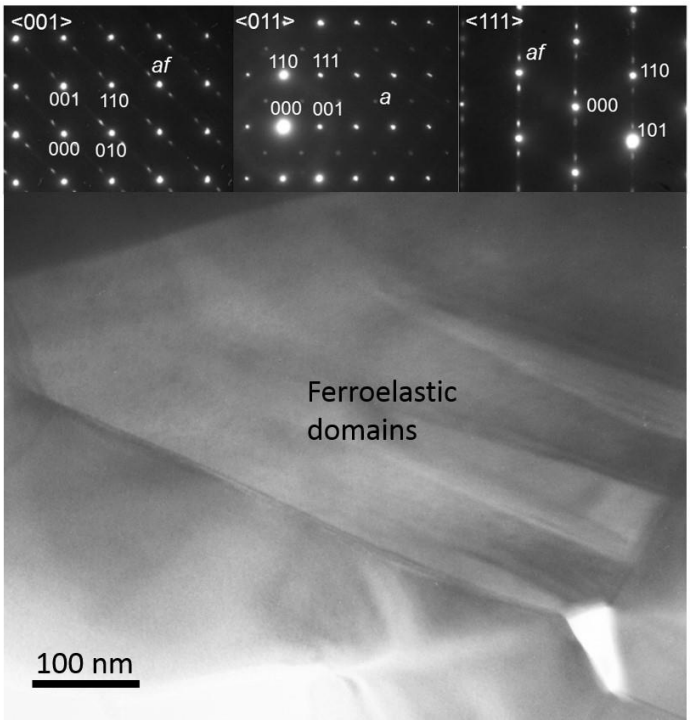

Figure 5.20: Bright field TEM showing ferroelastic domains typical of the PZ-like structure. Inset are <100>, <011> and <111> ZADPs. *af* = ¼{hk0} reflections associated with antipolar order in the PZ-like structure. *a* = ½{ooo} reflections associated with antiphase rotations of the octahedra and consistent with an $a^0b^-b^-$ tilt system.

A bright field image of $x = 0.35$ is shown in Figure 5.21 along with <001>, <110>, and <111> ZADPs. Very few grains revealed a clear domain structure, suggesting each is effectively a single domain. Electron diffraction patterns reveal a dominant superstructure that gives rise to a combination of ½{*ooo*}, ½{*eoo*} and ½{*eeo*} reflections, defining the likely tilt system as $a^-a^-c^+$ consistent with *Pnma* symmetry [24]. Although the dominant discrete superstructure reflections may be indexed according to a *Pnma* cell, there are diffuse reflection which lie at ~1/4{*ooe*} positions similar to those observed for $x = 0.20$. The appearance of 1/4{*ooe*} reflections and their diffuse character suggests there is still

some tendency towards quadrupling of the cell in a manner reminiscent of $PbZrO_3$. The diffuse reflections imply residual short range, antipolar clustering of the A-site ions such that there is simultaneously a strong commensurate doubling of the cell in accordance with *Pnma* symmetry ($a^-a^-c^+$) but also a short range incommensurate modulation with a wavelength of ~$2\sqrt{2}a$.

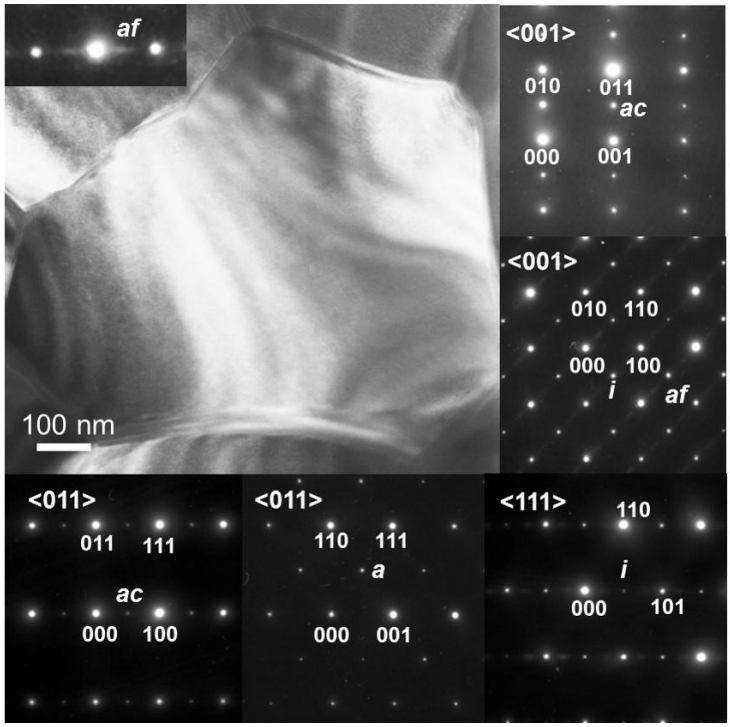

Figure 5.21: Bright field image and <<001>, <110, and <111> zone axis diffraction patterns from compositions with x = 0.35. ½{eeo} superstructure reflections are denoted '*ac*' and arise from antiparallel cation displacement, ½{ooe} reflections (*i*) arise from in phase tilting, ½{ooo} (*a*) are generated by antiphase tilting. Diffuse ¼{ooe} (*af*) reflections arise from antipolar clusters and are highlighted in the expanded inset.

5.4.3 Electrical microstructure and *P-E* loops

Electrical properties of BLFT ceramics are almost identical to those in BNFT ceramics. Impedance spectroscopy reveal a single semi-circular arc (Figure 5.22 (a)) with a capacitance of ~ 16 pFcm^{-1} indicating a bulk (grain) response that dominated the resistivity of the ceramic. The coincidence in frequency of the peak maximum in Z'' and M'' spectra in Figure 5.22 (b) demonstrated the ceramic to be electrically homogenous and this feature was observed in all samples. The calculated activation energies for bulk are > 1 eV for all compositions. Large electric fields (8 kV/mm) can be applied to BLFT ceramics as shown in Figure 5.24, but similar to BNFT no PE to FE/AFE switching nor any measurable strains were observed.

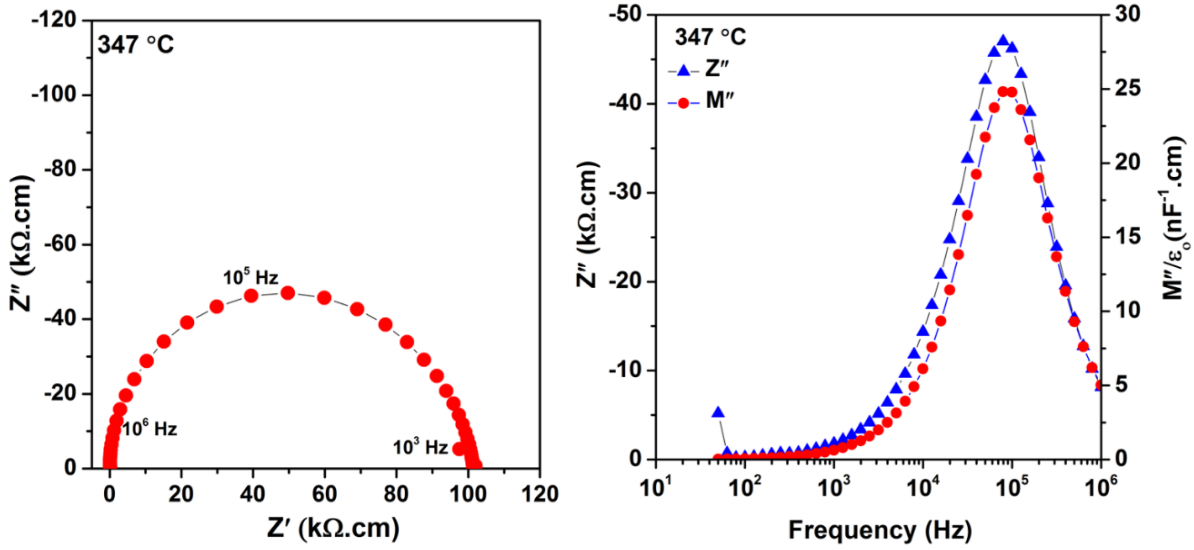

Figure 5.22: (a) Z* and (b) a combined Z'' and M'' spectroscopic plot for x = 0.05 at 347 ºC.

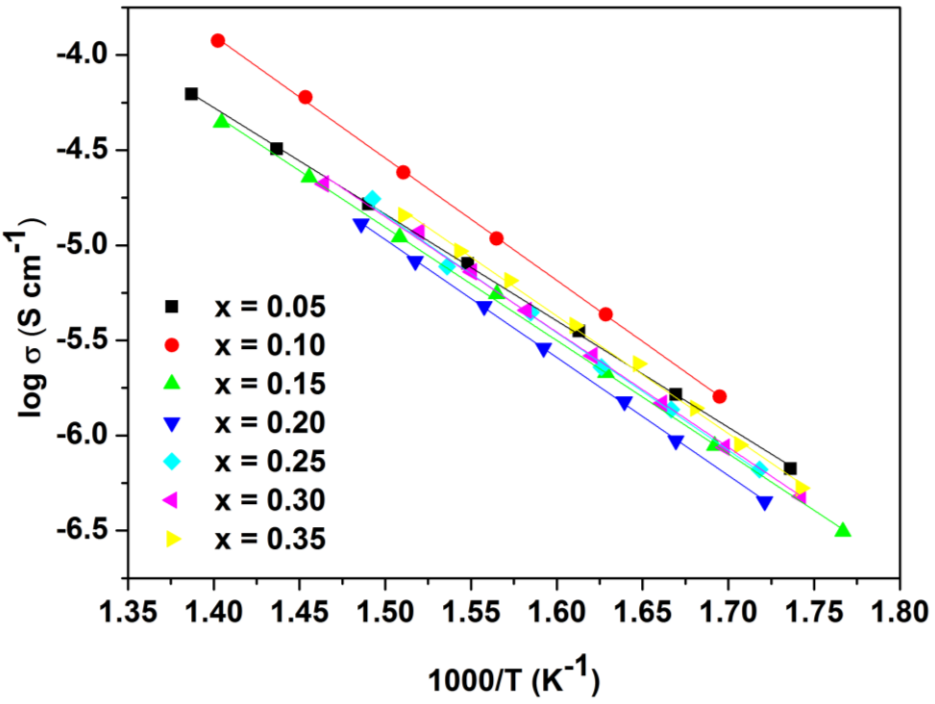

Figure 5.23: Arrhenius plots of bulk conductivity for BLFT ($0.05 \leq x \leq 0.35$) ceramics.

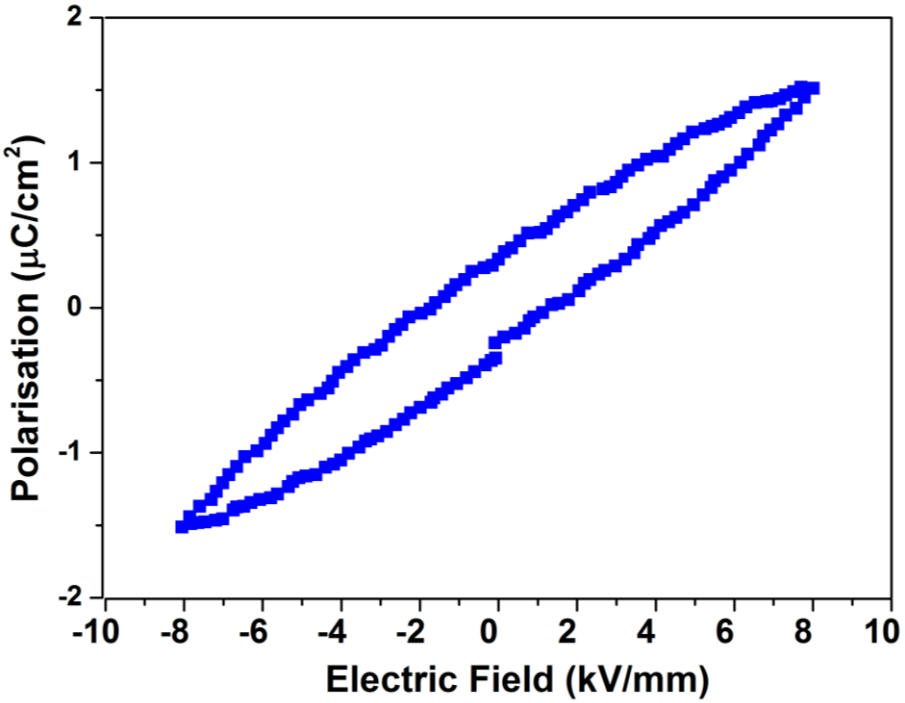

Figure 5.24: Polarisation *vs* electric field for BLFT(x = 0.05) at room temperature.

5.4.4 General discussion on BLFT ceramics

The discrete structural changes observed by XRD and dielectric data as a function of composition and temperature married to the absence of a second arc in the impedance spectroscopy measurements indicate that the ceramics are structurally and electrically homogeneous. Presumably, the enhanced homogeneity in comparison with previous studies of La doped $BiFeO_3$ [6] arises because of the formation of A-site vacancies ($Ti_{Fe}^{\cdot} = 1/3V_{La}'''$) which enhance diffusion rates. Nonetheless, for the first time in La doped $BiFeO_3$ compositions, the local and domain structure can be reliably interpreted without the influence of macroscopic chemical inhomogeneity. Most importantly, the frustration effects discussed and documented extensively in, e.g. the PZT phase diagram [28] in the vicinity of phase boundaries may be evaluated. In PZT, Woodward et al. [28] reported an unusual nanodomain structure at the AFE/FE phase boundary within the *R*3*m* phase. The observed nanodomains existed within larger domains and were interpreted as local monoclinic (*Pm*) regions which amalgamated to give an average *R*3*m* structure. For compositions at the AFE/FE boundary in this contribution a similar situation is observed but with greater clarity as the domain variants of the antiphase tilt structure are an order of magnitude greater than the ferroelastic/ferroelectric nanotwins. Levin and Reaney [29] observed a similar phenomenon in $Na_{1/2}Bi_{1/2}TiO_3$ ceramics which they reported to contain long range antiphase tilt regions (μm) inside which ferroelastic/ferroelectric nanotwins (10-20 nm) resided.

The observation of short range antipolar order in the PE phase for compositions with x = 0.35 has no parallels with PZT since there is no room temperature PE phase reported in the associated phase diagram. Nonetheless, the concept of polar clusters (short range order) existing above the PE-FE T_C in ferroelectrics is very well accepted. Polar clusters are however, effectively invisible to diffraction techniques since there is no additional superstructure generated. If a similar phenomenon were considered above the PE-AFE T_C then weak, diffuse ¼{*ooe*} would be the natural consequence and are observed in the present study.

The BLFT solid solution series may therefore be considered to exhibit clear aspects of pseudosymmetry particularly in the vicinity of structural phase transitions. A pseudosymmetric composition is defined as containing an ubiquitous distribution of regions whose local symmetry is lower than the average macroscopic symmetry. The driving forces for the appearance of pseudosymmetry are nanoscale chemical distributions whose impact becomes most apparent as phase boundaries are approached and competition between local regions for the dominant symmetry is enhanced. Levin and co-workers [30] determined aspects of pseudosymmetry across the morphotropic phase boundary in $(Na,K)_{1/2}Bi_{1/2}TiO_3$ solid solutions in which similar generic features were described. Similarly, features of the morphotropic and AFE/FE phase boundaries in the PZT phase diagram [28] may be reinterpreted and attributed to the generic phenomenon of pseudosymmetry.

5.5 Conclusions

In summary, we conclude that solubility limit in the binary system $BiFeO_3$-$REFeO_3$ is very low and therefore phase transitions and electrical properties of two new solid solutions BNFT and BLFT ceramics were studied. Both series show low losses and bulk activation energies in excess of 1 eV. The activation energies are comparable to those in more conventional ferroelectrics such as $BaTiO_3$ [31]. No apparent piezoelectricity is observed in both series. However, control over processing and low loss in these ceramics makes them potentially useful endmembers for developing lead free piezoelectric materials. The dielectric data in both series shows strong relaxation near $T_{N,}$ and T_C was observed to decrease with an increase in $REFeO_3$ concentrations. XRD results for BNFT revealed a structural phase transition from *R*3*c* to *Pbam* at $x = 0.15$. The phase transitions in BNFT ceramics are consistent with previous studies. However, the BLFT ceramics showed better homogeneity in comparison to previous studies on La doped BF allowing a better interpretation of the local structure and domain structure in these ceramics by using TEM. TEM and XRD studies on BLFT revealed a series of structural phase transitions, from *R*3*c* for samples with $x < 0.15$ to ($0.15 < x < 0.30$) and macroscopic *Pnma* phase for $x = 0.35$ with clusters of antipolar order. The dielectric data showed strong relaxation near T_N however, this did not impinge upon the broad anomalies which

correspond to PE-AFE and PE-FE transitions. These anomalies occurred as a function of composition and were confirmed using *in-situ* XRD.

The domain structure in the FE phase of BLFT near the AFE boundary was complex with ferroelastic nanotwin domains present, inconsistent with the macroscopic tilt domain structure. A model has been proposed where the macroscopic tilt domains are considered to be an amalgamation of lower symmetry twins in which the average macroscopic polarisation vector remains [111], consistent with the average symmetry by XRD. The presence of diffuse 1/4{*ooe*} reflections in addition to strong discrete, doubled superstructure reflections for $x = 0.35$ was considered as evidence that antipolar clusters were residual in the *Pnma* phase adjacent to the AFE/PE boundary. Finally, it is concluded that aspects of pseudosymmetry may be clearly resolved in BLFT compositions through detailed TEM and electron diffraction studies in the vicinity of the phase boundaries where the local symmetry invariably appears lower than the average macroscopic symmetry.

5.6 References

[1] D. Arnold, K. Knight, F. Morrison, and P. Lightfoot, "Ferroelectric-Paraelectric Transition in $BiFeO_3$: Crystal Structure of the Orthorhombic β Phase," *Phys. Rev. Lett.*, vol. 102, no. 2, 2009.

[2] P. Fischerl, M. PoIomska, I. Sosnowska, and M. Szymanski, "Temperature dependence of the crystal and magnetic structures of $BiFeO_3$," *J. Phys. C Solid State Phys.*, no. 13, pp. 1931–1940, 1980.

[3] V. L. Mathe, K. K. Patankar, M. B. Kothale, S. B. Kulkarni, P. B. Joshi, and S. A. Patil, "Preparation, structural analysis and dielectric properties of $Bi_xLa_{1-x}FeO_3$ perovskite," *Pramana-Journal Phys.*, vol. 58, pp. 1105–1113, 2002.

[4] V. L. Mathe, K. K. Patankar, R. N. Patil, and C. D. Lokhande, "Synthesis and dielectric properties of $Bi_{1-x}Nd_xFeO_3$ perovskites," *J. Magn. Magn. Mater.*, vol. 270, no. 3, pp. 380–388, 2004.

[5] G. L. Yuan and S. W. Or, "Enhanced piezoelectric and pyroelectric effects in single-phase multiferroic $Bi_{1-x}Nd_xFeO_3$ (x = 0–0.15) ceramics," *Appl. Phys. Lett.*, vol. 88, p. 62905, 2006.

[6] S. Karimi, I. M. Reaney, Y. Han, J. Pokorny, and I. Sterianou, "Crystal chemistry and domain structure of rare-earth doped $BiFeO_3$ ceramics," *J. Mater. Sci.*, vol. 44, no. 19, pp. 5102–5112, 2009.

[7] S. Karimi, I. M. Reaney, I. Levin, and I. Sterianou, "Nd-doped $BiFeO_3$ ceramics with antipolar order," *Appl. Phys. Lett.*, vol. 94, p. 112903, 2009.

[8] K. Kalantari, I. Sterianou, S. Karimi, M. C. Ferrarelli, S. Miao, D. C. Sinclair, and I. M. Reaney, "Ti-Doping to Reduce Conductivity in $Bi_{0.85}Nd_{0.15}FeO_3$ Ceramics," *Adv. Funct. Mater.*, vol. 21, pp. 3737–3743, 2011.

[9] I. M. Reaney, I. MacLaren, L. Wang, B. Schaffer, A. Craven, K. Kalantari, I. Sterianou, S. Miao, S. Karimi, and D. C. Sinclair, "Defect chemistry of Ti-doped antiferroelectric $Bi_{0.85}Nd_{0.15}FeO_3$," *Appl. Phys. Lett.*, vol. 100, no. 18, p. 182902, 2012.

[10] R. D. Shannon, "Revised Effective Ionic Radii and Systematic Studies of Interatomic Distances in Halides and Chalcogenides," *Acta Crystallogr. Sect. A*, vol. 32, p. 751, 1976.

[11] R. D. Shannon, "Dielectric polarizabilities of ions in oxides and fluorides," *J. Appl. Phys.*, vol. 73, no. 1, p. 348, 1993.

[12] K. Kalantari, I. Sterianou, D. C. Sinclair, P. A. Bingham, J. Pokorný, and I. M. Reaney, "Structural phase transitions in Ti-doped $Bi_{1-x}Nd_xFeO_3$ ceramics," *J. Appl. Phys.*, vol. 111, no. 6, p. 64107, 2012.

[13] I. Levin, S. Karimi, V. Provenzano, C. L. Dennis, H. Wu, T. P. Comyn, T. J. Stevenson, R. I. Smith, and I. M. Reaney, "Reorientation of magnetic dipoles at the antiferroelectric-paraelectric phase transition of $Bi_{1-x}Nd_xFeO_3$ ($0.15 \leq x \leq 0.25$)," *Phys. Rev. B*, vol. 81, p. 20103, 2010.

[14] I. Levin, M. G. Tucker, H. Wu, V. Provenzano, C. L. Dennis, S. Karimi, T. Comyn, T. Stevenson, R. I. Smith, and I. M. Reaney, "Displacive phase transitions and magnetic structures in Nd-substituted $BiFeO_3$," *Chem. Mater.*, vol. 23, no. 8, pp. 2166–2175, 2011.

[15] G. Shirane and A. Takeda, "Phase Transitions in Solution of $PbZrO_3$ and $PbTiO_3$ Small concentrations of $PbTiO_3$," *J. Phys. Soc. Japan*, vol. 7, no. 1, 1952.

[16] Z. X. Cheng, X. L. Wang, A. H. Li, X. L. Wang, S. X. Dou, K. Ozawa, H. Kimura, S. J. Zhang, and T. R. Shrout, "Structure, ferroelectric properties, and magnetic properties of the La-doped bismuth ferrite," *J. Appl. Phys.*, vol. 103, p. 07E507, 2008.

[17] Y.-K. Jun, W.-T. Moon, C.-M. Chang, H.-S. Kim, H. S. Ryu, J. W. Kim, K. H. Kim, and S.-H. Hong, "Effects of Nb-doping on electric and magnetic properties in multi-ferroic $BiFeO_3$ ceramics," *Solid State Commun.*, vol. 135, no. 1–2, pp. 133–137, 2005.

[18] T. Kiruma, S. Kawamoto, I. Yamada, M. Azuma, M. Takano, and Y. Tokura, "Magnetocapacitance effect in multiferroic $BiMnO_3$," *Phys. Rev. B*, vol. 67, no. 3, p. 180401, 2003.

[19] H. B. Lal, R. Srivastava, and K. G. Srivastava, "Magnetoelectric effect in Cr_2O_3 single crystal as studied by dielectric-constant method," *Phys. Rev.*, vol. 154, no. 2, pp. 505–507, 1967.

[20] Y. A. Park, K. M. Song, K. D. Lee, C. J. Won, and N. Hur, "Effect of antiferromagnetic order on the dielectric properties of $Bi_2Fe_4O_9$," *Appl. Phys. Lett.*, vol. 96, no. 9, p. 092506, 2010.

[21] Y. F. Cui, Y. G. Zhao, L. B. Luo, J. J. Yang, H. Chang, M. H. Zhu, D. Xie, and T. L. Ren, "Dielectric, magnetic, and magnetoelectric properties of La and Ti codoped $BiFeO_3$," *Appl. Phys. Lett.*, vol. 97, no. 22, p. 222904, 2010.

[22] J. T. S. Irvine, D. C. Sinclair, and A. R. West, "Electroceramics: characterization by impedance spectroscopy," *Adv. Mater.*, vol. 2, no. 3, pp. 132–138, 1990.

[23] T. Rojac, M. Kosec, and D. Damjanovic, "Large electric-field induced strain in $BiFeO_3$ ceramics," *J. Am. Ceram. Soc.*, vol. 94, no. 12, pp. 4108–4111, 2011.

[24] D. I. Woodward and I. M. Reaney, "Electron diffraction of tilted perovskites," *Acta Crystallogr. Sect. B Struct. Sci.*, vol. 61, no. 4, pp. 387–399, 2005.

[25] I. MacLaren, R. Villaurrutia, and A. Peláiz-Barranco, "Domain structures and nanostructures in incommensurate antiferroelectric $Pb_xLa_{1-x}Zr_{0.9}Ti_{0.1}O_3$," *J. Appl. Phys.*, vol. 108, no. 3, p. 034109, 2010.

[26] A. M. Glazer, “Structure and disorder in single crystal Lead Zirconate, $PbZrO_3$,” *Acta Crystallogr.*, vol. B49, pp. 846–852, 1993.

[27] M. Tanaka and R. Saito, “Electron Microscopic Studies on domain structure $PbZrO_3$,” *Jpn. J. Appl. Phys.*, vol. 21, no. 2, pp. 291–298, 1982.

[28] D. I. Woodward, J. Knudsen, and I. M. Reaney, “Review of crystal and domain structures in the $PbZr_xTi_{1-x}O_3$ solid solution,” *Phys. Rev. B - Condens. Matter Mater. Phys.*, vol. 72, no. 10, pp. 1–8, 2005.

[29] I. Levin and I. M. Reaney, “Nano- and mesoscale structure of $Na_{1/2}Bi_{1/2}TiO_3$: A TEM Perspective,” *Adv. Funct. Mater.*, vol. 22, no. 16, pp. 3445–3452, 2012.

[30] I. Levin, I. M. Reaney, E.-M. Anton, W. Jo, J. Rödel, J. Pokorný, L. A. Schmitt, H.-J. Kleebe, M. Hinterstein, and J. L. Jones, “Local structure, pseudosymmetry, and phase transitions in $Na_{1/2}Bi_{1/2}TiO_3$–$K_{1/2}Bi_{1/2}TiO_3$ ceramics,” *Phys. Rev. B*, vol. 87, no. 6, p. 060102, 2013.

[31] O. P. Thakur, A. Feteira, B. Kundys, and D. C. Sinclair, “Influence of attrition milling on the electrical properties of undoped-$BaTiO_3$,” *J. Eur. Ceram. Soc.*, vol. 27, no. 7, pp. 2577–2589, 2007.

Chapter 6: (1-x)$K_{1/2}Bi_{1/2}TiO_3$-xBLFT/BNFT Ceramics

6.1 Introduction

$K_{1/2}Bi_{1/2}TiO_3$ (KBT) is ferroelectric material with high T_C of ~380 °C [1]. Despite challenges in processing, KBT has attracted attention because of two major reasons: (i) high T_C and (ii) tetragonal symmetry at room temperature (RT). The latter potentially allows construction of an MPB by combining materials of rhombohedral symmetry with KBT, such as $Na_{1/2}Bi_{1/2}TiO_3$ (NBT) and $BiFeO_3$ (BF). KBT-based systems generally do not exhibit very high d_{33} and in most cases relaxor behaviour is promoted by substitution of another endmember. This results in an enhancement in strain giving a high effective d^*_{33} making them attractive for actuator applications [2-4]. Studies on (1-x)BF-xKBT have revealed promising properties with d^*_{33} ~ 275 pm/V at RT [2].

In a previous chapter, the inherent conductivity of BF was discussed which hinders application of high electric fields to access optimum electromechanical properties. Our study showed that low loss materials may be fabricated in the ternary series $BiFeO_3$-$REFeO_3$-$RE_{2/3}TiO_3$ (BREFT, RE = La, Nd). Although the ceramics were capable of sustaining large electric fields, their electromechanical response was poor. However, the easy processing and low conductivities offered by BREFT suggested that they might be ideal as an endmember of a solid solution within which there is potential to optimise d_{33} and/or d^*_{33}. Therefore, selected compositions (0.80$BiFeO_3$-0.15$LaFeO_3$-0.05$La_{2/3}TiO_3$) and (0.82$BiFeO_3$-0.15$NdFeO_3$-0.03$Nd_{2/3}TiO_3$), denoted by BLFT and BNFT hereafter, were used as endmembers to form a solid solution with KBT. BLFT and BNFT were shown to have an antiferroelectric structure with *Pbam* symmetry similar to that of $PbZrO_3$. Therefore, KBT-BLFT/BNFT imitates $Pb(Zr,Ti)O_3$ (PZT) where $PbZrO_3$ and $PbTiO_3$ have antiferroelectric orthorhombic and ferroelectric tetragonal structures, respectively. Thus, the overall premise was to imitate the crystal chemistry of PZT and simultaneously control dielectric losses associated with the reduction of Fe^{3+} to Fe^{2+} during processing at high temperature. Note that (1-x)KBT–xBLFT is studied in a wide range ($0 \leq x \leq 0.70$) but (1-x)KBT–xBNFT is studied only in the range ($0 \leq x \leq 0.15$) since

in the former optimum properties lay close to the endmember KBT. The following sections discuss both systems together because of similarities in the obtained results.

6.2 Structural analysis

6.2.1 XRD results

Figure 6.1 and 6.2 show room temperature XRD traces for ceramics fabricated in the system (1-*x*)KBT–*x*BLFT ($0 \leq x \leq 0.70$) and (1-*x*)KBT–*x*BNFT ($0 \leq x \leq 0.15$), respectively. All the observed peaks are indexed to a single perovskite structure. K^{+}, Bi^{+3}, La^{3+}/Nd^{3+} and $\boldsymbol{V}_{\boldsymbol{Nd}}^{'''}/\boldsymbol{V}_{\boldsymbol{LA}}^{'''}$ reside on the A-site, while Ti^{4+} and Fe^{3+} are on the B-site of the perovskite structure. Note that the composition are stoichiometric and donor doping on the B-site is compensated by the cation vacancy on the A-site. For undoped KBT (x = 0), the structure is tetragonal with space group *P*4*mm*, having lattice parameters a = 0.3921 (10) nm and c = 0.3999 (14) corresponding to c/a of ~1.019 broadly consistent with previous studies [5]. With the addition of the BLFT/BNFT, the tetragonal splitting disappears and no splitting can be seen at $x > 0.03$. In (1-*x*)KBT-*x*BF, a tetragonal structure similar to KBT is reported to exist up to $x \leq 0.25$ [2]. The region between $x = 0.25 \leq x \leq 0.5$ is not well investigated but based on the optimum properties observed at $x = 0.25$, Morzov et al. [2] proposed the existence of a pseudocubic phase in the K-rich region similar to that observed at high temperatures in undoped KBT, i.e. coexistence of tetragonal and cubic phases [6]. Another pseudocubic structure is reported to exist at x = 0.6 [7]. At $x > 0.6$, a rhombohedral structure similar to BF is reported for the system [2,7,8]. The pseudocubic structure at $x = 0.6$ is considered to be formed by the coexistence of polar rhombohedral and non-polar cubic phases [8].The rhombohedral phase in BF-based systems is characterised by splitting in the 111_C peak [9]. However in our study no evidence of the formation of a rhombohedral phase was observed within the studied range. The lack of the rhombohedral splitting is most likely associated with the incorporation of RE ions with lower polarizability than Bi^{3+} in cuboctahedral coordination. We note that RE ions promote antipolar rather than polar order in BF with space group *Pbam*, which manifest as splitting of the 200_C peak [10,11]. However, 200_C splitting associated with orthorhombic (*Pbam*) symmetry was not observed in the studied range for either system.

The XRD traces for BLFT/BNFT with $x \geq 0.04$, may be indexed using a cubic structure with space group *Pm*3*m* but *P-E* loops (discussed in later sections) shows non-zero remanence up to $x = 0.30$ (BLFT). Therefore, the symmetry for these ceramics cannot be cubic and ferroelectric order, though supressed or meso/short ranged, still persists at higher concentrations. It is possible that tetragonality persists until higher concentrations but deviation from the ideal cubic structure is too small to be detected by XRD. The most likely scenario is that pseudocubic phase at RT is similar to that observed at higher temperature in undoped KBT ceramics. To understand the structure further Raman spectroscopy was performed as a function of composition and temperature.

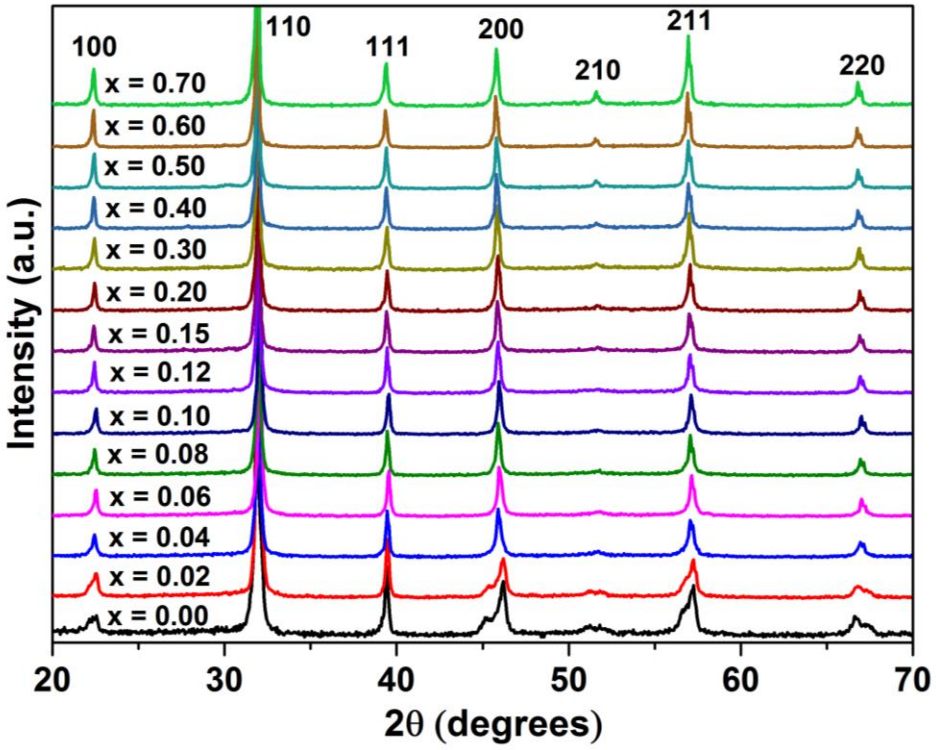

Figure 6.1: Room temperature XRD traces for (1-*x*)KBT– *x*BLFT ($0 \leq x \leq 0.70$) ceramics.

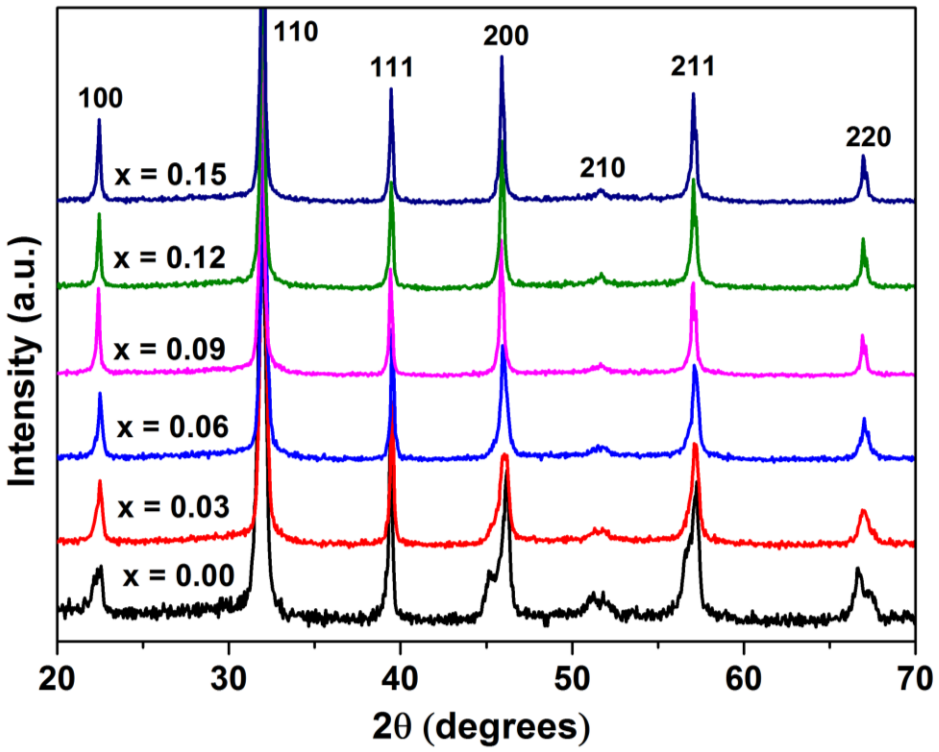

Figure 6.2: Room temperature XRD traces for (1-*x*)KBT– *x*BNFT ($0 \leq x \leq 0.15$) ceramics.

6.2.2 Raman spectroscopy

Raman spectroscopy was performed to further understand structural evolution of ceramics in the system (1-*x*)KBT–*x*BLFT ($0 \leq x \leq 0.70$) and (1-*x*)KBT– *x*BNFT ($0 \leq x \leq 0.15$). No attempt is made to assign modes to the observed bands but instead the spectra are used in a comparative manner to study evolution of the characteristic modes associated with the tetragonal phase of KBT. Figure 6.3 shows Raman spectra of KBT as a function of temperature. Raman bands of KBT are relatively broad, associated with the A-site disorder in these ceramics. In KBT-based ceramics the presence of a mode at 200 cm^{-1} and the doublet around 300 cm^{-1} indicate tetragonal symmetry [12, 13], confirming XRD results shown in Figure 6.1 and 6.2. On increasing temperature, the 200 cm^{-1} weakens and the 300 cm^{-1} mode begins to merge into a single peak. By 300 °C, the doublet has complete merged into a broad singlet and the mode at 200 cm^{-1} almost disappears, presumably due

to the transformation to a cubic/pseudocubic structure consistent with TEM and XRD studies on KBT by the authors of refs. [5] and [6].

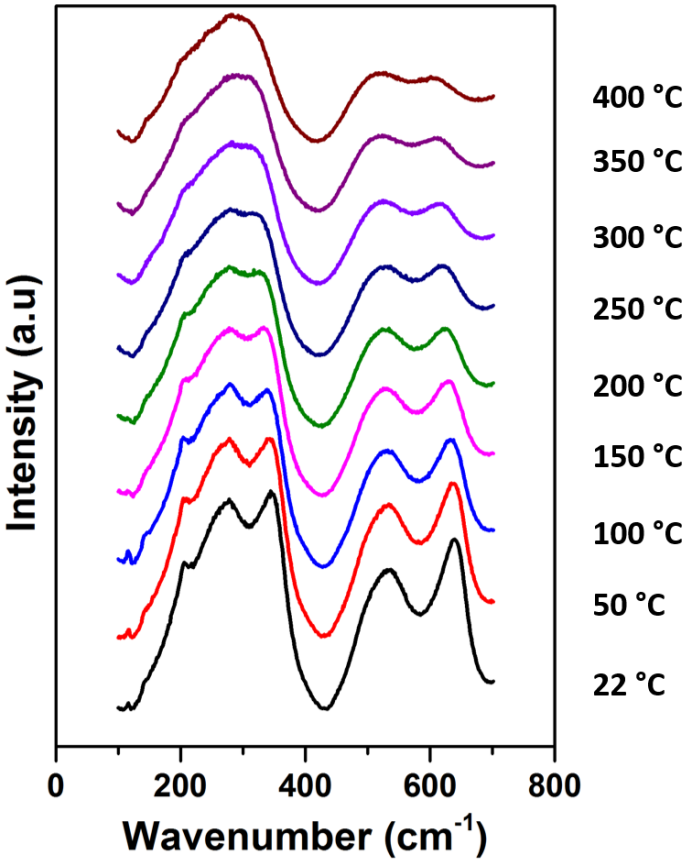

Figure 6.3: Raman spectra of KBT ceramics as a function of temperature.

Figure 6.4 shows Raman spectra as a function of composition for (1-*x*)KBT–*x*BLFT ($0 \leq x \leq 0.70$) and KBT–*x*BNFT ($0 \leq x \leq 0.15$). The evolution in characteristic tetragonal modes as a function of composition is similar to that observed in KBT as a function of temperature. Unlike in XRD studies where the tetragonal splitting disappears at x > 0.03, the tetragonal mode at 200 cm^{-1} persists up to $x = 0.15$ and thus confirms the existence of a local tetragonal phase at high concentrations. At $x > 0.30$, the characteristic tetragonal mode disappears. Exact compositional values at which a structural changes occur are open to interpretation since there is ambiguity in interpretation of the spectra but nonetheless a

pseudocubic phase is apparent in the solid solution over a wide compositional range, with the tetragonal phase dominating at compositions close to KBT.

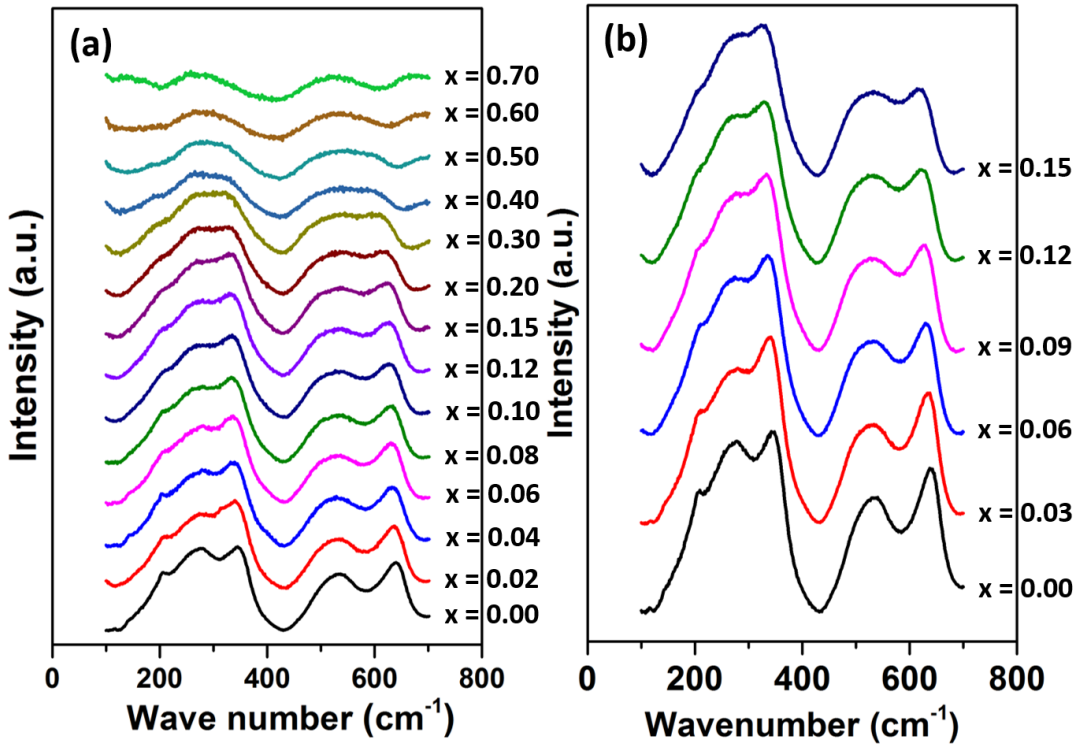

Figure 6.4: RT Raman spectra for (a) (1-*x*)KBT–*x*BLFT ($0 \leq x \leq 0.70$) and (b) (1-*x*)KBT– *x*BNFT ($0 \leq x \leq 0.15$) ceramics.

6.3 Microstructure

Figure 6.5 shows SEM images of (1-*x*)KBT–*x*BLFT ($0 \leq x \leq 0.20$) ceramics. The grain size of KBT was 200-300 nm but as BLFT concentration increased there was gradual increase, though the grain size remained ≤ 1 μm in all compositions. Higher concentrations of BLFT ($x > 0.20$) (not shown) do not result in any significant effect up to $x = 0.70$. Figure 6.6 shows SEM images of (1-*x*)KBT–*x*BNFT ($0 \leq x \leq 0.15$), with a similar trend in grain size and microstructure to that observed in the (1-*x*)KBT-*x*BLFT series.

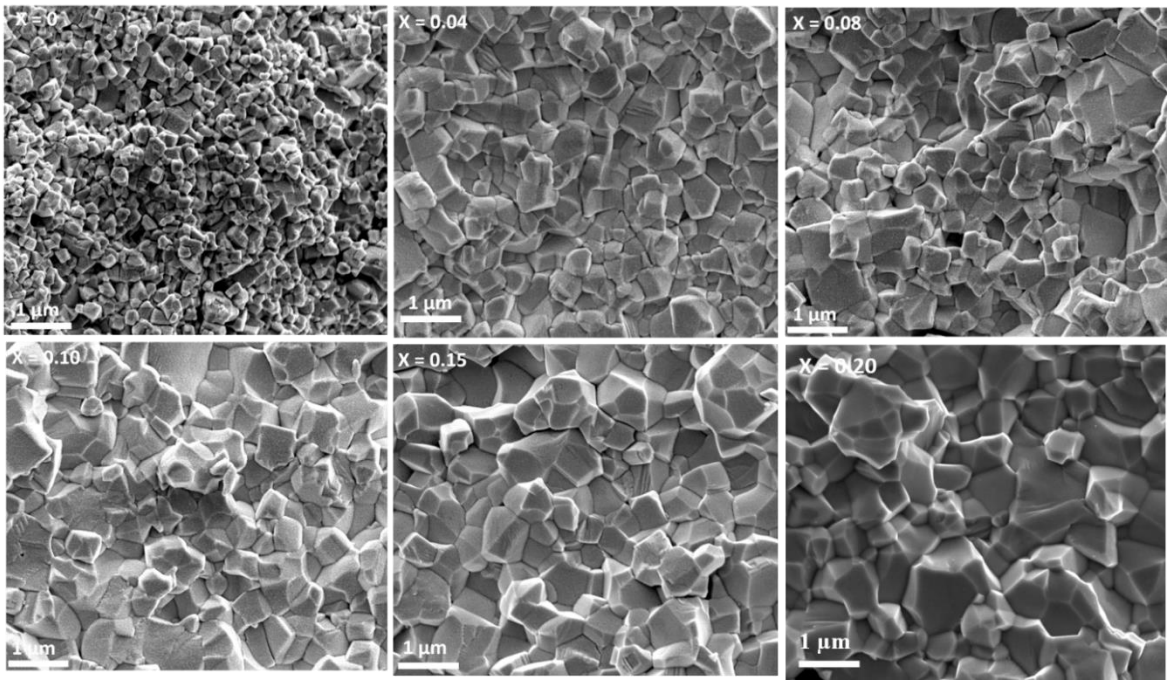

Figure 6.5: SEM images of (1-*x*)KBT–*x*BLFT ($0 \leq x \leq 0.20$) ceramics

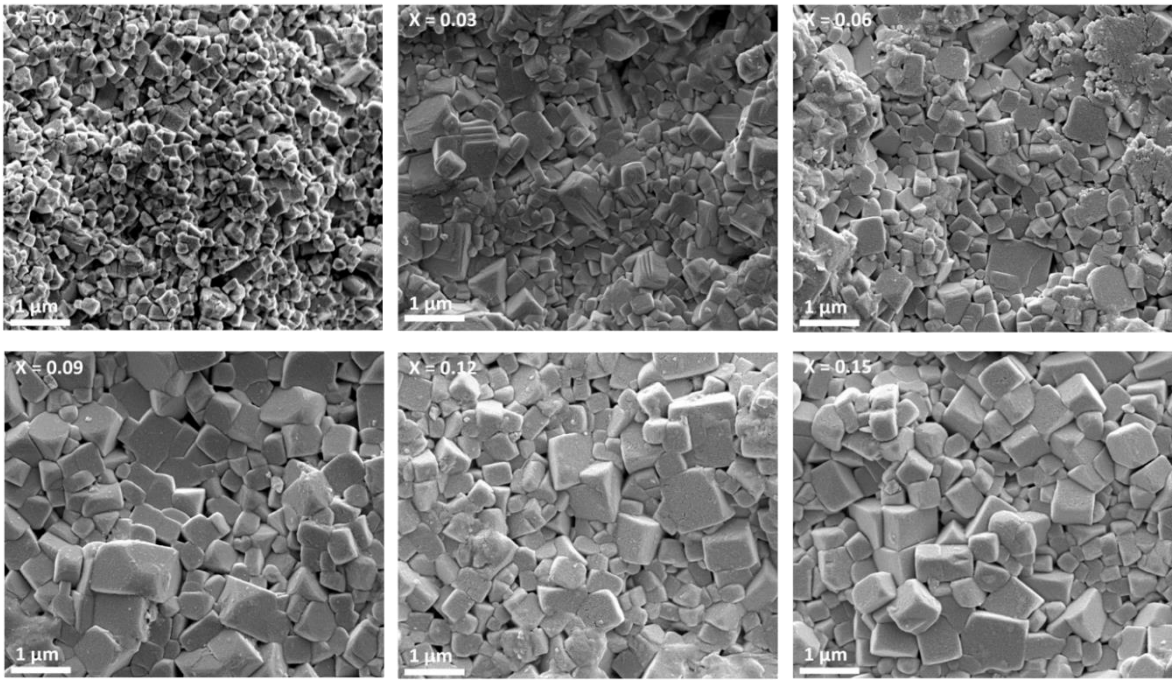

Figure 6.6: SEM images of (1-*x*)KB –*x*BLFT ($0 \leq x \leq 0.20$) ceramics

To determine the domain structure of BLFT doped ceramics, TEM studies were undertaken on selected samples. Figure 6.7 shows dark field images taken using a (110) reflection with the electron beam close to <110> zone axis. In KBT, planar defects ~ 10-20 nm apart are evident, typical of a micro/mesoscale ferroelectric domain structure. For $x = 0.1$, only weak, broad striations in contrast are observed, typical a polar state in which the scale length of the ferroelectric order has been significantly reduced through the substitution of BLFT. The images may therefore be interpreted as a arising from a solid solution in which there has been a transition from a long range ordered ferroelectric to a short range ordered relaxor (possible sub-relaxor) phase. Inset is the <110> zone axis diffraction pattern. The absence of superstructure reflections demonstrates that substitution of BLFT up to $x = 0.15$ does not induce octahedral rotations. (1-*x*)KBT-*x*BNFT is expected to show similar behaviour.

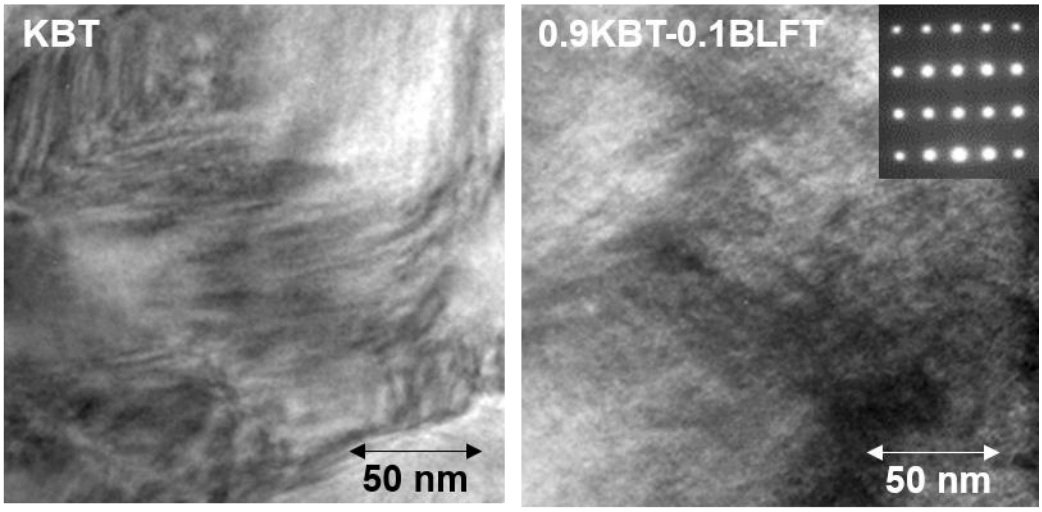

Figure 6.7: Dark Field images for (1-*x*)KBT-*x*BLFT ($x = 0$ and $x = 0.10$) in <110> zone axis. Inset shows the <110> zone axis diffraction pattern.

6.4 Dielectric properties

Figure 6.8 shows dielectric constant and tan δ as a function of temperature for the series (1-*x*)KBT-*x*BLFT ($0 \leq x \leq 0.70$). To avoid too much data being presented to the reader in

Figure 6.8, not all dielectric curves are shown for $x \leq 0.15$ but the trend is similar to that of (1-*x*)KBT-*x*BNFT, shown in Figure 6.9.

The endmember with $x = 0$, has been reported to show weak relaxation behaviour usually attributed to disorder of the A-site cations [1,14,15]. A similar behaviour is observed but space charge polarisation affects the permittivity as indicated by very high losses at low frequencies. The degree of relaxation is usually judged by two parameters: (i) frequency dependence of peak maximum in permittivity (T_m) and (ii) increase in peak width [16]. Both parameters increase with the substitution of BLFT/BNFT. Such behaviour has been observed for many KBT-based systems such as KBT-$Bi(Mg_{1/2}Ti_{1/2})O_3$ [16] and KBT-$BiScO_3$ [17].

In many piezoelectric systems such as $Bi_{1/2}Na_{1/2}TiO_3$-$BaTiO_3$ [18] [19] and La doped $Pb(Zr,Ti)O_3$ [20], strong frequency dependence in permittivity corresponds to the existence of nanodomains, whereas classical ferroelectric domains correspond to minimal frequency dependence. Similar behaviour is observed here and the frequency dispersion in permittivity at room temperature corresponds well to the TEM studies for sample $x = 0.10$ (Figure 6.7), where discrete macro/meso domain walls were not observed.

It should also be noted that relatively high losses at room temperature (excluding $x = 0$) are primarily because of relaxation and not from long range conduction. The situation can be understood by looking at the trend in tan δ at different frequencies. At room temperature tan δ increases with increase in frequency, associated with energy dissipated due to the relaxation as the frequency increases. Losses dominated by conduction can be observed above T_m where an opposite trend in frequency is observed (high losses at low frequency).

A sharp rise in tan δ (1 kHz) is observed at much lower temperature ~250 °C for $x = 0.70$ as compared to ~400 °C for $x = 0.10$ in (1-*x*)KBT-*x*BLFT ceramics (Figure 6.8). A similar trend is observed in (1-*x*)KBT-*x*BNFT ceramics, where tan δ (1 kHz) rises sharply at ~ 350 ° for $x = 0.15$ as compared to ~450 °C at $x = 0.03$ (Figure 6.9). Studies (previous chapter) have shown that BLFT/BNFT are more resistive in comparison to pure BF, however KBT maintains lower losses (< 0.05 at 1 MHz) at much higher temperature ~500 °C (Figure 6.9) in comparison to BLFT, where a sharp increase in tan δ (1 MHz) is

observed at 300 °C (Figure 5.16). Respective properties of the endmembers can therefore rationalise the observed trends. Based on this, ceramics near to the KBT endmember are more favourable for application at high temperatures and low frequencies.

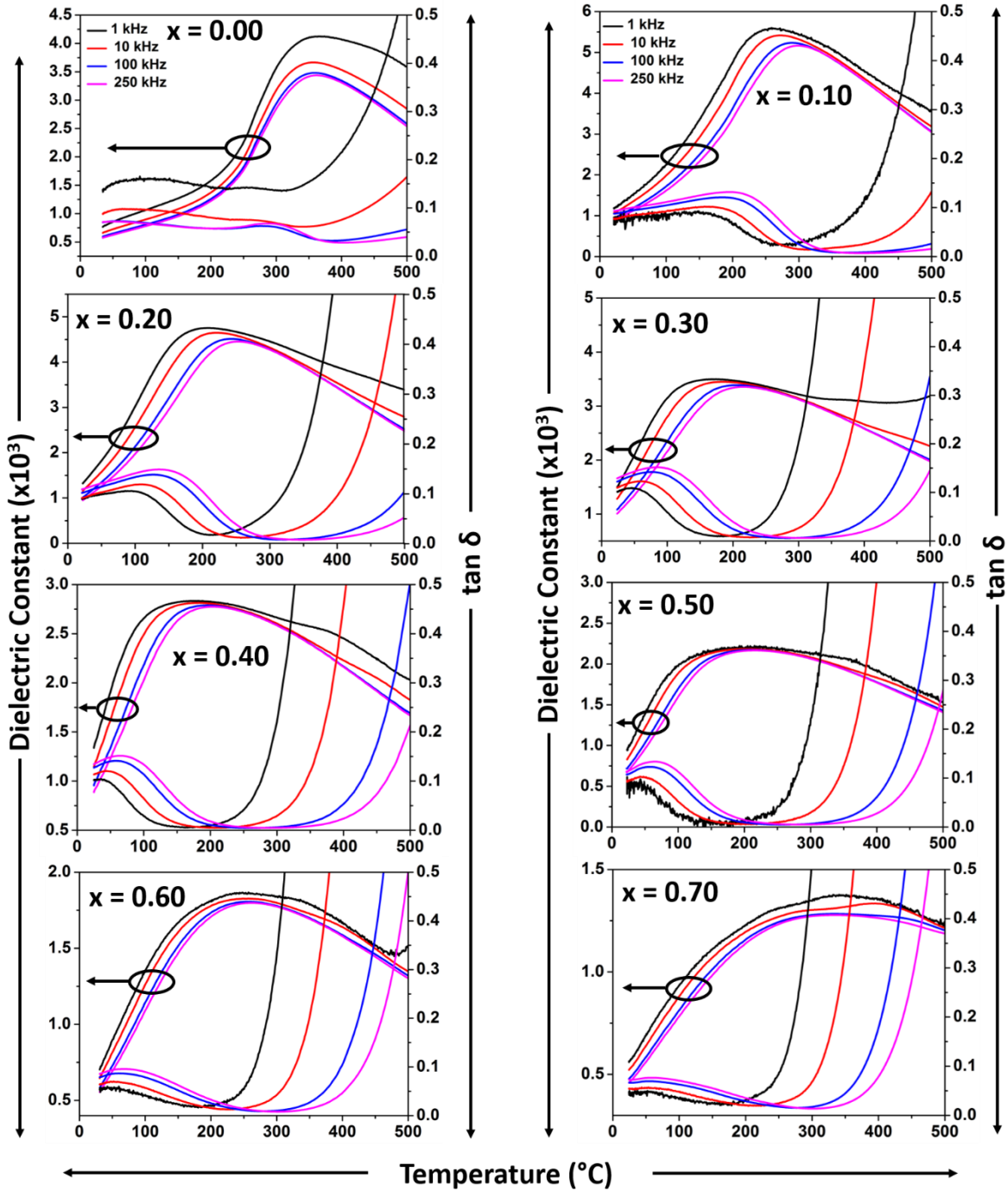

Figure 6.8: Dielectric constant and tan δ as a function of temperature for (1-*x*)KBT-*x*BLFT ceramics at fixed frequencies of 1, 10, 100 and 250 kHz.

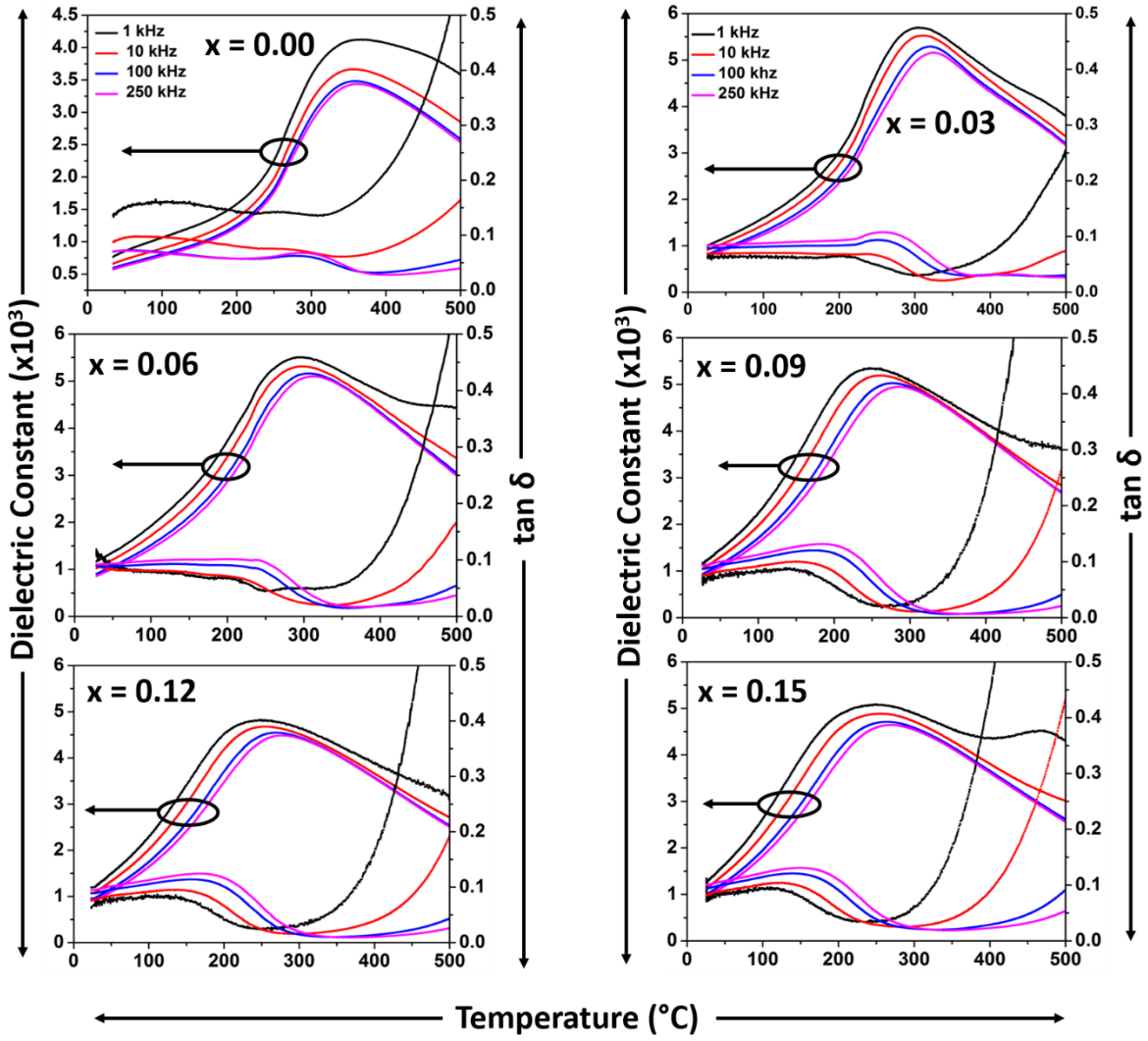

Figure 6.9: Dielectric constant and tan δ as a function of temperature for (1-*x*)KBT-*x*BNFT ceramics at fixed frequencies of 1, 10, 100 and 250 kHz.

6.5 Electromechanical Properties

6.5.1 Small signal response

Figure 6.10 shows d_{33} values as function of composition in the series (1-x)KBT-xBLFT and (1-x)KBT-xBNFT ($0 \leq x \leq 0.15$). All samples were poled at 5 kV/mm at a temperature of 100 °C. A maximum in d_{33} is observed at x = 0.04 for KBT-BLFT and at x = 0.03 for (1-x)KBT-xBNFT.

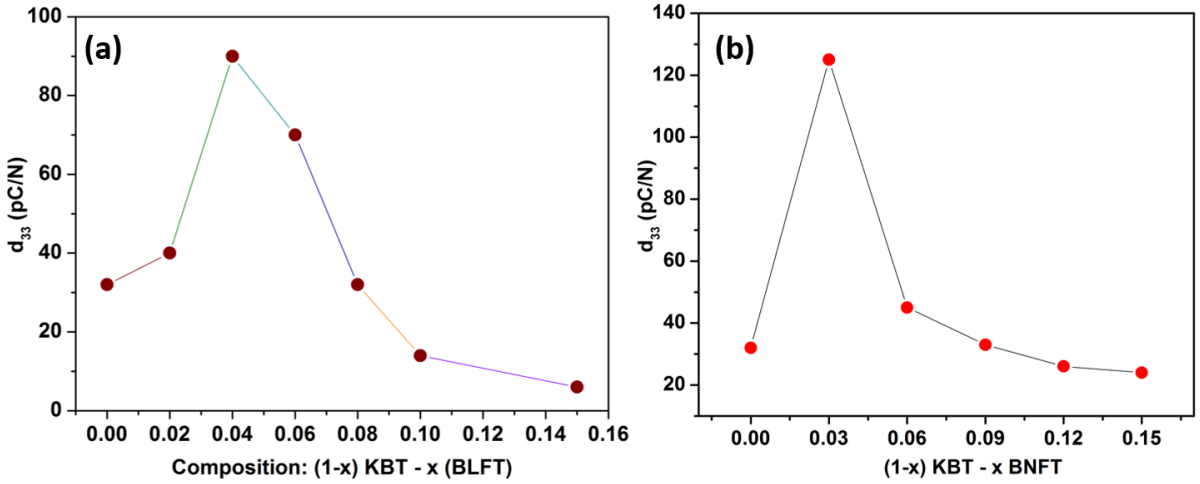

Figure 6.10: (a) d_{33} as a function of composition for (1-x)KBT-xBLFT ($0 \leq x \leq 0.15$); (b) d_{33} as a function of composition for (1-x)KBT-xBNFT ($0 \leq x \leq 0.15$)

The increase in d_{33} may result from compositional changes, but d_{33} as high as 120 pC/N is achieved in undoped KBT ceramics by improving densities [21]. It is proposed therefore, that d_{33} is primarily enhanced through improvement in densities compared to undoped KBT. Upon further increase in composition a drastic decrease in d_{33} is observed. The trend in d_{33} suggest that concentrations of BLFT/BNFT > 5 % are large enough to supress the formation of macro ferroelectric domains, resulting in polar nano/meso regions. At x > 0.15, d_{33} < 5 pC/N and below the detection limit of the equipment for x > 0.4.

6.5.2 Large signal response

Polarisation (P) and strain (S) vs. electric field (E) bipolar loops were measured up to 8 kV/mm at a frequency of 1 Hz. As an example, d^*_{33} as a function of electric field for the composition 0.9KBT-0.1BLFT is shown in Figure 6.11. No significant increase in d^*_{33} is observed at electric fields larger than 6 kV/mm. 6 kV/mm was therefore concluded to be the optimum driving field for ceramics in the series KBT-BLFT/BNFT. Figure 6.12 shows P and S vs. E bipolar loops at an electric field 6 kV/mm (1 Hz) for (1-x)KBT-xBLFT ceramics.

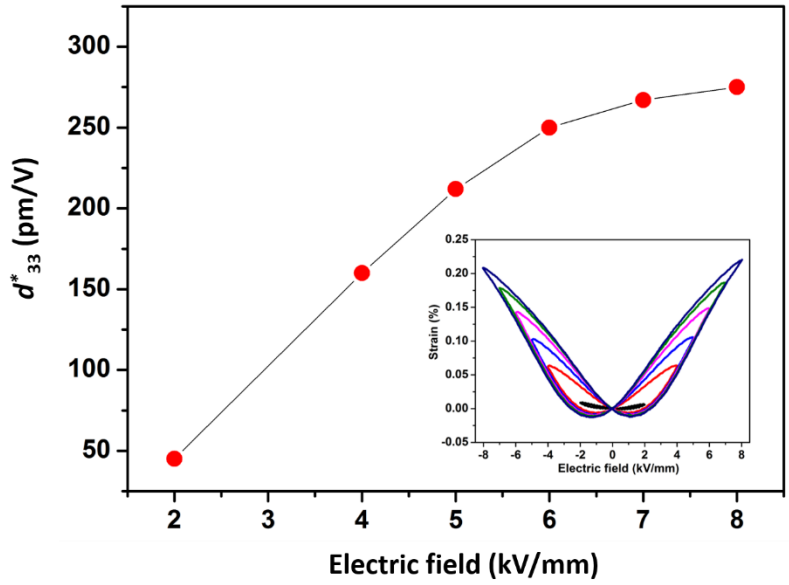

Figure 6.11: d^*_{33} as a function of electric field for 0.90KBT-0.1BLFT ceramics. Insets shows bipolar loops of 0.90KBT-0.1BLFT ceramics from which the d^*_{33} values are acquired.

The endmember (x = 0) exhibits leaky P-E loops consistent with the large tan δ values observed in dielectric data (Figure 6.8). However, for $x \geq 0.04$, ceramics are not leaky and can sustain large electric fields. Remanent polarisation (P_r) decreases from ~ 13.4 μC/cm^2 at x = 0.04 to ~ 1 μC/cm^2 at x = 0.40, hence slimmer loops are observed with increase in BLFT concentrations. Low P_r values are consistent with low d_{33} values observed for these ceramics. The decrease in P_r and hence hysteresis confirms the suppression of ferroelectric

order but the maximum polarisation (P_{max}) does not follow the same trend. P_{max} initially increases from ~ 24 μC/cm^2 at x = 0.04 to ~ 27 μC/cm^2 at x = 0.10 and then gradually decreases to ~ 23 μC/cm^2 at x = 0.20. A likely explanation is that although ferroelectric order is disrupted by BLFT, the application of an electric field induces long range polar order, thus maintaining a high P_{max} up to x = 0.20. However at composition x > 0.2, where P_r is lower than 2 μC/cm^2, the P_{max} drops significantly indicating that a dominant paraelectric phase assemblage for which the electric field is no longer able to induce long range ferroelectric order (P_r > 5 μC/cm^2).

The *S*-*E* loops correspond well with *P*-*E* loops. Typical butterfly loops are observed for ceramics at x = 0.04, exhibiting a negative strain of ~0.034 % consistent with the high P_r and d_{33} values observed for this composition. As BLFT concentration is increased, the negative strain decreases with an enhancement in the positive strain. Similar phenomenon have been observed in many other lead free ceramics [22-24], such as the $Bi_{1/2}Na_{1/2}TiO_3$-$Bi_{1/2}K_{1/2}TiO_3$–$K_{0.5}Na_{0.5}NbO_3$ system [24], where the addition of $K_{0.5}Na_{0.5}NbO_3$ is reported to disrupt the ferroelectric order with decrease in negative strain and enhancement of positive strain. The strains becomes more and more electrostrictive as x increases and an almost hysteresis free, pure electrostrictive strain is observed at x = 0.30. Electrostrictive strains in the poling direction can be related to maximum polarisation in the same direction using the equation given below [25].

$$\boldsymbol{S_3 = Q_{33} P_3^2} \qquad \text{Equation 6.1,}$$

Where Q_{33} is electrostrictive coefficient. S_3 and P_3 are the strain and polarisation in the direction of poling, respectively. Therefore, the highest polarisation corresponds to a maximum strain, which is observed here. In ceramics with x > 0.20, P_{max} decreases significantly and therefore the accompanied strains are commensurately lower. Ceramics in the (1-*x*)KBT-*x*BNFT series show a similar trend (Figure 6.13) to that observed in (1-*x*)KBT-*x*BLFT ceramics but KBT-BNFT ceramics are superior to the BLFT counterpart in maximum d_{33}^*, Figure 6.14. For actuators, compositions with highest d_{33}^* are considered as optimum and therefore, only 0.90KBT-0.10BLFT and 0.91KBT- 0.09BNFT, hereafter denoted by L10 and N9, respectively, are studied further.

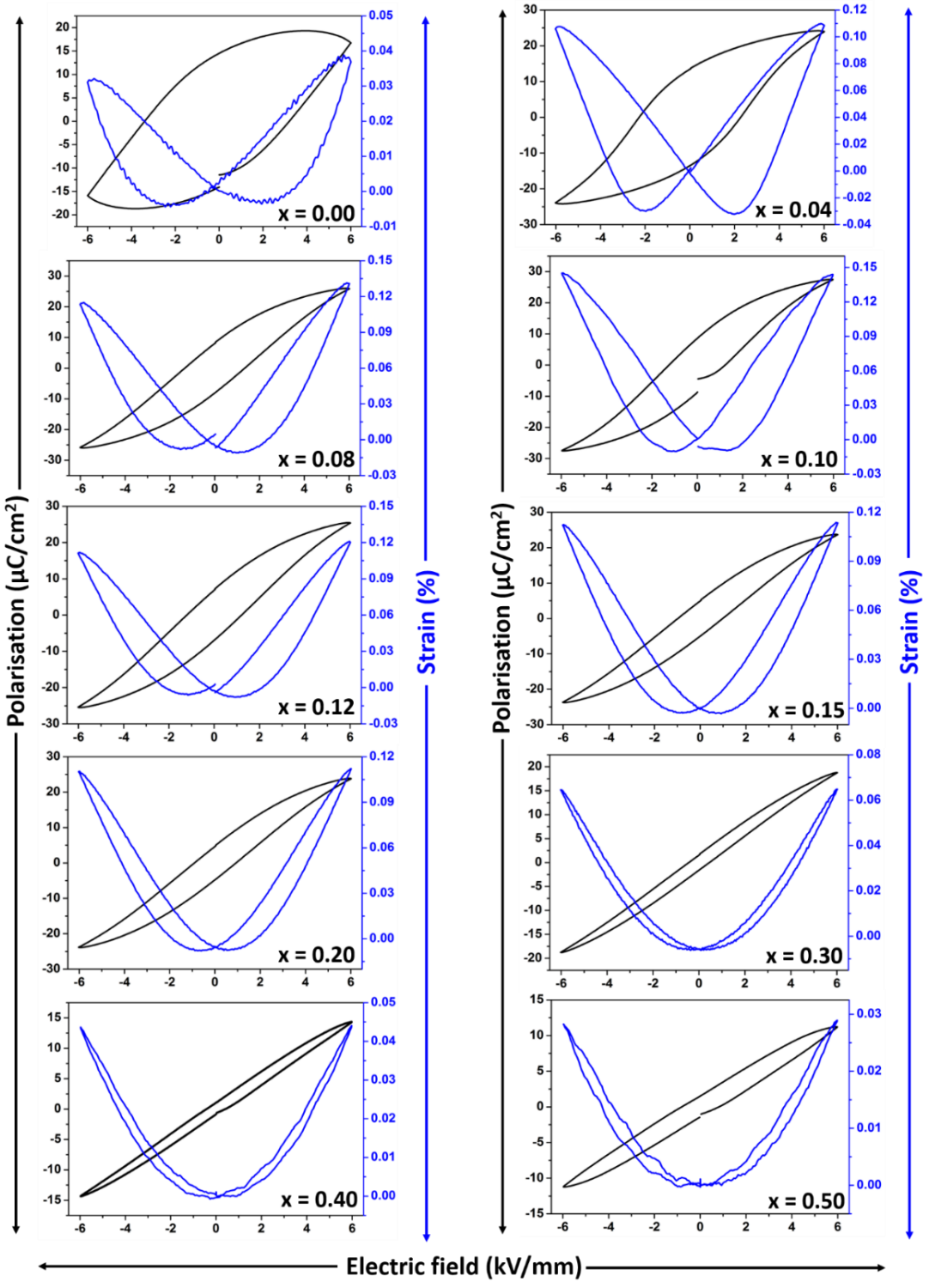

Figure 6.12: Polarisation and strain vs. electric filed for (1-*x*)KBT-*x*BLFT ($0 \leq x \leq 0.50$) ceramics at a frequency of 1 Hz

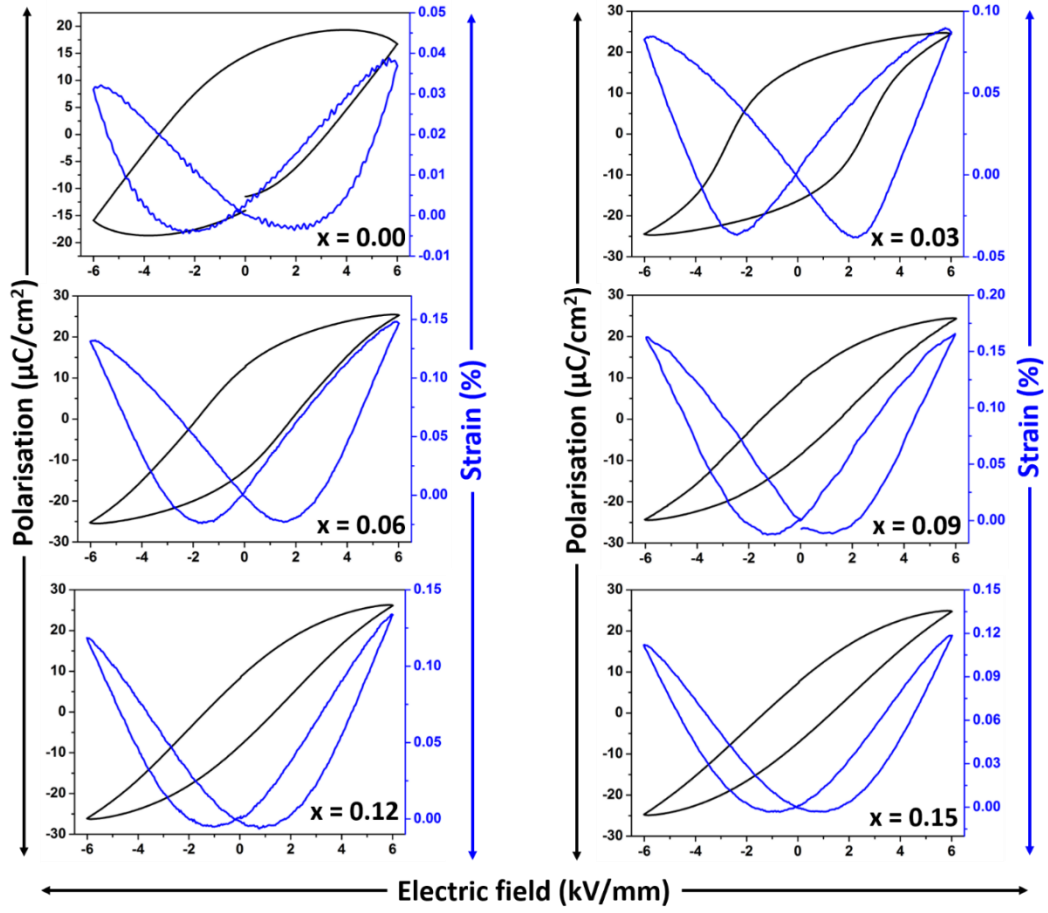

Figure 6.13: Polarisation and strain vs. electric filed for (1-*x*)KBT-*x*BNFT ($0 \leq x \leq 0.15$) ceramics at a frequency of 1 Hz

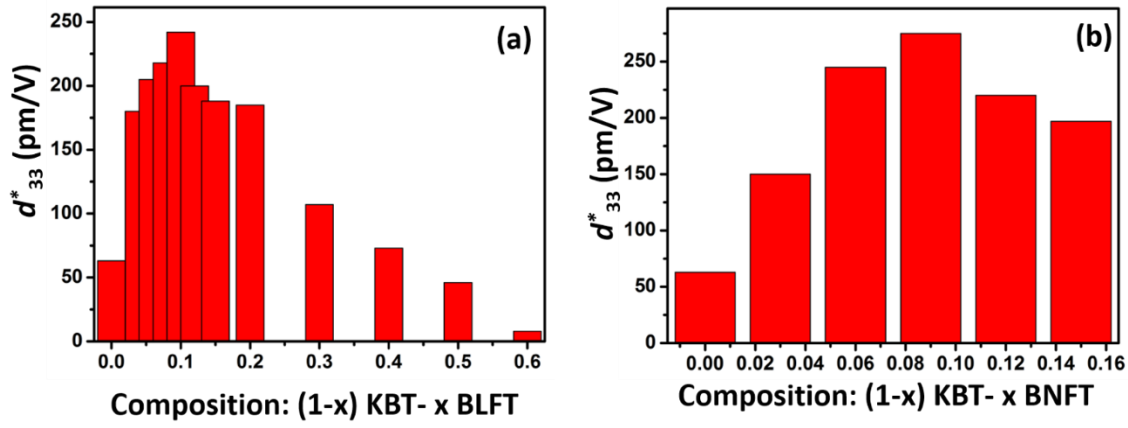

Figure 6.14: d^*_{33} as a function of composition for (a) (1-*x*)KB-*x*BLFT; (b) (1-*x*)KBT-*x* BNFT

Q_{33} values for L10 and N9 were calculated from slope of square of polarisation (P^2) vs. S (Figure 6.15) yielded values comparable to that of prototypical relaxor ferroelectric $Pb(Mg_{1/3}Nb_{2/3})O_3$ [26].

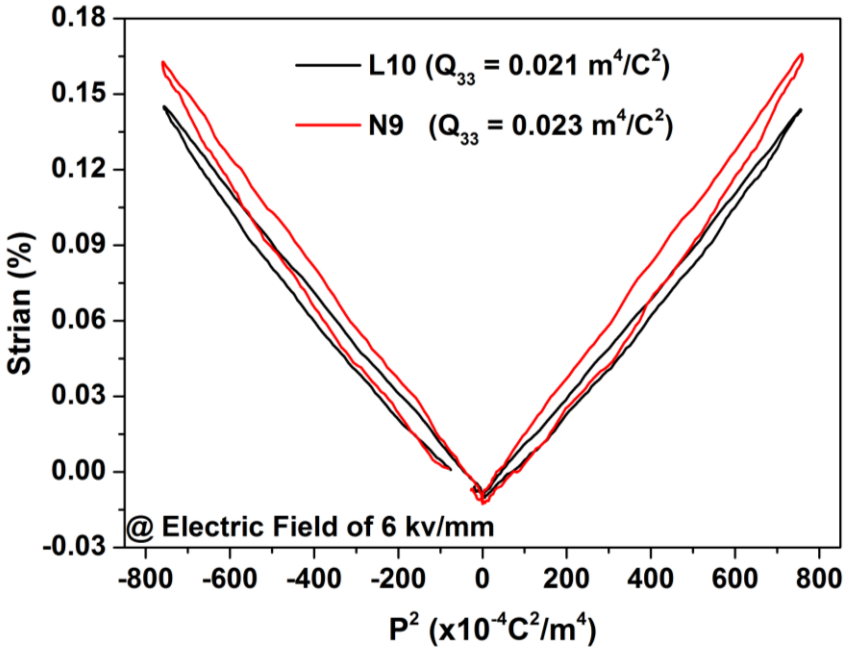

Figure 6.15: P^2 vs. S loops for L10 and N9 at an electric field of 6 kV/mm.

6.6 Impedance spectroscopy

To study the electrical microstructure, impedance spectroscopy was performed on samples of L10 and N9. Complex impedance (Z*) plots started to appear at temperature > 500 °C for these compositions. Both compositions showed a single semi-circle in Z* plot (Figure 6.16), which can be modelled by a single parallel resistance-capacitor (RC) element. The associated dielectric constant extracted from the arc is about 2271 and 2090 for L10 and N9 respectively, which is consistent with the permittivity values at fixed frequency (100 kHz) at comparable temperatures, (see Figure 6.8 and 6.9) and hence the arc is associated with a bulk response [27]. The peak in reactance (Z") and electric modulus (M") versus frequency plot (Figure 6.16) were also found to be coincident, which means that both bulk (grain) and grain boundary have similar time constants (τ = RC) and the samples are electrically homogenous.

Activation energies were calculated from Arrhenius plots of temperature dependence of the bulk conductivities shown in Figure 6.17 and were found to be > 1.2 eV for both samples. Resistivities of both the samples are of the order of 10^5 to 10^6 Ω.cm at temperatures between 500-600 °C. Though room temperature resistivities could not be measured, extrapolation of the high temperature data indicated resistivities of > 10^9 Ω.cm, ideal for actuator applications.

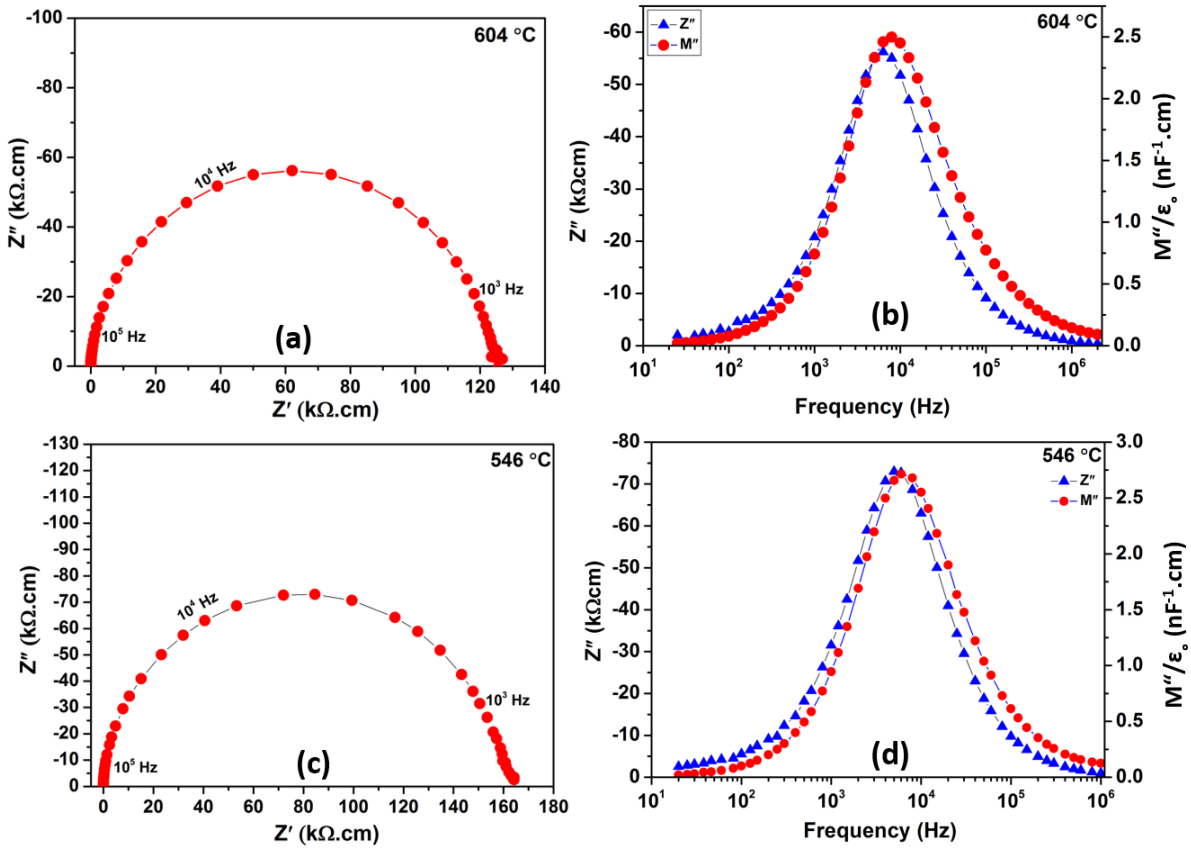

Figure 6.16: (a) complex impedance (Z*) spectroscopic plot for L10 at 604 °C; (b) combined Z" and M" spectroscopic plot for L10 at 604 °C; (c) complex impedance spectroscopic (Z*) plot for N9 at 546 °C; (d) combined Z" and M" spectroscopic plot for N9 at 546 °C.

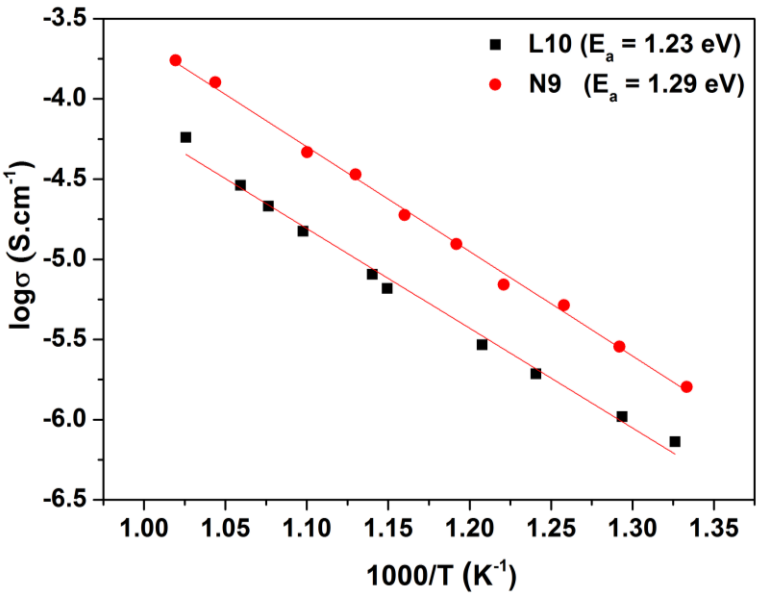

Figure 6.17: Arrhenius plots for L10 and N9.

6.7 Temperature stability of electromechanical strains

Real world applications demand materials that can perform at elevated temperatures. Therefore, the electromechanical strains achieved in L10 and N9 were studied as a function of temperature. Figure 6.18 shows *P-E* and *S-E* bipolar loops at selected temperatures for L10. As temperature increases, the P_r decreases with more than 60 % of the room temperature lost at 175 °C (Figure 6.19 (b)) resulting in very slim loops. However, the maximum polarisation remains almost temperature insensitive and < 10 % variation is observed from the value observed at RT (Figure 6.19 (b)). The strain is also broadly insensitive to temperature and only shows a variation of < 15 % between RT to 175 °C (Figure 6.19 (a)).

Figure 6.20 shows *P-E* and *S-E* bipolar loops at selected temperatures for N9. A similar behaviour to that of L10 is observed (Figure 6.21 (b)) but the temperature stability is slightly better with variation in strain < 10 % from room temperature to 175 °C. Here, it is important to mention that 175 °C is not the operating limit of the material but data could not be collected above 175 °C for bulk ceramics due to safety restrictions on the equipment used. The next chapter describes how multilayers are fabricated and how L10 and N9 sustain stable strains up to 300 °C.

A purely electrostrictive material does not show any hysteresis [28], and the strain output according to equation 6.1 depends on the electrostrictive coefficient (Q) and polarisation (P). The effect of temperature on Q is very low [26,29,30], therefore temperature dependence of polarisation affects the strain values, as observed in prominent lead-based relaxors [31,30]. For ferroelectrics, the operational range is practically limited by the Curie temperature (T_C). As a rule of thumb, operational range in PZT-based ferroelectrics is half of the T_C for the material [32].

L10 and N9 show relaxor-like behaviour but the strains are not purely electrostrictive like those observed in PMN-PT [28]. The room temperature *P-E* loops show remanence, a signature of ferroelectric order. As temperature increase, the ferroelectric order is destabilised as shown by large reduction in P_r and therefore almost hysteresis free loops are observed at 175 °C, similar to pure electrostrictors. However, there is minimal effect on maximum polarisation and strain. These ceramics do not show any anomaly in dielectric data (Figure 6.8 and 6.9) which can be associated with depolarisation temperature, a bottle neck for high temperature applications in NBT-based ceramics [33,34]. However, the ε_r for both compositions sharply increases with increase in temperature. For example, ε_r (1 kHz) of L10 increases from 1190 to 4020 when temperature is increased from RT to 175 °C. Since ε_r is essentially a measurement of polarisation, according to equation 6.1, the electrostrictive strain should increase with increase in temperature. On the other hand we see a drastic decrease (more than 60 %) in P_r (Figure 6.19) and therefore the contributions to strain values from the domain switching will be mostly lost at higher temperatures. This decrease in strain may be compensating the enhanced electrostrictive strain predicted by equation 6.1, thereby giving a temperature stable output. Above 175 °C, ε_r approaches a broad peak maximum, hence (< 10 % from 175-300 °C) explaining the temperature stability of electrostrictive strains at higher temperatures. The observations here are based on electrical properties and the exact nature of strain mechanism may be far more complex than this simplistic explanation, which warrants a detailed *in-situ* structural and microstructural study.

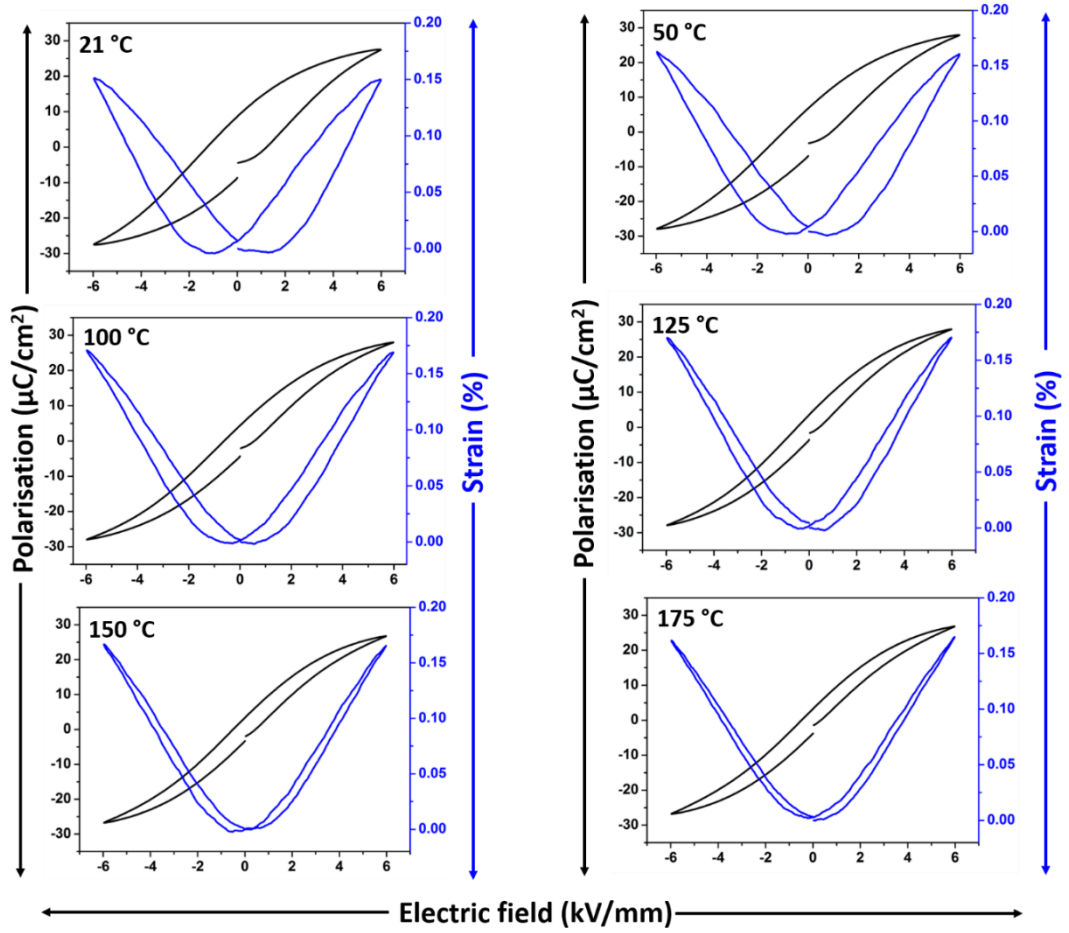

Figure 6.18: Polarisation and strain vs. electric field bipolar loops for composition L10 at different temperatures.

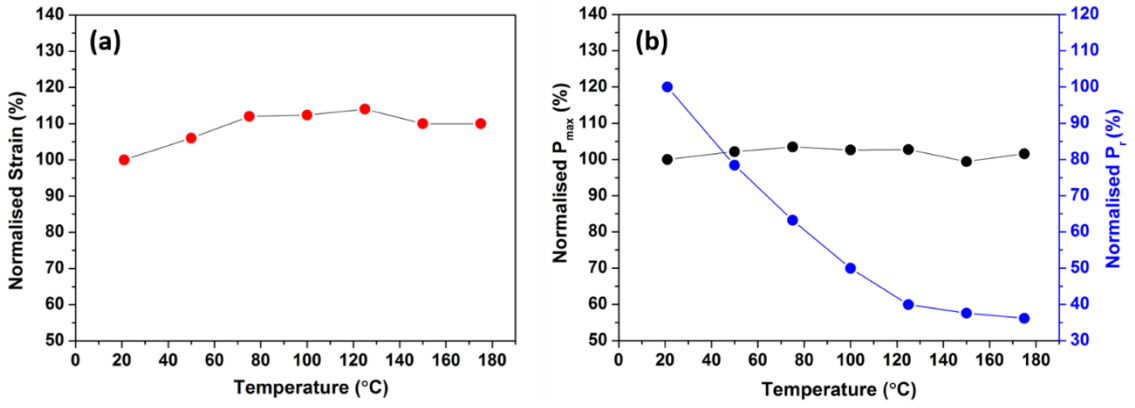

Figure 6.19: (a) Normalised strain as a function of temperature for composition L10; (b) Normalised maximum and remanent polarisation as a function of temperature for composition L10.

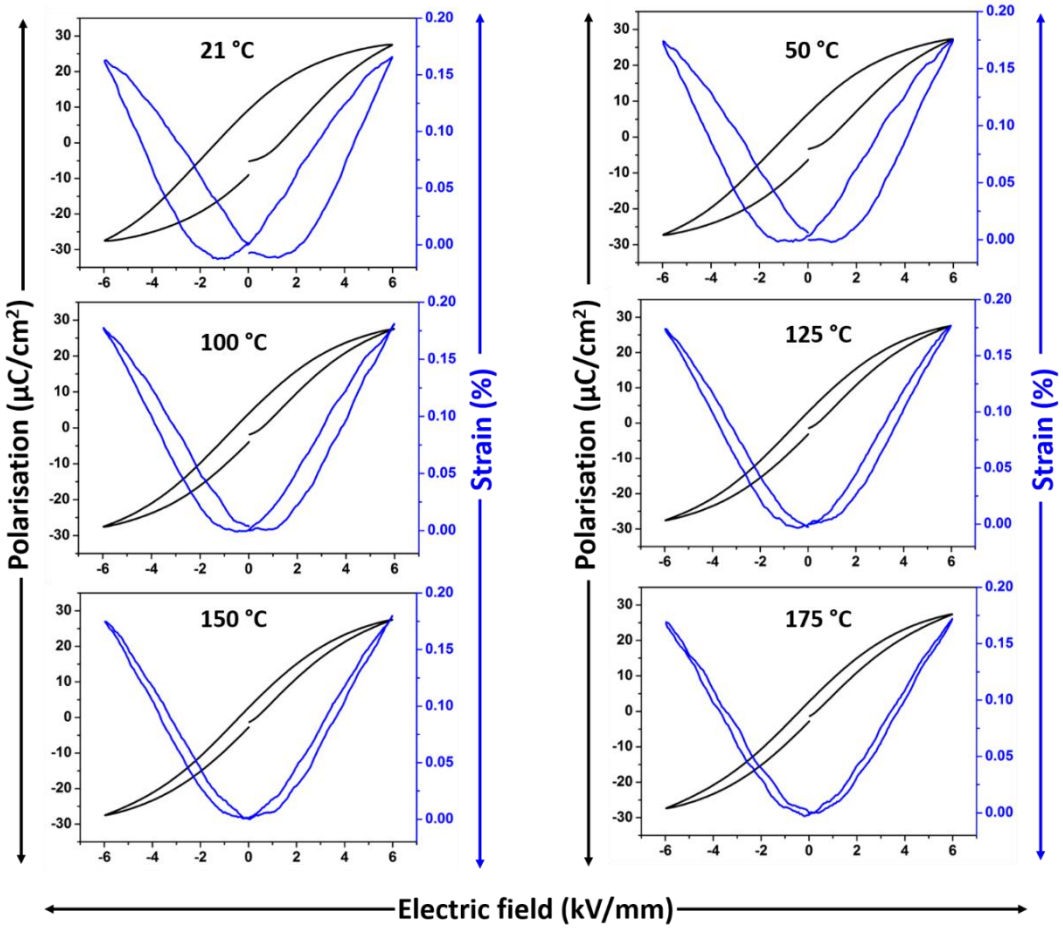

Figure 6.20: Polarisation and strain vs electric field bipolar loops for composition N9 at different temperatures.

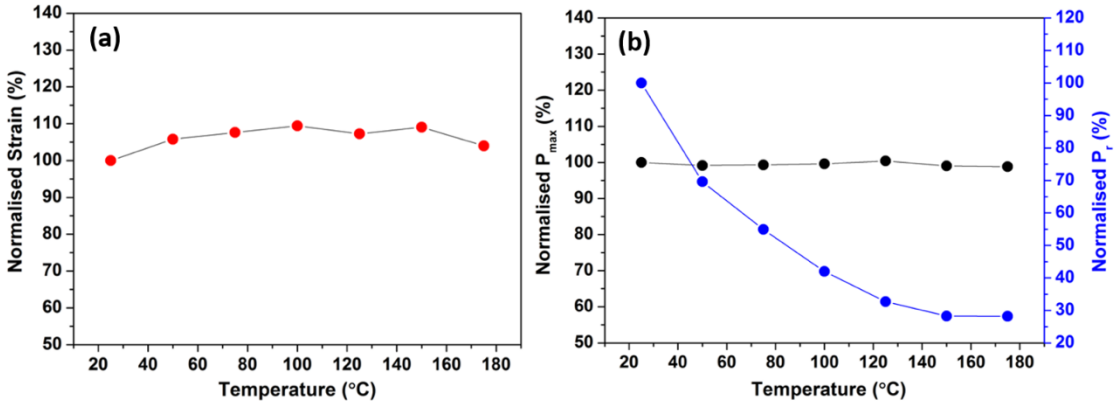

Figure 6.21: (a) Normalised strain as a function of temperature for composition N9; (b) Normalised maximum and remanent polarisation as a function of temperature for composition N9.

6.8 Electrical Fatigue

Electrical fatigue refers to degradation of switchable polarisation and maximum strain, when a material is exposed to repetitive electrical loadings. Fatigue behaviour depends on the type of applied electric field. Therefore, different loadings such as unipolar, sesquipolar and bipolar will result in different levels of fatigue [35]. Actuators are usually operated under unipolar field but certain parts of the device may encounter mixed electrical loading [36]. Bipolar loading results in more severe fatigue as compared to unipolar loading as shown by many studies on PZT-based ceramics [37-39]. Therefore, actuators cycling under bipolar loading may be considered as an accelerated fatigue test [40].

Various fatigue mechanism such as pinning of domains due to point defects [41], screening of electric field due to formation of a damaged layer beneath the electrode [42] and formation of microscopic cracks [43][44] have been discussed in literature to explain the fatigue behaviour due to bipolar loading. Electric cycling can result in significant degradation of both strain and polarisation, as shown in Figure 6.22 for PZT-based ferroelectric materials with the composition $Pb_{0.99}La_{0.01}(Zr_{0.525}Ti_{0.475})O_3$ [42].

Figure 1 (a and b) in reference [42]

Figure 6.22: Polarisation and strain vs. electric field curves for $Pb_{0.99}La_{0.01}(Zr_{0.525}Ti_{0.475})O_3$ bulk ceramics at cycle no. 1, 3×10^4 and 3.2×10^5 [42]

Studies on lead-free ceramics have also revealed that certain promising materials such as $0.94Bi_{1/2}Na_{1/2}TiO_3–0.06BaTiO_3$ show severe degradation in properties when exposed to repetitive electrical cycling [45]. Long term reliability is an important factor that can limit applicability of a material in actuators despite attractive strain values. Therefore, both L10 and N9 were exposed to bipolar loading of 5 kV/mm (5 Hz) for 1 million cycles to assess long term reliability of these ceramics. 5 kV/mm is about three time the coercive field of these ceramics. Figure 6.23 (a) shows normalised values of polarisation and strain as a function of bipolar cycles. Both polarisation and strain shows minimal degradation with

values less than 4 % and 5 % respectively. Figure 6.23 (b) shows comparison of bipolar *S-E* loops between the 1st and millionth cycle. The maximum strain value has decreased by < 5 % and no asymmetry in the loop is observed indicating fatigue resistant behaviour for these ceramics. Figure 6.24 shows (a) normalised polarisation and strain values as a function bipolar cycles (b) comparison between the 1st and millionth cycle for N9, which exhibits similar fatigue resistant to that of L10.

Studies on electrostrictive materials such as La doped $Pb(Zr,Ti)O_3$ [46,47] and in the system $B_{1/2}Na_{1/2}TiO_3$-$K_{1/2}Bi_{1/2}TiO_3$-$K_{0.5}Na_{0.5}NbO_3$ [48] have shown superior fatigue resistant behaviour in comparison to their ferroelectric counterparts. Therefore, the predominantly electrostrictive nature of L10 and N9 contributes to the observed fatigue resistant behaviour. Moreover point defects, especially oxygen vacancies, are known to have a bad influence on fatigue resistance [49,50]. Both L10 and N9 show high resistivities (section 6.6) which can be associated with low defect concentration and therefore a superior fatigue resistant response [51].

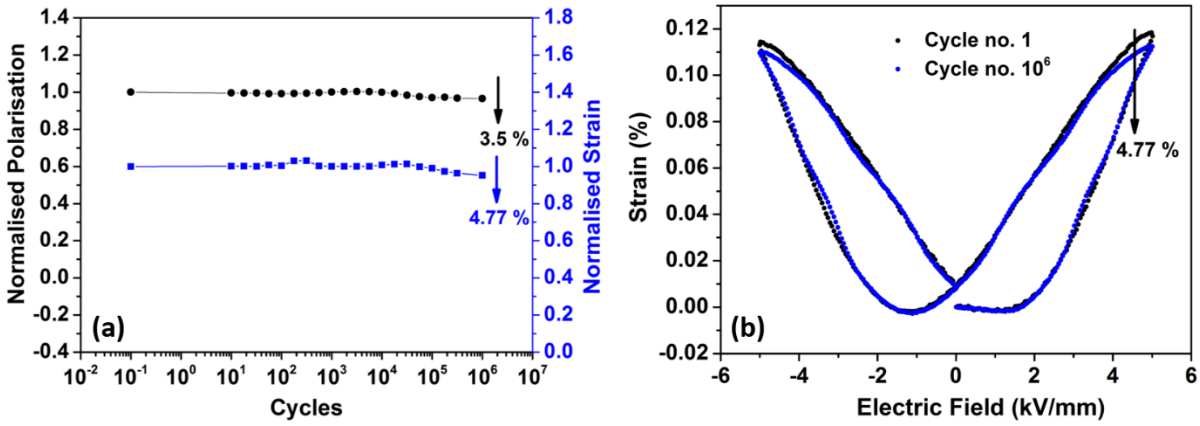

Figure 6.23: (a) Polarisation and strain for L10 ceramics as a function of switching cycle; (b) *S-E* loops for L10 ceramics at 1st and millionth cycle at 10 Hz

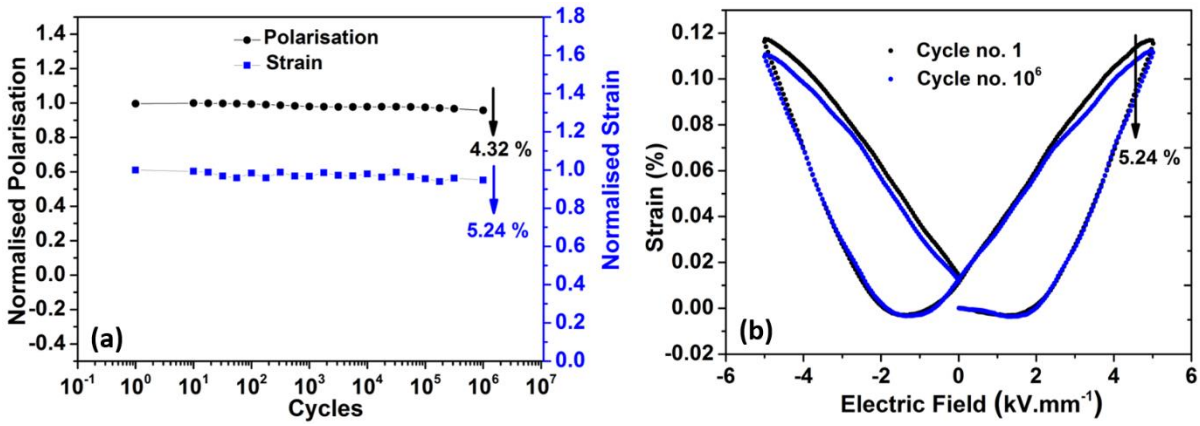

Figure 6.24: (a) Polarisation and strain for bulk N9 ceramics as a function of switching cycle; (b) *S*-*E* loops for N9 bulk ceramics at 1st and millionth cycle at 10 Hz

6.9 Conclusions

Ceramics in the systems (1-*x*)KBT-*x*BLFT ($0 \leq x \leq 0.70$) were fabricated using conventional solid state synthesis route. With increase in *x*, the structure transforms from tetragonal to pseudocubic at $x \geq 0.04$. A maximum d_{33} of 90 pC/N was observed at $x = 0.04$. Upon further increase in BLFT concentration, relaxor-like behaviour is promoted and a decrease in d_{33} and P_r is observed. The positive strain increases with increase in *x* and reaches a maximum at $x = 0.10$ with a value of 0.15 % at 6 kV/mm and then decreases with further increase in *x*. However there are no abrupt increases/decreases in strain as a function of *x* and the changes are gradual. It is proposed that the transition from a tetragonal to a paraelectric cubic phase is also gradual through an intermediate pseudocubic phase which may be polymorphic similar to the high temperature phase in KBT, i.e. a combination of diminishing tetragonal domains and cubic regions with no domains, with non-polar cubic phase dominating at higher concentration of *x*. The key finding of the study was that the maximum strain values achieved were broadly insensitive to temperature and vary <15 % from RT-175 °C. The same composition was also fatigue resistant with degradation of < 5 % after one million bipolar cycles at of 5 kV/mm (~3 E_C). Temperature stable and fatigue resistant properties of these ceramics make them an attractive lead-free material for actuator applications operating in harsh environments. To study the effect of a different rare earth the system, (1-*x*)KBT-*x*BNFT ($0 \leq x \leq 0.15$) was

also investigated which revealed similar trends but marginally superior properties to its BLFT counterpart. A maximum strain of 0.16 % (6 kV/mm) was observed at x = 0.09, which was also temperature stable and fatigue resistant. Based on these observations we expect that the system (1-x)KBT- x($BiFeO_3$-$REFeO_3$-$RE_{2/3}TiO_3$) with RE = Ce, Pr and Sm may also produce appreciable electrostrictive strains in the vicinity of x = 0.10, assuming a similar RE content in the BREFT endmember.

6.10 References

[1] Y. Hiruma, A. Rintaro, H. Nagata, and T. Takenaka, "Ferroelectric and Piezoelectric Properties of $(Bi_{1/2}K_{1/2})TiO_3$ Ceramics," *Jpn. J. Appl. Phys.*, vol. 44, no. 7A, pp. 5040–5044, 2005.

[2] M. I. Morozov, M.-A. Einarsrud, and T. Grande, "Polarization and strain response in $Bi_{0.5}K_{0.5}TiO_3$-$BiFeO_3$ ceramics," *Appl. Phys. Lett.*, vol. 101, no. 25, p. 252904, 2012.

[3] A. Zeb and S. J. Milne, "Large Electromechanical Strain in Lead-Free Binary System $K_{0.5}Bi_{0.5}TiO_3$- $Bi(Mg_{0.5}Ti_{0.5})O_3$," *J. Am. Ceram. Soc.*, vol. 97, no. 8, pp. 2413–2415, 2014.

[4] Z. Pan, Q. Wang, J. Chen, C. Liu, L. Fan, L. Liu, L. Fang, and X. Xing, "Enhanced Piezoelectric Properties of Tetragonal $(Bi_{1/2}K_{1/2})TiO_3$ Lead-Free Ceramics by Substitution of Pure Bi-Based $Bi(Mg_{2/3}Nb_{1/3})O_3$," *J. Am. Ceram. Soc.*, vol. 98, no. 1, pp. 104–108, 2015.

[5] V. V Ivanova, A. G. Kapyshev, Y. N. Venevtsev, and G. S. Zhdanov, "X-ray determination of the symmetry of elementary cells of the ferroelectric materials $(K_{0.5}Bi_{0.5})TiO_3$ and $(Na_{0.5}Bi_{0.5})TiO_3$ and of high-temperature phase transitions in $(K_{0.5}Bi_{0.5})TiO_3$," *Izv. Akad. Nauk SSSR*, vol. 26, pp. 354–356, 1962.

[6] M. Otoničar, S. D. Škapin, B. Jančar, R. Ubic, and D. Suvorov, "Analysis of the Phase Transition and the Domain Structure in $K_{0.5}Bi_{0.5}TiO_3$ Perovskite Ceramics by In Situ XRD and TEM," *J. Am. Ceram. Soc.*, vol. 93, no. 12, pp. 4168–4173, 2010.

[7] H. Matsuo, Y. Noguchi, M. Miyayama, M. Suzuki, A. Watanabe, S. Sasabe, T. Ozaki, S. Mori, S. Torii, and T. Kamiyama, "Structural and piezoelectric properties of high-density $Bi_{0.5}K_{0.5}TiO_3$–$BiFeO_3$ ceramics," *J. Appl. Phys.*, vol. 108, no. 10, p. 104103, 2010.

[8] T. Ozaki, H. Matsuo, Y. Noguchi, M. Miyayama, and S. Mori, "Microstructures Related to Ferroelectric Properties in $(Bi_{0.5}K_{0.5})TiO_3$ –$BiFeO_3$," *Jpn. J. Appl. Phys.*, vol. 49, no. 9, p. 09MC05, 2010.

[9] S. Karimi, I. M. Reaney, I. Levin, and I. Sterianou, "Nd-doped $BiFeO_3$ ceramics with antipolar order," *Appl. Phys. Lett.*, vol. 94, p. 112903, 2009.

[10] A. Khesro, R. Boston, I. Sterianou, D. C. Sinclair, and I. M. Reaney, "Phase transitions , domain structure, and pseudosymmetry in La- and Ti-doped $BiFeO_3$.," *J. Appl. Phys.*, vol. 119, no. 5, p. 054101, 2016.

[11] S. Karimi, I. M. Reaney, Y. Han, J. Pokorny, and I. Sterianou, "Crystal chemistry and domain structure of rare-earth doped $BiFeO_3$ ceramics," *J. Mater. Sci.*, vol. 44, no. 19, pp. 5102–5112, 2009.

[12] J. Kriesel, A. M. Glazer, G. Jones, P. A. Thomas, L. Abello, and G. Lucazeau, "An x-ray diffraction and Raman spectroscopy investigation of A-site substituted perovskite compounds: the $(Na_{1-x}K_x)_{0.5}Bi_{0.5}TiO_3$ ($0 \leq x \leq 1$) solid solution," *J. Phys. Condens.*

Matter, vol. 12, pp. 3267–3280, 2000.

[13] E. A. Patterson, D. P. Cann, J. Pokorny, and I. M. Reaney, "Electromechanical strain in $Bi(Zn_{1/2}Ti_{1/2})O_3$–$(Bi_{1/2}Na_{1/2})TiO_3$–$(Bi_{1/2}K_{1/2})TiO_3$ solid solutions," *J. Appl. Phys.*, vol. 111, no. 9, p. 094105, 2012.

[14] J. Yang, Y. Hou, C. Wang, M. Zhu, and H. Yan, "Relaxor behavior of $(K_{0.5}Bi_{0.5})TiO_3$ ceramics derived from molten salt synthesized single-crystalline nanowires," *Appl. Phys. Lett.*, vol. 91, no. 2, p. 23118, 2007.

[15] Z. F. Li, C. L. Wang, W. L. Zhong, J. C. Li, and M. L. Zhao, "Dielectric relaxor properties of $K_{0.5}Bi_{0.5}TiO_3$ ferroelectrics prepared by sol–gel method," *J. Appl. Phys.*, vol. 94, no. 4, p. 2548, 2003.

[16] B. Hu, M. Zhu, J. Guo, Y. Wang, M. Zheng, and Y. Hou, "Origin of Relaxor Behavior in $K_{1/2}Bi_{1/2}TiO_3$-$Bi(Mg_{1/2}Ti_{1/2})O_3$ Investigated by Electrical Impedance Spectroscopy," *J. Am. Ceram. Soc.*, vol. 99, no. 5, pp. 1637-1644, 2016.

[17] C. Kruea-In, G. Rujijanagul, F. Y. Zhu, and S. J. Milne, "Relaxor behaviour of $K_{0.5}Bi_{0.5}TiO_3$-$BiScO_3$ ceramics," *Appl. Phys. Lett.*, vol. 100, no. 20, p. 202904, 2012.

[18] W. Zeng, X. Zhou, J. Chen, J. Liao, C. Zhou, Z. Cen, T. Yang, H. Yang, Q. Zhou, G. Chen, and C. Yuan, "Origin of high piezoelectric activity in perovskite ferroelectric ceramics," *Appl. Phys. Lett.*, vol. 104, no. 24, p. 242910, 2014.

[19] C. Ma, X. Tan, E. Dul'Kin, and M. Roth, "Domain structure-dielectric property relationship in lead-free (1-x) $(Bi_{1/2}Na_{1/2})TiO_3$- $xBaTiO_3$ ceramics," *J. Appl. Phys.*, vol. 108, no. 10, p. 104105, 2010.

[20] L. A. Schmitt, K. A. Schönau, R. Theissmann, H. Fuess, H. Kungl, and J. Michael, "Composition dependence of the domain configuration and size in $Pb(Zr_{1-x}Ti_x)O_3$ ceramics" *J. Appl. Phys.*, vol. 101, no. 7, p. 074107, 2007.

[21] J. König and D. Suvorov, "Evolution of the electrical properties of $K_{0.5}Bi_{0.5}TiO_3$ as a result of prolonged sintering," *J. Eur. Ceram. Soc.*, vol. 35, no. 10, pp. 2791–2799, 2015.

[22] V. D. N. Tran, T. H. Dinh, H. S. Han, W. Jo, and J. S. Lee, "Lead-free $Bi_{1/2}(Na_{0.82}K_{0.18})_{1/2}TiO_3$ relaxor ferroelectrics with temperature insensitive electrostrictive coefficient," *Ceram. Int.*, vol. 39, pp. S119–S124, 2013.

[23] J. Hao, Z. Xu, R. Chu, W. Li, and P. Fu, "Good temperature stability and fatigue-free behavior in Sm_2O_3-modified $0.948(K_{0.5}Na_{0.5})NbO_3$–$0.052LiSbO_3$ lead-free piezoelectric ceramics," *Mater. Res. Bull.*, vol. 65, pp. 94–102, 2015.

[24] K. T. P. Seifert, W. Jo, and J. Rödel, "Temperature-Insensitive Large Strain of $(Bi_{1/2}Na_{1/2})TiO_3$ -$(Bi_{1/2}K_{1/2})TiO_3$-$(K_{0.5}Na_{0.5})NbO_3$ Lead-Free Piezoceramics," *J. Am. Ceram. Soc.*, vol. 93, no. 5, pp. 1392–1396, 2010.

[25] S.-T. Zhang, A. B. Kounga, W. Jo, C. Jamin, K. Seifert, T. Granzow, J. Rödel, and D. Damjanovic, "High-strain lead-free antiferroelectric electrostrictors," *Adv. Mater.*, vol. 21, no. 46, pp. 4716–4720, 2009.

[26] J. Kuwata, K. Uchino, and S. Nomura, "Electrostrictive coefficients of Pb $(Mg_{1/3}Nb_{2/3})O_3$ ceramics," *Jpn. J. Appl. Phys.*, vol. 19, no. 11, pp. 2099–2103, 1980.

[27] J. T. S. Irvine, D. C. Sinclair, and A. R. West, "Electroceramics: characterization by impedance spectroscopy," *Adv. Mater.*, vol. 2, no. 3, pp. 132–138, 1990.

[28] J. Zhao, Q. M. Zhang, N. Kim, and T. Shrout, "Electromechanical Properties of Relaxor Ferroelectric Lead Magnesium Niobate—Lead Titanate Ceramics," *Jpn. J. Appl. Phys.*, vol. 34, pp. 5658–5663, 1995.

[29] F. Li, L. Jin, Z. Xu, D. Wang, and S. Zhang, "Electrostrictive effect in $Pb(Mg_{1/3}Nb_{2/3})O_3$-$xPbTiO_3$ crystals," *Appl. Phys. Lett.*, vol. 102, no. 2013, p. 152910, 2013.

[30] K. Uchino, S. Nomura, L. E. Cross, S. J. Jang, and R. E. Newnham, "Electrostrictive Effect in Lead Magnesium Niobate Single Crystals.," *J. Appl. Phys.*, vol. 51, no. 2, pp. 1142–1145, 1979.

[31] K. Uchino, *Piezoelectric Actuators and Ultrasonic Motors*. Springer US, 1997.

[32] J. Holterman and P. Groen, *An Introduction to Piezoelectric Materials and Applications*. Stiching Applied Piezo, 2013.

[33] M. Acosta, W. Jo, and J. Rödel, "Temperature- and frequency-dependent properties of the $0.75Bi_{1/2}Na_{1/2}TiO_3$-$0.25SrTiO_3$ lead-free incipient piezoceramic," *J. Am. Ceram. Soc.*, vol. 97, no. 6, pp. 1937–1943, 2014.

[34] S.-T. Zhang, A. B. Kounga, E. Aulbach, W. Jo, T. Granzow, H. Ehrenberg, and J. Rödel, "Lead-free piezoceramics with giant strain in the system $Bi_{0.5}Na_{0.5}TiO_3$–$BaTiO_3$–$K_{0.5}Na_{0.5}NbO_3$. II. Temperature dependent properties," *J. Appl. Phys.*, vol. 103, no. 3, p. 34107, 2008.

[35] D. C. Lupascu and J. Rödel, "Fatigue in bulk lead zirconate titanate actuator materials," *Adv. Eng. Mater.*, vol. 7, no. 10, pp. 882–898, 2005.

[36] J. Nuffer, D. C. Lupascu, and J. Rödel, "Damage evolution in ferroelectric PZT induced by bipolar electric cycling," *Acta Mater.*, vol. 48, no. 14, pp. 3783–3794, 2000.

[37] D. C. Lupascu, E. Aulbach, J. Rödel, and J. Rödel, "Mixed electromechanical fatigue in lead zirconate titanate," *J. Appl. Phys.*, vol. 93, no. 9, p. 5551, 2003.

[38] N. Balke, D. C. Lupascu, T. Granzow, and J. Rödel, "Fatigue of lead zirconate titanate ceramics. I: Unipolar and DC loading," *J. Am. Ceram. Soc.*, vol. 90, no. 4, pp. 1081–1087, 2007.

[39] C. Verdier, D. C. Lupascu, and J. Rödel, "Stability of defects in lead-zirconate-titanate

after unipolar fatigue," *Appl. Phys. Lett.*, vol. 81, no. 14, pp. 2596–2598, 2002.

[40] J. Nuffer, D. C. Lupascu, A. Glazounov, H. J. Kleebe, and J. Rödel, "Microstructural modifications of ferroelectric lead zirconate titanate ceramics due to bipolar electric fatigue," *J. Eur. Ceram. Soc.*, vol. 22, no. 13, pp. 2133–2142, 2002.

[41] V. Y. Shur, E. L. Rumyantsev, E. V. Nikolaeva, and E. I. Shishkin, "Formation and evolution of charged domain walls in congruent lithium niobate," *Appl. Phys. Lett.*, vol. 77, no. 22, pp. 3636–3638, 2000.

[42] N. Balke, H. Kungl, T. Granzow, D. C. Lupascu, M. J. Hoffmann, and J. Rödel, "Bipolar fatigue caused by field screening in $Pb(Zr,Ti)O_3$ ceramics," *J. Am. Ceram. Soc.*, vol. 90, no. 12, pp. 3869–3874, 2007.

[43] E. C. Subbarao, V. Srikanth, W. Cao, and L. E. Cross, "Domain switching and microcracking during poling of lead zirconate titanate ceramics," *Ferroelectrics*, vol. 145, no. 1, pp. 271–281, 1993.

[44] Q. Jiang, W. Cao, and L. E. Cross, "Electric fatigue in lead zirconate titanate ceramics," *J. Am. Ceram. Soc.*, vol. 77, no. 1, pp. 211–215, 1994.

[45] Z. Luo, J. Glaum, T. Granzow, W. Jo, R. Dittmer, M. Hoffman, and J. Rödel, "Bipolar and unipolar fatigue of ferroelectric BNT-based lead-free piezoceramics," *J. Am. Ceram. Soc.*, vol. 94, no. 2, pp. 529–535, 2011.

[46] D. E. Dausch, "Ferroelectric Polarization Fatigue in PZT-Based RAINBOWs and Bulk Ceramics," *J. Am. Ceram. Soc.*, vol. 60, pp. 2355–2360, 1997.

[47] W. Pan, C. F. Yue, and O. Tosyali, "Fatigue of ferroelectric polarization and the electric field induced strain in lead lanthanum zirconate titanate ceramics," *J. Am. Ceram. Soc.*, vol. 75, no. 196418, pp. 1534–1540, 1992.

[48] J. Hao, Z. Xu, R. Chu, W. Li, and J. Du, "Lead-free electrostrictive $(Bi_{0.5}Na_{0.5})TiO_3$–$(Bi_{0.5}K_{0.5})TiO_3$–$(K_{0.5}Na_{0.5})NbO_3$ ceramics with good thermostability and fatigue-free behavior," *J. Mater. Sci.*, vol. 50, no. 15, pp. 5328–5336, 2015.

[49] C. Park and D. Chadi, "Microscopic study of oxygen-vacancy defects in ferroelectric perovskites," *Phys. Rev. B*, vol. 57, no. 22, pp. R13961–R13964, 1998.

[50] L. He and D. Vanderbilt, "First-principles study of oxygen-vacancy pinning of domain walls in $PbTiO_3$ Lixin," *Phys. Rev. B*, vol. 68, no. 14, p. 134103, 2003.

[51] N. Kumar and D. P. Cann, "Electromechanical strain and bipolar fatigue in $Bi(Mg_{1/2}Ti_{1/2})O_3$-$(Bi_{1/2}K_{1/2})TiO_3$-$(Bi_{1/2}Na_{1/2})TiO_3$ ceramics," *J. Appl. Phys.*, vol. 114, no. 5, p. 054102 , 2013.

Chapter 7: Multilayer Actuator based on composition N9

7.1 Introduction

Generally, ceramic materials are capable only to produce a strain of about ~ 0.1 % at electric fields of ~ 2 kV/mm [1]. Several thousands of volts are therefore required to achieve any useful displacements. In most cases, it is not feasible to operate actuators by applying such high voltages. To mitigate the problem thin layers are fabricated to reduce the operating voltages. However reducing the thickness decreases the total amount of displacement and hence to achieve an appreciable displacement, the thin layers are structured into a multilayer, with each layer electroded individually. A schematic is shown in Figure 7.1, illustrating that a multilayer actuator (MLA) of n layers and thickness (t) will require a driving voltage of V/n to attain the same magnitude of strain achieved by a monolithic component of same thickness at a driving voltage of V.

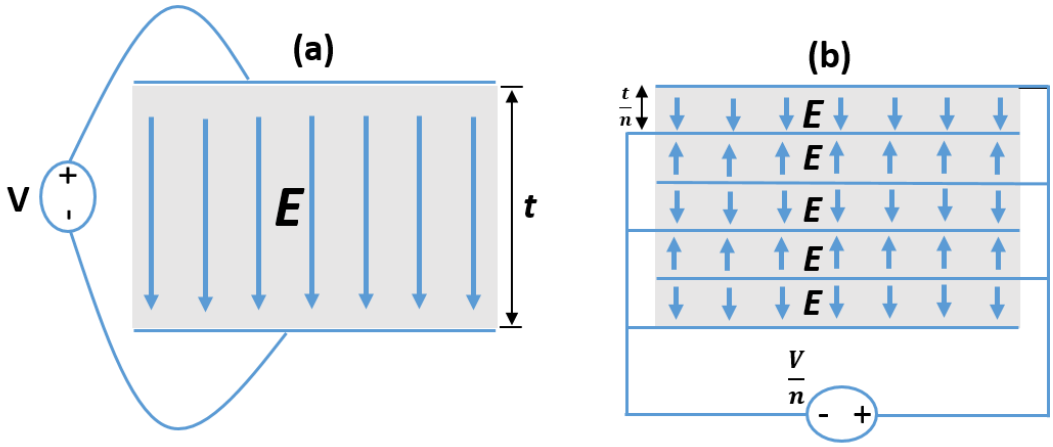

Figure 7.1: (a) single layer piezoelectric component; (b) multilayer piezoelectric component. Grey colour represent the ceramic material. (redrawn after [2]).

Low operating voltages make MLAs the design of choice for piezoceramics to be used in the end product. Stack actuators fabricated from pre-sintered ceramic through 'cut and bond method' have the disadvantage of relatively high thickness and require large amount of processing time, inhibiting large scale production [3]. On the other hand co-fired multilayers offer the advantage of fabrication of thin layers and reduce the manufacturing time to meet the demand of large scale production. The manufacturing process of multilayers is different from the fabrication of bulk ceramics. Processing multilayers can pose several challenges due to presence of binders and co-firing of internal electrodes [4]. Therefore, it is very important to show that the materials with potentially useful properties can be fabricated as multilayers without out significant degradation in properties. In a previous chapter a lead-free material N9 was shown to be suitable for high temperature actuators. In this chapter, fabrication and characterisation of a prototype MLA of the same material is discussed.

7.2 Processing of MLA

The processing of MLA starts from tape casting of ceramic sheets, followed by printing of electrodes. The layers are then stacked, laminated and heat treated at appropriate temperatures for binder burnout and sintering. A schematic for processing of an MLA is shown in Figure 7.2.

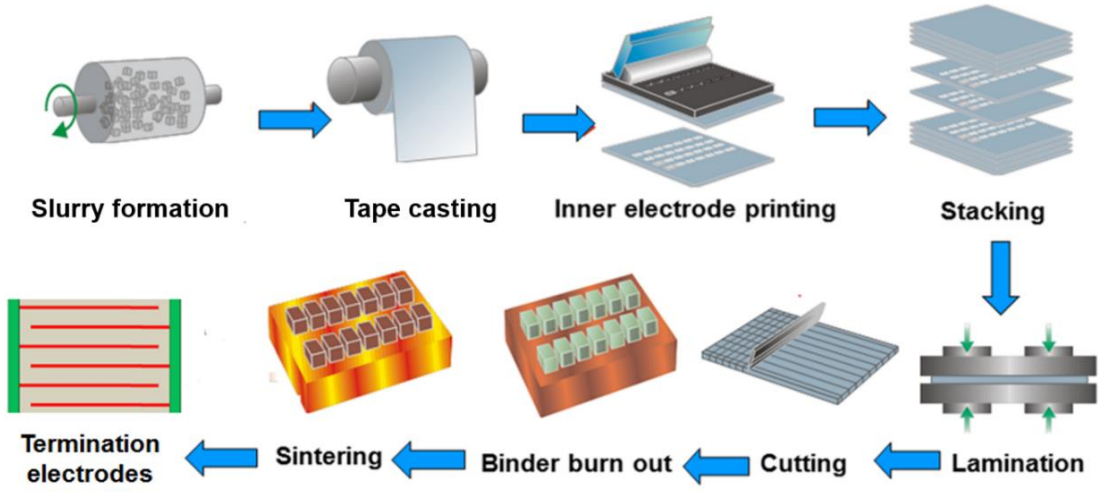

Figure 7.2: Schematic of MLA fabrication by tape casting technique. (Adapted from [5])

7.2.1 Slurry formation

Calcined powders were prepared by solid state reaction method explained in chapter 4. The powders were sieved through a 255 µm mesh to dissociate any agglomerates. At this stage binder, plasticizers, dispersant and solvents were added to the calcined powders in the ratios summarised in Table 7.1. The mixture was ball milled overnight and then further homogenised by using a high speed mixture at 1200 rpm for 15 minutes. No study was performed to compare results across different types of binders or plasticizers, however the contents of each additive were optimised by trial and error until a crack free ceramic tape was fabricated.

Table 7.1: contents of slurry

contents	Description	Weight (%) of calcined powders
Calcined Powders	$Bi_{0.5288}Nd_{0.0153}K_{0.455}Fe_{0.0873}Ti_{0.9127}O_3$ **(N9)**	100
Binder	Butvar B-98	10
Plasticizer	Kollisolv PEG 400	5
Plasticizer	Benzyle butyle phthalate	5
Dispersant	Hypermer KD-1	0.2
Solvent	ethanol and ethyl methyl ketone in 50/50 ratio	40

7.2.2 Tape Casting

Green ceramic tapes were prepared by casting the mixture onto moving silicon coated polyethylene terephthalate (PET) carrier film using a Mistler TCC-1200 with a single doctor blade. A schematic of tape casting process is shown in Figure 7.3 (a). The gap between carrier and the doctor blade is adjustable and can be fixed to a particular clearance depending on the desired layer thickness. In this study, the gap between blade and carrier was fixed to 400 µm, which corresponded to a dried layer thickness of about 100 µm. The Mistler TCC-1200 equipment allows to control the temperature of bed and speed of carrier. Both speed and temperature can be easily adjusted from the controller shown in Figure 7.3 (b). The speed of carrier is optimised on the basis of slurry thickness and temperature is selected for the solvent used. In this study the speed of carrier was fixed to 60 rpm and the tape was cast at room temperature.

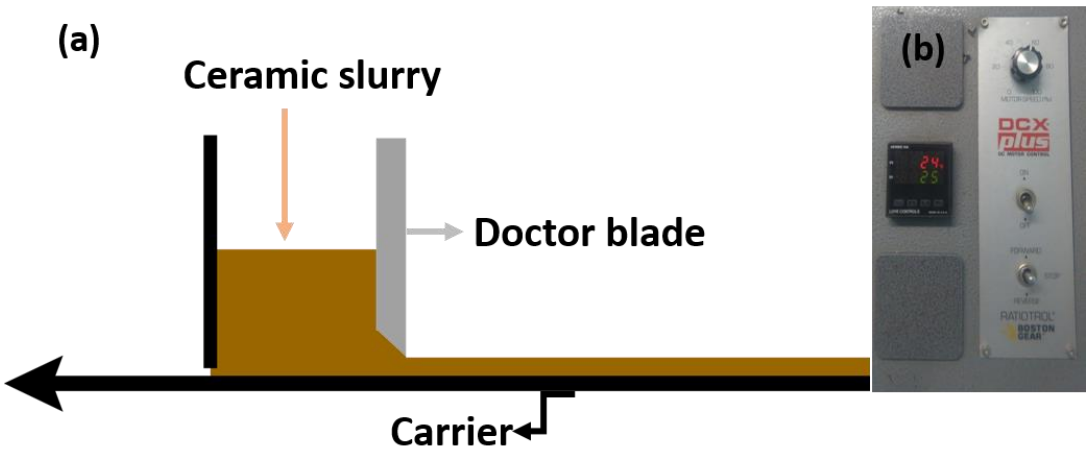

Figure 7.3: (a) Schematic representation of tape casting process. The arrow head is indicating direction of motion of PET carrier (adapted from [6]); (b) Optical image of the controller on the tape caster.

7.2.3 Printing electrodes

Platinum (Pt) ink (M637C Heraeus Electronic Materials) was used to screen print electrodes on N9 tape using a DEK 247 screen printer. In this technique the electrode ink is squeezed through a mesh with permeable areas of defined geometry onto the ceramic tape as illustrated schematically in Figure 7.4 (a). Figure 7.4 (b) shows an optical image of Pt electrode printed on to N9 ceramic tape. Each electrode is rectangular in shape with an area of 9.2 mm × 7.2 mm.

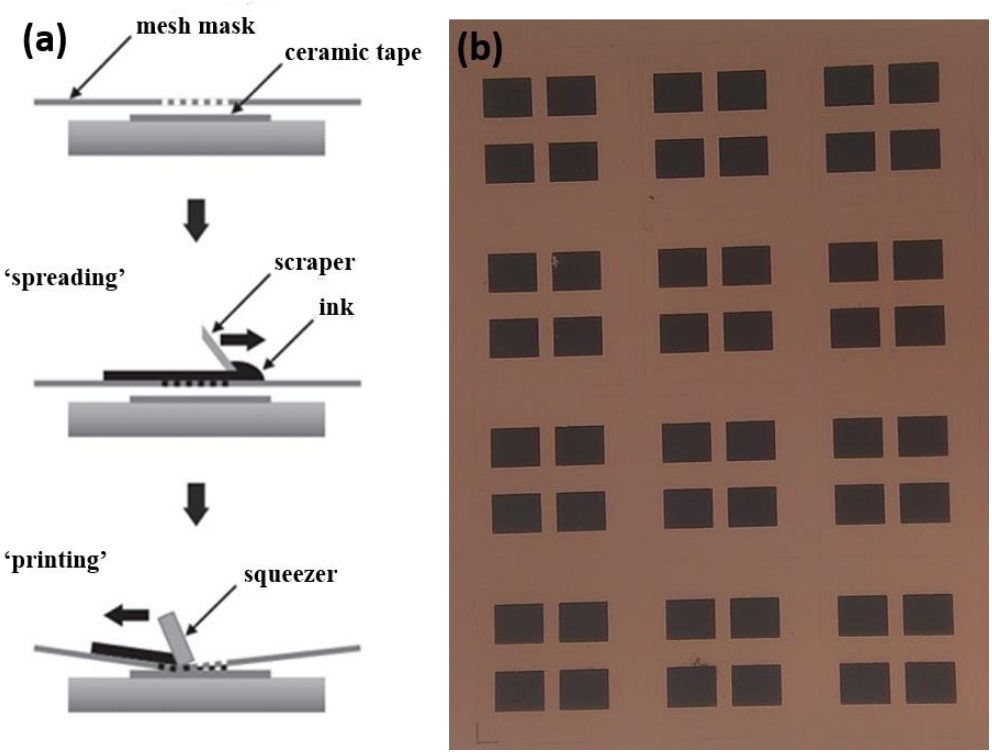

Figure 7.4: (a) Schematic of screen printing (adapted from [7]); (b) optical image of platinum electrodes screen printed onto N9 tape.

7.2.4 Cutting and lamination

The green tape with Pt electrodes shown on Figure 7.4 (b) was mounted on the cutting tool shown in Figure 7.5 (a). Upon application of pressure the sheet of electroded tape is

separated into squares of (30 mm x 30 mm), with each square containing four electrodes as shown in top right of Figure 7.5 (b). The tape is then peeled off the carrier film and stacked into a multilayer structure using the tools shown in Figure 7.5 (b). Each stack consisted of 10 electrode layers with 2 buffer layers both on top and bottom. Using a sharp knife the stack was cut to make four multilayer samples. During the stacking process each layer was moisturised with isopropanol to promote adhesion between layers and achieve better lamination. This idea of moisturising the layers during the stacking process was developed to cope with the issue of delamination. Delamination was clearly evident in samples not moisturised even after use of room temperature uniaxial press, hot uniaxial press and cold isostatic press. However with moisturising, only hand pressing was enough to laminate the layers into a compact stack. The drawback of this method however, is that manual pressing of thin layers may produce defects in the ceramic layer and/or electrodes. For future studies it is recommended that the tape is stored in a freezer. At low temperatures the tape will not dry out quickly and hence better lamination may be achieved.

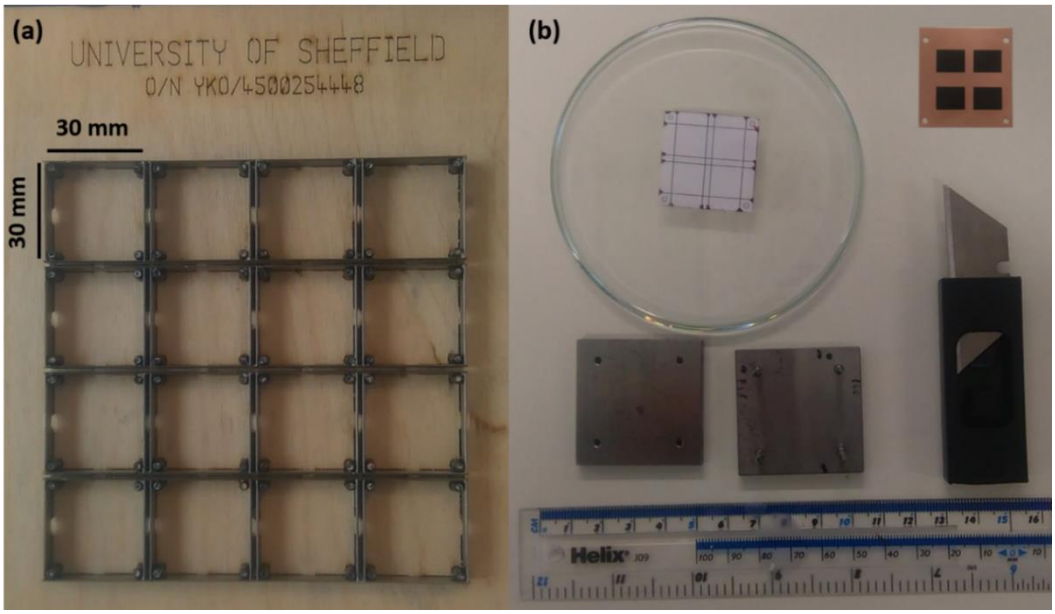

Figure 7.5: (a) Optical image of cutting tool; (b) optical image of the tools used for stacking layers and cutting the stacks after wards. On the top right is an optical image of a single layer with four electrodes.

7.2.5 Binder burnout and sintering

Binders give strength to green tape. Plasticizers promote fluidity in the slurry and allows easy casting. Therefore, addition of these additives is essential to fabrication of thin ceramic layers, however they need to be cleanly burnt out before sintering. The plasticizers used in this study burns at about 300 °C [8-9]. The binder starts burning at 350 °C but the process is completed at 550 °C [10]. Based on the information above, a two-step burnout profile (Figure 7.6) was used to get rid of the additives before sintering. Note that heating rate before binder burnout is 1°C/min to make sure the burning takes place slowly and the gases evolved during the process are not released too rapidly. After binder burnout the samples were sintered at 1090 °C for 2 h. The sintering temperature is the same as that used for bulk ceramics. However, unlike bulk samples, the multilayers were not buried in calcined powders during sintering due to difficulties in cleaning afterwards. The multilayer samples were instead wrapped in their own tape to mimic the conditions employed for sintering bulk ceramics.

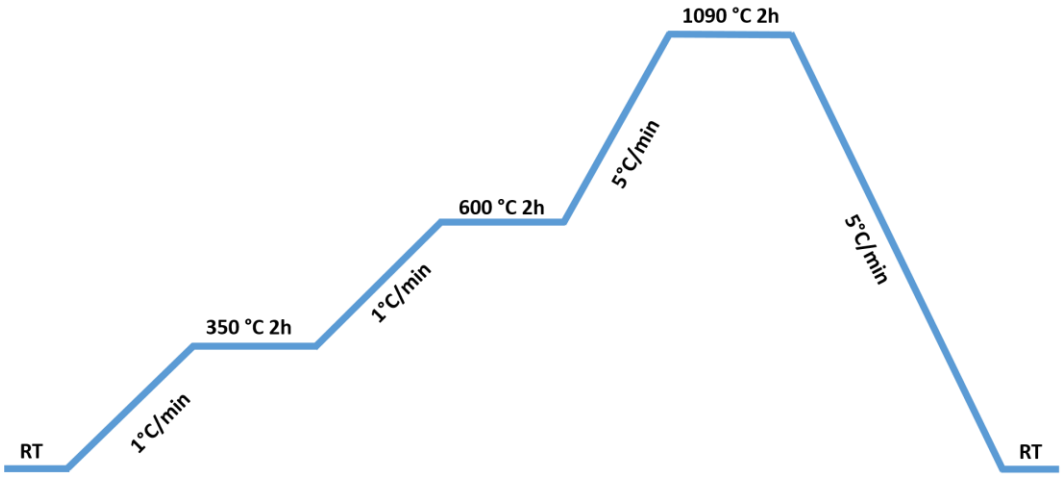

Figure 7.6: Binder burn out and sintering profile for N9 MLA.

7.2.6 Cleaning and termination electrodes

The sides of electrodes were cleaned through careful grinding until electrodes were clearly visible under optical microscope. Silver paste was then used to connect the set of 5 electrode on each side as illustrated in Figure 7.7.

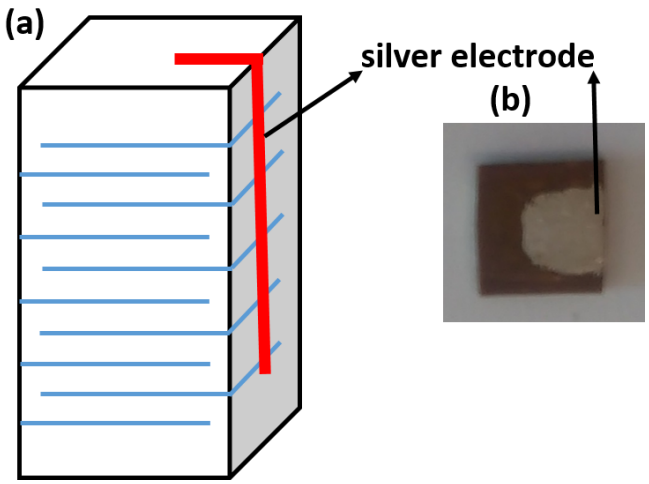

Figure 7.7: (a) schematic cross section of the N9 MLA. The red line represents silver used as external electrode. The blue lines are representative of Pt used as internal electrodes; (b) Optical image of the N9 MLA.

7.3 Characterisation of MLA

7.3.1 Phase analysis and microstructure

Figure 7.8 (a) shows room temperature XRD trace obtained from crushed sintered layers (without electrodes) of N9 MLA. A single phase with pseudocubic perovskite structure identical to that obtained for bulk is observed. Figure 7.8 (b) shows a SEM image obtained from as-sintered N9 MLA. The grain size and morphology is similar to that observed in bulk ceramics.

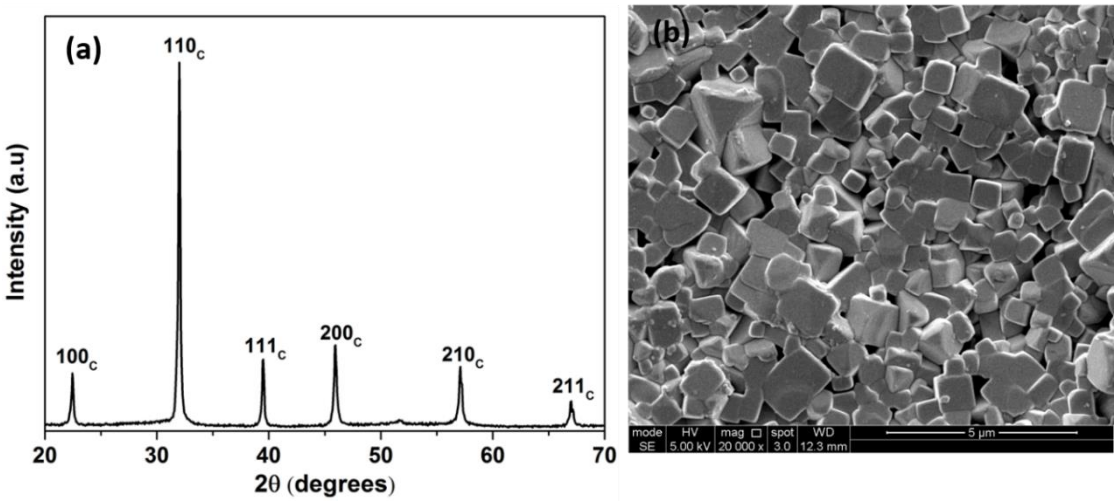

Figure 7.8: (a) XRD trace of crushed sintered ceramics after annealing them at 500 °C overnight; (b) SEM image obtained from as sintered surface of MLA.

7.3.2 Multilayer cross section and active electrode area

Figure 7.9 shows a representative optical image of the cross section of N9. All ten electrode layers are clearly visible. From optical images each ceramic layer was estimated to be ~ 83 µm. The area of active region of each electrode was ~ (5.6 mm × 5.6 mm = 31.36 mm^2). This value was obtained by breaking a sintered MLA along the electrode layer. It is assumed that all other samples will have the same shrinkage and this value of area is used for all tested MLAs. In general good lamination was observed in the fabricated MLAs, however occasional delaminated regions (encircled Figure 7.9) were

also observed. No apparent interaction of the Pt electrode with the ceramic is observed showing compatibility of Pt metal with N9 ceramics. The delaminated regions however reminds us that processing, still needs further optimisation.

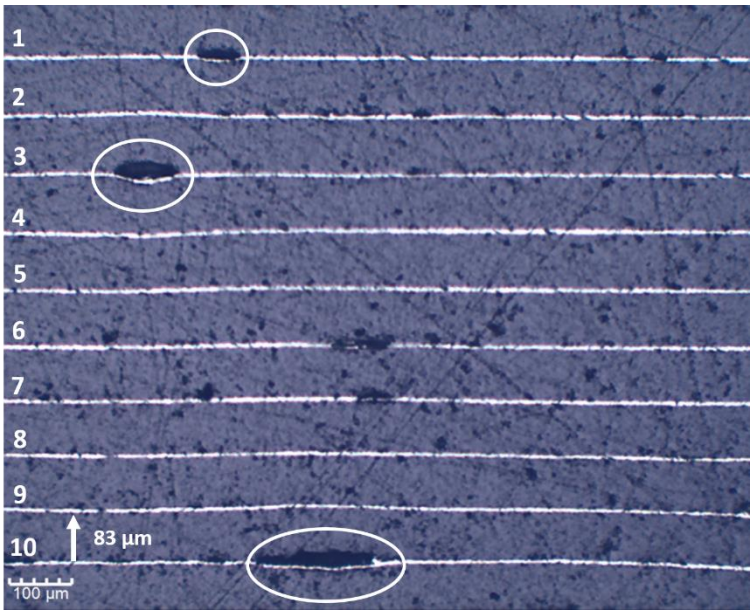

Figure 7.9: Representative optical image of N9 MLA cross section. Delaminated regions are encircled.

7.3.3 Dielectric properties

Figure 7.10 shows a comparison of dielectric constant and tan δ as a function of temperature at 1 kHz between bulk and MLA. The overall behaviour of both MLA and bulk ceramic is same, with a broad Curie maximum and decrease in tan δ with increasing temperature. However, there is a clear mismatch between the permittivity values at high temperature and tan δ at low temperatures. Difference in dielectric properties between MLA and bulk can be attributed to an increase in loss of volatile species, reaction of electrode with ceramic, delamination between electrode and ceramic and presence of residual carbon. In this case the latter two reasons seem to be more prominent as loss of volatile species from the interior of an MLA is unlikely considering the travel length, and no apparent reaction is observed at the interface between Pt and ceramic. Also we note that delaminated regions are occasional and the major effect is therefore believed to be the

presence of residual carbon. Cumming et al. [11] observed a reduction of 50 % in tan δ of $0.52(0.35Bi(Mg_{1/2}Ti_{1/2})O_3–0.3BiFeO_3–0.35BiScO_3)–0.48PbTiO_3$ multilayers, when the binder burnout time was increased from 2 h to 4 h. A similar optimisation in burning profile for N9 MLA would be helpful in reducing the observed difference between bulk and MLA.

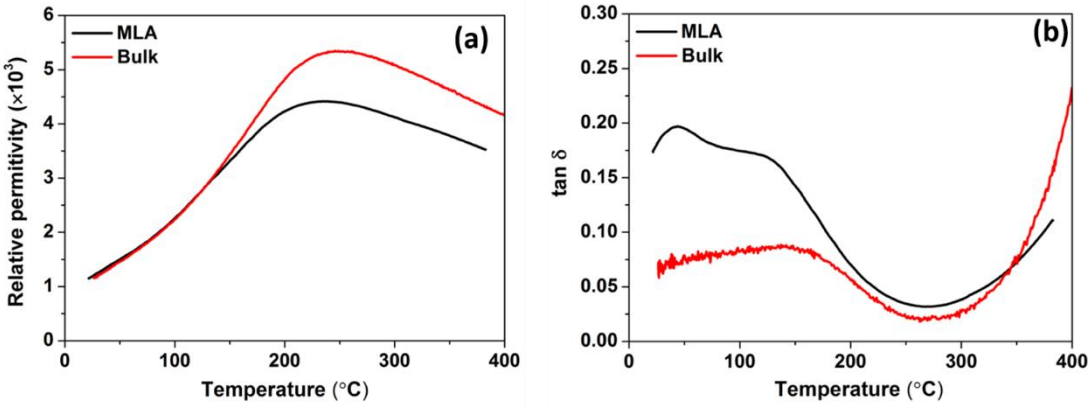

Figure 7.10: (a) Comparison of dielectric constant vs. temperature between bulk and MLA at 1 kHz; (b) Comparison of tan δ vs. temperature between bulk and MLA at 1 kHz. Different samples processed under nominally same conditions exhibited almost same dielectric response.

7.3.4 Polarisation and displacement vs. voltage at room temperature

Figure 7.11 shows room temperature response for polarisation and displacement vs. voltage. A displacement of 2 µm was observed at a voltage of 489 V, which correspond to an electric field of 6 kV/mm. This shows that similar to bulk materials MLAs are also capable of sustaining large electric fields. The loops are slim with a low remanent polarisation of 7 µC/cm^2 and the strains are predominantly electrostrictive as observed in bulk ceramics. Figure 7.12 shows a comparison of polarisation and strain vs. electric field between bulk and MLA. Maximum polarisation in MLA is 19 µC/cm^2 less than that observed for bulk (27 µm/cm^2). A similar decrease in polarisation was also reported by Sapper et al. for $0.91(Bi_{1/2}Na_{1/2})TiO_3–0.06BaTiO_3–0.03(K_{0.5}\ Na_{0.5})NbO_3$ multilayers. The authors found that that maximum polarisation of bulk ceramic decreases from 24 µm/cm^2

to 14 μm/cm^2 in MLA of the same composition [12]. Such a decrease is attributed to problems mentioned in the preceding section.

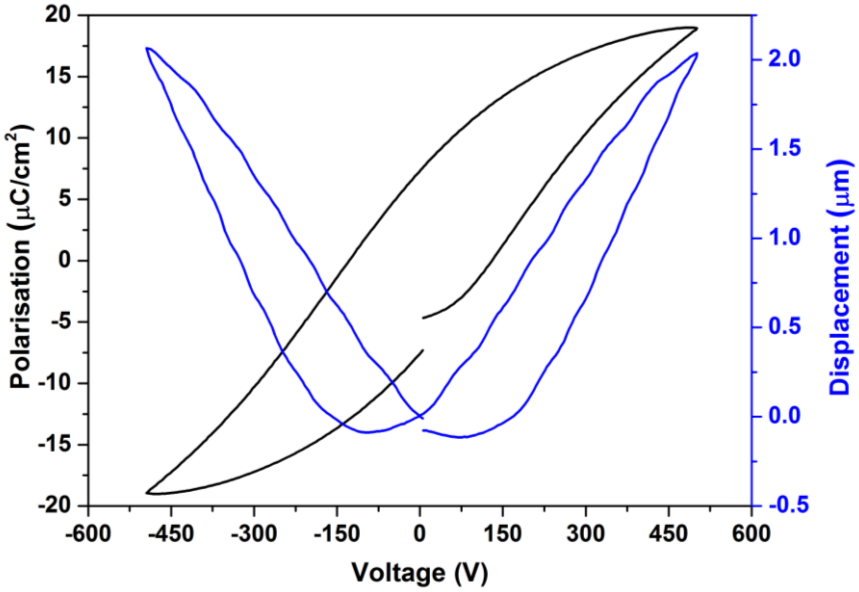

Figure 7.11: polarisation and displacement vs. voltage for N9 MLA at 1 Hz and room temperature. (Magnitude of displacement magnitude varied from 1.4 to 2 μm across different samples processed and tested under same conditions.)

Electrostrictive strains are directly proportional to square of polarisation [13]. Therefore a low polarisation should theoretically result in lower strains. However surprisingly the strain in MLA (0.26 %) is much greater than that observed in bulk ceramics (0.16 %). Such a behaviour can only be rationalised, if the actual strain arising from electromechanical coupling is amplified by a bending effect. Nagata et al. observed a very large strain 0.63 % in $Na_{1/2}Bi_{1/2}TiO_3$-based multilayers at a driving fields at 80 kV/mm. The authors attributed it to formation of Moonie structures at the electrode ceramic interface due to delamination at high driving fields [14]. A Moonie structure is a metal-ceramic composite, where the metal is attached to a piezoelectric ceramic in such a way that the space between ceramic and metal is like a crescent. This arrangement uses the radial motion of a piezoelectric ceramic to enhance displacement along the axial direction [15]. It is speculated that such an enhancement mechanism may be responsible for the

larger displacement observed here due to presence of delaminated regions. Four different MLA samples fabricated under nominally similar conditions tested under same electric field exhibited almost same response in polarisation vs. electric field loops, however the magnitude of displacement varied from 1.4 to 2 µm across different samples, when operated at 498 V. This further confirms that the magnitude of displacement is effected by some external geometrical parameters which are different in different samples, most probably the concentration of delaminated regions. However, it is important to note that such an external amplification aid to the displacement does not affect the temperature stability of the device [16], which is discussed in the next section.

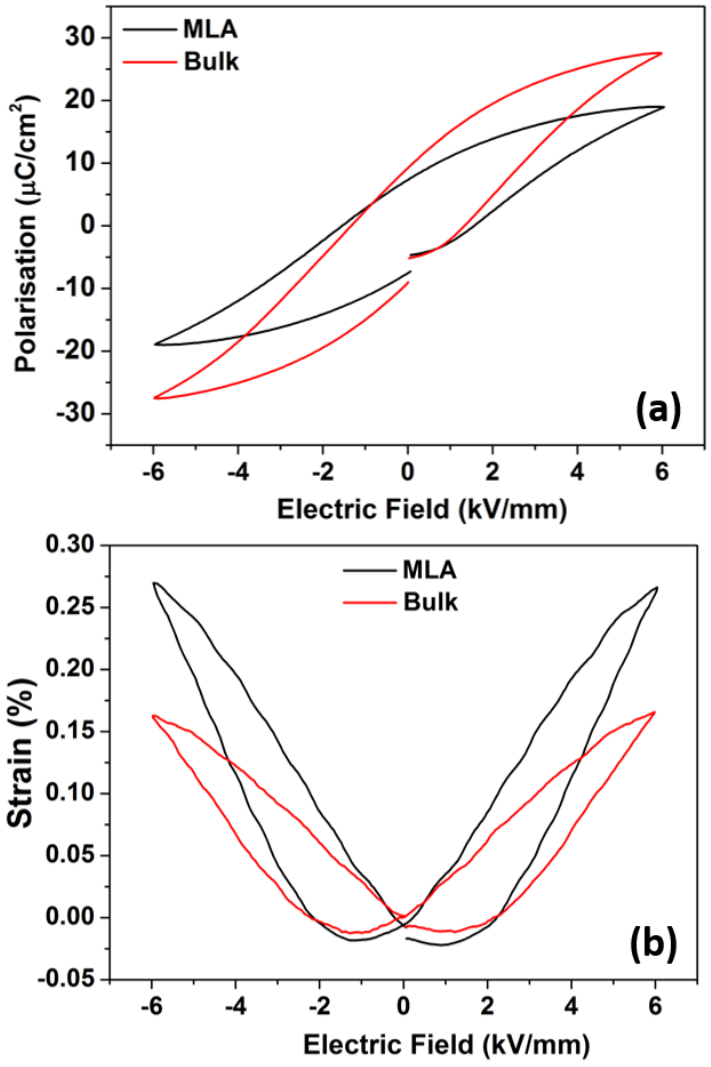

Figure 7.12: (a) polarisation vs electric field loops for MLA and bulk at 1 Hz; (b) strain vs electric field loops for MLA and bulk at 1 Hz.

7.3.5 Temperature stability of displacement

Since the MLA operates at low voltages (498 V), the safety restrictions on testing bulk ceramics at high temperatures do not apply here. Therefore, the MLA was tested to much higher temperature (300 °C) in comparison to bulk (175 °C) revealing a wide range of temperature stability for N9 ceramics. Figure 7.13 shows displacement of N9 MLA as a function of temperature. The MLA shows a temperature stable displacement from room temperature to 300 °C with a variation in strain (ΔS) of 15 %.

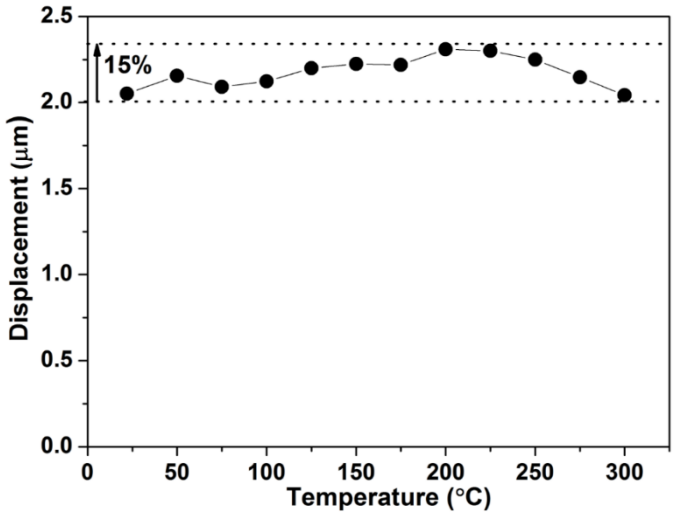

Figure 7.13: Displacement of N9 MLA as a function of temperature.

The actual bipolar displacement vs. voltage loops at selected temperatures are shown in Figure 7.14. The loops gets slimmer with increase in temperature and yield temperature insensitive displacement similar to bulk over in wider temperature range.

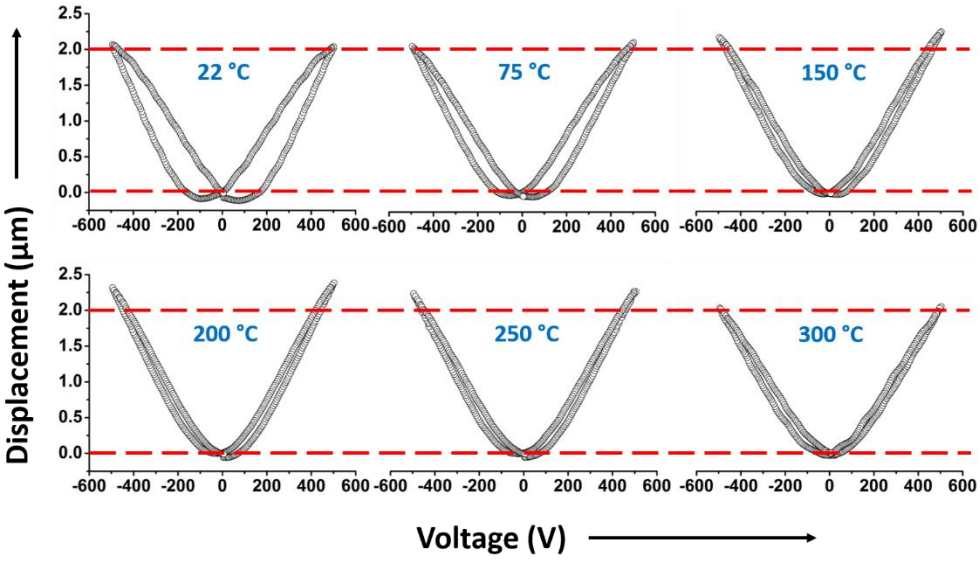

Figure 7.14: Bipolar loops of N9 at selected temperatures. Red lines are guide to eye for 0 and 2 µm displacement.

The stability of displacement in such a wide range not only distinguished N9 from all other comparable lead-free ceramics, but also makes it superior to PZT and PMN-based formulations. A comparison of N9 stability with leading lead containing ceramics is given in Table 7.2. The values in Table 7.2 are taken from figures in the respective references.

Table 7.2. Temperature stability of N9 vs. leading lead based materials.

Material	Temperature Range	ΔS	Reference
0.9PMN-0.1PT	RT-70 °C	> 40%	[17]
PZT-5H	RT-80 °C	~ 40 %	[18]
PIC 151	RT-170 °C	20 %	[19]
PZT 4	RT-160 °C	15 %	[20]
N9	**RT-300 °C**	**15 %**	**This Work**

7.3.6 Fatigue

To study the fatigue behaviour the N9 MLA was cycled one million times at an electric field of 5 kV/mm and a frequency of 5 Hz. Decrease in displacement after one 1 million cycles was observed to be 8.42 % (Figure 7.15) which is slightly larger than that observed in bulk (5.24 %). Balke et al. [21] studied fatigued PZT bulk ceramics and observed that the ceramics are more damaged near the electrodes. Upon removal of the damaged region near the electrodes, the authors were able to recover 90 % of the polarisation and hence concluded that overall fatigue of the ceramic is dominated by degradation occurring near the electrodes. Such a phenomenon will result in larger reduction of polarisation in a multilayer structure due to large electrode area. In addition to this in MLAs, the active region is clamped by the non-active parts of ceramic. Hence a strain mismatch between the two regions may result in cracks, which may lead to failure of MLA [22]. However, a difference of only ~ 3 % with respect to bulk implies that no large cracks are initiated in N9 MLA after 10^6 cycles. The MLA also does not show any signs of electrode delamination after continuous cycling, had that happened, a sharp change in polarisation and displacement would have been inevitable. Therefore, it is concluded that the N9 retains its fatigue resistant behaviour in the multilayer structure.

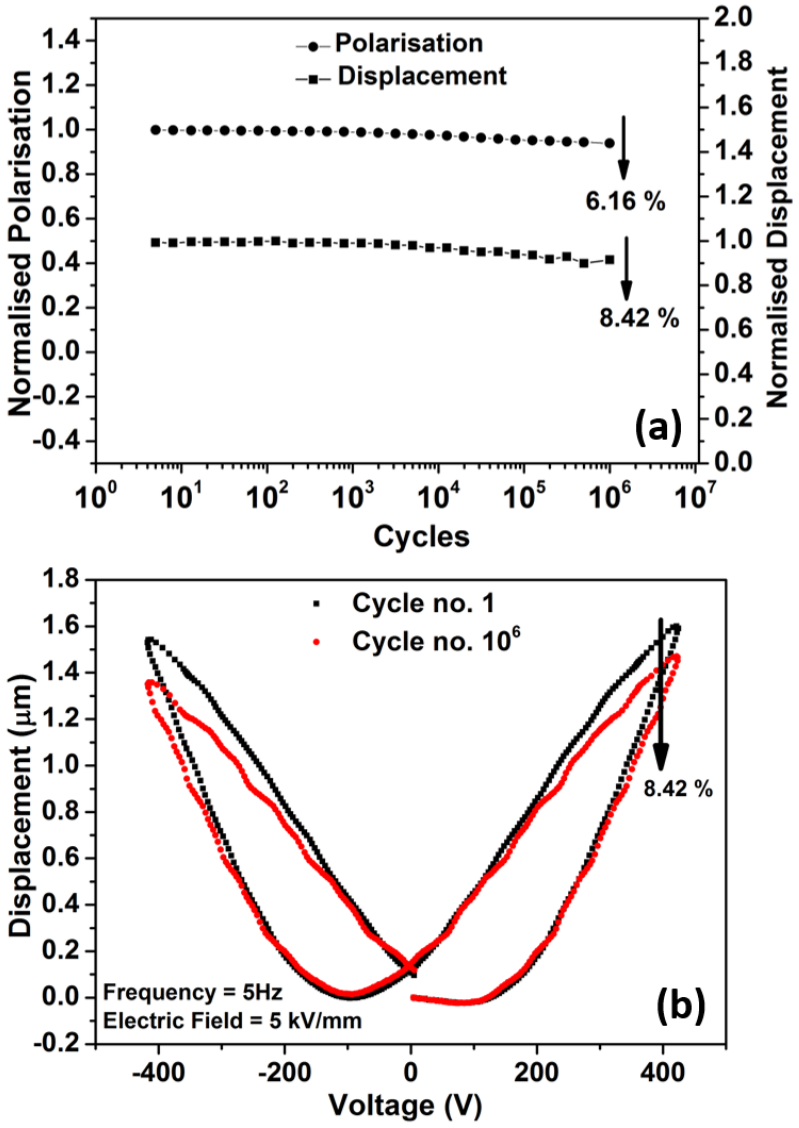

Figure 7.15: Polarisation and displacement as function of switching cycle performed at driving field of 5 kV/mm and a frequency of 5 Hz. (b) Comparison of displacement vs. voltage loop between 1st and one millionth cycle.

7.4 Conclusions

It is demonstrated that N9 ceramics can be successfully fabricated into multilayer structure by using tape casting technique. N9 ceramics shows same behaviour in both monolithic and multilayers structure. However, differences in physical values are observed, which are attributed to processing issues, especially lamination of green layers and optimisation of binder burnout temperature and/or selection of better binders. Improving these processing steps will result in properties with better agreement with bulk ceramics. Nonetheless, the fabricated MLAs have unearthed several key results for the promising N9 ceramics. The N9 ceramics have been shown to be compatible with Pt electrodes and no apparent reaction between the metal and ceramic is observed. The MLAs are able to sustain large electric fields without any significant reduction in output displacement stroke after 1 million bipolar cycles. The most important result is however the temperature stability of N9 ceramics. Temperature stable displacements from RT to 300 °C, makes N9 ceramic ideal for applications in high temperature actuators.

7.5 References

[1] Jan Peters, *Applied Piezo*. Stiching Applied Piezo, 2011.

[2] J. Holterman and P. Groen, *An Introduction to Piezoelectric Materials and Applications*. Stiching Applied Piezo, 2013.

[3] J. Pritchard, C. R. Bowen, and F. Lowrie, "Multilayer actuators: Review," *Br. Ceram. Trans.*, vol. 100, no. 6, pp. 265–273, 2001.

[4] L. Gao, H. Guo, S. Zhang, and C. Randall, "Base Metal Co-Fired Multilayer Piezoelectrics," *Actuators*, vol. 5, no. 1, p. 8, 2016.

[5] "https://commons.wikimedia.org/wiki/File:MLCC-Manufacturing-Process.png." visited on 3-08-16.

[6] "https://commons.wikimedia.org/wiki/File:Tape_casting.svg." visited on 3-08-16.

[7] "http://flow.kaist.ac.kr/bbs/board.php?bo_table=fluelcell&wr_id=29." visited on 3-08-16..

[8] "http://www.sigmaaldrich.com/catalog/product/sigma/06855?lang=en&region=GB." visited on 3-08-16.

.[9] "http://www.sigmaaldrich.com/catalog/product/aldrich/308501?lang=en&

region=GB." visted on 3-08-16.

[10] http://www.butvar.com/pdfs/en/butvar_properties_and_uses.pdf. visited on 3-08-16 .

[11] D. J. Cumming, T. Sebastian, I. Sterianou, J. Rödel, and I. M. Reaney, "Bi(Me)O_3 – $PbTiO_3$ 3 high T_C piezoelectric multilayers," *Mater. Technol.*, vol. 28, no. 5, pp. 247–253, 2013.

[12] E. Sapper, A. Gassmann, L. Gjødvad, W. Jo, T. Granzow, and J. Rödel, "Cycling stability of lead-free BNT-8BT and BNT-6BT-3KNN multilayer actuators and bulk ceramics," *J. Eur. Ceram. Soc.*, vol. 34, no. 3, pp. 653–661, 2014.

[13] J. Kuwata, K. Uchino, and S. Nomura, "Electrostrictive coefficients of $Pb(Mg_{1/3}Nb_{2/3})O_3$ ceramics," *Jpn. J. Appl. Phys.*, vol. 19, no. 11, pp. 2099–2103, 1980.

[14] H. Nagata, Y. Hiruma, and T. Takenaka, "Electric-field-induced strain for $(Bi_{1/2}Na_{1/2})TiO_3$-based lead-free multilayer actuator," *J. Ceram. Soc. Japan*, vol. 118, no. 1380, pp. 726–730, 2010.

[15] R. E. Newnham, A. Dogan, Q. C. Xu, K. Onitsuka, J. Tressler, and S. Yoshikawa, "Flextensional 'moonie' actuators," *Proc. IEEE, Ultrason. Symp.*, pp. 509–513, 1993.

[16] A. Dogan, S. Yoshikawa, K. Uchino, and R. E. Newnham, “The effect of geometry on the characteristics of the moonie transducer and reliability issue,” *Proc. IEEE, Ultrason. Symp.*, pp. 935–940, 1994.

[17] C. Galassi, M. Dinescu, K. Uchno, and M. Sayer, *Piezoelectric Materials: Advances in Science, Technology and Applications*, vol. 76. Springer Netherlands, 2000.

[18] D. Wang, Y. Fotinich, and G. P. Carman, “Influence of temperature on the electromechanical and fatigue behavior of piezoelectric ceramics,” *J. Appl. Phys.*, vol. 83, no. 10, p. 5342, 1998.

[19] M. Acosta, “Strain Mechanisms in Lead-Free Ferroelectrics for Actuators,” Technische Universität Darmstadt, 2015.

[20] Y. Saito, H. Takao, T. Tani, T. Nonoyama, K. Takatori, T. Homma, T. Nagaya, and M. Nakamura, “Lead-free piezoceramics,” *Nature*, vol. 432, pp. 84-87, 2004.

[21] N. Balke, H. Kungl, T. Granzow, D. C. Lupascu, M. J. Hoffmann, and J. Rödel, “Bipolar fatigue caused by field screening in $Pb(Zr,Ti)O_3$ ceramics,” *J. Am. Ceram. Soc.*, vol. 90, no. 12, pp. 3869–3874, 2007.

[22] S. L. Dos Santos E Lucato, D. C. Lupascu, M. Kamlah, J. Rödel , and C. S. Lynch, “Constraint-induced crack initiation at electrode edges in piezoelectric ceramics,” *Acta Mater.*, vol. 49, no. 14, pp. 2751–2759, 2001.

Chapter 8: Further Compositional Development of PbO-free piezoelectrics based on KNN.

8.1 Introduction

As discussed in previous chapters, $K_{1/2}Bi_{1/2}TiO_3$-based ceramics were compositionally tailored to meet the basic requirements for high temperature actuator applications. The optimum composition N9 was shown to be capable of producing a strain of 0.16 % at 6 kV/mm which was fatigue resistant and temperature stable up to 300 °C. However, the drive field for N9 to achieve 0.16% strain is 6 kV/mm as compared to PZT4 which requires a field of 2 kV/mm to achieve a strain of ~ 0.14 %. The high drive field is mitigated by fabricating thinner layers in multilayer structures to reduce the applied voltage but a decrease in thickness of each layers implies an increase in the number of layers to achieve the same magnitude of displacement, consuming more electrode material (Pt or Ag-Pd) and increasing the cost of the final device. The work presented in this chapter was carried out with the aim to compositionally develop PbO-free ceramics for actuators which can produce appreciable strains at low drive field sustainable to high temperatures.

Amongst the potentially useful PbO-free materials only $BaTiO_3$ and $(K,Na)NbO_3$-based ceramics have low coercive fields. However, $BaTiO_3$ compositions optimised for piezoelectric performance have a low T_C (<100 °C) and are therefore not suitable for high temperature actuator applications [1]. $(K,Na)NbO_3$ was therefore selected as the target material for synthesising PbO-free ceramics capable of operating at low drive fields. Following on from previous chapters, it was proposed to utilise $0.82BiFeO_3$-$0.15NdFeO_3$-$0.03Nd_{2/3}TiO_3$ (BNFT) in solid solution with KNN with the intention of suppressing the orthorhombic to tetragonal transition temperature ($T_{O\text{-}T}$) to sub-ambient and hence exploit the large tetragonal region from room temperature (RT) to T_C.

In the solid solution $K_{1-x}Na_xNbO_3$, optimum piezoelectric properties are observed in the region between x = 0.4-0.6. The piezoelectric properties are similar throughout this compositional range but Na rich compositions (x = 0.6) have lower $T_{O\text{-}T}$ in comparison to x = 0.5 [2,3].Since BNFT was suspected to have only limited solid solubility [4], KNN x

= 0.6 was chosen to maximise the possibility of moving the $T_{O\text{-}T}$ to sub-ambient. Moreover, K rich compositions are prone to volatilisation and are thus more difficult to process with the correct stoichiometry [5]. During the course of the studies the solid solution was proven, to be very limited, (~ 1 %) and hence the difference between endmember BNFT and $BiFeO_3$ (BF) became irrelevant because the concentration of Nd and Ti for 1 % of BNFT was less than the impurities contained in the starting materials. Therefore, after preliminary studies with BNFT, the solid solution between KNN-BF became the focus of this chapter. A comparison between 0.99KNN-0.01BF and 0.99KNN-0.01BNFT is given in Appendix I. Finally, Li^{+1} was doped on the A-site of the optimised KNN-BF compositions to decrease further the $T_{O\text{-}T}$. The temperature dependence of the piezoelectric properties for all the optimised compositions was investigated.

8.2 The (1-*x*) $K_{0.4}Na_{0.6}NbO_3$-*x*$BiFeO_3$ (KNN-BF) system

8.2.1 Phase analysis

Figure 8.1 shows room temperature XRD traces of sintered ceramics in the system (1-*x*)KNN-*x*BF for *x* = 0, 0.005, 0.0075, 0.01, 0.125 , 0.015, 0.02 and 0.03. All peaks could be indexed according to a single phase perovskite phase. For KNN-based ceramics, the (200) doublet profile may be used to determine the structure. For orthorhombic, the I_{002}/I_{020} = 2:1 (I = intensity) [6] whereas for the tetragonal phase the reverse is observed) with I_{002}/I_{200} = 1:2 [7]. At *x* = 0, clear splitting of the 200 peak is observed at 2θ ~46° in agreement with the orthorhombic structure widely reported for $K_{0.5}Na_{0.5}NbO_3$ ceramics [3]. A gradual decrease in splitting and intensity ratios is observed with increase in concentration of BF. At *x* = 0.0125, peaks merge which corresponds to the co-existence of tetragonal and orthorhombic phase. At *x* = 0.0150, a shoulder appears on the left hand side of (200) but does not show the clear splitting expected from a pure tetragonal phase. At *x* = 0.03 the structure appears pseudocubic showing only one broad peak. In the context of the trends described, the peak broadening is attributed to competition on the nanoscale between tetragonal and orthorhombic phases however, we note that it may also arise from chemical heterogeneity in the sample [8].

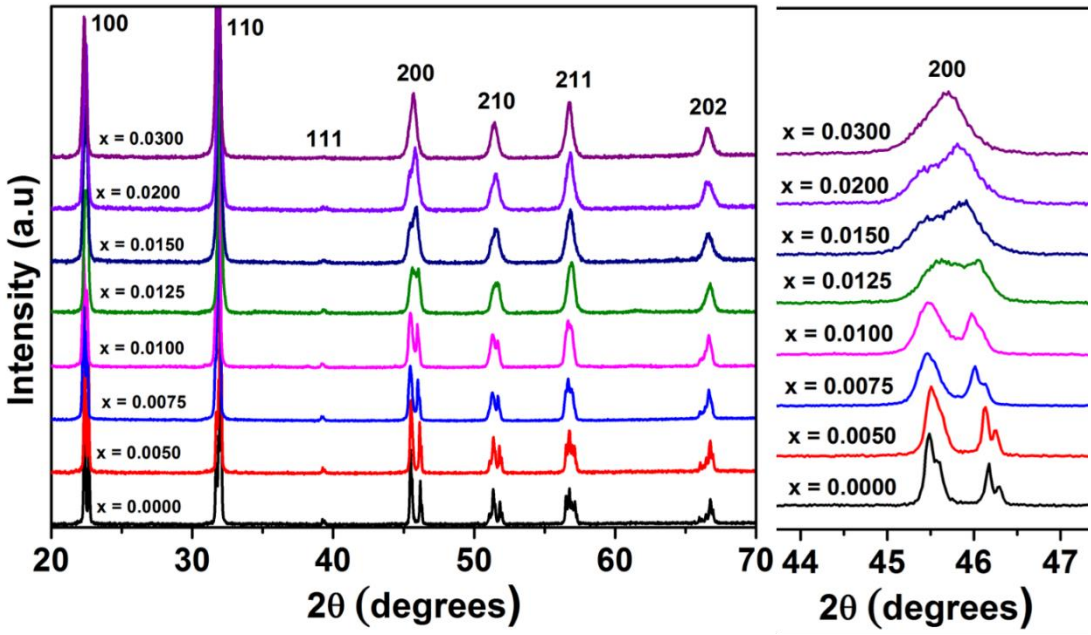

Figure 8.1: Room temperature XRD traces of (1-*x*)KNN-*x*BF ($0 \leq x \leq 0.03$) ceramics.

8.2.2 Microstructure

Figure 8.2 shows SEM images of as-sintered (1-*x*)KNN-*x*BF ($0 \leq x \leq 0.03$) ceramics. The ceramic exhibit a bimodal grain distribution and the average grain size decreased with increase in BF concentration. At $x = 0$ and 0.005, some grains have exaggerated growth (> 5 µm) as indicated in the corresponding SEM images. Abnormal grain growth is often attributed to liquid phase sintering [9-11]. Each large grain observed is believed to be the coalescence of many small grains which self-assemble into a larger clusters. The sintering temperature of KNN is near to melting point and it is difficult to obtain a dense ceramic without liquid phase [12]. Zhen et al. [13] showed that such abnormal grains possess a particular core-shell structure and tend to be detrimental to piezoelectric properties. It is noted that grain size is considered to influence piezoelectric properties [14] but no attempt was made to control the microstructure in this study whose prime focus was on compositional development. At $x = 0.0075$, the average grain size (~0.5-1.5 µm) decreased sharply and this concentration was considered critical to suppress grain growth with only gradually further reductions to ~100-400 nm for $x = 0.03$.

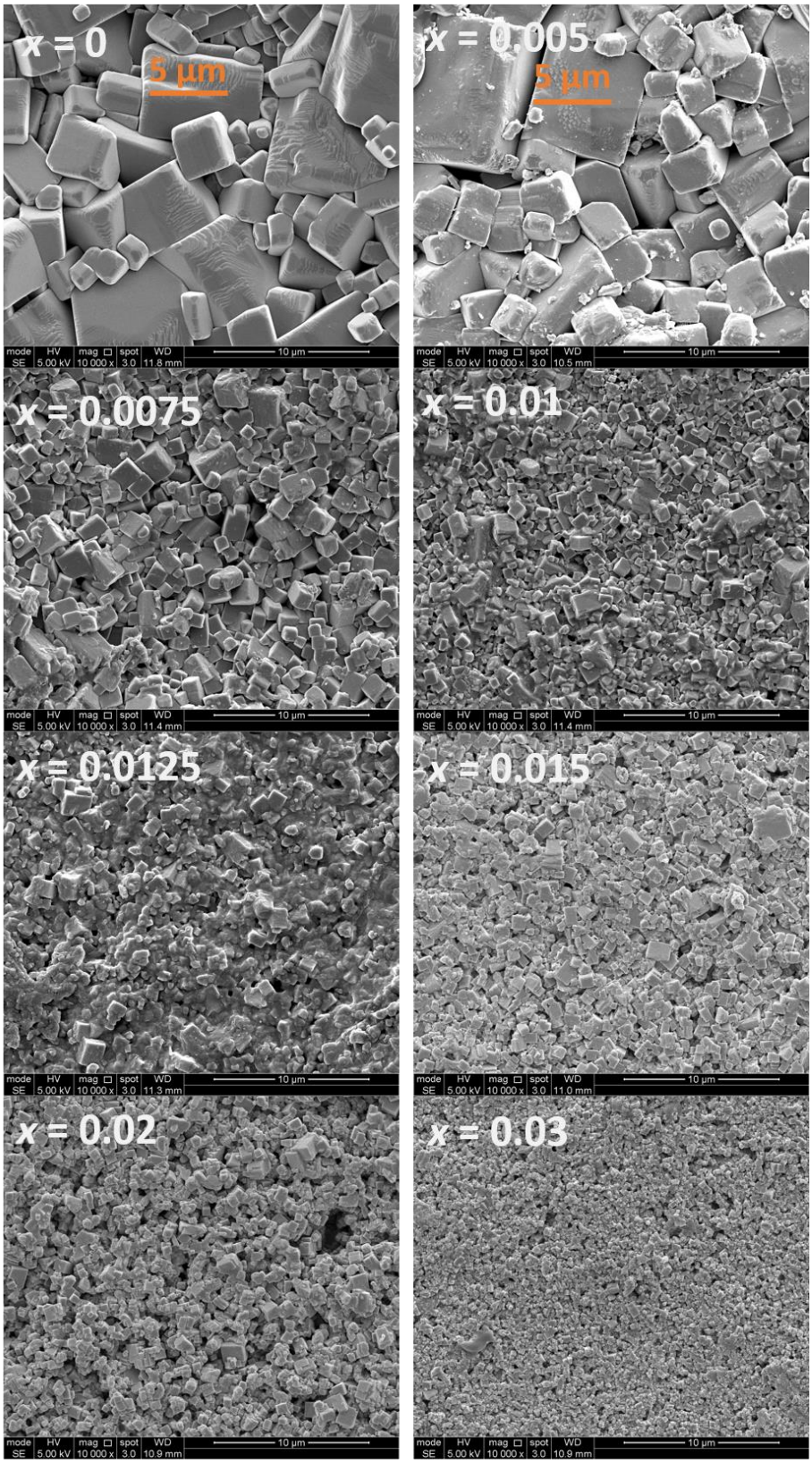

Figure 8.2: SEM images of as sintered (1-*x*)KNN-*x*BF ($0 \leq x \leq 0.03$) ceramics.

8.2.3 Dielectric Properties

Figure 8.3 shows ε_r as a function of temperature for all compositions studied in the KNN-BF series. At $x = 0$, the $T_{O\text{-}T}$ was ~175 °C, lower than that for $K_{0.5}Na_{0.5}NbO_3$ composition (~ 200 °C). The $T_{O\text{-}T}$ decreases with increase in BF concentration from ~175 °C ($x = 0$) to ~108 °C ($x = 0.01$) confirming that small additions of BF effectively reduce the $T_{O\text{-}T.}$ At $x = 0.0125$, the $T_{O\text{-}T}$ transition is not sharp but instead a diffuse maximum is observed consistent with the overlapped peaks observed in XRD. On further increase in BF concentration, no anomaly associated with the $T_{O\text{-}T}$ is observed. By extrapolation from $x = 0.01$, $T_{O\text{-}T}$ may have well moved to below room temperature and/or may have smeared out due to chemical heterogeneity. It is noted that the sharp peak observed for the tetragonal to cubic transition (T_C) in samples with $x \leq 0.01$ has also broadened for $x > 0.01$ samples. In addition, samples with $x > 0.01$ showed smaller magnitude of relative permittivity at a peak maximum which is strongly frequency dependent. Low ε_r is attributed to low densities (Table 6.4) but its frequency dependence is most evident in the range 1 to 10 kHz. Above 100 kHz, ε_r is frequency independent. Such behaviour indicates contributions to ε_r from space charge polarisation at lower frequencies due to ion migration which relax at > 1 kHz [15]. The frequency dependence and thus the contribution from space charge polarisation increases with x, presumably due to uncontrolled evaporation of volatile species such as Bi, Na and K. A similar trend was observed for these ceramic in tan δ (not shown), where high losses were observed at lower frequencies arising from long range conduction of free charge carriers.

Figure 8.4 shows a comparison of tan δ as a function of temperature for all samples at a fixed frequency of 100 kHz. Except for $x = 0.015$, all compositions showed a tan $\delta < 0.05$ at room temperature but $x > 0.01$ showed a greater rise in loss with increase in temperature compared with $x \leq 0.01$.

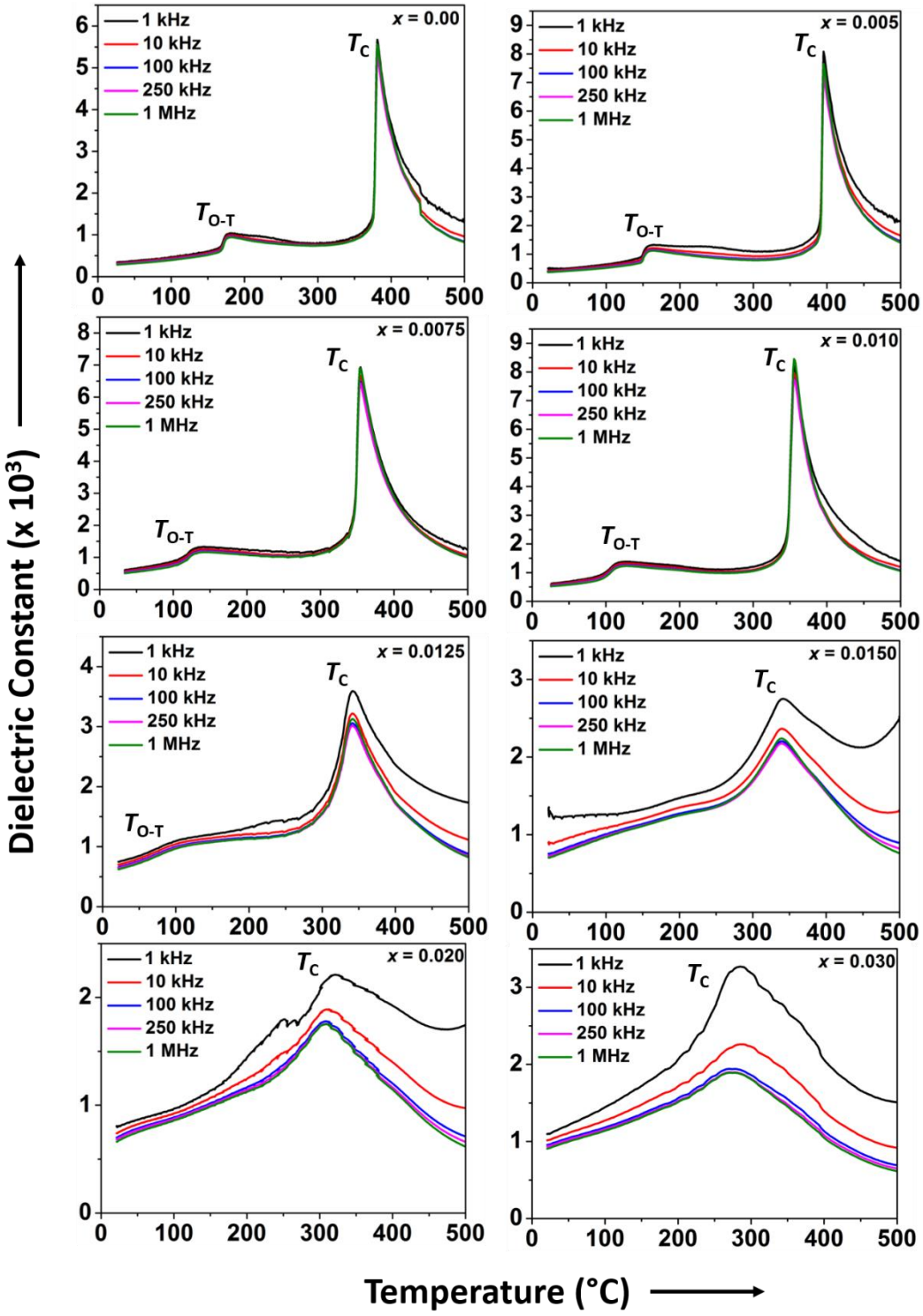

Figure 8.3: relative permittivity as a function of temperature at constant frequencies of 1, 10, 100, 250 kHz and 1 MHz for (1-*x*)KNN-*x*BF ($0 \leq x \leq 0.03$) ceramics.

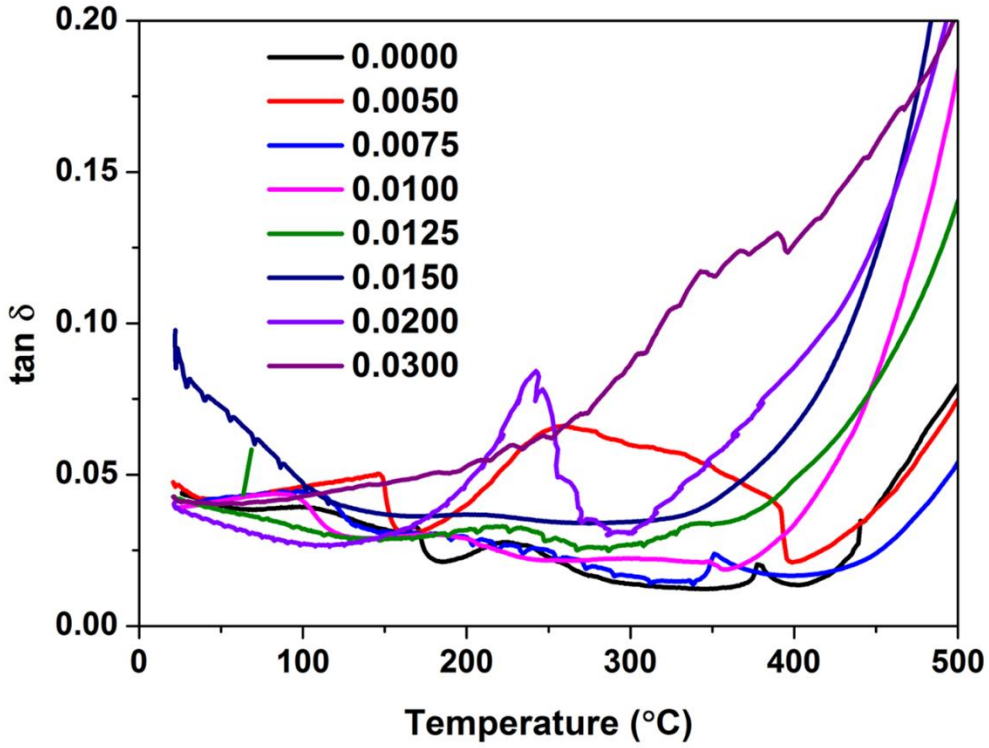

Figure 8.4: tan δ as a function of temperature at a fixed frequency of 100 kHz for (1-*x*)KNN-*x*BF ($0 \leq x \leq 0.03$) ceramics.

8.2.4 Small signal response

Figure 8.5 shows the d_{33} values for (1-*x*)KNN-*x*BF ($0 \leq x \leq 0.03$) ceramics after DC poling at 40 kV/mm for 5 minutes. At $x = 0$, a d_{33} of 82 pC/N is observed consistent with previous studies [16,17]. The d_{33} increases with addition of BF and reaches a maximum of 182 pC/N at $x = 0.01$. The increase in d_{33} is attributed to a decrease in $T_{O\text{-}T}$ as observed in dielectric data. A sharp decrease in d_{33} is observed for $x > 0.01$. Here, it is important to note that the densities also dramatically drop for these compositions as shown in Figure 8.5. The low d_{33} may not be therefore representative of composition but instead reflects poorly processed samples with low densities and high conductivities. High conductivities do not allow sufficient poling and often result in electrical break down. The $T_{O\text{-}T}$ is expected to be around room temperature for $x = 0.0125$-0.015 which, in principle, should lead to higher d_{33} values, provided methodologies are discovered to decrease the resistivities and increase the densities of these ceramics.

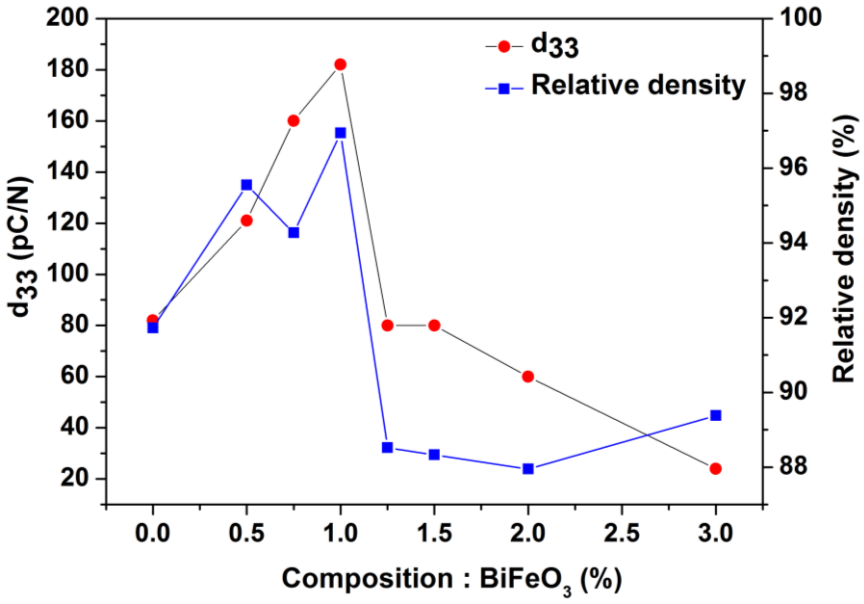

Figure 8.5: d_{33} and relative density as a function of composition in the system (1-x)KNN-xBF ($0 \leq x \leq 0.03$).

8.2.5 Large signal response

Large electric fields could not be applied to ceramics with $x > 0.01$ due to their high conductivities. In some samples, polarisation (P) vs. electric field (E) loops were obtained but they were rounded in shape with remanent polarisation (P_r) higher than maximum polarisation (P_{max}) indicative of high leakage current in these ceramics. A representative P-E loop for sample with $x = 0.015$ is shown in the Figure 8.6. It is therefore concluded that samples with $x > 0.01$ are not good enough to be characterised at large fields without further efforts to increase density and increase resistivity.

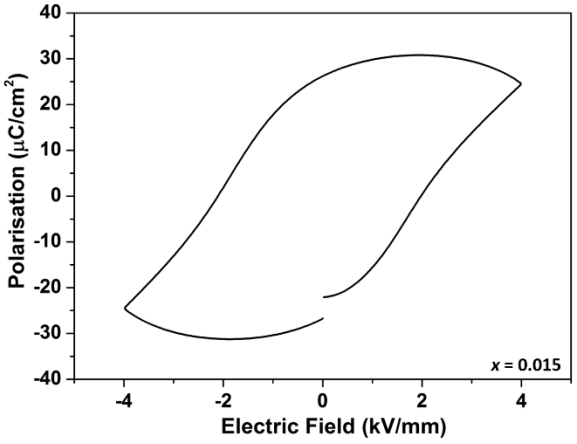

Figure 8.6: *P-E* loop at room temperature for sample at *x* = 0.015.

Figure 8.7 shows *P* and strain (*S*) vs. *E* loops for samples (1-*x*)KNN-*x*BF with $0 \leq x \leq 0.01$. The sample at $x = 0.005$ also shows leaky behaviour and hence the value of P_r value is meaningless. However, the samples with $x = 0.0075$ and 0.01 exhibited well saturated loops with a high P_r of ~28 μC/cm^2 and a low coercive field (E_C) of < 1 kV/mm. We also note that the *P-E* loops for $x = 0.0075$ and 0.01 are square-shaped. According to Haerting and Zimmer [18] the degree of squarness (R_{sq}) of a *P-E* loop can be calculated from the empirical formula introduced in equation 8.1, which for an ideal square loop is equal to 2.

$$\boldsymbol{R_{sq}} = \frac{\boldsymbol{P_r}}{\boldsymbol{P_s}} + \frac{\boldsymbol{P_{1.1}E_C}}{\boldsymbol{P_r}} \qquad \text{Equation 8.1,}$$

where P_r : remanent polarisation, *P*s: saturation polarisation, $P_{1.1}E_C$: polarisation at 1.1 times of coercive field.

The sample $x = 0.0075$ and 0.01 have R_{sq} of 1.94 and 1.95 respectively which is near to the ideal value of 2. The squareness of the loops indicate these ceramics have a uniform grain size and better homogeneity [19], which results in an instantaneous domain switching at a well-defined coercive fields. The corresponding *S* vs. *E* loops show that strain has increased from 0.06 % at $x = 0$ to 0.09 % at $x = 0.01$ upon application of an electric field of 4 kV/mm. An electric field of 4 kv/mm is used to compare compositions. Figure 8.8 (a) shows that well saturated *P-E* loops are obtained at an electric field of 2 kV/mm for optimised compositions with $x = 0.01$. The coercive field was estimated to be

0.8 kv/mm from current (*I*) vs. *E* curve (Figure 8.8 (b)), where a sharp peak is observed at the point of switching. Figure 8.8 (c) shows the corresponding *S*-*E* loops showing a peak to peak strain of 0.08 % at 2 kV/mm. However only the positive strain of 0.05 % is useful for practical application. Appearance of negative strain in the *S*-*E* loops is further confirmation of the long range ferroelectric order observed from *P*-*E* loops. The strain values are affected by both intrinsic and extrinsic contribution [20]. The extrinsic contributions are mainly dominated by domain wall motion, which due to low coercive field contribute at lower electric field and hence optimum d^*_{33} value (250 pm/V) is observed at 2 kV/mm and any further increase in electric field does not increase $d^*_{33,}$ Figure 8.8 (d).

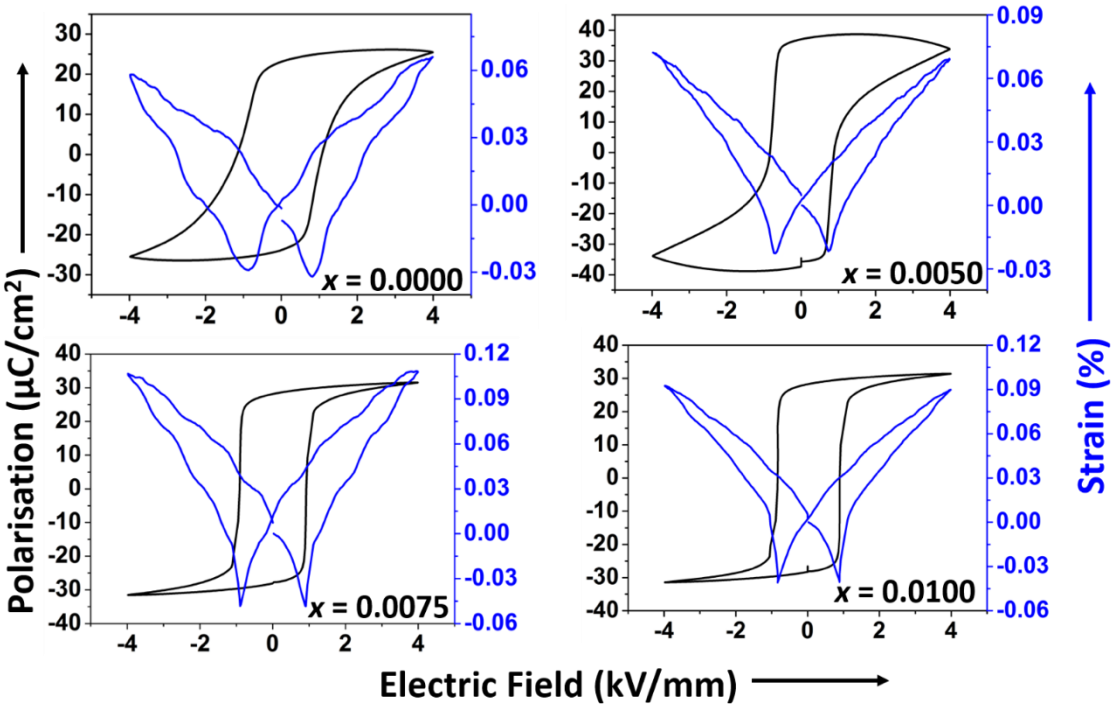

Figure 8.7: Polarisation and strain vs. electric field for *x* = 0, 0.005, 0.0075 and 0.01.

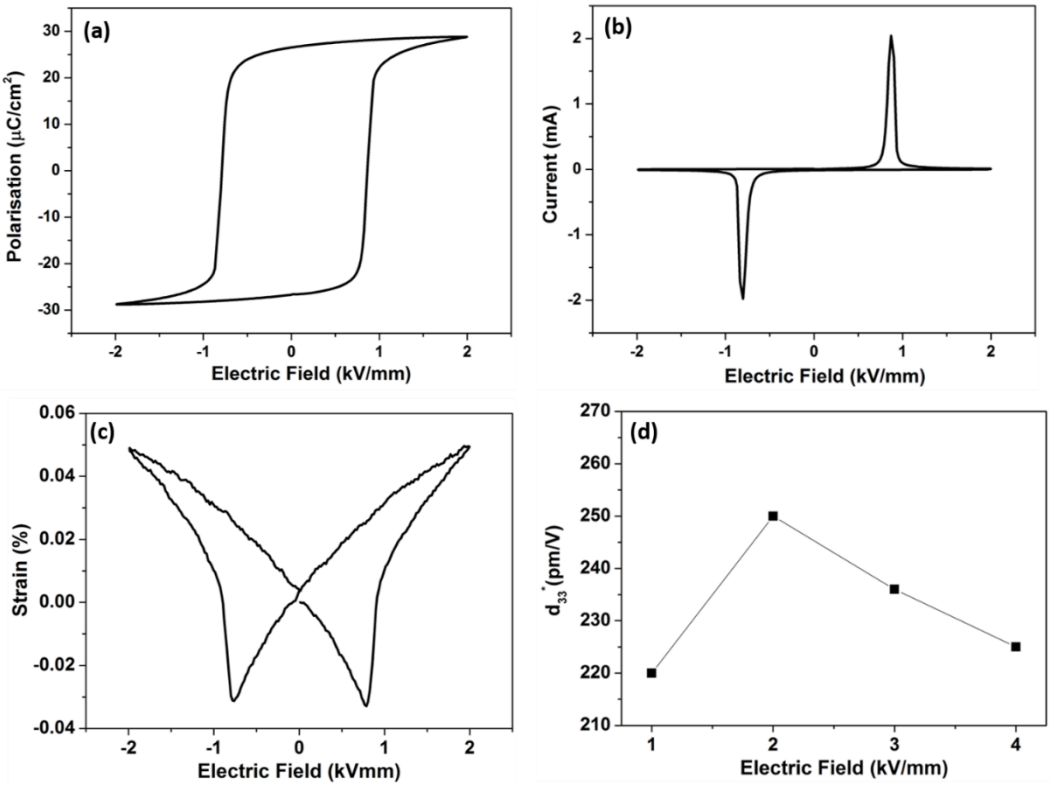

Figure 8.8: (a) *P-E* loops; (b) *I-E* loops; (c) *S-E* loops at room temperature for x = 0.01; (d) d_{33}^* as a function of electric field for x = 0.01.

8.2.6 Temperature dependence of piezoelectric coefficients

Room temperature characterisation of the KNN-BF ceramics concluded that optimised piezoelectric properties are obtained in ceramics at x = 0.01 with a d_{33} = 182 pC/N, d_{33}^* = 250 pm/V and a planar electromechanical coupling coefficient, k_p = 50 %. However, the primary interest is in the temperature dependence of the room temperature properties. Note that hereafter x = 0.01 is denoted as KNN1.

Figure 8.9 shows k_p as a function of temperature. k_p values are stable up to 90 °C with a variation of ~ 5 % and then linearly decrease at temperatures greater than 100 °C to ~50 % of its efficiency at 300 °C. The $T_{O\text{-}T}$ for KNN1 is 108 °C, therefore it can be concluded that k_p is stable in the orthorhombic state but that degradation occurs when the structure changes to tetragonal symmetry.

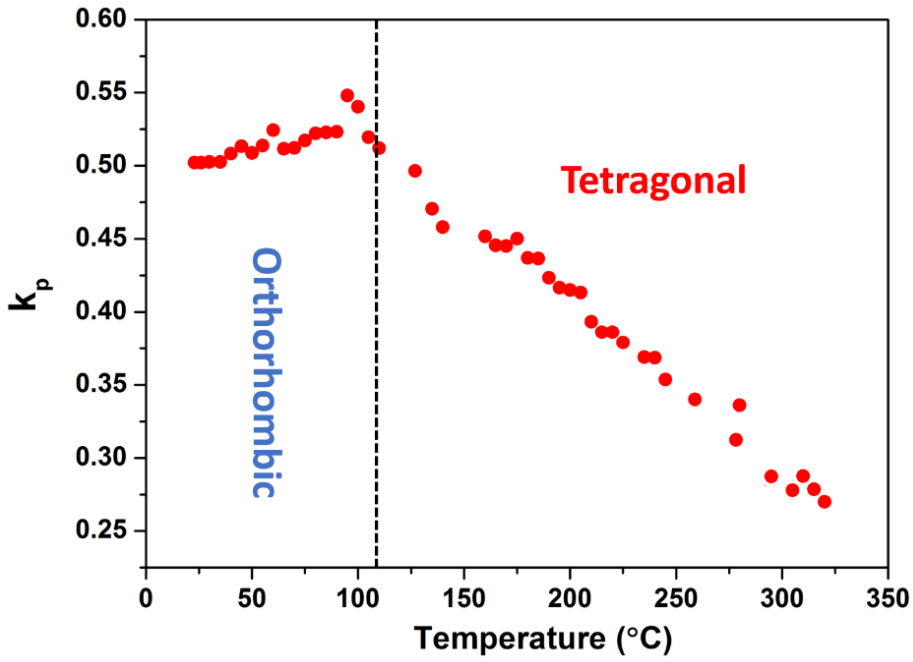

Figure 8.9: k_p as a function of temperature for KNN1.

Figure 8.10 (a) shows *P-E* loops at selected temperature from 22 to 90 °C. The coercive field decreases with increase in temperature, associated with easy domain switching at higher temperatures but the maximum polarisation remains unchanged. Figure 8.10 (b) show bipolar loops from 22 to 90 °C. The change in positive strain is about 15 % from 22 to 75 °C. The strain increases to ~ 0.10 % near the phase transition and then decreases with further increase in temperature. The bipolar strain is stable up to 75 °C but as expected decreases above the $T_{O\text{-}T}$ transition. In the tetragonal phase the *P-E* loops become tilted with an increase in coercive field. This suggest that increased domain wall motion often associated with higher temperatures (closer to the PE-FE transition) is counteracted by the structural change from orthorhombic to tetragonal phase. Figure 8.11 summarises key parameters for KNN1 as function of temperature.

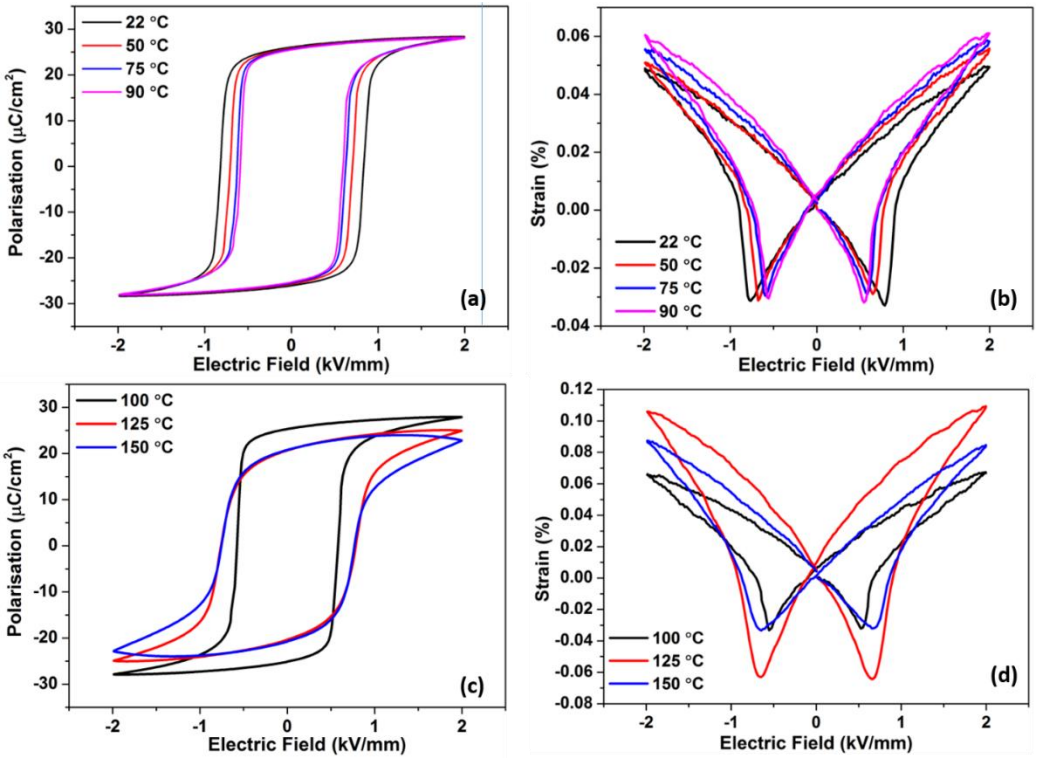

Figure 8.10: (a) *P-E* loops at selected temperatures from 22 – 90 °C; (b) *S-E* loops at selected temperatures from 22- 90 °C; (c) *P-E* loops at selected temperatures from 100-150 °C; (d) *S-E* loops at selected temperatures from 100 – 150 °C.

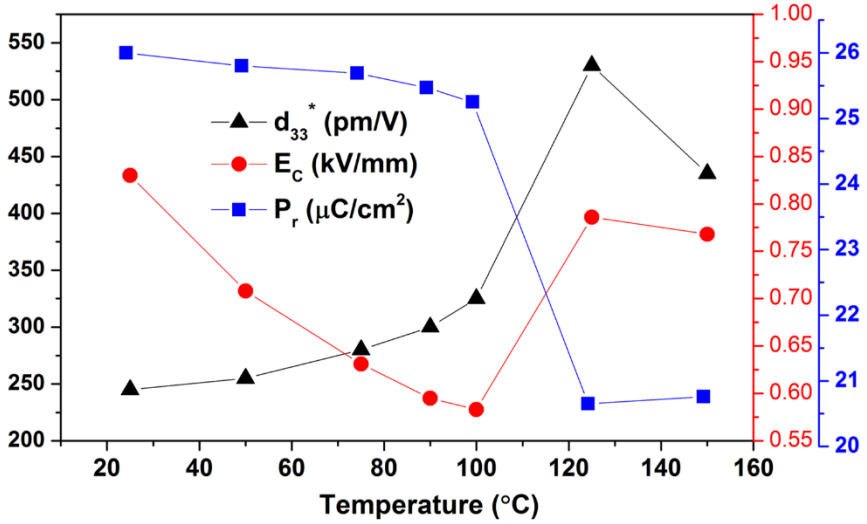

Figure 8.11: d_{33}^{*}, E_C and P_r of KNN1 as a function of temperature.

8.3 Li doped KNN1 ($0.99K_{0.4}Na_{0.6}NbO_3$-$0.01BiFeO_3$)

The study of ceramics in the series KNN-BF revealed that compositions with $T_{O\text{-}T}$ around or below room temperature could not fabricated into dense ceramics and were too conductive for for effective poling. Nonetheless, composition KNN1 showed promising piezoelectric properties with d_{33} = 182 pC/N, d^*_{33} = 250 pm/V, k_p = 50 % which deteriorated above $T_{O\text{-}T.}$ Li is known to reduce $T_{O\text{-}T}$ in KNN-based ceramics [21-23] and therefore to compare compositions with a room temperature polymorphic phase transition with that of the orthorhombic phase in KNN-BF ceramics, Li was substituted into the KNN1, according to the general formula, $0.99K_{0.4-x}Li_xNa_{0.6}NbO_3$-$0.01BiFeO_3$ (x = 0.02 and 0.04, denoted as L2 and L4 respectively).

8.3.1 Phase analysis

Figure 8.12 shows room temperature XRD traces for L2 and L4 in which all peaks were indexed according to a single perovskite phase. Peak splitting is observed as Li concentration is increased from x = 0.02 to 0.04, characteristic of a structural change from orthorhombic to tetragonal. The enlarged image of the peak splitting around 2θ of 46° reveals that compositions are not purely tetragonal [24] and that both tetragonal and orthorhombic phases co-exist for x = 0.04, albeit with the former as the dominant phase.

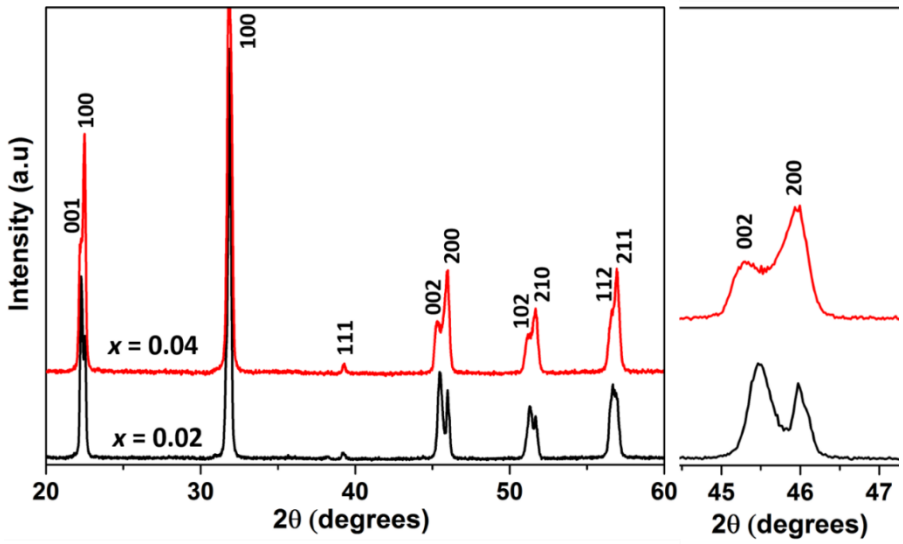

Figure 8.12: Room temperature XRD traces for L2 and L4.

8.3.2 Microstructure

Figure 8.13 shows SEM images of as-sintered L2 and L4 ceramics, which shows a dense microstructure consistent with the observed bulk densities. Similar to KNN-BF, a bimodal grain distribution is observed with grains ranging from 400 nm to 5 µm. As discussed earlier the formation of large grains is associated with liquid phase, enhanced further by Li due to its low melting temperature (< 900 °C).

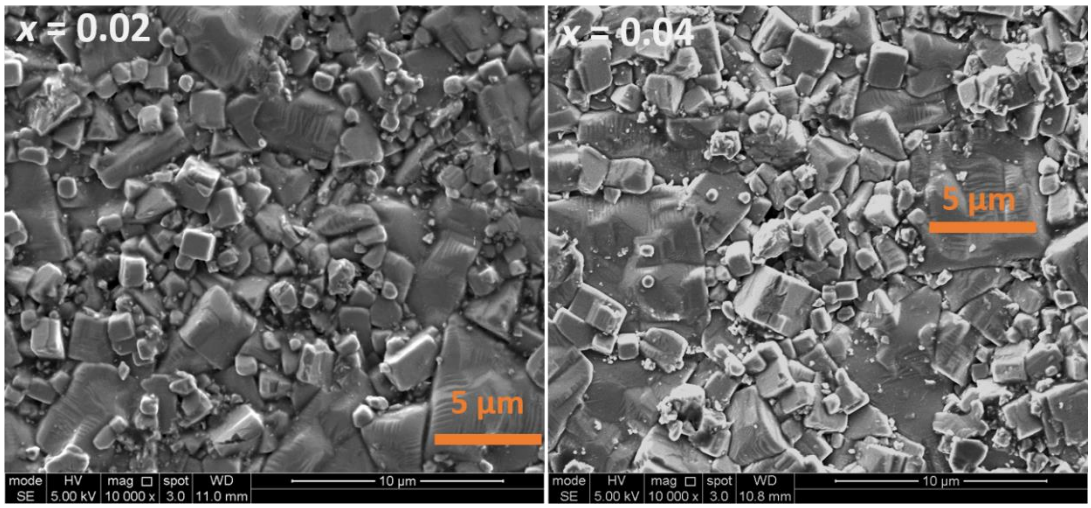

Figure 8.13: SEM images of as sintered L2 and L4 ceramics.

8.3.3 Dielectric properties

Figure 8.14 shows the relative permittivity as a function of temperature in which the $T_{O\text{-}T}$ is apparent at ~75°C for x = 0.02 and decreases to room temperature for x = 0.04, consistent with XRD data. Figure 8.15 shows tan δ vs. temperature for L2 and L4 ceramics at 100 kHz. All sample shows a tan δ of ~ 5 % at room temperature and no significant increase in loss until 400 °C. The T_C for x = 0.02 is 384 °C and no major changes in T_C are observed when the concentration of Li is increased to 4 %.

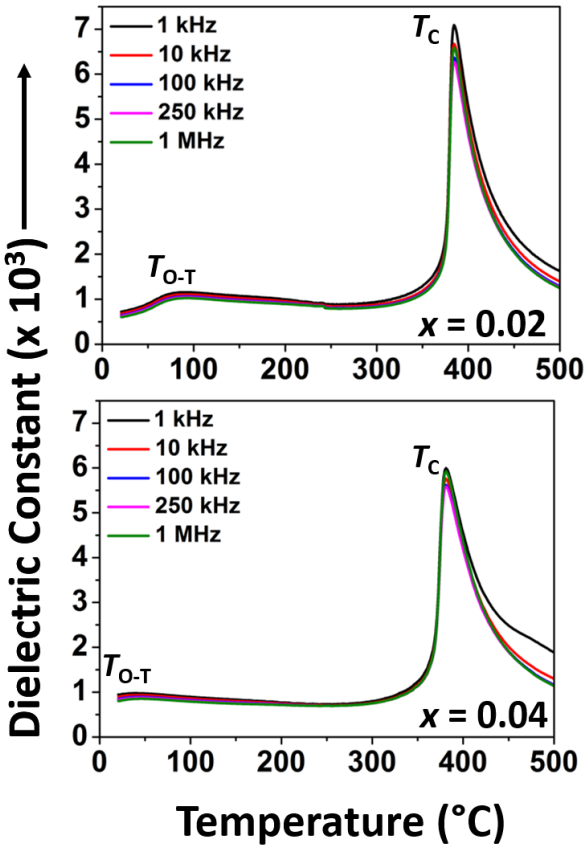

Figure 8.14: relative permittivity as a function of temperature at constant frequencies of 1, 10, 100, 250 kHz and 1 MHz for L2 and L4 ceramics.

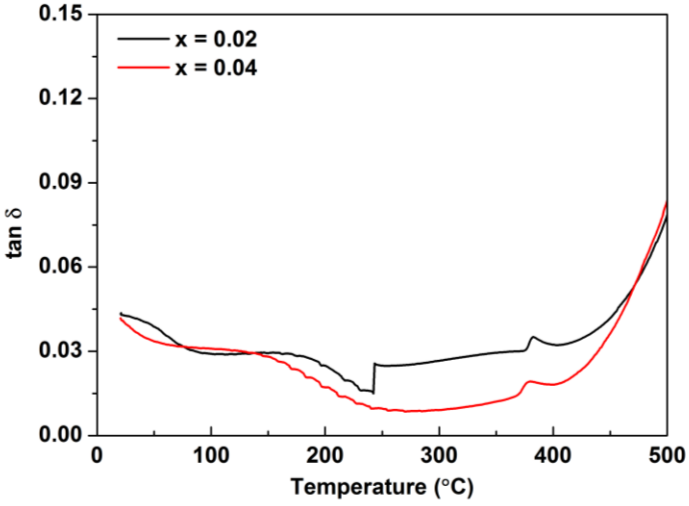

Figure 8.15: tan δ as a function of temperature at a fixed frequency of 100 kHz for L2 and L4 ceramics.

8.3.4 Small signal response

The samples were poled at 40 kV/mm for 5 minutes before measuring d_{33}. d_{33} increased from 182 pC/N for KNN1 to 200 pC/N with 2 mol. % Li (L2) and then jumped to 260 pC/N, when Li concentration was increased to 4 % (L4). The large enhancement in d_{33} at x = 0.04 is attributed to the co-existence of tetragonal and orthorhombic phases at room temperature evident from XRD and dielectric data confirming that structural instabilities near room temperature enhance piezoelectricity.

8.3.5 Large signal response

Figure 8.16 shows d^*_{33} as a function of electric field. L2 shows optimum strain 0.055 % at 2 kv/mm, which correspond to a d^*_{33} (275 pm/V). L4 yield a strain of 0.12 % at 3 kv/mm, which correspond to a d^*_{33} value of 400 pm/V.

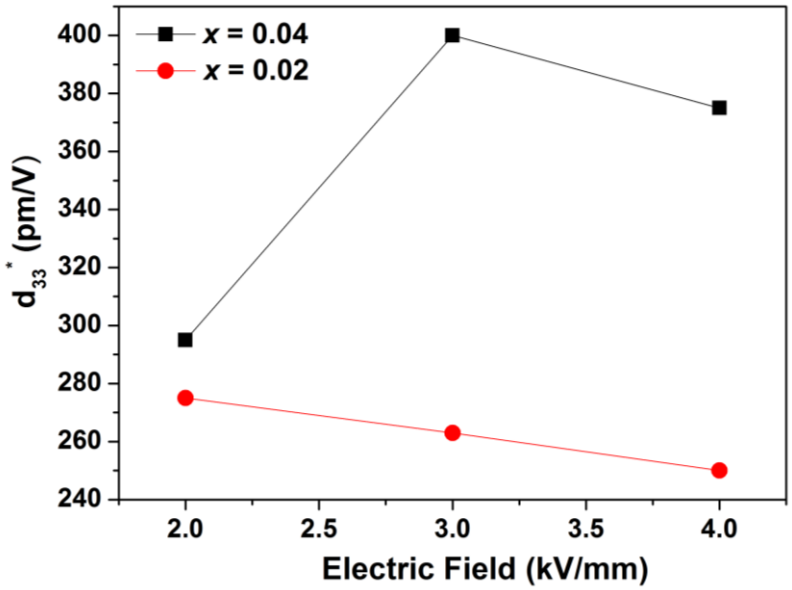

Figure 8.16: d^*_{33} as function of electric field for L2 and L4

Figure 8.17 shows *P*, *S* and *I* vs. *E* for samples L2 and L4. L*2* shows similar square-shaped *P-E* loops observed for KNN1. Bipolar loops shows an enhancement in strain and the

optimum d^*_{33} values increases from 250 pm/V for KNN1 to 275 pm/V for L2. The *I-E* loops indicates that the coercive field of L2 has increased to 1.05 kV/mm from 0.8 kv/mm for KNN1. In comparison to L2, the *P-E* loops for sample L4 are tilted, similar to the *P-E* observed for KNN1 in the tetragonal phase above 100 °C (Figure 8.10 (c)). A significant enhancement in strain is observed for L4 with d^*_{33} = 400 pm/V. The *P-E* loops for x = 0.04 show that the coercive field is ~ 2 kV/mm. In comparison to L2, the peaks in *I-E* loops are not sharp for L4 consistent with the tilted *P-E* loops.

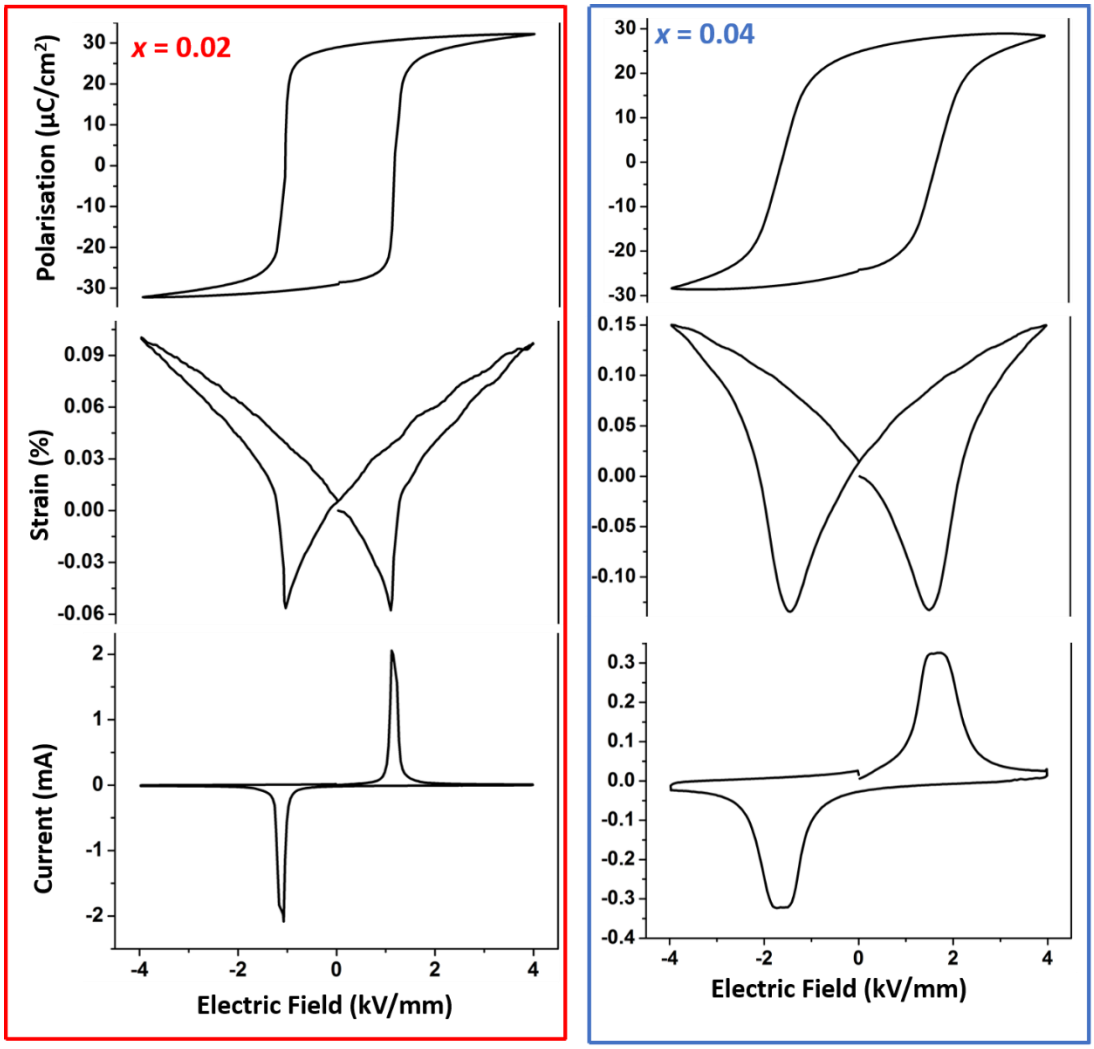

Figure 8.17: *P*, *S* and *I* vs. *E* for sample L2 and L4.

8.3.6 Temperature dependence of piezoelectric coefficients

Excellent room temperature piezoelectric properties were observed for x = 0.04 with d_{33} = 260 pC/N, d^*_{33} = 400 pm/ V and k_p = 46 %. To study the temperature dependence of L4, k_p, P and S were studied as a function of temperature. Figure 8.18 shows planar coupling coefficient as a function of temperature, k_p stable to ~ 60 °C and then decreases monotonically with increase in temperature losing about 45 % of the RT k_p value by 300 °C, similar to the behaviour observed for KNN1 in the tetragonal phase.

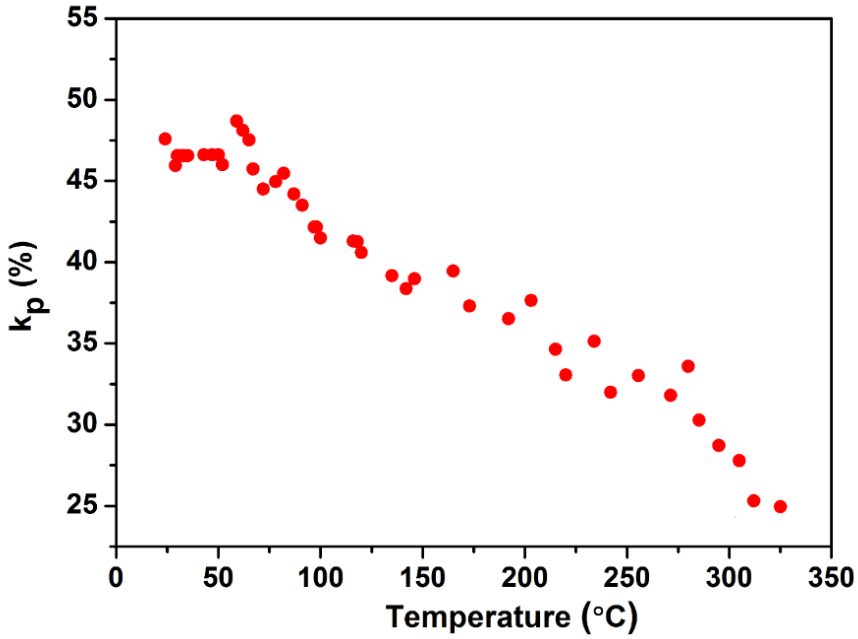

Figure 8.18: k_p as a function of temperature for sample L4.

Figure 8.18 shows that as temperature increases the maximum polarisation decreases along with the overall strain achieved at room temperature. Various parameters as a function of temperature extracted from Figure 8.19 are shown in Figure 8.20. d^*_{33} decreases with increase in temperature and loses about 40 % as temperature increases from RT to 150 °C. At 50 °C , E_c shows an increase in comparison to room temperature, likely associated with the transformation from a mixed O-T phase to tetragonal phase and then decreases with increase in temperature due to increased domain mobility at high temperatures. Remanent polarisation decreases with increase in temperature but shows a

slight increase at higher temperature, which may be due to the values being effected by an increase in conductivity.

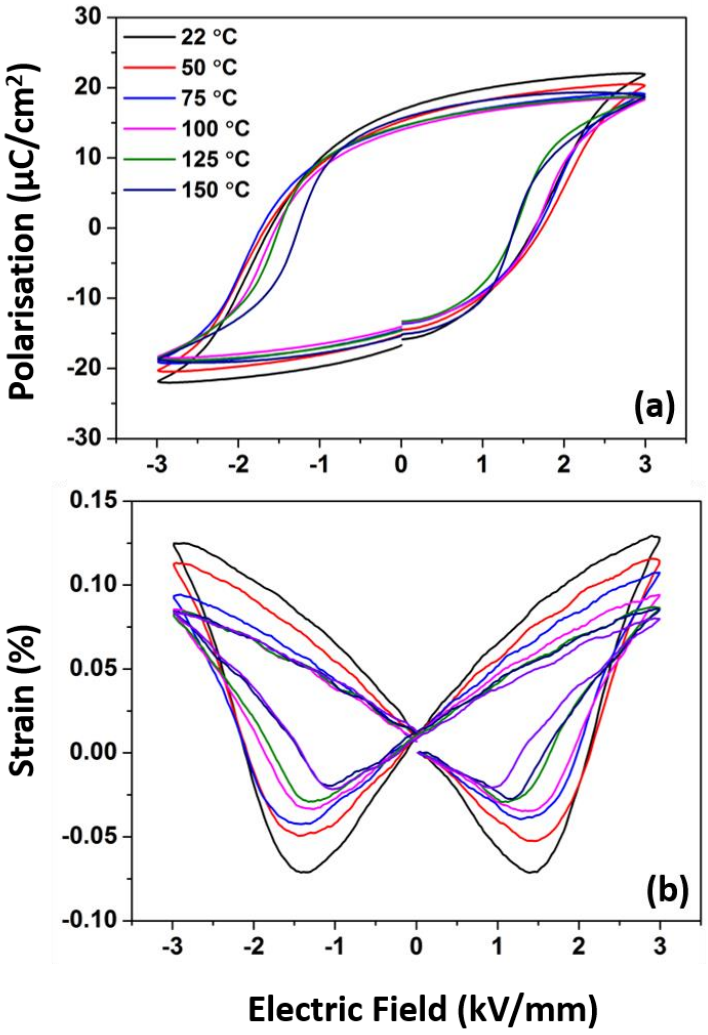

Figure 8.19: *P-E* and *S-E* loops as a function of temperature for sample L4.

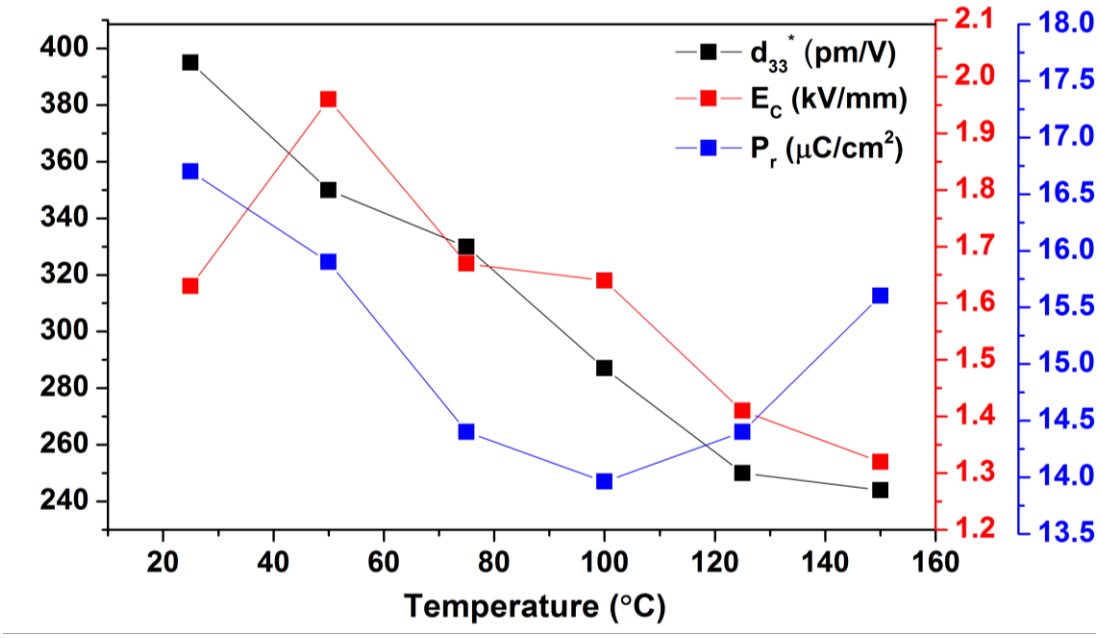

Figure 8.20: d_{33}^* P_r and E_C as a function of temperature for sample L4.

8.4 General Discussion

KNN-based ceramics are preferred because of their high T_C and are clearly better than any other lead-free ceramics on a classical d_{33}/ d_{33}^* vs. T_C plots. However, the d_{33}/ d_{33}^* vs. T_C plots are misleading when it comes to real world applications. For example, L4 shows excellent piezoelectric properties with d_{33} =260 pC/N and d_{33}^* = 400 pm/V with a high T_C of 382 °C. This ceramic will represent itself well on d_{33}/d_{33}^* vs. T_C plot, but *in-situ* measurements show that piezoelectric properties are severely temperature dependent. The premise of this chapter was to compromise the high piezoelectric coefficients for stability by pushing the polymorphic phase out of the operating window and achieve a single tetragonal phase, In this respect BNFT/BF has been shown to be a poor choice since compositions with x > 0.01 % could not be fabricated into dense ceramics. Furthermore, the piezoelectric properties continuously degrade even in the pure tetragonal phase and hence the absence of structural phase transition may not be a sufficient condition to achieve temperature stable properties in KNN-based ceramics. Despite these issues, incentives such as the potential for co-firing with low cost Ni [25] and Cu electrodes [26] internal electrodes make KNN a commercially attractive material for actuator

applications. The enhancement in properties at the PPT is well-established [27], but the extent of enhancement is composition dependent and therefore compositional tailoring with KNN still remains an active area of research. Recently it was reported that $CaZrO_3$ gives rise to a diffuse $T_{O\text{-}T}$ transition leading to an enhancement in temperature stability at high electric field [28]. Therefore, it may be an effective strategy to search out dopants that can promote diffuse $T_{O\text{-}T}$ transitions, which may lead to better temperature stability in KNN-based ceramics. However temperature stability at lower electric fields is yet to be achieved.

8.5 Conclusions

An investigation of the KNN-BF system revealed that dense ceramics were only obtained for $x \leq 0.01$ (KNN1). KNN1 showed optimum properties with d_{33}= 182 PC/N, d^*_{33} = 250 pm/V and k_p = 50 %, $T_{O\text{-}T}$ = 108 °C and T_C = 355 °C. Temperature stability was observed in the orthorhombic phase with k_p showing a variation of ~ 5 % from RT- 90 °C with the variation in d^*_{33} 15 % from RT-75 °C. However, large variations are observed as the temperature approaches the onset of $T_{O\text{-}T}$ with properties monotonically degrading in the tetragonal phase field as T_C is approached. Li doping successfully reduced the $T_{O\text{-}T}$ to room temperature and excellent room temperature piezoelectric properties were observed for L4. However, L4 showed similar trends in degradation of properties, when the sample was exposed to high temperatures. The temperature dependence in the tetragonal phase is not understood but it is proposed that the samples may undergo partial depoling due to changes in domain configuration. For better understanding of the temperature dependence in tetragonal phase, domain structure and polarisation switching needs to be investigated at the microscopic scale using *in-situ* TEM and/or PFM. Regardless of the origins of the temperature dependence, it can be concluded that prospects of achieving temperature stable properties with addition of Li in KNN-BF system over a wide range are slim and further research is required. This study concludes that temperature stability in a limited range can be achieved in KNN-BF as long as $T_{O\text{-}T}$ is ~100-120 °C and that these compositions may find applications in which the temperature remains close to ambient (~100 °C).

8.6 References

[1] W. Liu and X. Ren, "Large piezoelectric effect in Pb-free ceramics," *Phys. Rev. Lett.*, vol. 103, no. 25, p. 257602, 2009.

[2] L. Wu, J. L. Zhang, C. L. Wang, and J. C. Li, "Influence of compositional ratio K/Na on physical properties in $(K_xNa_{1-x})NbO_3$ ceramics," *J. Appl. Phys.*, vol. 103, no. 8, p. 84116, 2008.

[3] J. Tellier, B. Malic, B. Dkhil, D. Jenko, J. Cilensek, and M. Kosec, "Crystal structure and phase transitions of sodium potassium niobate perovskites," *Solid State Sci.*, vol. 11, no. 2, pp. 320–324, 2009.

[4] M. Jiang, X. Liu, and C. Liu, "Effect of $BiFeO_3$ additions on the dielectric and piezoelectric properties of $(K_{0.44}Na_{0.52}Li_{0.04})(Nb_{0.84}Ta_{0.1}Sb_{0.06})O_3$ ceramics," *Mater. Res. Bull.*, vol. 45, no. 2, pp. 220–223, 2010.

[5] D. Wang, F. Hussain, A. Khesro, A. Feteria, Y. Tian, Q. Zhao and I. M. Reaney, "Composition and temperature dependence of piezoelectricity in $(1-x)(K_{1-y}Na_y)NbO_3$-$x(Bi_{1/2}Na_{1/2}ZrO_3)$ lead-free ceramics." *J. Am. Ceram. Soc.*, 2016 (accepted).

[6] W. Feng, H. Du, C. Chen, and Y. Huang, "Electric-Field-Driven Phase Transition Process in $(K,Na,Li)(Nb,Ta,Sb)O_3$ Lead-Free Piezoceramics," *J. Am. Ceram. Soc.*, vol. 99, no. 1, pp. 135–140, 2016.

[7] J. S. Zhou, K. Wang, F. Z. Yao, T. Zheng, J. G. Wu, D. Q. Xiao, J. G. Zhu, and J. F. Li, "Multi-scale thermal stability of niobate-based lead-free piezoceramics with large piezoelectricity," *J. Mater. Chem. C*, vol. 3, no. 34, pp. 8780–8787, 2015.

[8] P. Bomlai, P. Wichianrat, S. Muensit, and S. J. Milne, "Effect of calcination conditions and excess alkali carbonate on the phase formation and particle morphology of $Na_{0.5}K_{0.5}NbO_3$ powders," *J. Am. Ceram. Soc.*, vol. 90, no. 5, pp. 1650–1655, 2007.

[9] H.-C. Song, K.-H. Cho, H.-Y. Park, C.-W. Ahn, S. Nahm, K. Uchino, S.-H. Park, and H.-G. Lee, "Microstructure and Piezoelectric Properties of $(1-x)(Na_{0.5}K_{0.5})NbO_3$– $xLiNbO_3$ Ceramics," *J. Am. Ceram. Soc.*, vol. 90, no. 6, pp. 1812–1816, 2007.

[10] G. Han, J. Ryu, C. W. Ahn, W. H. Yoon, J. J. Choi, B. D. Hahn, J. W. Kim, J. H. Choi, and D. S. Park, "High piezoelectric properties of KNN-based thick films with abnormal grain growth," *J. Am. Ceram. Soc.*, vol. 95, no. 5, pp. 1489–1492, 2012.

[11] W. Jo, D.-Y. Kim, and N.-M. Hwang, "Effect of Interface Structure on the Microstructural Evolution of Ceramics," *J. Am. Ceram. Soc.*, vol. 89, no. 8, pp. 2369–2380, 2006.

[12] K. Wang and J.-F. Li, "$(K,Na)NbO_3$-based lead-free piezoceramics: Phase transition, sintering and property enhancement," *J. Adv. Ceram.*, vol. 1, no. 1, pp. 24–37, 2012.

[13] Y. Zhen and J.-F. Li, “Abnormal Grain Growth and New Core–Shell Structure in (K,Na)NbO_3 -Based Lead-Free Piezoelectric Ceramics,” *J. Am. Ceram. Soc.*, vol. 90, no. 11, pp. 3496–3502, 2007.

[14] M.-S. Kim, S.-J. Jeong, I.-S. Kim, J.-S. Song, and Y.-W. Oh, “($Na_xK_{0.98}$-$xLi_{0.02}$)($Nb_{0.8}Ta_{0.2}$)O_3 Lead-Free Piezoelectric Ceramics,” *Jpn. J. Appl. Phys.*, vol. 48, no. 1, p. 10204, 2009.

[15] V. Lingwal, B. S. Semwal, and N. S. Panwar, “Relaxational Behavior of Mixed $NaNbO_3$-$KNbO_3$ System,” *Ferroelectrics*, vol. 332, no. 1, pp. 219–225, 2006.

[16] L. Egerton and M. dolores Dillon, “Piezoelectric and Dielectric Properties of Ceramics in the System Potassium-Sodium Niobate,” *Mater. Sci.*, vol. 42, no. 9, pp. 438–442, 1959.

[17] E. Jaeger R.E L., “Hot Pressing of Potassium-Sodium Niobates,” *J. Am. Ceram. Soc.*, vol. 45, no. 5, pp. 209–213, 1962.

[18] G. H. Haertling and W. J. Zimmer, “Analysis of hot-Pressing Parameters for Lead Zirconate-Lead Titanate Ceramics Containing Two Atom Percent Bismuth,” *Am. Ceram. Soc. Bull.*, vol. 45, no. 1084–9, 1966.

[19] G. H. Haertling, “Ferroelectric Ceramics: History and Technology,” *J. Am. Ceram. Soc.*, vol. 82, p. 797, 1999.

[20] N. J. Donnelly, T. R. Shrout, and C. A. Randall, “Addition of a Sr, K, Nb (SKN) combination to PZT(53/47) for high strain applications,” *J. Am. Ceram. Soc.*, vol. 90, no. 2, pp. 490–491, 2007.

[21] E. Hollenstein, D. Damjanovic, and N. Setter, “Temperature stability of the piezoelectric properties of Li-modified KNN ceramics,” *J. Eur. Ceram. Soc.*, vol. 27, no. 13–15, pp. 4093–4097, 2007.

[22] F. Rubio-Marcos, J. J. Romero, M. G. Navarro-Rojero, and J. F. Fernandez, “Effect of ZnO on the structure, microstructure and electrical properties of KNN-modified piezoceramics,” *J. Eur. Ceram. Soc.*, vol. 29, no. 14, pp. 3045–3052, 2009.

[23] P. Zhao, B.-P. Zhang, and J.-F. Li, “High piezoelectric d_{33} coefficient in Li-modified lead-free (Na,K)NbO_3 ceramics sintered at optimal temperature,” *Appl. Phys. Lett.*, vol. 90, no. 24, p. 242909, 2007.

[24] Y. Guo, K. Kakimoto, and H. Ohsato, “($Na_{0.5}K_{0.5}$)NbO_3–$LiTaO_3$ lead-free piezoelectric ceramics,” *Mater. Lett.*, vol. 59, no. 2, pp. 241–244, 2005.

[25] H. Hayashi, S. Kawada, M. Kimura, Y. Nakai, T. Tabata, K. Shiratsuyu, K. Nada, and H. Takagi, “Reliability of nickel inner electrode lead-free multilayer piezoelectric ceramics,” *Jpn. J. Appl. Phys.*, vol. 51, no. 9 PART 2, pp. 4–8, 2012.

[26] L. Gao, S.-W. Ko, H. Guo, E. Hennig, and C. A. Randall, “Demonstration of Copper Co-

Fired (Na, K)NbO_3 Multilayer Structures for Piezoelectric Applications," *J. Am. Ceram. Soc.*, vol. 99, no. 6, pp. 2017-2023, 2016.

[27] J. Wu, D. Xiao, and J. Zhu, "Potassium-sodium niobate lead-free piezoelectric materials: Past, present, and future of phase boundaries," *Chem. Rev.*, vol. 115, no. 7, pp. 2559–2595, 2015.

[28] F.-Z. Yao, K. Wang, W. Jo, K. G. Webber, T. P. Comyn, J.-X. Ding, B. Xu, L.-Q. Cheng, M.-P. Zheng, Y.-D. Hou, and J.-F. Li, "Diffused Phase Transition Boosts Thermal Stability of High-Performance Lead-Free Piezoelectrics," *Adv. Funct. Mater.*, vol. 26, pp. 1217–124, 2016.

Chapter 9: Conclusions and Future Work

9.1 Conclusions

This study has resulted in discovery of a new lead-free material based on $K_{1/2}Bi_{1/2}TiO_3$, which not only exhibit temperature stable and fatigue resistant properties superior to all other comparable lead-free materials but also to commercial PZT formulations (see Table 7.2). However on the way to the optimum composition many different compositions were studied which have resulted in some key findings summarised below.

9.1.1 The $(1-x)BiFeO_3$- $xRE_{2/3}TiO_3$ (RE=Nd, La) system

The system with RE = Nd has very limited solubility and a stable perovskite structure cannot be formed with $x \geq 0.03$. For RE = La the stability was improved but the perovskite structure was unstable for $x \geq 0.05$. A-site vacancies compensate for Ti^{4+} in structure and hence at the sintering temperature, $Bi_2Fe_4O_9$ thermodynamically co-exists with the perovskite phase.

9.1.2 The $(0.97-x)BiFeO_3$-$xNdFeO_3$-$0.03Nd_{2/3}TiO_3$ system

Studies on this system revealed that a structural phase transition occurs from ferroelectric *R*3*c* to antiferroelectric *Pbam* at $x = 0.15$ similar to that reported by Karimi et al. for Nd doped $BiFeO_3$ [1]. However, the important finding was that doping of Ti on the B-site results in ceramics with activations energies > 1 eV which are insulating enough to sustain electric fields as large as 7 kV/mm. However, the system did not yield any useful electromechanical strain within the tested region and are not potentially useful for actuator application. Nonetheless, the $PbZrO_3$-like symmetry, low losses and reproducibility of this system makes it a useful lead-free endmember.

9.1.3 The (0.95-*x*)$BiFeO_3$-*x*$LaFeO_3$-0.05$La_{2/3}TiO_3$ system

Studies on this system revealed that a series of structural phase transitions, from *R*3*c* for samples with $x < 0.15$ to *Pbam* ($0.15 < x < 0.30$) and macroscopic *Pnma* phase for $x = 0.35$ with clusters of antipolar order. These ceramics also showed enhanced resistivity in comparison to undoped $BiFeO_3$ and could sustain large electric fields up to 8 kV/mm but the system does not yield usable electromechanical strain within the tested range but, similar to its Nd counterpart, it can be a useful endmember. TEM studies revealed clear aspects of pseudosymmetry in this system, particularly in the vicinity of structural phase transitions, where the local symmetry was found to be lower than the average macroscopic symmetry.

In summary RE dopants on A-site in $BiFeO_3$ stabilise the structure and the issues associated with processing of undoped $BiFeO_3$ are diminished. In addition, RE dopants induce a series of phase transition from ferroelectric to antiferroelectric and then paraelectric phase with increase in dopant concentration. Partial substitution of Fe^{3+} by Ti^{4+} suppress the high conductivities and make application of high electric field possible. More importantly the stoichiometric nature of these compositions excludes the possibility of RE precipitates due to donor doping on the B-site of $BiFeO_3$ [2].

9.1.4 The (1-*x*)$K_{1/2}Bi_{1/2}TiO_3$–*x*(0.8$BiFeO_3$-0.15$LaFeO_3$-0.05$La_{2/3}TiO_3$) system

Studies on this system revealed that the structure transforms from tetragonal at $x = 0$ to pseudocubic at $x \geq 0.04$. The ferroelectric order is gradually disrupted as *x* increases and relaxor-like behaviour is promoted. These changes are accompanied by a gradual decrease in negative strain and an increase in positive strain. Maximum strain value of 0.15 % (6 kV/mm) was obtained at $x = 0.10$ (L10). The optimised composition showed predominantly electrostrictive strain but is not purely electrostrictive which was only achieved in this system at higher concentration of *x* but with a diminished strain values. The maximum strain was found to be temperature stable from RT-175 °C comparable to PZT-based ceramics [3]. In addition, these ceramics have also shown superior fatigue

resistant properties to most PZT-based ceramics after being exposed to 1 million bipolar cycles [4]. Furthermore the optimum composition showed high resistivity (10^5 Ω.cm at 600 °C) which allowed the application of high electric fields at high temperatures.

9.1.5 The (1-*x*)$K_{1/2}Bi_{1/2}TiO_3$–*x*(0.82$BiFeO_3$-0.15$NdFeO_3$-0.03$Nd_{2/3}TiO_3$) system

This system shows similar generic features to its La counterpart, but with superior strain (0.16 % at 6 KV/mm) at the optimum composition (x = 0.09, N9). N9 showed similar temperature stability and was also both electrically insulating and fatigue resistant. Therefore, the optimised composition in this system was chosen for fabrication of prototype multilayer actuator.

9.1.6 MLA based on the composition N9

The multilayer actuator showed similar behaviour to that observed in monolithic ceramics, which demonstrates that multilayer structure can be readily fabricated from the optimised composition using Pt electrodes. However, differences in physical values were observed, which can be diminished by optimisation of the processing techniques. However the key finding was the observation of temperature stable outputs from RT to 300 °C. Furthermore, the MLAs showed a fatigue of only 3 % more than that observed in the bulk ceramics after 1 million bipolar cycles, which makes these ceramics ideal for high temperature actuator applications.

9.1.7 (1-*x*)$K_{0.4}Na_{0.6}NbO_3$–*x*$BiFeO_3$

Study on this system revealed that dense ceramics could not be obtained in this system for x > 0.01. Unlike the KBT-based ceramics, KNN based ceramics are conventional ferroelectrics and hence the strains are mostly from inverse piezoelectricity rather than electrostriction. The addition of BF resulted in shifting of the tetragonal to orthorhombic transition ($T_{O\text{-}T}$) towards room temperature and an optimum strain of 0.05 % (2 kV/mm) was achieved at x = 0.01. In KNN-based ceramics the temperature stability is strongly

hampered by the ferroelectric to ferroelectric phase transition and hence the Curie temperature becomes less important. The orthorhombic phase is temperature stable but as the $T_{O\text{-}T}$ for $x = 0.01$ is ~ 108 °C, the material can only operate close to room temperature. Furthermore, the tetragonal phase in these ceramics does not give temperature stable piezoelectric co-efficients and properties monotonically decrease with increase in temperature.

9.1.8 The $0.99K_{0.4-x}Li_xNa_{0.6}NbO_3$- $0.01BiFeO_3$ system

Studies on this system reveal that enhanced piezoelectric properties can be achieved by bringing the $T_{O\text{-}T}$ near room temperature but the co-existence of the two phases is strongly polymorphic and is not temperature stable [5]. However optimum properties were observed at $x = 0.04$, which yielded a strain a 0.12 % at 3 kV/mm. A major breakthrough in KNN-based ceramics would be formation of temperature independent phase boundary which has so far not been achieved.

9.2 Future work

The aim of the project was to fabricate a lead-free material for actuators that can operate at high temperature comparable to those of conventional piezoelectrics. The target has been largely achieved with the discovery of temperature stable ceramics available in the pseudo-binary solid solution of (1-*x*)KBT-*x*($BiFeO_3$-$REFeO_3$-$RE_{2/3}TiO_3$). However, the material with such interesting properties has given rise to several questions which could not be addressed in the limited time of a PhD. Therefore, a scheme of future work is outlined mainly focused on the optimised compositions L10 and N9. The future work is of interest to both academia and industry.

9.2.1 Technological Needs

In this work, it is demonstrated that N9 and L10 show moderately high strains comparable to PZT-based ceramics and that these ceramics are fatigue resistant and electrically insulating. The first and foremost interest form an industrial perspective will be reproduction of these ceramics at large scales should PbO based compositions fail to attain exemptions in future legislation. Though the temperature stability at high temperature and fatigue resistance at room temperature is promising, real world applications needs to consider other properties as well which may vary from application to application. For example frequency dependence of the electromechanical strain and their behaviour at sub-ambient temperatures. Some applications can be even more demanding, e.g. for fuel injectors material properties such as blocking force, fracture toughness and humidity sensitivity needs to be considered. Therefore, N9 and L10 needs to be assessed for different possible applications. Initial studies on blocking force measurements are already underway and will be completed soon.

9.2.2 Basic Science

Though the materials are very insulating up to 300 °C, there is a sharp rise in tan δ at 350 °C at lower frequency (1 kHz). The conduction mechanism of these materials is not understood at the moment. Therefore, impedance spectroscopy at different oxygen partial pressures need to be carried out to understand the nature of charge carriers and conduction

mechanisms. Once the nature of charge carriers is identified further doping strategies can be adopted to push the operational range even further beyond 300 °C.

A pseudocubic structure is observed by XRD diffraction, however the exact nature of this pseudocubic phase in not fully understood at the moment. A detailed TEM needs to be performed to understand the exact nature of these phases. This work will be focus of intense study in collaboration with Dr Igor Levin at the National Institute of Standards and Technology, Gathersburg, USA.

The temperature stability of these studies is truly unique and therefore *in-situ* structural and microstructural studies with temperature and electric field will be useful to understand the origins of temperature stability in these ceramics.

9.3 References

[1] S. Karimi, I. M. Reaney, I. Levin, and I. Sterianou, "Nd-doped $BiFeO_3$ ceramics with antipolar order," *Appl. Phys. Lett.*, vol. 94, p. 112903, 2009.

[2] I. M. Reaney, I. MacLaren, L. Wang, B. Schaffer, A. Craven, K. Kalantari, I. Sterianou, S. Miao, S. Karimi, and D. C. Sinclair, "Defect chemistry of Ti-doped antiferroelectric $Bi_{0.85}Nd_{0.15}FeO_3$," *Appl. Phys. Lett.*, vol. 100, no. 18, p. 182902, 2012.

[3] S. O. Leontsev and R. E. Eitel, "Progress in engineering high strain lead-free piezoelectric ceramics," *Sci. Technol. Adv. Mater.*, vol. 11, no. 4, p. 44302, 2010.

[4] N. Balke, H. Kungl, T. Granzow, D. C. Lupascu, M. J. Hoffmann, and J. Rödel, "Bipolar fatigue caused by field screening in $Pb(Zr,Ti)O_3$ ceramics," *J. Am. Ceram. Soc.*, vol. 90, no. 12, pp. 3869–3874, 2007.

[5] J. F. Li, K. Wang, F. Y. Zhu, L. Q. Cheng, and F. Z. Yao, "$(K, Na)NbO_3$-based lead-free piezoceramics: Fundamental aspects, processing technologies, and remaining challenges," *J. Am. Ceram. Soc.*, vol. 96, no. 12, pp. 3677–3696, 2013.

10 Appendix I

10.1 Comparison of 0.99KNN-0.01BF and 0.99KNN-0.01BNFT

As a result of the promising properties as an endmember in solid solution with $K_{1/2}Bi_{1/2}TiO_3$, BNFT was tried as an endmember with KNN. However, the BNFT was practically limited $x = 0.01$ with the concentration of Nd and Ti less than the impurities in starting material. Table 10.1 summarises properties of 0.99KNN-0.01BF and 0.99KNN-0.01BNFT. Figure 10.1 and 10.2 gives comparisons between XRD traces and dielectric data respectively. Table 10.1 and Figures 10.1 and 10.2 illustrate that the role of Nd and Ti is negligible, justifying eliminating them as part of further study.

Table 10.1: Comparison of properties between 0.99KNN-0.1BF and 0.99KNN-0.01BNFT

Property	**0.99KNN-0.01BF**	**0.99KNN-0.01BNFT**
Relative density	**97 %**	**95 %**
d_{33} (pC/N)	**182**	**170**
d^*_{33} (pm/V)	**250**	**270**
k_p (%)	**50**	**45**
$T_{O\text{-}T}$ (°C)	**108**	**108**
T_C (°C)	**356**	**344**

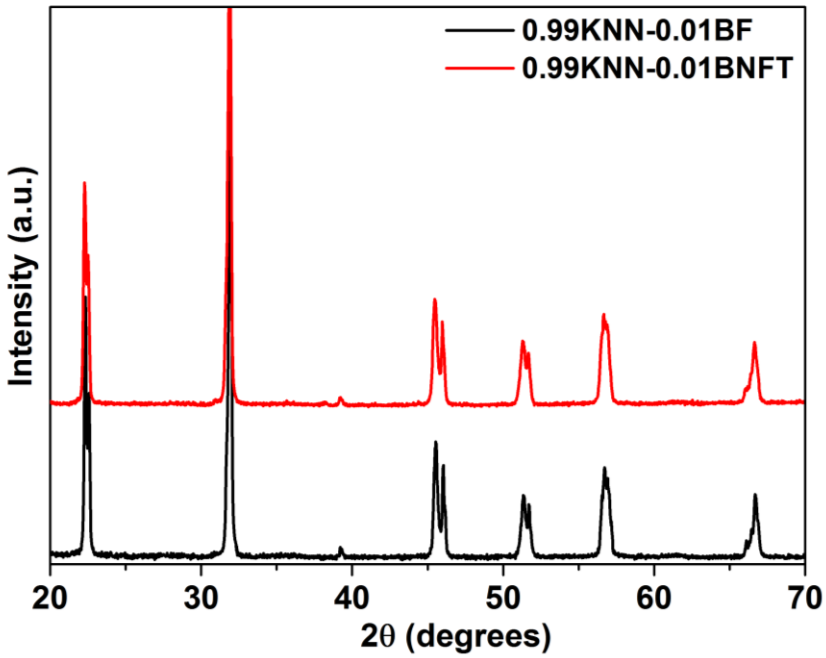

Figure 10.1: Room temperature XRD traces for 0.99KNN-0.1BF and 0.99KNN-BNFT.

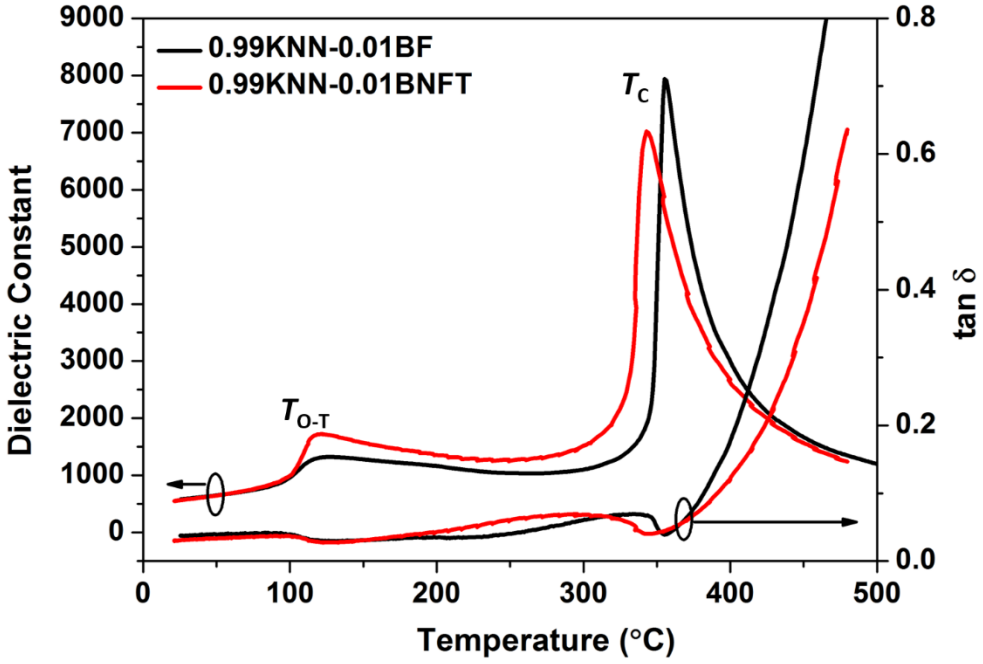

Figure 10.2: Dielectric constant and tan δ for 0.99KNN-0.1BF and 0.99KNN-BNFT.